Growth, characterization and phase transformation in YMnO3 thin films

Ionela Iliescu

UNIVERSITÉ DE GRENOBLE

THÈSE

Pour obtenir le grade de

DOCTEUR DE L'UNIVERSITÉ DE GRENOBLE

Spécialité : **Matériaux, Mécanique, Génie civil, Electrochimie**

Arrêté ministériel : 7 août 2006

Présentée par

Ionela ILIESCU

Thèse dirigée par **Michel BOUDARD**

préparée au sein du **Laboratoire des Matériaux et du Génie Physique, UMR 5628 CNRS/Grenoble INP**
dans **l'École Doctorale I-2MEP2 : Ingénierie – Matériaux, Mécanique, Environnement, Energétique, Procèdes, Production**

Croissance, caractérisation et transformation de phase dans des couches minces d'$YMnO_3$

Thèse soutenue publiquement le **19 février 2015**,
devant le jury composé de :

M. Valentin CRACIUN
Directeur de recherche, INFLPR, Bucarest (Président)
M. Octavio PEÑA
Directeur de recherche, ISCR Rennes (Rapporteur)
M. José SANTISO LÓPEZ
Directeur de recherche, ICN2 Barcelona (Rapporteur)
M. Stéphane PIGNARD
Professeur, LMGP-INP (Membre)
Mme. Odette CHAIX-PLUCHERY
Chargée de Recherche, LMGP-CNRS (Membre)
M. Michel BOUDARD
Chargé de Recherche, LMGP-CNRS (Membre)

To my parents,

to Andrei

Remerciements

Ce travail de thèse a été réalisé au Laboratoire des Matériaux et du Génie Physique à Grenoble. Je remercie son directeur Franz Bruckert et ex- directeur Bernard Chenevier pour m'avoir accueillie dans le laboratoire.

Je tiens à remercier vivement mon directeur de thèse Michel Boudard d'avoir encadré mon travail. Merci d'avoir été présent pour me guider dans mon travail de recherche, pour votre optimisme qui m'a motivée pendant ces trois années pour tous les conseils et la patience et en fin pour les discussions agréables autour d'un thé. Vous m'avez beaucoup appris.

Je remercie également tous les membres de mon jury. Merci à Octavio Peña et José Santiso qui ont accepté la charge d'être rapporteurs, merci pour le temps consacré à la lecture de ce manuscrit. Merci également à Valentin Craciun, Stéphane Pignard et Odette Chaix qui ont accepté d'examiner ce manuscrit et de faire partie de mon jury de thèse.

Je remercie tous les permanents du LMGP, pour leur accompagnement pendant cette thèse.

Merci beaucoup à Odette Chaix pour son aide avec les mesures et les données Raman et la lecture et re-lecture des articles publiés, les commentaires pertinents et tous les conseils et son temps.

Merci à Stephane Pignard de m'avoir initié à la technique MOCVD et de m'avoir aidé aux premiers dépôts.

Merci à Hervé Roussel toujours prêt à rendre service, pour les mesures RSM, pour ses explications très pédagogiques.

Merci à Béatrice Doisneau pour l'aide avec l'analyse EDX et pour toutes les discussions agréables autour du microscope.

Merci à Laetitia Rapenne pour l'aide avec le TEM et l'acquisition des images.

Merci à Patrick Chaudouet de m'avoir formé sur le SEM au début de cette thèse et les conversations intéressantes.

Merci à Carmen Jiménez pour avoir résolu les problèmes sur les réacteurs de dépôt MOCVD.

Je remercie à Mikhail Anikin pour m'avoir aidé à résoudre les problèmes liés au dépôt MOCVD.

Merci à Jean-Luc Deschanvres pour les explications du fonctionnement du logiciel Stratagem.

Merci à Matthieu Jouvert pour les mesures AFM.

Merci à tous les autres permanents du laboratoire (Erini Sarigiannidou, Daniel Bellet etc.) avec qui ça a été agréable de discuter.

Enfin, merci au personnel administratif et de support: Michèle San Martin, Josiane Viboud, Arnaud Robin, Anne Fracchia, Nicole Douard, Virginie Charrière.

Merci à tous les collaborateurs extérieurs.

Tout d'abord un grand merci au laboratoire INFLPR, département Laser de Bucarest (Roumanie) qui m'a accueillie pour un petit stage, permettant l'élaboration d'échantillons par PLD. Je remercie Ion Mihailescu, le directeur du laboratoire pour sa gentillesse et le temps accordé. Je suis très reconnaissante à Felix Sima, qui m'a proposé cette collaboration et qui a fait tout son possible pour m'aider et également à Gabriel Socol. Merci de m'avoir initié au PLD et aussi pour le temps agréable passé « chez moi ».

Merci à l'Institut Néel et en particulier à Eric Eyraud de m'avoir formée à la manipulation du SQUID et à Yves Deschanels pour la formation BS2. Merci à Didier Dufeu pour l'aide autour de ces instruments.

Merci à Florence Robaut pour les mesures de microsonde et pour l'analyse d'une partie de données.

Merci à tous les non-permanents du laboratoire avec qui j'ai passé des moments agréables ou qui m'ont aidé. Merci à mes collègues Alejandro Schulman et José Luis Ampuero pour l'élaboration d'une partie des échantillons céramique.

Merci à Nikos Tsavdaris, Yun Ji Shin, Kanaparin Ariyawong, Sophie Guillemin, Daniel Langley, Sven Tengeler, Tuyen Nguyen, Romain Parize, Mélanie Lagrange, Pauline Serre, Renaud Viennet, Martin Seiss, Fabiana Saporiti, Nicholas DiLuozzo, Louis Fradetal, Lijie He, Shanting Zhang, Lu Shi…

Table of contents

List of abbreviations ……iv
General introduction ……..……1
1. Introduction to multiferroic $YMnO_3$ ……..…..3
1.1 Context ……....4
1.2 Introduction to $RMnO_3$ family. $YMnO_3$ as a rare earth manganese oxide ……....8
1.3 Phase stability of $YMnO_3$ ……12
1.4 Hexagonal $YMnO_3$ phase ……14
1.4.1 Magnetism in hexagonal $YMnO_3$ phase ……14
1.4.2 Ferroelectricity in hexagonal $YMnO_3$ phase ……15
1.5 Orthorhombic $YMnO_3$ phase ……....16
1.5.1 Magnetism in orthorhombic $YMnO_3$ phase ……...18
1.5.2 Ferroelectricity in orthorhombic $YMnO_3$ phase ……20
1.6 Literature review in $YMnO_3$ thin films ……21
1.6.1 Hexagonal $YMnO_3$ films ……...21
1.6.2 Orthorhombic $YMnO_3$ films ……..26
References ……..29
2. Experimental techniques ……..…..38
2.1 Elaboration techniques ……..39
2.1.1 Pulsed-Injection Metal Organic Chemical Vapor Deposition (PI-MOCVD) …39
2.1.2 Pulsed Laser Deposition (PLD) ……46
2.1.3 Solid state reaction technique ……47
2.1.4 Single crystal growth ……48
2.2 Characterization techniques ……..48
2.2.1 Structural characterization……..48
2.2.1.1 X-Ray diffraction (θ-2θ scans, GIXRD, XRR, RSM) ……..48
2.2.1.2 Raman spectroscopy ……55
2.2.2 Microstructural and surface characterization ……56
2.2.2.1 Scanning Electron Microscopy (SEM) ……56
2.2.2.2 Transmission Electron Microscopy (TEM) ……..57
2.2.2.3 Atomic Force Microscopy (AFM) ……59
2.2.3 Chemical composition analysis ……..60
2.2.3.1 Energy-Dispersive X-ray spectroscopy (EDX) ……60
2.2.3.2 Electron Probe Microanalysis (EPMA) ……60
2.2.4 Physical characterization: SQUID magnetometry ……62
References ……...64
3. $YMnO_3$ film deposition and process optimization ……65
3.1 The choice of the substrate ……...66
3.2 MOCVD deposition ……..68
3.2.1 Choice of deposition temperature ……..70
3.2.2 Choice of Y and Mn atomic concentrations in the injected solution ……....75
3.3 PLD deposition ……78
3.4 Determination of the film thickness and chemical composition ……...79
3.5 Summary and conclusions ……83

References ……...84
4. Structural and magnetic characterization of $YMnO_3$ films on Si (100) substrates …….85
4.1 Characterization of amorphous as-deposited YMO films ……86
4.1.1 Structural characterization of amorphous as-deposited YMO films ……86
4.1.2 Magnetic characterization of amorphous as-deposited YMO films ……91
4.2 Characterization of hexagonal as-deposited YMO films ……..93
4.2.1 h-YMO films elaborated in the horizontal PI-MOCVD setup ……...93
4.2.2 h-YMO films elaborated in the vertical PI-MOCVD setup ……100
4.2.3 h-YMO films elaborated by PLD ……103
4.2.4 Magnetic characterization of h-YMO films ……106
4.3 Characterization of orthorhombic as-deposited YMO films ……..111
4.3.1 o-YMO films elaborated by PI-MOCVD……111
4.3.2 o-YMO films elaborated by PLD ……119
4.3.3 Magnetic characterization of o-YMO films ……122
4.4 Summary and conclusions ……123
References ……126
5. Phase transformations and thermal stability studies in $YMnO_3$ films on Si(100) substrates ……...128
5.1 Phase transformations in amorphous as-deposited YMO films ……..129
5.1.1 Ex-situ heat treatments on as-deposited amorphous YMO films ……129
5.1.2 In-situ Raman experiment on as-deposited amorphous YMO film ……134
5.1.3 In-situ TEM experiment on as-deposited amorphous YMO film ……138
5.2 Stability of the as-deposited o-YMO phase ……140
5.2.1 In-situ Raman experiment on as-deposited o-YMO film ……140
5.3 Magnetic characterization ……...143
5.4 Discussion and summary ……146
References ……148
6. Epitaxial orthorhombic $YMnO_3$ films grown on (100)-perovskite substrates ($SrTiO_3$, $LaAlO_3$ and $(LaAlO_3)_{0.3}(Sr_2AlTaO_6)_{0.7}$) ……..149
6.1 Structural study of epitaxial o-YMO thin films ……..151
6.2. Magnetic characterization ……..170
6.3. Structural study of non-stoichiometric YMO films ……...172
6.4. Magnetic characterization of non-stoichiometric YMO films ……...181
6.5 Summary and conclusions ……..182
References ……184
General conclusions ……..185
Appendix A ……190
Appendix B ……193
Appendix C ……195
Appendix D ……198
Appendix E ……200
Appendix F ……202
Appendix G ……203
Publication list ……...205
Résumé français ……206

List of abbreviations

Abbreviations

ABO_3	general formula of perovskites
AFM	Atomic Force Microscopy
BSE	Backscattered Electrons
EDX	Energy-Dispersive X-ray spectroscopy
ED	Electron Diffraction
EPMA	Electron Probe Microanalysis
FC	Field Cooled
FEG-SEM	Field Emission Gun Scanning Electron Microscopy
FFT	Fast Fourier Transform
FWHM	Full Width at Half Maximum
HRTEM	High Resolution Transmission Electron Microscopy
LAO	$LaAlO_3$ (Lanthanum Aluminate)
LSAT	$(LaAlO_3)_{0.3}(Sr_2AlTaO_6)_{0.7}$
MOCVD	Metalorganic Chemical Vapor Deposition
PI-MOCVD	Pulsed Injection Metalorganic Chemical Vapor Deposition
PLD	Pulsed Laser Deposition
SAED	Selected Area Electron Diffraction
SE	Secondary Electrons
SQUID	Superconducting Quantum Interference Device
STO	$SrTiO_3$ (Strontium Titanate)
TEM	Transmission Electron Microscopy
tmhd	2,2,6,6-tetramethylheptane-3,5-dionate
WDS	Wavelength Dispersive Spectroscopy
XRD	X-Ray Diffraction
YMO	$YMnO_3$ (yttrium manganese oxide)
ZFC	Zero Field Cooled

Latin symbols

c	concentration
C	composition
d	interatomic distance
D	diffusion coefficient
E	electric field/ electron energy
H	magnetic field
I	intensity
J	atom diffusion coefficient
k	Cliff-Lorimer factor
K	Scherrer factor
L	crystallite size
M	magnetization
n	diffraction order
p	pressure
P	polarization

R	rare earth, Y and Sc
R_e	Reynolds number
T	temperature
T_N	Néel temperature
T_C	Curie temperature

Greek symbols

β	FWHM
ε	strain
θ	Bragg angle
λ	wavelength
ρ	mass density
μ	viscosity
σ	stress
ω_c	critical angle

General introduction

The multiferroics are multifunctional materials with great potential for electronic applications. Besides the attractive technological applications, the multiferroic materials are very interesting and rich from a fundamental point of view due to the strong electronic correlations present in these systems. The multiferroics possess several so-called ferroic orders: (anti-) ferromagnetism, (anti-) ferroelectricity and/or ferroelasticity. The understanding of the mutual coupling between these properties is the subject of a lot of research and development. Each new multiferroic is a challenge in the interpretation of the microscopic origin of the ferroic mechanisms. In order to provide new coupling mechanisms and tunable properties, the scientific work in the last two decades was concentrated on artificial multiferroics as composite materials or as thin films, multilayers and nanostructures. Giant room temperature magnetoelectric and magnetocapacitance effects were found in perovskite $TbMnO_3$ by Kimura et al. Since then, an extensive study on perovskite-type materials has been carried out. At the same time, the number of potential applications and devices has increased. One of the most popular is the 4-state memory device, which is based on the control of the ferroelectric polarization (P) by a magnetic field and, inversely, the switching of magnetization (M) by an electric field. Therefore, four distinct memory states are possible (+P, -P, +M, -M).

Motivated by these attractive properties, we have been interested in a representative member of rare earth manganite ($RMnO_3$): $YMnO_3$. This compound is multiferroic in both hexagonal and orthorhombic (perovskite) structure below ~ 70 K and ~ 40 K, respectively. Although these temperatures are too low for the technological applications, we may expect to be able to modify these ordering temperatures. In fact, through the crystalline structure and microstructural characteristics, the properties of the films are often tuned by the effect of the substrate.

During this thesis, both hexagonal (considered as stable) and orthorhombic (generally regarded as metastable) $YMnO_3$ phases were investigated in the form of thin films. Initially, we have studied how the non-epitaxial growth on silicon substrates affects the microstructure of the orthorhombic and hexagonal $YMnO_3$ films. Contrary to the literature general belief, we were puzzled to find that the metastable orthorhombic $YMnO_3$ phase was easily obtained on silicon substrates by two different deposition methods (MOCVD and PLD). Further, we put to the test the stability of the orthorhombic $YMnO_3$ phase by thermal annealing and we have observed that this phase in stable

in a particular temperature range. In a second stage, we have studied the epitaxial growth of the orthorhombic $YMnO_3$ phase on different perovskite-type substrates (STO, LAO and LSAT).

The work during this thesis is organized in six chapters as follows:

Chapter 1 introduces the reader in the field of multiferroics, explains the main mechanism of ferroelectricity and magnetism, the principal types of multiferroic materials with focus then on rare earth manganites. A review on $YMnO_3$ is given with emphasis on the state-of-the-art on thin films on both polymorphs.

In Chapter 2 are described the experimental methods and characterization techniques used during this thesis. Firstly, the deposition (MOCVD, PLD) and the solid state synthesis techniques are presented. Afterwards, the techniques used to characterize the structure, microstructure, composition and magnetic properties are detailed.

The deposition conditions and their optimization are presented in Chapter 3, with emphasis on the selective growth of either hexagonal or orthorhombic $YMnO_3$ phase.

Chapter 4 is focused on the characterization from different perspectives of amorphous, hexagonal and orthorhombic $YMnO_3$ films on silicon substrates.

In chapter 5 the results concerning the stabilization of orthorhombic $YMnO_3$ phase are presented. The phase transformation from amorphous to orthorhombic $YMnO_3$ films is illustrated by temperature-dependent experiments and the results are commented.

The epitaxial growth of the orthorhombic $YMnO_3$ phase on perovskite-type substrates is presented in Chapter 6.

Finally, this work ends with the summary and the general conclusions of the thesis.

Chapter 1

Introduction to multiferroic $YMnO_3$

Summary

1.1 Context ……4

1.2 Introduction to $RMnO_3$ family. $YMnO_3$ as a rare earth manganese oxide ……8

1.3 Phase stability of $YMnO_3$ ……12

1.4 Hexagonal $YMnO_3$ phase ……14

1.4.1 Magnetism in hexagonal $YMnO_3$ phase ……14

1.4.2 Ferroelectricity in hexagonal $YMnO_3$ phase ……15

1.5 Orthorhombic $YMnO_3$ phase ……16

1.5.1 Magnetism in orthorhombic $YMnO_3$ phase ……18

1.5.2 Ferroelectricity in orthorhombic $YMnO_3$ phase ……20

1.6 Literature review in $YMnO_3$ thin films ……21

1.6.1 Hexagonal $YMnO_3$ films ……21

1.6.2 Orthorhombic $YMnO_3$ films ……26

References ……29

This chapter covers the basics of multiferroicity, the magnetic and ferroelectric materials of perovskite structure and their main applications. The stability of the rare earth manganese oxides family is also discussed with a particular emphasis on $YMnO_3$ and its two possible forms: orthorhombic and hexagonal. Moreover, the aim of this thesis being the growth of $YMnO_3$ thin layers, a literature review on this topic is presented, identifying the main properties of this material.

1.1 Context

The increasing demand for new functional materials, notably in the field of data storage and spintronics, has led to an intensified research in the last two decades. One of the most attractive candidates for this type of applications are the oxides, among which the ternary manganese oxides of $AMnO_3$ type play a key role. Some of these materials possess two or more spontaneous ferroic orders in the same phase and in the absence of external fields, called multiferroicity. These forms of ferroic order are ferromagnetism, ferroelectricity and ferroelasticity which were recently completed by ferrotoroidicity (spontaneous magnetic vortex) as new member in the family. Ferroic materials are characterized by a spontaneous order, whose direction can be switched by an external field: a ferromagnet is described by a spontaneous magnetization (M) and displays hysteresis under an applied magnetic field (H), a ferroelectric has a spontaneous polarization (P) and shows hysteresis under an applied electric field (E) and a ferroelastic possess a spontaneous strain (ε) and exhibits hysteresis under an applied stress (σ). Figure I.1 summarizes the couplings and cross-couplings existing in ferroics and multiferroics. Magnetization, polarization and strain are controlled through the magnetic field, electric field and stress respectively. In a multiferroic, the coexistence of at least two orders leads to additional cross-couplings.

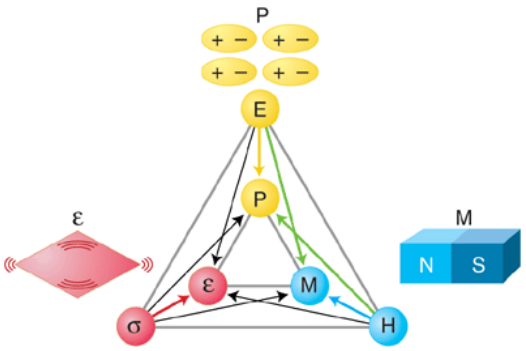

Fig*ure I.1. Schematic diagram showing the control coupling in ferroics and multiferroics. Note that ferrotoroidicity is not included (from [1]).*

For example, the polarization can be controlled by a magnetic field or by stress; similarly the magnetization can be tuned by electric fields or stress. In this manuscript, without further specification, the multiferroicity will denote the coexistence of magnetism and ferroelectricity. In

the following, a brief introduction on multiferroic materials is presented. The main goal is to give an overview of the subject; the details can be found in the cited papers.

Another example of functional properties coexistence are in the magnetoelectric materials which exhibit a coupling between magnetic and electric order parameters. It is important to note that, although magnetoelectrics present a coupling of magnetism with ferroelectricity, they are not synonyms with multiferroics. Two counter-examples are Cr_2O_3, which is a magnetoelectric antiferromagnet without electric ordering, and hexagonal $YMnO_3$ which is a ferroelectric antiferromagnet in which magnetoelectric effect is forbidden by symmetry. Thus, the magnetoelectric coupling can exist independently of the nature of magnetic or electric orders. Figure I.2 epitomizes the relation between multiferroic and magnetoelectric materials. More about multiferroics and magnetoelectrics can be found in the Eerenstein et al.'s [2] review on this subject.

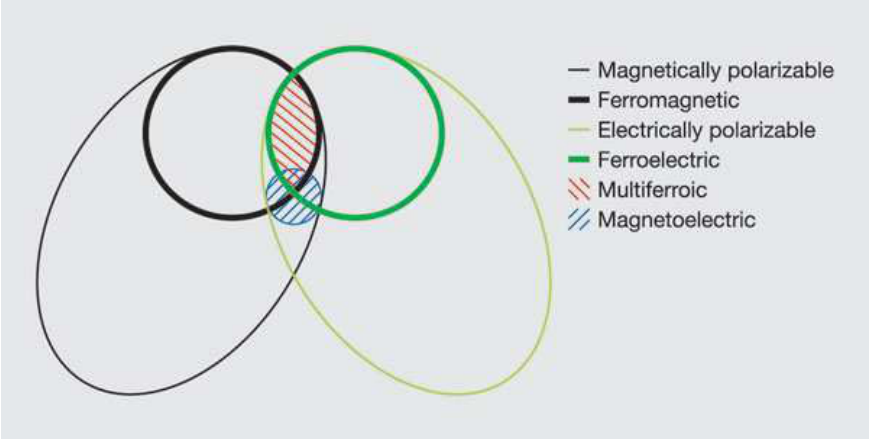

Figure I.2. The relation between the properties of multiferroic and magnetoelectric materials (from [2]).

Firstly conjectured by P. Curie and then reconsidered by P. Debye and L. Landau, the rigorous theory of magnetoelectricity reaches its final form with the prediction of I. Dzyaloshinskii on magnetoelectric effect in Cr_2O_3, experimentally proven a few months later by D.N. Astrov. Comparatively, the history of multiferroics is more recent. The term multiferroic was first used by H. Schmidt in 1994, although some multiferroic materials (previously named magnetic ferroelectrics) have been known to exist from the 1960s [3]. Since then, scarce studies have been made in the next decades mainly because of the limited choice of compounds, the lack of general theoretical concepts and, finally, because of the insufficient perspectives regarding practical

applications. The revival of the field started in the 2000s with some resonant publications as those of Nicola A. Spaldin and Manfred Fiebig [1] as well as the corroborated efforts of the scientific community. The interest in these types of ferroic materials is motivated by their potential of exhibiting considerable coupling effects between the magnetic and ferroelectric state. This may be the basis of new devices where the magnetic switching is controlled by electric voltages and not magnetic fields [4]. Furthermore, thin films multiferroics have experienced a progress in the growth, characterization and understanding of their properties which is a further step toward their incorporation into practical devices [5]. Contrary to the bulk form, in multiferroic films the properties are easy to tailor through epitaxial strain or atomic engineering of interfaces and crystal chemistry.

The search and synthesis of multiferroic materials has proven to be a difficult problem, as the ferroic orders seems to be mutually exclusive. Indeed, while a ferroelectric material must be an insulator, a ferromagnetic material is generally a conductor. As far as the electronic chemistry of the compound is concerned, there is also an antagonism: the magnetism requires the presence of localized electrons, mostly in the partially filled *d* or *f* shells of transition-metal, while most of ferroelectrics must have a d^0-type electron configuration of transition ions. In regard to the symmetry, ferromagnets need the broken time symmetry and spatial invariance. In contrast, ferroelectricity possesses time invariance and broken spatial symmetry as a structural distortion is necessary for the emergence of polarization. Furthermore, simultaneous presence does not guarantee strong coupling, as the microscopic mechanisms of ferroelectricity and magnetism are quite different [6].

These microscopic mechanisms governing the multiferroic coupling are complex and a lot of research was done in this direction. The obtained results have permitted to classify the multiferroics in two categories: type-I (known as proper multiferroics) and type-II (improper multiferroics) [7] [8]. If the microscopic origin of magnetism is quite well understood and basically the same for all magnets, i.e. localized electrons in partially filled *d* or *f* shells of the transitional metals or rare earths, in the case of ferroelectrics things are more complicated. Several different sources have been identified and have conducted to the previous classification. Thus, in type-I multiferroics, ferroelectricity and magnetism have different sources and are independent. This also implies different transition temperature (close or above room

temperature) and usually weak coupling between the two (e.g. $BiFeO_3$, hexagonal $YMnO_3$ etc.). Ferroelectricity can be caused by the presence of transition metal with *d* empty configuration ($BaTiO_3$), charge ordering, lone pairs (due to Bi^{3+}, Pb^{2+}) or geometric ferroelectricity by rotation of rigid Mn-O polyhedra ($YMnO_3$). There are several subtypes, depending on the mechanism of ferroelectricity in them, assorted by group of materials [7]:

- Perovskites ($BaTiO_3$, $Pb(ZrTi)O_3$), in which ferroelectricity is caused by the off-center shifts of the transition metal covalent bond with oxygen.
- Lone pairs materials ($BiFeO_3$, $BiMnO_3$, $PbVO_3$) in which Bi^{3+} and Pb^{2+} induce ferroelectricity. The *6s* electrons, that do not participate in the chemical bonds, have a high polarizability and the ordering of these lone pairs in one direction give rise to ferroelectricity.
- Charge ordering materials ($LuFe_2O_4$, $(PrCa)MnO_3$, Fe_3O_4, $RNiO_3$) in which ferroelectricity is often observed in compounds with different valences of transition metals. The alternation of ions with different valences generates inequivalent sites and bonds, and thus, a polarization.
- Geometric ferroelectric materials ($YMnO_3$) in which ferroelectricity is due to rotations and tilting of block structures. In the case of hexagonal $RMnO_3$ materials, the MnO_5 trigonal bipyramid tilts and rotates in order to ensure the closest packed structure. These structural modifications result in loss of inversion symmetry in the structure and promote ferroelectricity.

In type-II multiferroics, ferroelectricity and magnetism are strongly coupled because magnetic order causes ferroelectricity, thus this type exists only in the ordered magnetic state. In 2003, Kimura et al. [9] first reported in $TbMnO_3$ the presence of spontaneous polarization when the transition in the magnetized state occurs. A similar effect was observed for $TbMn_2O_5$ by Hur et al. [10]. Since then, a variety of type-II multiferroics materials showing this effect have been discovered. Although presenting a strong coupling between ferroic orders, the application potential of these materials is reduced due to the low coexistence temperatures. From the generating mechanism point of view, improper type-II multiferroics are divided into spiraling cycloid type and collinear type:

- Spiral type in which ferroelectricity appears when a magnetic spiral cycloid phase establishes. The mechanism, related to spin-orbit coupling is also based on symmetry violation, required for ferroelectricity.
- Collinear type materials, where ferroelectricity is based on magnetostriction. A chain of alternating charges with opposite structures, through magnetostrictive effect shorts the (anti)ferromagnetic bonds, producing a polarization.

1.2 Introduction to $RMnO_3$ family. $YMnO_3$ as a rare earth manganese oxide

Among all multiferroic materials, within the framework of this thesis we are interested in rare earth manganites and, in particular, to $YMnO_3$. In this section, the $RMnO_3$ compounds family are introduced and their structural properties and phase diagram are given with focus on $YMnO_3$.

$RMnO_3$ (R= rare earth, Y or Sc) family crystallizes in two types of crystalline structures at ambient conditions: orthorhombic or hexagonal. Note that yttrium has often been classified as a rare earth element and behaves chemically identical to the lanthanide series, with a radius between that of dysprosium and holmium. Hence, when referring to rare earth manganite, yttrium (and scandium) manganites will be denoted too. The orthorhombic structure (Figure I.5a) of $GdFeO_3$-type (space group *Pnma* or *Pbnm*, depending on the choice of symmetry axes) occurs for large ionic radii of R (R= La-Dy). This structure is derived from the ideal cubic perovskite structure of general formula ABO_3, where A and B are large and small cations, respectively, shown in Figure I.3.

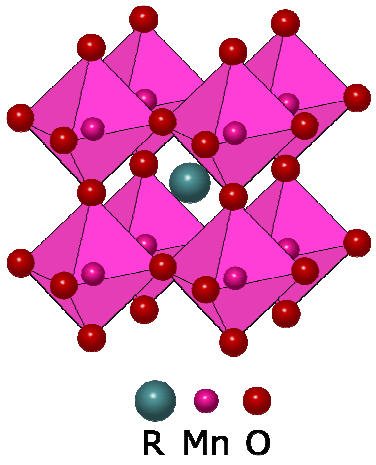

Figure I.3. The ideal perovskite cubic structure (after [11]).

Cubic perovskites are based on a cubic close packing of AO_3 with B cations in octahedral positions. Each A cation is equidistantly coordinated by twelve O anions and each B cation is coordinated to six O anions, arranged at the corners of a regular octahedron. Thus, the O anions are neighboring two B cations and four A cations. This network generates empty space around A ions, which is surrounded by eight BO_6 octahedrons. If the ideal perovskite structure is characteristic for materials such as $SrTiO_3$, in the case of rare-earth manganites it is distorted. This distortion is linked to the structural frustration as a result of different ionic sizes of R and Mn. An indicator for the stability of a perovskite structure is given by the Goldschmidt tolerance factor. The compatibility with the structure is achieved if the A radii matches in size with the O^{2-} anions to form cubic close-packed layers and B cations fit into the interstitial sites formed by O^{2-} anions in order to have a corner-shared BO_6 octahedra. Under this condition, the ionic radii of A, B and O must satisfy the relation:

$r_A + r_O = \sqrt{2}(r_B + r_O)$. The Goldschmidt tolerance factor is defined as $t = \frac{r_A + r_O}{\sqrt{2}(r_B + r_O)}$ [12]. For an ideal perovskite t=1, while for distorted perovskites (t < 1), other crystal geometries such as orthorhombic or rhombohedral become favorable because A cations are too small to fully occupy the BO_6 interstices. As a result, the octahedra will tilt in order to reduce the empty space inside BO_6 interstices. If t > 1, A cations are too big to fit the BO_6 interstices and the structure accommodates to other symmetries with different building blocks. As an experimental fact, the Goldschmidt tolerance factor for almost all known perovskites ranges between 0.75 and 1. Due to the fact that it is based on empirical concepts, the t factor is not a sufficient condition for the formation of the perovskite structure and exceptions from this rule exists even in the most favorable range (see further).

The structure of rare earth manganite $RMnO_3$ is strongly affected by the size of the rare earth element and the temperature (see Figure I.4). A comparative structural description of orthorhombic and hexagonal structures, illustrating the building blocks of each structure, is shown in Figure I.5.

Hexagonal structure (space group $P6_3cm$) is more energetically favorable, i.e. stable, for small ionic radii of $RMnO_3$ family (R=Y, Ho-Lu). In this case, the BO_6 octahedra transforms into BO_5 trigonal bypiramids. Each B ion is surrounded by three in-plane and two apical O anions,

forming the BO_5 trigonal bypiramids which are separated by planes of A cations, 8-fold coordinated.

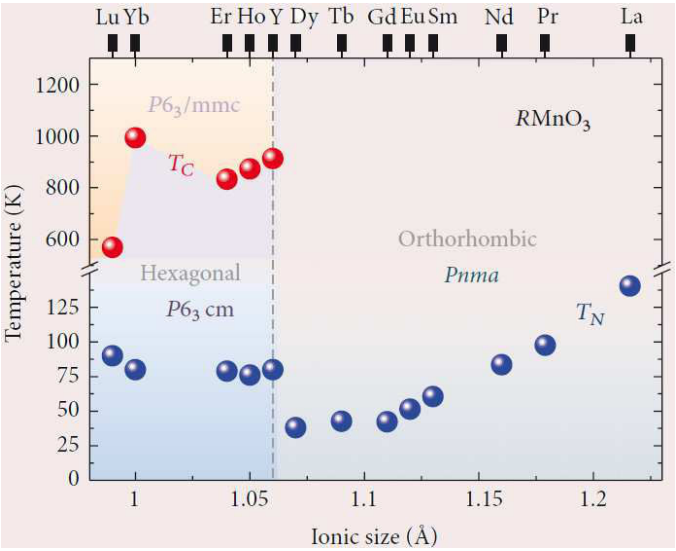

Figure I.4. Crystalline structure of the $RMnO_3$ depending on the ionic size of the rare earth (from [13]) and the Néel temperature (T_N) and Curie temperature (T_C) .

In other words, the structure can be described by stacks of ABCACB dense oxygen planes. Figure I.4 summarizes the structural (lattice symmetry) and physical properties (Néel temperature - T_N, Curie temperature - T_C) of the $RMnO_3$ family depending on the size of the R ion.

Although each crystal structure is itself very stable, small modifications in the A and B site, non-stoichiometry, doping, synthesizing conditions etc. are sufficient to change the properties of the compound. For example, the magnetic order changes from E-type to A-type (see Figure I.13) when increasing the ionic radius of A-site from Lu to La [14]. Similarly, the *b* and *c* parameters of the orthorhombic structure increase when increasing the size of the rare earth while the mean tilting angle of the MnO_6 octahedra decreases [15]. In the following, a detailed description of the structural and physical properties of $YMnO_3$ is given.

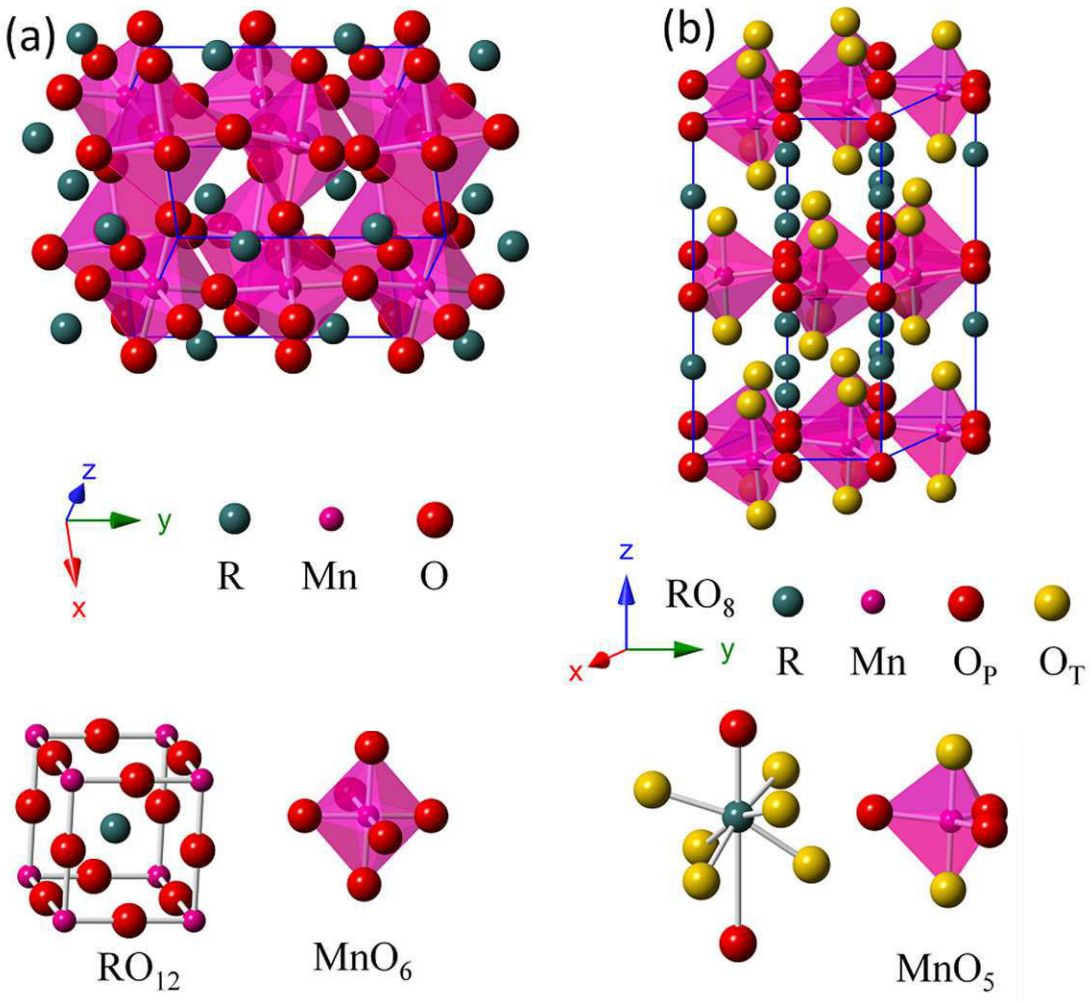

Figure I.5.a) Orthorhombic $RMnO_3$ crystal structure with MnO_6 and RO_{12} as building blocks; b) Hexagonal $RMnO_3$ crystal structure with MnO_5 and RO_8 as building blocks (from [16]) .

Among $RMnO_3$, yttrium manganese oxide or yttrium manganite ($YMnO_3$) has attracted a lot of interest, particularly in the last decade because of its potential applications in non-volatile ferroelectric memories (Fe-RAM), spintronics, sensor, actuators etc. Although the integration of $YMnO_3$ in commercial devices is not available in the present, the prospect of designing new magnetic ferroelectrics based on it is explored and several patents are reported [17] [18]. Fujimura et al. [19] firstly proposed the use of thin films of hexagonal $YMnO_3$ grown by rf magnetron sputtering, as non-volatile memory devices. Since then, an extensive work was carried out on $YMnO_3$ in bulk or film form. Figure I.6 illustrates the evolution of research

publication on $YMnO_3$ from the 60s up to the present date plotted as occurrence of the word "$YMnO_3$" in title, mainly on Science Web database.

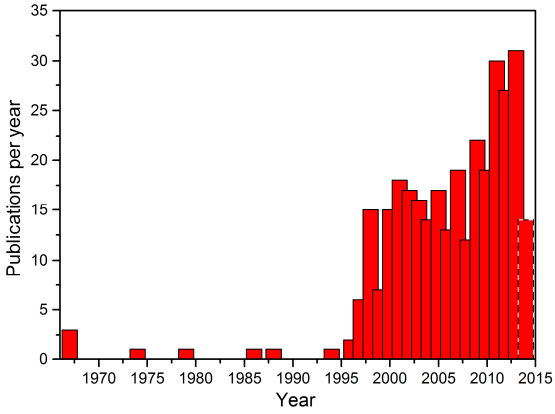

Figure I.6. Publications per year for which '$YMnO_3$' appears in the title. Source: Web of Science and Web).

1.3 Phase stability of $YMnO_3$

The Goldschmidt tolerance factor, used as an indicator for the stability and distortion of crystal structures, is generally considered as the factor controlling the boundary between the hexagonal and orthorhombic structures. From this perspective, the orthorhombic perovskite phase is stable for $t > 0.855$, corresponding to $r_R > r_{Dy}$ while for $t < 0.855$ ($r_R < r_{Ho}$), the hexagonal phase prevails [20].

The transition from the hexagonal phase to the orthorhombic perovskite was investigated by several authors by high pressure synthesis as the orthorhombic phase is the denser one [21], or by substitution [22].

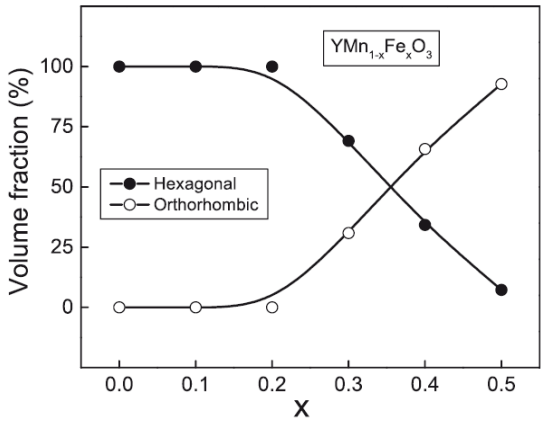

Figure I.7. Volume fraction of hexagonal and orthorhombic phases of $YMn_{1-x}Fe_xO_3$ (from [22]).

An example of phase diagram stability with the substitution, is reproduced in Figure I.7. It is observed that with the increase in the Fe doping, there is a progressive increase of the orthorhombic phase against the stable hexagonal phase of the parent compound $YMnO_3$. From a thermodynamic point of view, the report of Graboy et al. [23] treating the stability of the two phases, considers the Gibbs free energy of $RMnO_3$ formation from R_2O_3 and Mn_2O_3 at 900°C and ambient pressure. Their findings are summarized in the graph of Figure I.8. It is observed that the transition between orthorhombic and hexagonal polytypes takes place around R=Ho, which is in agreement with the results based on geometrical considerations (Goldschmidt tolerance factor). By extrapolating the thermodynamic data as a straight line below the stability boundary, they state that the metastable phase can be stabilized in the form of epitaxial films if the difference between the formation Gibbs energies of two polymorphs does not exceed 10-15 kJ mol^{-1}. In this case, the energy difference can be compensated by the energy of the film-substrate coherent interface. However, the stability of the metastable polymorph depends on the film thickness: more the energy gap is larger, less the amount (thickness) of the stabilized film is important. Kaul et al. [24] have demonstrated for $GdMnO_3$ and $EuMnO_3$ films stabilized in hexagonal phase, that beyond a critical thickness of about 70 nm the hexagonal phase can no longer be stabilized.

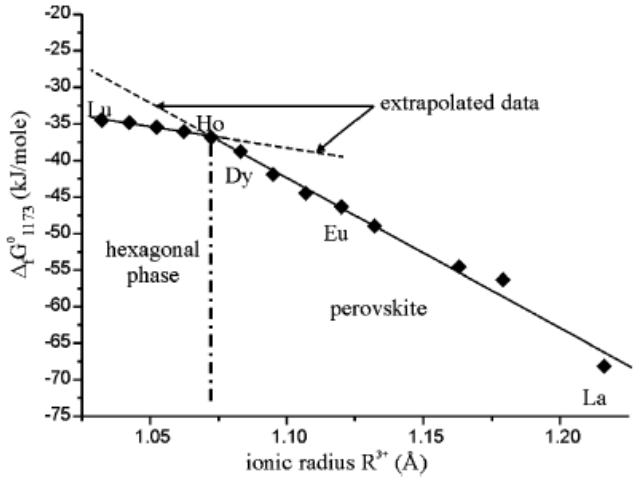

Figure I.8. Free $RMnO_3$ energy formation from R_2O_3 and Mn_2O_3 at 900°C and ambient pressure (from [23]).

A comparative description between hexagonal and orthorhombic $YMnO_3$ is presented in the next sections.

1.4 Hexagonal $YMnO_3$ phase

Firstly synthetized by the group of E. F. Bertaut from Grenoble in 1963 in the form of single crystals [25], hexagonal $YMnO_3$ (h-YMO) was extensively studied and successfully obtained in ceramic form [26] [27], thin films [28] [29] and nanostructures [30] [31]. As a reminder, the structure of the hexagonal phase (space group $P6_3cm$ with lattice parameters a=b=6.1453 Å and c=11.3714 Å [32]) consists of ABCACB stacking of close packed oxygen layers with Mn^{3+} having 5-fold coordination and located at the center of MnO_5 trigonal bypiramids. These basic MnO_5 units build a layer by interconnection of their vertices to form a triangular tiling. The Y cations, with 8-fold coordination, form a corrugated layer in-between these triangular tilings. A brief review of the magnetic and electric properties is given in the following section.

1.4.1 Magnetism in hexagonal $YMnO_3$ phase

The magnetic structure of h-YMO has been studied since the early neutron-diffraction measurements by Bertaut et al. [33]. According to their data, the magnetism in h-YMO can be interpreted by two possible models of α and β types in which the Mn^{3+} spins have a triangular arrangement in the basal plane ab at 120°, as shown in Figure I.9.

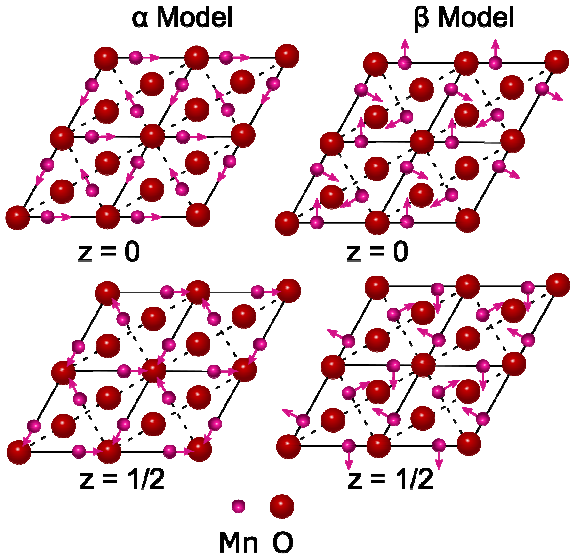

Figure I.9. Magnetic structure of hexagonal $YMnO_3$ showing the main models: α-type (left) and β-type (right). The spin configuration is marked by arrows (after [33]).

The coupling between planes can be ferromagnetic (model α) or antiferromagnetic (model β), but a distinction between the two was not possible. It turned out that even the recent neutron

diffraction studies [34, 35] could not tell because of the high similarities in the patterns intensities. This drawback was overcome by a new technique called optical Second Harmonic Generation spectroscopy developed by Fiebig et al. [36]. The authors have determined that the model α fulfills the symmetry requirements. The Néel temperature is T_N=72 K, but a spin reorientation occurs below T_R=41 K where the change of magnetic structure goes along with a 90° spin rotation and a modification of the antiferromagnetic domain structure. The principal magnetic interaction is based on antiferromagnetic superexchange between co-planar Mn-O-Mn, while the Mn-O-O-Mn superexchange between adjacent planes is two orders of magnitude weaker [37].

1.4.2 Ferroelectricity in hexagonal $YMnO_3$ phase

The mechanism of ferroelectricity in the h-YMO was described by van Aken et al. [38] as arising from a structural transition (so called "improper" or "geometrical" ferroelectric in contrast with "proper" ferroelectric where the polarization comes from the atomic displacements). They found that a buckling of the MnO_5 polyhedra, combined with an unusual Y coordination and the triangular layered MnO_5 network is responsible for the ferroelectric behavior. The paraelectric-ferroelectric transition is associated to the transition from the centrosymmetric space group $P6_3/mmc$ to non-centrosymmetric $P6_3cm$ without no re-hybridization or change in chemical bonding between the para- and ferroelectric phases. In the paraelectric phase, all ions are bound in planes parallel to the *ab* plane, whereas below the ferroelectric transition temperature, the mirror planes perpendicular to the hexagonal *c* axis are lost. Besides that, the buckling of the MnO_5 bipyramids, results in a shorter *c* axis which generates an in-plane shift of apical O^{2-} ions toward the two longer Y-O bond and a vertical shift of the Y^{3+} ions away from the $P6_3/mmc$ mirror plane, while keeping the distance to apical O constant. As a consequence of these shifts, an asymmetric environment of the Y ions is produced and, thus, a net electric polarization (see Figure I.10). The Curie temperature found for the ferroelectric transition is around 914 K [39].

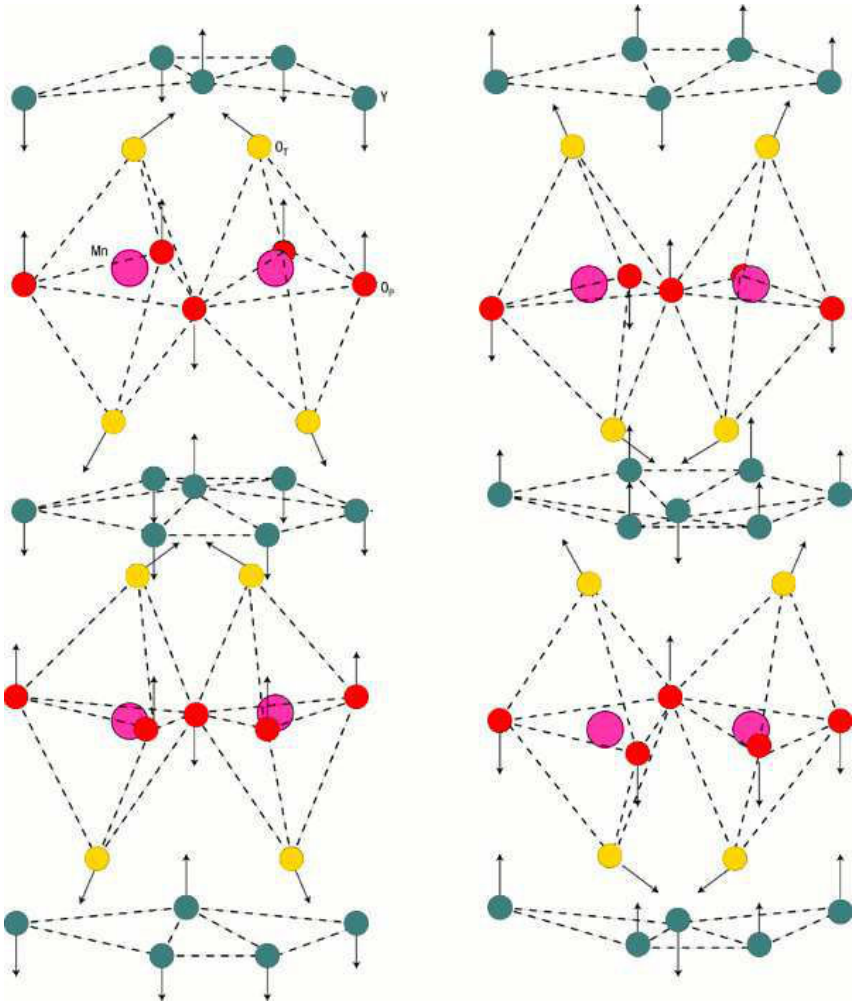

Figure I.10. Schematic view of the $YMnO_3$ in two enantiomorphous polarization states. The directions of the atomic displacements moving from the centrosymmetric to the ferroelectric structure is drawn by arrows (adapted from [38]).

1.5 Orthorhombic $YMnO_3$ phase

Less studied compared to the hexagonal analogous polymorph, orthorhombic $YMnO_3$ (o-YMO) started to present interest with the confirmation of the multiferroicity, which was not a priori expected (the centrosymmetric *Pnma* group does not allow ferroelectricity). Figure I.11 illustrates the percentage of publications dedicated to the o-YMO phase vs. h-YMO phase from the total shown in Figure I.6.

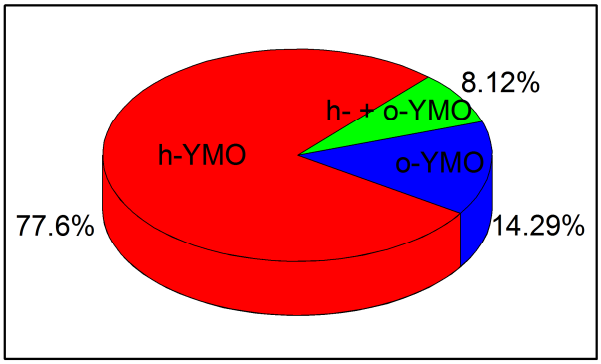

Figure I.11. Percentage of publications dedicated to the o-YMO phase vs. h-YMO phase.

As shown before, the structure of o-YMO (space group *Pnma* with the cell parameters *a*=5.8361 Å, *b*=7.3571 Å and *c*=5.2580 Å [40]) consists of basic polyhedral units built up by Mn^{3+} ions at the center of MnO_6 octahedra. These units are interconnected by sharing their vertices along three perpendicular directions and Y cations occupy the holes between them. Alternatively, the structure can be described by considering that Y^{3+} and O^{2-} ions form an FCC close packed lattice (ABCABC stacking) and Mn^{3+} occupy octahedral holes.

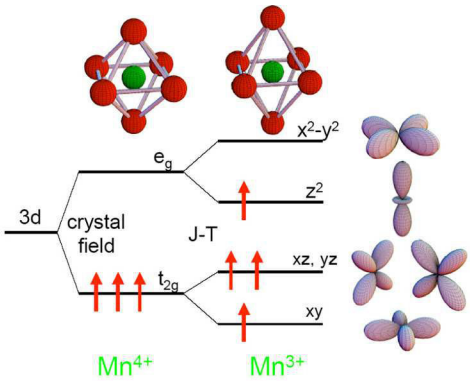

Figure I.12. Electron configuration of the 3d-electron states due to octahedral crystal field (Mn^{4+}) and due to the Jahn-Teller effect (Mn^{3+}) (from [41]).

The electronic structure of the Mn^{3+} is [Ar]$3d^4$. The incomplete d^4 levels are split by the crystalline field (octahedral environment) in two energy sub-levels: a t_{2g} triplet and an e_g doublet giving rise to the electron configuration $t_{2g}^3 e_g^1$ according to Hund rule [42]. This degenerate electronic configuration of the MnO_6 "molecule" is not energetically stable and the octahedra will undergo a geometrical distortion, called Jahn-Teller, to lower its energy. For the Mn^{4+} ion (in the case of mixed valence perovskites) the electronic configuration is $3d^3$ and thus only the t_{2g}

level is occupied. In this case, the Jahn-Teller distortion no longer takes place. The electronic configurations of Mn^{3+} and Mn^{4+} are shown in Figure I.12. This Jahn-Teller effect appears for the entire $RMnO_3$ family with orthorhombic structure (octahedral site).

1.5.1 Magnetism in orthorhombic $YMnO_3$ phase

Before starting to present the magnetic structure of o-YMO phase we remind here a few notions of antiferromagnetism. The antiferromagnetic order can be characterized as commensurate (the periodicity of the spins repeats that of the crystal lattice) or incommensurate (no link between spin arrangement and lattice). In turn, the commensurate magnetism can present several arrangements (A-, G-, C-, E –type) depicted in Figure I.13a. The incommensurate antiferromagnetism can exist in the form of sinusoidally modulated spin density waves or as cycloidal order depicted in Figure I.13b.

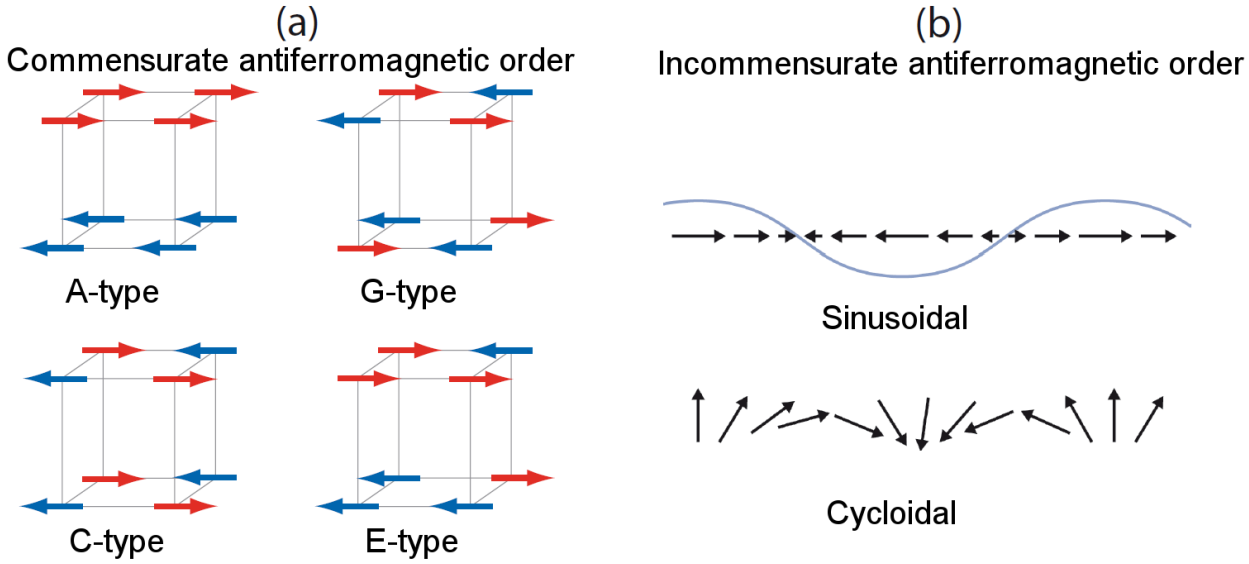

Figure I.13. Examples of a) commensurate antiferromagnetic order types and b) incommensurate antiferromagnetic order types (adapted from [43]).

The magnetic structure of o-YMO was studied with interest and its description was under debate for a while. A short discussion of the important developments is given in the following. Note that all results are expressed in *Pnma* notation.

According to the neutron diffraction measurements of Munoz et. al. [42], the o-YMO enters in an incommensurate antiferromagnetic order state below T_N=42 K. The magnetic structure was

found to be sinusoidally modulated with the magnetic moments of Mn^{3+} ions parallel to the propagation vector **k** = (k_x, 0, 0). An anomaly was observed at 28.7 K, later assigned to a lock-in transition into a temperature independent wave vector [44]. The DC susceptibility measurement performed by the same authors confirms the paramagnetic-antiferromagnetic transition at around 40 K. However, the AC susceptibility results show a maximum at 11 K, which was assumed to correspond to the freezing temperature of a spin glass phase existing below 11 K. It may be important to mention that these results are obtained on a polycrystalline o-YMO sample with nominal formula $YMnO_{3.04}$ which implies a Mn^{4+} amount and with a proportion of ~10% of hexagonal YMO phase, both taken into account for the structure refinements. The incommensurate magnetic order and the spin frustration are typical marks of orthorhombic $RMnO_3$ series in which the Mn-O-Mn bonds inside octahedra are close to 145°. They are mainly due to a competition of ferro- and antiferromagnetic interactions, mediated by the superexchange mechanism, between the Mn^{3+} spins at nearest and next-nearest neighbor positions. This spin configuration is shown in Figure I.14.

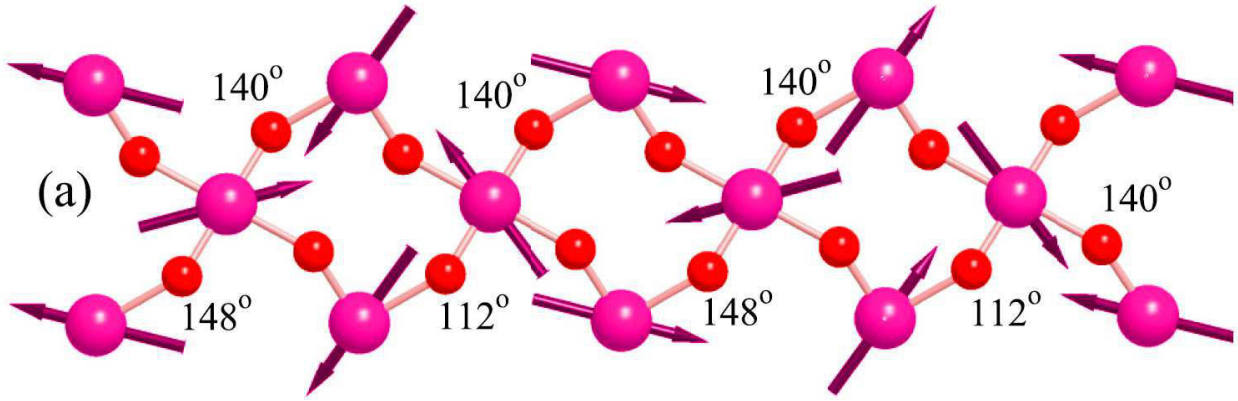

Figure I.14. Spins configuration in the ac plane. The Mn^{3+} ions are depicted as big pink spheres and the O^{2-} ions as small red spheres (adapted from [45]).

Recent publications, both experimental and theoretical, show that an E-type and a cycloidal spin phases coexist below a certain temperature [46] [47] [48]. The results in [47] give a complex picture of the o-YMO magnetism. Thus, the antiferromagnetic transition takes place at T_N=45 K. Between 40 and 45 K, a sinusoidal state with a spin canting along the *b*-axis is present. Below 40 K, the sinusoidal magnetic phase transforms into a cycloidal magnetic structure with magnetization along *b*-axis. At temperatures lower than 35 K, the coexistence of the cycloidal

and E-type state was observed. A schematic representation of these two configuration is shown in Figure I.15.

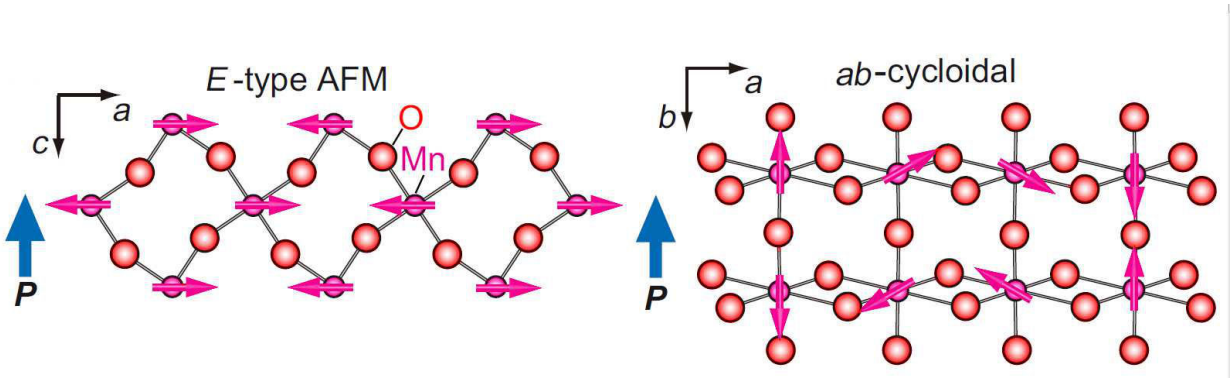

Figure I.15. Spin configuration in E-type and the ab-cycloidal states (adapted from [49]).

Slightly different transition temperature and ordered states were observed by Okuyama et al. [50]: paramagnetic to sinusoidal transition occurs at T_N=42 K while the E-type structure sets up below 30 K.

1.5.2 Ferroelectricity in orthorhombic $YMnO_3$ phase

If the magnetic structure of the o-YMO seems intricate, the situation is equally complex for the origin and modelization of the ferroelectricity. The ferroelectric polarization occurs at low temperature (T_C ~ 30 K [16]), intimately linked with the magnetic order, thus the o-YMO is a type-II multiferroic. According to Fontcuberta et al. [51] ferroelectricity in the collinear E-type state is driven by the asymmetric magnetostriction along the *a*- and *c*-axis which breaks the center of symmetry of the lattice producing a characteristic finite polarization along the *c*-axis. The atomic displacements (~ 10^{-3} Å) associated with the formation of alternating structure of Mn-O-Mn bond in *ac* plane give rise to electrical dipoles and thus ferroelectricity. This result was confirmed by Okuyama et al. on o-YMO single crystal [50]. The ferroelectric atomic displacements are illustrated in Figure I.16.

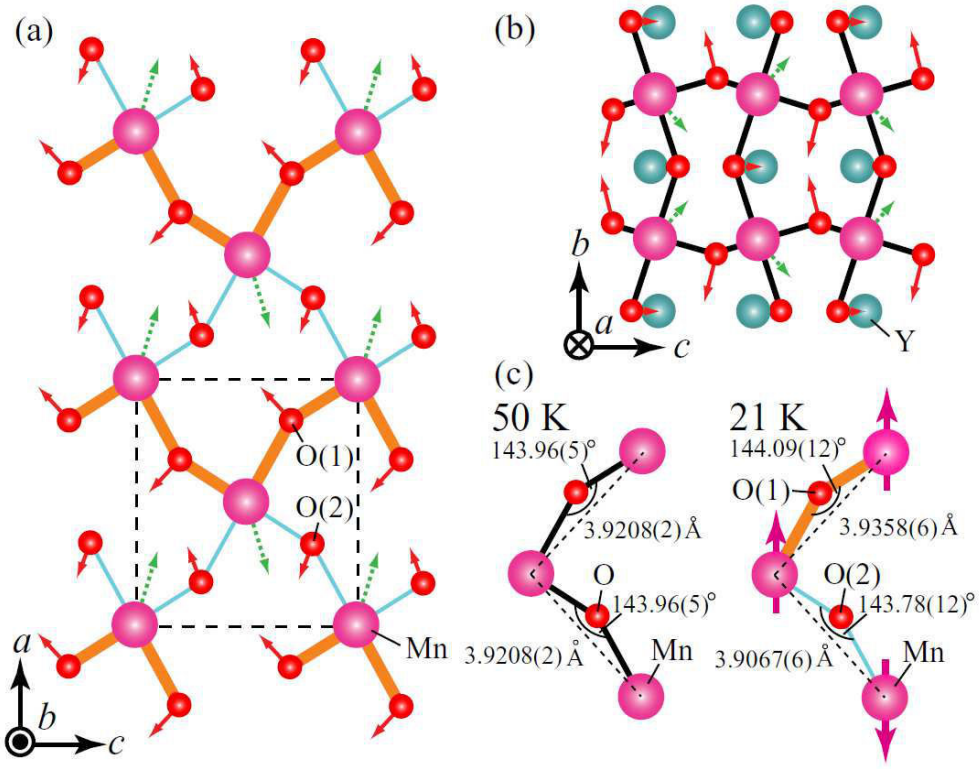

Figure I.16. Schematics of the ferroelectric atomic displacements projected onto (a) the ab plane and (b) the ac plane in the ferroelectric E-type phase. Dotted and solid arrows indicate the directions and the relative atomic displacements of Mn and O, respectively. Note that the displacements of O ions are doubled for the purpose of clarity. A unit cell is indicated by a broken line. (c) Changes in the Mn-O-Mn bond angles and distances between the neighboring Mn ions in the ab plane. In the ferroelectric phase (21 K), the E-type spin configuration is represented by large arrows. Here we assumed the ferromagnetic (antiferromagnetic) spin arrangement for Mn-O-Mn bond with larger (smaller) bond angle (adapted from [50].

1.6 Literature review in $YMnO_3$ thin films

1.6.1 Hexagonal $YMnO_3$ films

The group of Norifumi Fujimura from Osaka is the first who has proposed h-YMO in the form of thin films as a new candidate for nonvolatile memory devices [19]. Following this proposal, the interest in YMO films has increased exponentially. Many substrates and deposition methods

have been tested. The characterization methods, firstly focused on microstructure and ferroelectric properties have expanded to magnetic properties, multiferroicity, exchange bias etc. The films have been elaborated on different substrates: conductive, in order to measure the electric properties, with hexagonal symmetry in order to force the epitaxial growth, on silicon for the device integration or on other complex multilayered substrates for various purposes:

- Al_2O_3(0001) [52] [53] [54]
- Quartz [55]
- GaN(0001) [56] [57] [58]
- GaN/sapphire [59] [60]
- GaN/AlN/6H-SiC(001) [61]
- MgO
  - (100)-oriented [62] [63]
  - (111)-oriented [19] [64] [65] [66] [67] [62] [63] [68]
- Nb:STO
  - (001)-oriented [69]
  - (110)-oriented [69]
- STO(111) [52]
- NGO(110) [53]
- Pt sheet [70] [71]
- Pt(111)/(0001)sapphire [66] [64] [65] [72] [73] [74] [75] [76] [77] [78] [79] [80]
- Pt(111)/MgO(111) [19]
- Pt(111)/ZrO_2/SiO_2/Si [76]
- Pt/Ti/SiO_2/Si(100) [70] [81] [82] [83] [84]
- Pt/TiO_x/SiO_2/Si [85] [86] [87]
- Pt/STO(111) [88] [89] [90] [91] [92]
- YSZ
  - (111)-oriented [28] [93] [94] [95] [96]
  - (110)-oriented [97]
- SiON/Si(111) [98]
- SiO_2/Si(100) [99]

- Y_2O_3(111)/Si(111) [76] [72] [100] [101] [102]
- Y_2O_3/Si(100) [103] [104] [105]
- Y_2O_3/Si(111) [106] [107] [108]
- ZnO:Al/(0001)sapphire [19] [109] [110]
- $Zn_{0.99}Ga_{0.01}O$/(0001)sapphire [111]
- **Si**

  (111)-oriented [52] [70] [71] [81] [82] [100] [106] [110] [107] [112] [113] [114]

  (100)-oriented [53] [55] [103] [115] [116] [117] [118] [119] [120] [121] [122] [123] [123] [29] [124]

Like the substrates used, the deposition methods are also varied and the people working on this subject are widespread over the globe. Figure I.17 summarizes the growth methods for h-YMO films as well as the location of the laboratory in which this was conducted.

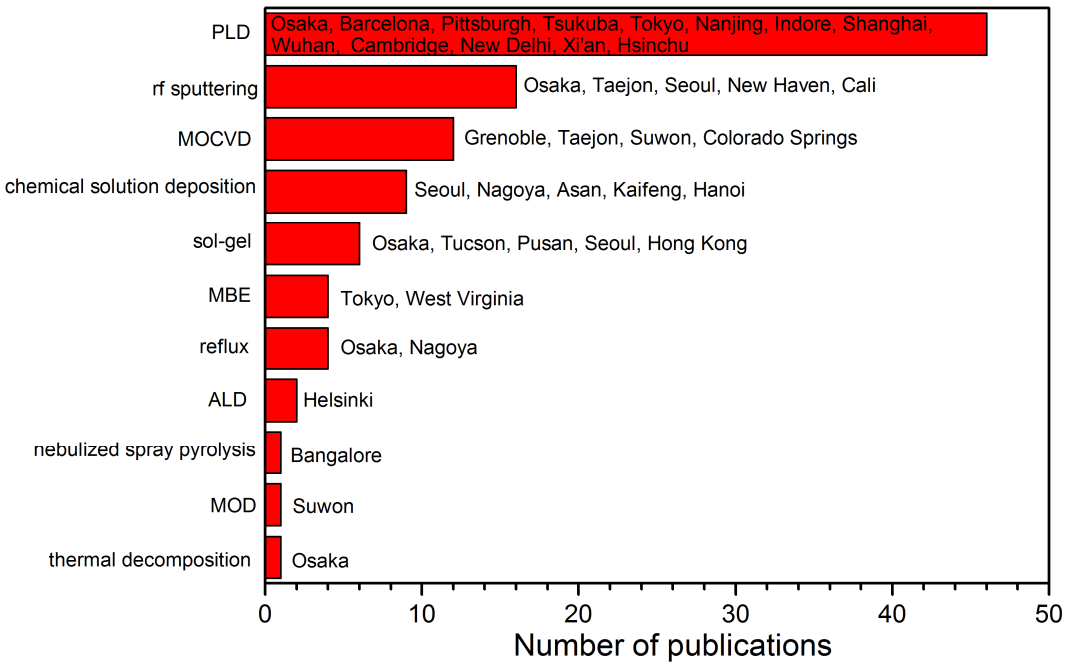

Figure I.17. Deposition methods and working teams for the growth of h-YMO films.

It is obvious that the PLD method is the most commonly used method, followed by rf sputtering and MOCVD. In our laboratory, hexagonal rare earth manganites have been successfully deposited by MOCVD on YSZ(111) substrates during the thesis of I. Gelard [125]. On bare Si (100)-oriented substrates the synthesis of hexagonal films was mainly performed by RF

sputtering. Among the only two papers [29] [126] which deal with the MOCVD growth, the second one is in Korean. In general, these papers focus on the structural and ferroic properties. None of them treats the magnetism of h-YMO on bare Si(100). The crystallization and microstructure was investigated by XRD and TEM techniques in [118] [120] [121] [122].

The results show that the h-YMO phase grows with the [0001] direction normal to the Si(100) surface when deposition takes place in $Ar+O_2$ atmosphere. Random orientations for the h-YMO phase are observed when using only Ar. An amorphous layer, assigned to $YMnO_3$ phase, and a native SiO_2 layer form between the crystalline h-YMO and Si(100) substrate. Also, the crystalline h-YMO is not uniform, but divided into two sub-layers: one polycrystalline YMO, on the top of which is growing the second layer *c*-axis oriented YMO (see Figure I.18a). They explain the existence of this multilayer structure as due to a compensation mechanism of the high stress induced by the *c*-axis oriented YMO layer. Using the rapid thermal annealing, the stress was released by the formation of polycrystalline YMO, which also changes the aspect of the sample from cracked to smooth surface. In [118], the formation of a Y_2O_3 layer (see Figure I.18b) was proven to be caused by the difference in the oxidizing abilities of Y, Mn and Si but also because of a Y/Mn non-stoichiometry in the bottom amorphous layer.

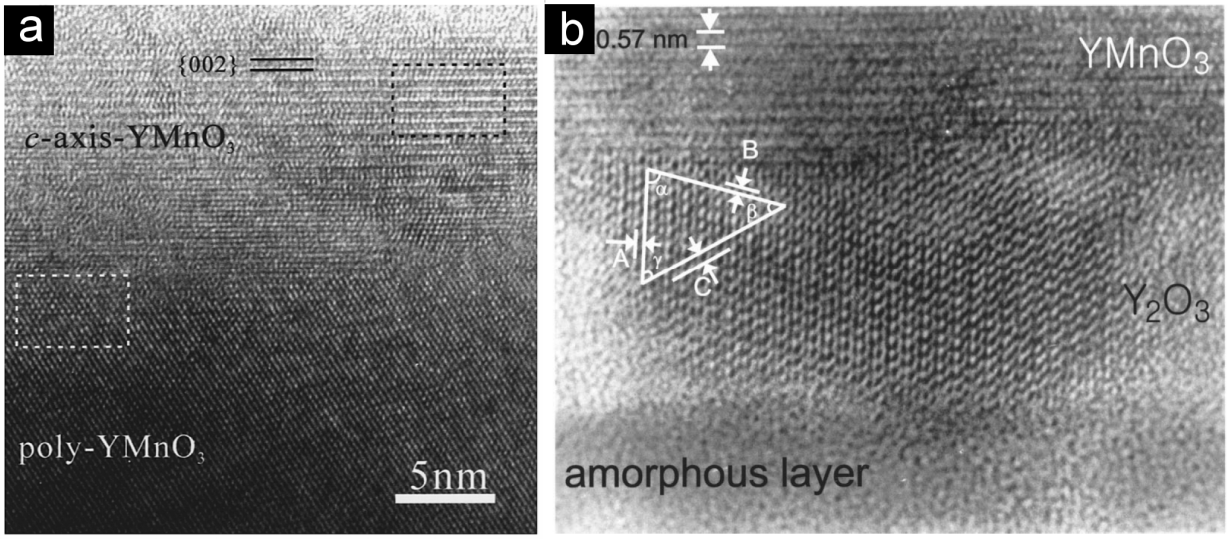

Figure I.18. HRTEM images showing: a) interfacial microstructure between the c-axis-oriented h-YMO layer and the polycrystalline h-YMO layer (from [122]); b) h-YMO film on top of the Y_2O_3 and amorphous layers (from [118]).

The ferroelectric properties were also measured. The authors cited above have found different ferroelectric behaviors depending on the film microstructure: purely *c*-axis films show very high leakage current density, bi-layer structures (*c*-axis and polycrystalline) show relatively low leakage, purely polycrystalline show the lowest leakage current density. The memory window of the purely polycrystalline is 0.64 V but is even better when obtained from a bi-layered structure.

The reports on the magnetism of the h-YMO films are summarized in the following. Fujimura et al. [65] have reported that the M(H) of h-YMO on MgO(100) substrate is identical with the ceramic YMO (typical antiferromagnetic ordering at 5K) although the χ(T) measurements do not reveal any anomaly below 200 K (subtraction of the large diamagnetic moment of the substrate makes it difficult). Kumar et al. [54] showed that, for h-YMO films grown on Al_2O_3(0001) substrate, an antiferromagnetic transition occurs at 70 K, in agreement with the bulk one but the magnetization does not decrease below 70 K, as one would expect for an antiferromagnetic system. Singh et al. [111] reported an antiferromagnetic transition at ~ 30 K for h-YMO films on Ga:ZnO/0001-sapphire. h-YMO films on MgO(100), MgO(111) and YSZ(111) substrates present an evolution of the antiferromagnetic ordering temperature with the strain states of the films [63]. Also, in some cases, a second phase transition, associated with the superspin-glass-like (SSG) transition was observed at T_{SR} ~ 40 K in h-YMO/YSZ(111) sample and ~28 K in h-YMO/MgO(100) sample). Posadas et al. [60] reported that the M(T) in ZFC-FC mode for h-YMO on GaN/sapphire presents a cusp at ~ 45 K which is associated with the Néel temperature, but without showing any data.

In the frustrated systems as hexagonal manganites, the spin-glass behavior is often seen (e.g. $ErMnO_3$ [127]). Another example concerns a Mn-rich h-YMO ceramic (Y/Mn=0.9) which first orders antiferromagnetically at 72 K and then undergoes a re-entrant spin-glass transition at 42 K [128]. Similarly, h-YMO nanoparticles display the spin-glass features at 43 K [129]. Polycrystalline h-YMO shows a divergence of ZFC and FC curves indicating the presence of overall weak ferromagnetism due to spin canting [130].

The temperature-dependent Raman phonons were investigated in [124] and a transition at 123 K was observed which can be associated with the Néel temperature as suggested by the authors.

1.6.2 Orthorhombic $YMnO_3$ films

The growth of o-YMO films was first proposed by Salvator et al. [131]. Their findings showed that the o-YMO phase was synthetized by PLD on STO(100), LAO(100) and $NdGaO_3$(110) substrates to the detriment of the stable hexagonal polymorph. The immediate impact of their publication was not visible because the multiferroic properties of bulk o-YMO were not well known. Recently, the interest in o-YMO film has known a revival with the observation of large magnetoelectric effects in orthorhombic $YMnO_3$ and $HoMnO_3$ [44]. Since then, the o-YMO films were grown by epitaxial stabilization on several perovskite-type substrates:

- **LAO**
  - (100)-oriented [131] [116] [115] [132]
  - (110)-oriented [133] [134]
- **STO**
  - (001)-oriented [115] [116] [131] [132] [133] [135] [136] [137] [138] [139] [140] [141]
  - (110)-oriented [133] [142] [140] [141]
  - (111)-oriented [139] [140] [141]
- Nb:STO
  - (001)-oriented [143] [144] [145] [146] [147] [148] [149]
  - (110)-oriented [147] [148]
- **LSAT(100)** [136]
- $LaNiO_3$/STO(001) [135]
- NGO(110) [131]
- $YAlO_3$(010) [150] [47] [151]

The main growing method employed was PLD, except for a few examples of o-YMO films deposited by MOCVD [132] or ALD [116] [115]. The STO substrates with different orientations and Nb doped STO, equally used as substrate and bottom electrode, were found to be the most common choice when growing o-YMO films, as seen above.

The crystalline domain structure, the magnetic behavior and the ferroelectric properties have been extensively studied during the Phd thesis of X. Marti [152]. The author found that o-YMO grown on STO(001) substrates presents two equivalent crystal domains 90° in-plane rotated with

the epitaxial relationship: $[001]_{YMO}//[110]_{STO}$ and $[100]_{YMO}//[110]_{STO}$. The epitaxial strain of these domains is anisotropic: the [001] direction is fully relaxed while the [100] and [010] directions are contracted and elongated, respectively and can be controlled by changing the P_{O2} during deposition, the film thickness or by annealings. The strain state acts on the magnetism: relaxed films are antiferromagnetic while strained films present additionally a weak ferromagnetic component. A splitting of the ZFC-FC magnetization curves was observed (see Figure I.19a and b).

A similar behavior has been seen for o-YMO films on LAO(100) substrates [153]. The authors have not discussed the ZFC-FC splitting, neither the kink at ~ 11 K and they only mention the antiferromagnetic behavior below 40 K (see Figure I.19c).

The group of Y. Tokura [150] [47] [151] have deposited a single crystalline o-YMO film (010-oriented) on $YAlO_3$ which showed an antiferromagnetic (AFM) transition at T_N=45 K with weakly canted moments below T_N (associated with the ZFC-FC splitting).

Hsieh et al. [133] showed that for $[200]_{YMO}//[110]_{LAO}$ and $[002]_{YMO}//[110]_{STO}$ films, an AFM transition (T_N ~ 40 K) is observed regardless the orientation of the applied field. Additionally, a second magnetic spin reordering is observed at T_{SR} ~16–18 K.

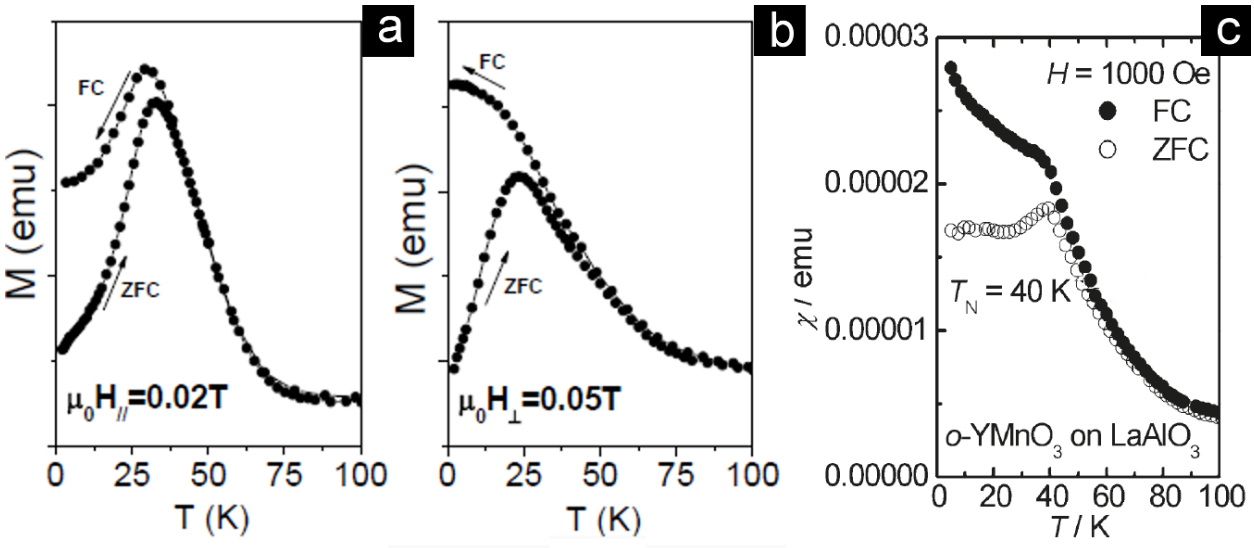

Figure I.19. ZFC-FC curves for YMO films on STO substrates measured with the magnetic field applied in-plane (a) and out-of-plane (b) (from [152] *) and for a YMO film on LAO substrate (c) (from* [153]*)*

This appears only when the field is applied along the *c*- and *b*-axis and is absent when measuring along the *a*-axis. However, in [010]-oriented *o*-YMO films on STO(001) substrates the AFM occurs at T_N=44 K and *T*SR at ~28 K (*a*-*c* plane) and 18 K (*b*-axis). The authors argue that the features of the second reordering may originate from the strain-induced lattice buckling and associated canting of Mn moments.

On polycrystalline o-YMO, Munoz et al. [42] showed the existence of a spin-glass behavior below 11 K, which has been associated with the disorder of the lattice introduced by the presence of Mn^{4+} ions.

References

1. Spaldin, N.A. and M. Fiebig, *The Renaissance of Magnetoelectric Multiferroics.* Science, 2005. **309**(5733): p. 391-392.
2. Eerenstein, W., N.D. Mathur, and J.F. Scott, *Multiferroic and magnetoelectric materials.* Nature, 2006. **442**(7104): p. 759-765.
3. Banerjee, S. and A.K. Tyagi, eds. *Functional Materials. Preparation, Processing and Applications*. 2011, Elsevier: London. 730.
4. Bibes, M. and A. Barthelemy, *Multiferroics: Towards a magnetoelectric memory.* Nat Mater, 2008. **7**(6): p. 425-426.
5. Ramesh, R. and N.A. Spaldin, *Multiferroics: progress and prospects in thin films.* Nat Mater, 2007. **6**(1): p. 21-29.
6. Cheong, S.-W. and M. Mostovoy, *Multiferroics: a magnetic twist for ferroelectricity.* Nat Mater, 2007. **6**(1): p. 13-20.
7. Khomskii, D., *Classifying multiferroics: Mechanisms and effects.* Physics, 2009. **2**: p. 20.
8. Jeroen van den, B. and I.K. Daniel, *Multiferroicity due to charge ordering.* Journal of Physics: Condensed Matter, 2008. **20**(43): p. 434217.
9. Kimura, T., et al., *Magnetic control of ferroelectric polarization.* Nature, 2003. **426**(6962): p. 55-58.
10. Hur, N., et al., *Electric polarization reversal and memory in a multiferroic material induced by magnetic fields.* Nature, 2004. **429**(6990): p. 392-395.
11. Green, M.A., A. Ho-Baillie, and H.J. Snaith, *The emergence of perovskite solar cells.* Nat Photon, 2014. **8**(7): p. 506-514.
12. Rabe, K.M., C.H. Ahn, and J.M. Triscone, *Physics of Ferroelectrics: A Modern Perspective*. 2007: Springer.
13. Wang, Y.T., C.W. Luo, and T. Kobayashi, *Understanding Multiferroic Hexagonal Manganites by Static and Ultrafast Optical Spectroscopy.* Advances in Condensed Matter Physics, 2013. **2013**: p. 13.
14. Zhou, J.S. and J.B. Goodenough, *Unusual Evolution of the Magnetic Interactions versus Structural Distortions in RMnO3 Perovskites.* Physical Review Letters, 2006. **96**(24): p. 247202.
15. Alonso, J.A., et al., *Evolution of the Jahn−Teller Distortion of MnO6 Octahedra in RMnO3 Perovskites (R = Pr, Nd, Dy, Tb, Ho, Er, Y): A Neutron Diffraction Study.* Inorganic Chemistry, 2000. **39**(5): p. 917-923.
16. Liu, S.-H., et al., *Structural transformation and charge transfer induced ferroelectricity and magnetism in annealed YMnO3.* AIP Advances, 2011. **1**(3): p. -.
17. Yano, Y. and T. Noguchi, *Ferroelectric thin film, electric device and method for preparing ferroelectric thin film*. 1999, Google Patents.
18. Griñó, J.F.I., et al., *Magnetoelectric device and method for writing non-volatile information into said magnetoelectric device*. 2009, Google Patents.
19. Fujimura, N., et al., *Epitaxially grown YMnO3 film: New candidate for nonvolatile memory devices.* Applied Physics Letters, 1996. **69**(7): p. 1011-1013.
20. Bos, J.-W.G., B.B. van Aken, and T.T.M. Palstra, *Site Disorder Induced Hexagonal−Orthorhombic Transition in Y3+1-xGd3+xMnO3.* Chemistry of Materials, 2001. **13**(12): p. 4804-4807.

21. Uusi-Esko, K., et al., *Characterization of RMnO3 (R = Sc, Y, Dy-Lu): High-pressure synthesized metastable perovskites and their hexagonal precursor phases.* Materials Chemistry and Physics, 2008. **112**(3): p. 1029-1034.
22. Sharma, N., et al., *Magnetic and dielectric behavior in YMn1−xFexO3 (x ≤ 0.5).* Journal of Applied Physics, 2014. **115**(21): p. 213911-213911-9.
23. Graboy, I.E., et al., *HREM Study of Epitaxially Stabilized Hexagonal Rare Earth Manganites.* Chemistry of Materials, 2003. **15**(13): p. 2632-2637.
24. Andrei R Kaul, O.Y.G.a.A.A.K., *The role of heteroepitaxy in the development of new thin-film oxide-based functional materials.* Russ. Chem. Rev., 2004. **73**(9).
25. Bertaut E. F., F.F., Fang P., *Les manganites de terres rares et d'yttrium: une nouvelle classe de ferroelectriques.* C. R. Acad. Sci., 1963. **256**.
26. Muneeswaran, M., C. Mascovani, and N.V. Giridharan, *Structural and multiferroic properties of YMnO3 ceramics synthesized by co-precipitation method.* AIP Conference Proceedings, 2013. **1512**(1): p. 1270-1271.
27. Ma, Y., et al., *In situ synthesis of multiferroic YMnO3 ceramics by SPS and their characterization.* Ceramics International, 2009. **35**(8): p. 3051-3055.
28. Dubourdieu, C., et al., *Thin films and superlattices of multiferroic hexagonal rare earth manganites.* Philosophical Magazine Letters, 2007. **87**(3-4): p. 203-210.
29. Choi, K.-J., W.-C. Shin, and S.-G. Yoon, *Ferroelectric YMnO3 thin films grown by metal-organic chemical vapor deposition for metal/ferroelectric/semiconductor field-effect transistors.* Thin Solid Films, 2001. **384**(1): p. 146-150.
30. Ye, Y., H. Fan, and J. Li, *Fabrication and texture evolution of hexagonal YMnO3 nanofibers by electrospinning.* Materials Letters, 2010. **64**(3): p. 419-421.
31. Tripathi, S. and V. Petkov, *Iso-structural phase transition in YMnO3 nanosized particles.* Applied Physics Letters, 2013. **102**(6): p. -.
32. Malo, S., et al., *Structural and magnetic properties of the solid solution (0<x<1) YMn1−x(Cu3/4Mo1/4)xO3.* Solid State Sciences, 2005. **7**(12): p. 1492-1499.
33. E.F. Bertaut, M.M., *Structure magnetique de MnYO3* Phys. Lett., 1963. **5**.
34. Park, J., et al., *Neutron-diffraction studies of YMnO3.* Applied Physics A, 2002. **74**(1): p. s796-s798.
35. Muñoz, A., et al., *Magnetic structure of hexagonal RMnO3 (R = Y, Sc) : Thermal evolution from neutron powder diffraction data.* Physical Review B, 2000. **62**(14): p. 9498-9510.
36. Fiebig, M., et al., *Determination of the Magnetic Symmetry of Hexagonal Manganites by Second Harmonic Generation.* Physical Review Letters, 2000. **84**(24): p. 5620-5623.
37. Toulouse, C., et al., *Lattice and spin excitations in multiferroic h-YMnO3.* Physical Review B, 2014. **89**(9): p. 094415.
38. Van Aken, B.B., et al., *The origin of ferroelectricity in magnetoelectric YMnO3.* Nat Mater, 2004. **3**(3): p. 164-170.
39. Huang, Z.J., et al., *Coupling between the ferroelectric and antiferromagnetic orders in YMnO3.* Physical Review B, 1997. **56**(5): p. 2623-2626.
40. Uusi-Esko, K., et al., *Characterization of RMnO3 (R=Sc, Y, Dy-Lu): High-pressure synthesized metastable perovskites and their hexagonal precursor phases.* Materials Chemistry and Physics, 2008. **112**(3): p. 1029-1034.
41. Institut, P.S.; Available from: http://www.psi.ch/swissfel/correlated-electron-phases.

42. Muñoz, A., et al., *The magnetic structure of YMnO3 perovskite revisited.* Journal of Physics: Condensed Matter, 2002. **14**(12): p. 3285.
43. O'Flynn, D.T., *Multiferroic properties of rare earth manganites*, in *Department of Physics*. 2010, University of Warwick: Warwick. p. 212.
44. Lorenz, B., et al., *Large magnetodielectric effects in orthorhombic HoMnO3 and YMnO3.* Physical Review B, 2004. **70**(21): p. 212412.
45. Solovyev, I.V., M.V. Valentyuk, and V.V. Mazurenko, *Magnetic structure and ferroelectric activity in orthorhombic YMnO3: Relative roles of magnetic symmetry breaking and atomic displacements.* Physical Review B, 2012. **86**(14): p. 144406.
46. Lee, J.-H., S. Song, and H.M. Jang, *Ferroelectric ground state and polarization-switching path of orthorhombic YMnO3 with coexisting E-type and cycloidal spin phases.* Physical Review B, 2013. **88**(1): p. 014116.
47. Wadati, H., et al., *Origin of the Large Polarization in Multiferroic YMnO3 Thin Films Revealed by Soft- and Hard-X-Ray Diffraction.* Physical Review Letters, 2012. **108**(4): p. 047203.
48. Mochizuki, M., N. Furukawa, and N. Nagaosa, *Spin Model of Magnetostrictions in Multiferroic Mn Perovskites.* Physical Review Letters, 2010. **105**(3): p. 037205.
49. K. H. Wu, H.J.C., Y. T. Chen, C. C. Hsieh, C. W. Luo, T. M. Uen, J. Y. Juang, J. Y. Lin, T. Kobayashi, M. Gospodinov, *Marked enhancement of Néel temperature in strained YMnO3 thin films probed by femtosecond spectroscopy* Europhysics Letters, 2011. **94**(2): p. 280.
50. Okuyama, D., et al., *Magnetically driven ferroelectric atomic displacements in orthorhombic YMnO3* Physical Review B, 2011. **84**(5): p. 054440.
51. J. Fontcuberta, I.F., L. Fabrega, F. Sanchez, X. Marti, V. Skumryev, *Ferroelectricity and strain effects in orthorhombic YMnO3 thin films.* Phase Transitions, 2011. **84**(5–6): p. 555–568.
52. Dho, J., et al., *Epitaxial and oriented YMnO3 film growth by pulsed laser deposition.* Journal of Crystal Growth, 2004. **267**(3–4): p. 548-553.
53. Kumar, M., R.J. Choudhary, and D.M. Phase, *Growth of different phases of yttrium manganese oxide thin films by pulsed laser deposition.* AIP Conference Proceedings, 2012. **1447**(1): p. 655-656.
54. Kumar, M., R.J. Choudhary, and D.M. Phase, *Valence band structure of YMnO3 and the spin orbit coupling.* Applied Physics Letters, 2013. **102**(18): p. -.
55. Yi, W.-C., et al., *Temperature dependence of capacitance/current–voltage characteristics of highly (0001)-oriented YMnO3 thin films on Si.* Applied Physics Letters, 2000. **77**(7): p. 1044-1046.
56. Keenan, C., et al., *Properties of YMnO3 self-assembled nanocrystalline prisms on GaN.* Applied Physics Letters, 2008. **92**(1): p. -.
57. Wu, H., et al., *Temperature- and field-dependent leakage current of epitaxial YMnO3/GaN heterostructure.* Applied Physics Letters, 2009. **94**(12): p. -.
58. Wu, H., et al., *Control of the epitaxial orientation and reduction of the interface leakage current in YMnO3/GaN heterostructures.* Journal of Physics D: Applied Physics, 2009. **42**(18): p. 185302.
59. Chye, Y., et al., *Molecular beam epitaxy of YMnO3 on c-plane GaN.* Applied Physics Letters, 2006. **88**(13): p. 132903-132903-3.

60. Posadas, A., et al., *Epitaxial growth of multiferroic YMnO3 on GaN.* Applied Physics Letters, 2005. **87**(17): p. -.
61. Balasubramanian, K.R., et al., *Growth and structural investigations of epitaxial hexagonal YMnO3 thin films deposited on wurtzite GaN(001) substrates.* Thin Solid Films, 2006. **515**(4): p. 1807-1813.
62. Wu, K.H., et al., *Marked enhancement of Néel temperature in strained YMnO3 thin films probed by femtosecond spectroscopy.* EPL (Europhysics Letters), 2011. **94**(2): p. 27006.
63. Wu, K.H., et al., *Epitaxial-Strain Effects on Electronic Structure and Magnetic Properties of Hexagonal YMnO3 Thin Films Studied by Femtosecond Spectroscopy.* Journal of Superconductivity and Novel Magnetism, 2013. **26**(4): p. 801-807.
64. Fujimura, N., et al. *Effect of A-site substitution on the magnetic and dielectric behaviors of YMnO3 based ferroelectric thin films*. in *Applications of Ferroelectrics, 2002. ISAF 2002. Proceedings of the 13th IEEE International Symposium on*. 2002.
65. Fujimura, N., et al., *Ferromagnetic and ferroelectric behaviors of A-site substituted YMnO3-based epitaxial thin films.* Journal of Applied Physics, 2003. **93**(10): p. 6990-6992.
66. Ito, D., N. Fujimura, and T. Ito, *Initial Stage of Film Growth of Pulsed Laser Deposited YMnO3.* Japanese Journal of Applied Physics, 2000. **39**(9S): p. 5525.
67. A. J. Francis, A.B.a.P.A.S., *Thin Film Synthesis of Metastable Perovskites: YMnO3.* Innovative Processing and Synthesis of Ceramics, Glasses and Composites IV, eds. N. Bansal, The American Ceramic Society, Inc. (Westerville, OH), Ceramic Transactions, 2000. **135**: p. 565-575.
68. Nakayama, M., et al., *Correlation between the intra-atomic Mn3+ photoluminescence and antiferromagnetic transition in an YMnO3 epitaxial film.* Applied Physics Express, 2014. **7**(2): p. 023002.
69. Zhao, H., et al., *A new multiferroic heterostructure of YMnO3/SnTiO3+x.* Scripta Materialia, 2011. **65**(7): p. 618-621.
70. Fujimura, N., et al., *YMnO3 Thin Films Prepared from Solutions for Non Volatile Memory Devices.* Japanese Journal of Applied Physics, 1997. **36**(12A): p. L1601.
71. Kitahata, H., et al., *Microstructure and Dielectric Properties of YMnO3 Thin Films Prepared by Dip-Coating.* Journal of the American Ceramic Society, 1998. **81**(5): p. 1357-1360.
72. Ito Daisuke, F.N., Ito Taichro, *The Progress of YMnO3/Y2O3/Si System for a Ferroelectric Gate Field Effect Transistor.* Ferroelectrics, 2002. **271**(1): p. 229-234.
73. Maeda, K., T. Yshimura, and N. Fujimura, *Magnetic and Ferroelectric Properties of YMnO3 Epitaxial Thin Films.* MRS Online Proceedings Library, 2006. **966**: p. null-null.
74. Maeda, K., T. Yoshimura, and N. Fujimura, *Influence of antiferromagnetic ordering on ferroelectric polarization switching of YMnO3 epitaxial thin films.* Ultrasonics, Ferroelectrics, and Frequency Control, IEEE Transactions on, 2007. **54**(12): p. 2641-2644.
75. Fujimura, N., et al., *Multiferroic behaviour of YMnO3 and YbMnO3 epitaxial films.* Philosophical Magazine Letters, 2007. **87**(3-4): p. 193-201.
76. Ito, D., et al., *Ferroelectric properties of YMnO3 epitaxial films for ferroelectric-gate field-effect transistors.* Journal of Applied Physics, 2003. **93**(9): p. 5563-5567.

77. Hironori, S., et al., *Improvement of Surface Morphology and Dielectric Property of YMnO3 Films.* Japanese Journal of Applied Physics, 2003. **42**(9S): p. 6003.
78. Norimichi, S., et al., *Pulsed-Laser-Deposited YMnO3 Epitaxial Films with Square Polarization-Electric Field Hysteresis Loop and Low-Temperature Growth.* Japanese Journal of Applied Physics, 2004. **43**(9S): p. 6613.
79. Kazuhiro, M., Y. Takeshi, and F. Norifumi, *Polarization Switching Behavior of YMnO3 Thin Film at around Magnetic Phase Transition Temperature.* Japanese Journal of Applied Physics, 2009. **48**(9S1): p. 09KB05.
80. Takeshi Yoshimura, K.M., Atsushi Ashida, Norifumi Fujimura, *Ferroelectric Properties of Magnetoferroelectric YMnO3 Epitaxial Films at around the Neel Temperature.* Key Engineering Materials 2010. **445**: p. 144-147.
81. Tadanaga, K., et al., *Preparation and Dielectric Properties of YMnO3 Ferroelectric Thin Films by the Sol-Gel Method.* Journal of Sol-Gel Science and Technology, 1998. **13**(1-3): p. 903-908.
82. Shin, W.-C., et al., *Preparation of ferroelectric YMnO3 thin films for nonvolatile memory devices by metalorganic chemical vapor deposition.* Integrated Ferroelectrics, 1998. **21**(1-4): p. 319-329.
83. Kim, D.-P.K.a.C.-I., *Dry Etching of YMnO3 Thin Films in Ar/Cl2 and CF4/Cl2 Plasmas.* J. Korean Phys.Soc. , 2003. **43**: p. 738.
84. Kim, D., et al., *Ferroelectric properties of YMnO3 films deposited by metalorganic chemical vapor deposition on Pt/Ti/SiO2/Si substrates.* Materials Letters, 2006. **60**(3): p. 295-297.
85. Cheon, C.I., et al., *Ferroelectric properties of YMnO3 thin films prepared by chemical solution deposition.* Integrated Ferroelectrics, 2001. **34**(1-4): p. 73-80.
86. Kazuyuki, S., et al., *Ferroelectric Property of Alkoxy-Derived YMnO3 Films Crystallized in Argon.* Japanese Journal of Applied Physics, 2003. **42**(9R): p. 5692.
87. Zhou, L., et al., *Structure and ferroelectric properties of ferroelectromagnetic YMnO3 thin films prepared by pulsed laser depositon.* physica status solidi (a), 2004. **201**(3): p. 497-501.
88. Laukhin, V., et al., *Electric-Field Control of Exchange Bias in Multiferroic Epitaxial Heterostructures.* Physical Review Letters, 2006. **97**(22): p. 227201.
89. Martí, X., et al., *Exchange biasing and electric polarization with YMnO3.* Applied Physics Letters, 2006. **89**(3): p. -.
90. V. Laukhin, X.M., V. Skumryev, D. Hrabovsky, F. Sanchez, M. V. Garcia-Cuenca, C. Ferrater, M. Varela, U. Luders, J. F. Bobo, J. Fontcuberta, *Electric field effects on magnetotransport properties of multiferroic Py/YMnO3/Pt heterostructures.* Philosophical Magazine Letters,, 2007. **87**(3–4): p. 183–191.
91. X. Marti, F.S., D. Hrabovsky, J. Fontcuberta, V. Laukhin, V. Skumryev, M.V. Garcia-Cuenca, C. Ferrater, M. Varela, U. Luders, J.F. Bobo, S. Estrade, J. Arbiol, F. Peiro, *Epitaxial growth of biferroic YMnO3(0001) on platinum electrodes.* Journal of Crystal Growth, 2007. **299** p. 288–294.
92. J. Fontcuberta, X.M., F. Sánchez, D. Hrabovsky, V. Laukhin, V. Skumryev, N. Di1, M.V. García-Cuenca, C. Ferrater, M. Varela, U. Lüders and J.F. Bobo, *Exchange biasing with YMnO3 epitaxial films.* Advances in Science and Technology, 2006. **52**: p. 62-69.

93. Kordel, T., et al., *Nanodomains in multiferroic hexagonal RMnO3 films (R = Y, Dy, Ho, Er).* Physical Review B, 2009. **80**(4): p. 045409.
94. Sheng, Z., et al., *Multiple Stable States with In-Plane Anisotropy in Ultrathin YMnO3 Films.* Advanced Materials, 2010. **22**(48): p. 5507-5511.
95. Gélard, I., et al., *Off-Stoichiometry Effects on the Crystalline and Defect Structure of Hexagonal Manganite REMnO3 Films (RE = Y, Er, Dy).* Chemistry of Materials, 2011. **23**(5): p. 1232-1238.
96. Neerushana, J., et al., *Structure and defect characterization of multiferroic ReMnO3 films and multilayers by TEM.* Nanotechnology, 2010. **21**(7): p. 075705.
97. Jin, Z., et al., *Ultrafast dynamics of the Mn3+ d-d transition and spin-lattice interaction in YMnO3 film.* Applied Physics Letters, 2012. **100**(2): p. 021106-021106-4.
98. Rokuta, E., et al., *Low leakage current characteristics of YMnO3 on Si(111) using an ultrathin buffer layer of silicon oxynitride.* Journal of Applied Physics, 2000. **88**(11): p. 6598-6604.
99. Ryu, M.K., et al., *Characterization of Ferroelectricity in the Pt/YMnO3/SiO2/Si Structure by C-V Measurement.* Ferroelectrics, 2002. **271**(1): p. 211-216.
100. Takeshi Yoshimura, N.F., Nobuaki Aoki, Kouzo Hokayama, Shigeki Tsukui, Keisuke Kawabata and Taichiro Ito, *Fabrication of YMnO3 Thin Films on Si Substrates by a Pulsed Laser Deposition Method.* Jpn. J. Appl. Phys., 1997. **36**: p. 5921-5924.
101. Kohei, H., et al., *Low-Temperature Growth and Characterization of Epitaxial YMnO3/Y2O3/Si MFIS Capacitors with Thinner Insulator Layer.* Japanese Journal of Applied Physics, 2005. **44**(9S): p. 6977.
102. Shogo Imada , S.S., Eisuke Tokumitsu and Hiroshi Ishiwara, *Epitaxial Growth of Ferroelectric YMnO3 Thin Films on Si(111) Substrates by Molecular Beam Epitaxy.* Jpn. J. Appl. Phys., 1998. **37**: p. 6497-6501.
103. Kim, Y.T., et al., *Atomic structure of random and c-axis oriented YMnO3 thin films deposited on Si and Y2O3/Si substrates.* Journal of Applied Physics, 2003. **94**(8): p. 4859-4862.
104. Lee, H.N., Y.T. Kim, and Y.K. Park, *Memory window of highly c-axis oriented ferroelectric YMnO3 thin films.* Applied Physics Letters, 1999. **74**(25): p. 3887-3889.
105. Choi, K.-J., W.-C. Shin, and S.-G. Yoon, *Characteristics of ferroelectric YMnO3 thin films for MFISFET by MOCVD.* Integrated Ferroelectrics, 2001. **34**(1-4): p. 101-111.
106. Yun, K.Y., et al., *Effects of Ar post-annealing on the electrical properties of Pt/YMnO3/p-Si and Pt/YMnO3/Y2O3/p-Si.* Integrated Ferroelectrics, 2001. **40**(1-5): p. 163-170.
107. Shin, W.-C., et al., *Characteristics of Pt/YMnO3/Y2O3/Si structure using a Y2O3 buffer layer grown by pulsed laser deposition.* Journal of Vacuum Science & Technology B, 2001. **19**(1): p. 239-243.
108. Yoshimura, T., et al., *Characterization of ferroelectricity in metal/ferroelectric/insulator/semiconductor structure by pulsed C–V measurement; Ferroelectricity in YMnO3/Y2O3/Si structure.* Journal of Applied Physics, 2000. **87**(7): p. 3444-3449.
109. Zhang, R., et al., *Piezoelectric, ferroelectric properties of multiferroic YMnO3 epitaxial film studied by piezoresponse force microscopy.* Journal of Crystal Growth, 2014. **390**(0): p. 56-60.

110. Aoki, N., et al., *Formation of YMnO3 films directly on Si substrate.* Journal of Crystal Growth, 1997. **174**(1–4): p. 796-800.
111. Singh, A.K., et al., *Effect of epitaxial strain on the magneto-electric coupling of YMnO3 thin films.* Journal of Applied Physics, 2009. **106**(1): p. -.
112. Yoshimura, T., N. Fujimura, and T. Ito, *Ferroelectric properties of c-oriented YMnO3 films deposited on Si substrates.* Applied Physics Letters, 1998. **73**(3): p. 414-416.
113. Dho, J. and M.G. Blamire, *Competing functionality in multiferroic YMnO3.* Applied Physics Letters, 2005. **87**(25): p. -.
114. Parashar, S., et al., *Electrical properties of ferroelectric YMnO3 films deposited on n-type Si(111) substrates.* Journal of Physics D: Applied Physics, 2003. **36**(17): p. 2134.
115. Uusi-Esko, K. and M. Karppinen, *Extensive Series of Hexagonal and Orthorhombic RMnO3 (R = Y, La, Sm, Tb, Yb, Lu) Thin Films by Atomic Layer Deposition.* Chemistry of Materials, 2011. **23**(7): p. 1835-1840.
116. Uusi-Esko, K., J. Malm, and M. Karppinen, *Atomic Layer Deposition of Hexagonal and Orthorhombic YMnO3 Thin Films.* Chemistry of Materials, 2009. **21**(23): p. 5691-5694.
117. Yi, W.-C., et al., *Ferroelectric characterization of highly (0001)-oriented YMnO3 thin films grown by chemical solution deposition.* Applied Physics Letters, 1998. **73**(7): p. 903-905.
118. Choi, J.H., J.Y. Lee, and Y.T. Kim, *Formation of Y2O3 interface layer in a YMnO3/Si ferroelectric gate structure.* Applied Physics Letters, 2000. **77**(24): p. 4028-4030.
119. Lee, H.N., Y.T. Kim, and S.H. Choh, *Comparison of memory effect between YMnO3 and SrBi2Ta2O9 ferroelectric thin films deposited on Si substrates.* Applied Physics Letters, 2000. **76**(8): p. 1066-1068.
120. Yoo, D.C., et al., *Effects of post-annealing on the microstructure and ferroelectric properties of YMnO3 thin films on Si.* Journal of Crystal Growth, 2001. **233**(1–2): p. 243-247.
121. Yoo, D.C., et al., *Crystallization behavior of ferroelectric YMnO3 thin films on Si(100) substrates.* Journal of Crystal Growth, 2002. **234**(2–3): p. 454-458.
122. Yoo, D.C., et al., *Microstructure control of YMnO3 thin films on Si (100) substrates.* Thin Solid Films, 2002. **416**(1–2): p. 62-65.
123. Kim, D.-P. and C.-I. Kim, *The etching characteristics of YMnO3 thin films in high density Ar/CF4 plasma.* Thin Solid Films, 2003. **434**(1–2): p. 130-135.
124. Liu, Y.-F., et al., *Temperature-Dependent Raman Spectrum of Hexagonal YMnO3 Films Synthesized by Chemical Solution Method.* Chinese Physics Letters, 2010. **27**(5): p. 056801.
125. Gelard, I., *Hétérostructures d'oxydes multiferroïques de manganites de terres rares hexagonaux RMnO3 – Elaboration par MOCVD à injection et caractérisations structurales et physiques*, in *Laboratoire des Matériaux et du Génie Physique*. 2009, Institut polytechnique de Grenoble: Grenoble.
126. Kim, E.-S.C., Jung-Hoon ; Kang, Seung-Gu, *Electrical Properties of ReMnO3 (Re:Y, Ho, Er) Thin Film Prepared by MOCVD Method.* Journal of the Korean Ceramic Society, 2002. **39**(12): p. 1128-1132.
127. Jang, S.Y., et al., *Oxygen vacancy induced re-entrant spin glass behavior in multiferroic ErMnO3 thin films.* Applied Physics Letters, 2008. **93**(16): p. -.

128. Chen, W.R., et al., *Re-entrant spin glass behavior in Mn-rich YMnO3.* Applied Physics Letters, 2005. **87**(4): p. -.
129. Zheng, H.W., et al., *Spin-glassy behavior and exchange bias effect of hexagonal YMnO3 nanoparticles fabricated by hydrothermal process.* Journal of Applied Physics, 2010. **107**(5): p. -.
130. Yoo, Y.J., et al., *Spin-glass behavior of Cr-doped YMnO3 compounds.* Journal of Applied Physics, 2012. **112**(1): p. -.
131. Salvador, P.A., et al., *Stabilization of YMnO3 in a Perovskite Structure as a Thin Film.* Chemistry of Materials, 1998. **10**(10): p. 2592-2595.
132. Bosak, A.A., et al., *Epitaxial phase stabilisation phenomena in rare earth manganites.* Thin Solid Films, 2001. **400**(1–2): p. 149-153.
133. Hsieh, C.C., et al., *Magnetic ordering anisotropy in epitaxial orthorhombic multiferroic YMnO3 films.* Journal of Applied Physics, 2008. **104**(10): p. -.
134. Hsieh, C.C., et al., *Electronic structure and magnetic anisotropies in orthorhombic multiferroic YMnO3 thin films.* Journal of Physics: Conference Series, 2009. **150**(4): p. 042062.
135. Chen, Z., et al., *The electrical and magnetic properties of epitaxial orthorhombic YMnO3 thin films grown under various oxygen pressures.* Applied Surface Science, 2011. **257**(18): p. 8033-8037.
136. Zandalazini, C., et al., *Uncompensated magnetization and exchange-bias field in La0.7Sr0.3MnO3/YMnO3 bilayers: The influence of the ferromagnetic layer.* Journal of Magnetism and Magnetic Materials, 2011. **323**(22): p. 2892-2898.
137. Barzola-Quiquia, J., et al., *Revealing the origin of the vertical hysteresis loop shifts in an exchange biased Co/YMnO 3 bilayer.* Journal of Physics: Condensed Matter, 2012. **24**(36): p. 366006.
138. Marti, X., et al., *Ferromagnetism in epitaxial orthorhombic YMnO3 thin films.* Journal of Magnetism and Magnetic Materials, 2009. **321**(11): p. 1719-1722.
139. Chen, Y.B., et al., *Significant ferrimagnetisms observed in superlattice composed of antiferromagnetic LaFeO3 and YMnO3.* Applied Physics Letters, 2013. **102**(4): p. -.
140. Marti, X., et al., *Exchange bias between magnetoelectric YMnO3 and ferromagnetic SrRuO3 epitaxial films.* Journal of Applied Physics, 2006. **99**(8): p. 08P302-08P302-3.
141. Martí, X., et al., *Crystal texture selection in epitaxies of orthorhombic antiferromagnetic YMnO3 films.* Thin Solid Films, 2008. **516**(15): p. 4899-4907.
142. Jiménez-Villacorta, F., et al., *Strain-driven transition from E-type to A-type magnetic order in YMnO3 epitaxial films.* Physical Review B, 2012. **86**(2): p. 024420.
143. Martí, X., et al., *Dielectric anomaly and magnetic response of epitaxial orthorhombic YMnO3 thin films.* Journal of Materials Research, 2007. **22**(08): p. 2096-2101.
144. Li, S.Z., et al., *Preparation of epitaxial orthorhombic YMnO3 thin films and the current–voltage rectifying effect.* Applied Physics A, 2009. **94**(4): p. 975-980.
145. Marti, X., et al., *Strain tuned magnetoelectric coupling in orthorhombic YMnO3 thin films.* Applied Physics Letters, 2009. **95**(14): p. -.
146. Fina, I., et al., *Dielectric anomalies in orthorhombic YMnO3 thin films.* Thin Solid Films, 2010. **518**(16): p. 4710-4713.
147. Fina, I., et al., *Magnetic switch of polarization in epitaxial orthorhombic YMnO3 thin films.* Applied Physics Letters, 2010. **97**(23): p. -.

148. J. Fontcuberta, I.F., L. Fabrega, F. Sanchez, X. Martı and V. Skumryev, *Ferroelectricity and strain effects in orthorhombic YMnO3 thin films.* Phase Transitions, 2011. **84**(5-6): p. 555–568.
149. Cheng, Z.X., et al., *Exchange bias in multiferroic BiFeO3 and YMnO3 multilayers: One more parameter for magnetoelectric manipulation.* Scripta Materialia, 2011. **65**(3): p. 249-252.
150. Nakamura, M., et al., *Multiferroicity in an orthorhombic YMnO3 single-crystal film.* Applied Physics Letters, 2011. **98**(8): p. -.
151. Haw, S.-C., et al., *Anisotropic orbital occupation and Jahn-Teller distortion of orthorhombic YMnO3 epitaxial films: A combined experimental and theoretical study on polarization-dependent x-ray absorption spectroscopy.* The Journal of Chemical Physics, 2014. **140**(15): p. 154503 1-4.
152. Martí, X., *Growth and characterization of magnetoelectric YMnO3 epitaxial thin films*, in *Departament de Física, Facultat de Ciències*. 2009, Universitat Autònoma de Barcelona: Bellaterra.
153. Uusi-Esko, K., *Synthesis and Characterization of Ternary Manganese Oxides*, in *Department of Chemistry*. 2011, Aalto University.

Chapter 2

Experimental techniques

Summary

2.1. Elaboration techniques ……...39
2.1.1 Pulsed-Injection Metal Organic Chemical Vapor Deposition (PI-MOCVD) ……..39
2.1.2 Pulsed Laser Deposition (PLD) ……...46
2.1.3 Solid state reaction technique ……47
2.1.4 Single crystal growth ……...48
2.2 Characterization techniques ……48
2.2.1 Structural characterization ……...48
2.2.1.1 X-Ray diffraction (θ-2θ scans, GIXRD, XRR, RSM) ……..48
2.2.1.2 Raman spectroscopy ……55
2.2.2 Microstructural and surface characterization ……...56
2.2.2.1 Scanning Electron Microscopy (SEM) ……56
2.2.2.2 Transmission Electron Microscopy (TEM) ……..57
2.2.2.3 Atomic Force Microscopy (AFM) ……59
2.2.3 Chemical composition analysis ……60
2.2.3.1 Energy-Dispersive X-ray spectroscopy (EDX) ……60
2.2.3.2 Electron Probe Microanalysis (EPMA) ……60
2.2.4 Physical characterization: SQUID magnetometry ……...62
References ……64

This chapter is dedicated to the description of the experimental techniques used during the present thesis: elaboration methods, structural and microstructural characterization, chemical composition measurements and physical characterization methods. First, the elaboration methods of the samples are detailed. Then, the structural and microstructural characterizations are presented. Afterwards, chemical characterization techniques are briefly discussed. Finally, the magnetic characterizations methods are described.

2.1 Elaboration techniques

2.1.1 Pulsed-Injection Metal Organic Chemical Vapor Deposition

Basic Principle

Metal Organic Chemical Vapor Deposition (MOCVD) is a widely used technique for materials preparation, such as semiconductors, oxides, superconductors, etc. with wide applications in solar cell, LEDs, lasers, FETs, photodetectors, etc. The principle of the technique is defined as "synthesis process in which the chemical constituents react in the vapor phase near or on a heated substrate to form a solid deposit" [1]. Volatile compounds (called precursors) containing the chemical elements of the material to be deposited are transported in vapor form via a carrier gas (O_2, Ar, N_2, H_2) to a heated substrate. If the precursors are not in the gaseous state, an evaporation system based on heating is required. When they are coming in contact with the substrate, complex chemical reactions take place. The solid layer is formed and the gaseous residues are evacuated by a pumping system.

The steps during a MOCVD synthesis can be summarized as follows [2]:

- introduction of precursors (forced flow or injection for MOCVD)
- transport of precursors
- evaporation of precursors (if necessary)
- diffusion of gases through the boundary layer
- adsorption of reactants
- reaction on the surface of substrate
- desorption of the organic radicals
- elimination of residues

Pulsed Injection Metal Organic Chemical Vapor Deposition (PI-MOCVD) is a variant of MOCVD deposition developed at LMGP laboratory by J.P. Senateur and is the subject of a patent [3]. The major characteristic of this method is the sequential injection of very small amounts (few mm^3) of a liquid solution of solid precursors diluted in a solvent. The injected microdroplets are evaporated instantaneously (flash evaporation) and the precise quantity is computer controlled by means of a high speed micro electro-valve. The metal organic precursors and the mixture formed with the solvent is transported by the carrier gas (argon + oxygen) into the reaction zone where they are decomposed. The chemical reactions occur on the substrate [4].

A complete investigation of the physical and chemical phenomena taking place in a PI-MOCVD process would be lengthy and outside the scope of this work. The main concepts are summarized in Figure II.1.

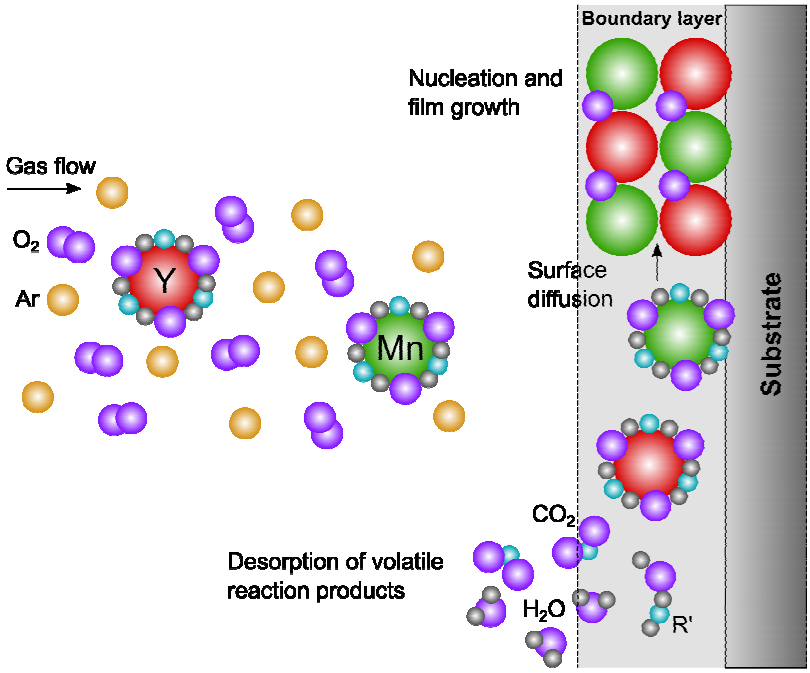

Figure II.1 Simple schematic representation of the PI-MOCVD process leading to the film growth starting from precursors.

As indicated by the name, MOCVD uses metal organic precursors (usually in solid form) which are diluted in a liquid solvent. To provide an adequate decomposition and thermal stability, the metallic organic precursors must have a good quality. Such reaction is needed in particular for the separation of the solvent used for dissolving the solid precursors.

In the reaction zone, an important role is played by the concept of boundary layer (see Figure II.1). The flow velocity of the fluid (gas) drops to zero at the surface of the substrate. This region is the boundary layer and its thickness is given by the formula [1]:

$$t = \sqrt{\frac{x}{R_e}}, \text{ where } R_e = \frac{\rho u_x}{\mu}$$

With

R_e = Reynolds number (characterizes the flow of the fluid)

ρ = mass density of the fluid

u_x = flow density of the fluid

x = distance from inlet to substrate

μ= viscosity of the fluid

Within this boundary layer, there is also a temperature and a concentration gradient of reactive species. The thickness of the boundary layer is an important parameter related with the deposition rate and the thickness of film. During deposition, the reactive gases and the produced gases diffuse in opposite directions through the boundary layer. A nucleus having reached or exceeded the critical size will grow by capturing the isolated atoms arriving from the gas phase or those which diffuse in the surface. Three types of growth are possible: 2D Franck van der Merwe (layer-by-layer growth), 3D Volmer-Weber (growth by island) or mixed 2D-3D Stranski-Krastanov (mixed layer-by-layer and island growth).

Although it is a chemical technique, many physical phenomena (fluid hydrodynamic phenomena, thermodynamics or chemical kinetics) take place which allows the control of deposition rate and quality of the film.

Compared to other CVD techniques, the PI-MOCVD has several advantages:

- A good control of the thickness through the total number of injections
- Control of the growth rate and vapor pressure through the injected volume and injector frequency
- Deposition of precise multilayers due to the simple control of different injection sources (simultaneously)
- Good stability of precursors due to the injection as microdroplets

Experimental setup

The films studied in this thesis were grown in two PI-MOCVD devices: a horizontal reactor, where the precursors are inserted on a moving tape perpendicular to the vertical substrate, and a vertical reactor where the precursors are injected directly into the chamber and then guided by the carrier gases from the bottom to the upper part where the substrate is placed upside down.

Horizontal reactor

The deposition chamber is represented in Figure II.2. This device has a horizontal quartz tube which can withstand high temperatures and low pressures, necessary during the film growth.

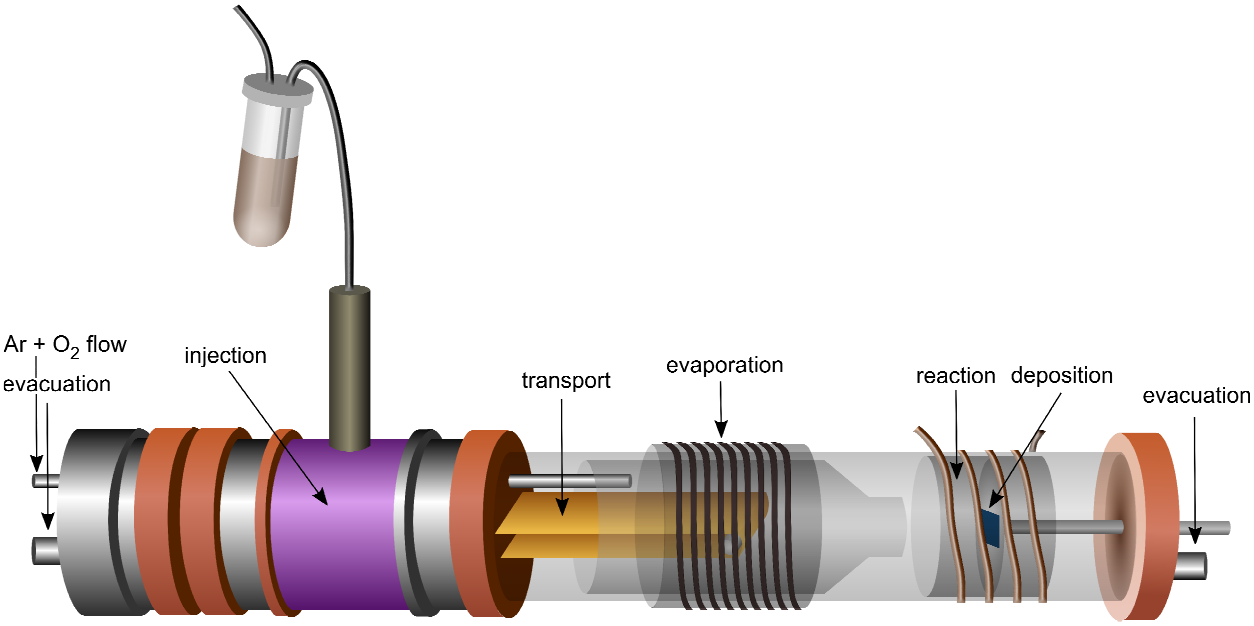

Figure II.2. Schematic of the horizontal PI-MOCVD system used for film deposition.

The precursor's micro-droplets are injected in a cold zone on a moving transport belt where the solvent is instantly evaporated due to the working pressure and recovered by the pump system. The quantity of solid precursor lying on the conveyor belt is mechanically carried out into an evaporation zone where the precursor vapors are produced. The vapors are then transported into the reaction zone where they are decomposed and the chemical reactions take place on the substrate. The substrate is placed on a graphite hot-wall susceptor, heated by a high frequency generator. In this PI-MOCVD setup, a computer regulates the opening time of the injector, the frequency of injection, and the speed of the conveyor belt [5].

According to their functionality, the experimental setup can be divided into several parts, as illustrated in Figure II.2:

- Injection
- Transport
- Evaporation

- Reaction
- Deposition
- Evacuation

A brief description of each part is given in the following.

Injection

In this part, the injection of the solution (precursors and solvent) is performed. An electromagnetic injector, depicted in Figure II.3, inserts a quantity of matter of about several mg in the deposition chamber.

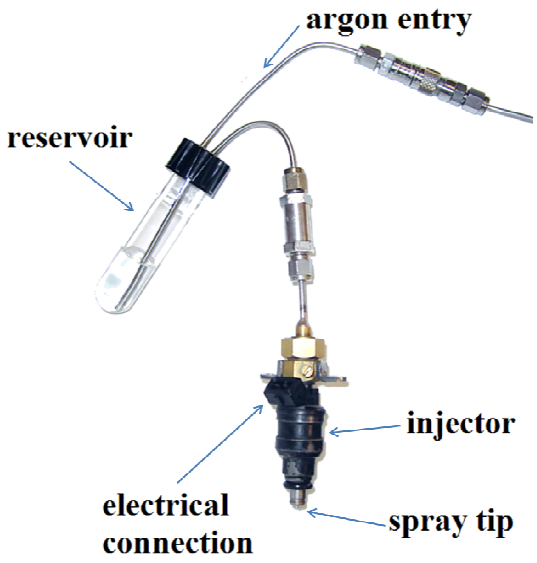

Figure II.3. Precursor injection system (from [6]).

It is supplied with a voltage of 12 V, commanded by a computer through a microvalve which determines the frequency and duration of the injector opening. An Ar pressure of 1.5 bar is maintained inside the reservoir allowing for the solution to ascend into the injector. This type of injector is identical to the modern car injectors used to inject fuel.

a. Transport

After the injection, the solution (precursor and solvent) droplets arrive into the deposition chamber. The solvent evaporates instantly due to the low vapor pressure that exists inside. The solid precursor reaches a rough stainless steel transport belt (conveyor) located below the injector. At the extremity of the deposition chamber a mixture of Ar and O_2, called carrier gas, is

introduced in order to transport the gaseous precursors to the substrate. A computer coordinated engine, supplied with a voltage of 4 V, determines the moving rate of the tape and consequently the amount of material that arrives in the evaporation zone.

b. Evaporation

The evaporation of the metal organic precursor is achieved via the temperature which should be higher than the vaporization temperature of each separate component. The precursor decomposition is ensured by two resistive heaters, one inside and one outside the quartz tube. The interior heater is placed under the transport tape and is represented by a rectangular piece made of stainless steel with dimensions of 3.3 cm x 8.3 cm. The exterior heater is spooled on a quartz tube that glides on the outside of the main quartz tube. It ensures a resistive heating and is powered at 220 V. A quartz nozzle is located at the end of the evaporation zone to accelerate the reactive gas species transport after the thermal decomposition.

c. and e. Reaction and Deposition

In this type of PI-MOCVD device, the chemical reactions (see Figure II.1) are initiated and maintained by the addition of thermal energy by a copper high frequency (HF) coil heater. The gas flow together with the reactive species reach the substrate surface perpendicularly, which rests on a circular stainless steel plate inside a cylindrical graphite susceptor. The plate is welded to a steel rod inside of which is introduced the thermocouple for the substrate temperature measurement. To ensure the thermal conduction between substrate and sample holder, silver paste is used as gluing agent. The susceptor (and therefore the substrate) temperature is controlled by a regulator linked to a HF power supply. As a result of chemical reactions activated by temperature, the film is deposited on the substrate.

f. Evacuation

The reaction residues resulted from the deposition are evacuated through the pumping system. These residues are mostly composed of carbonates, organic parts or precursor which did not react, water, etc. The two pumping outputs are designed to collect the gases and to condense them with the aid of a liquid nitrogen trap. The pressure is controlled by a primary pump (vane pump) connected to a pressure controller (throttle valve) located at the pump inlet which maintains a constant pressure during the deposition (5 Torr).

Vertical reactor

The principle of the film deposition presented for horizontal reactor remains valid in the case of the vertical reactor. A picture of the experimental device is shown in Figure II.4.

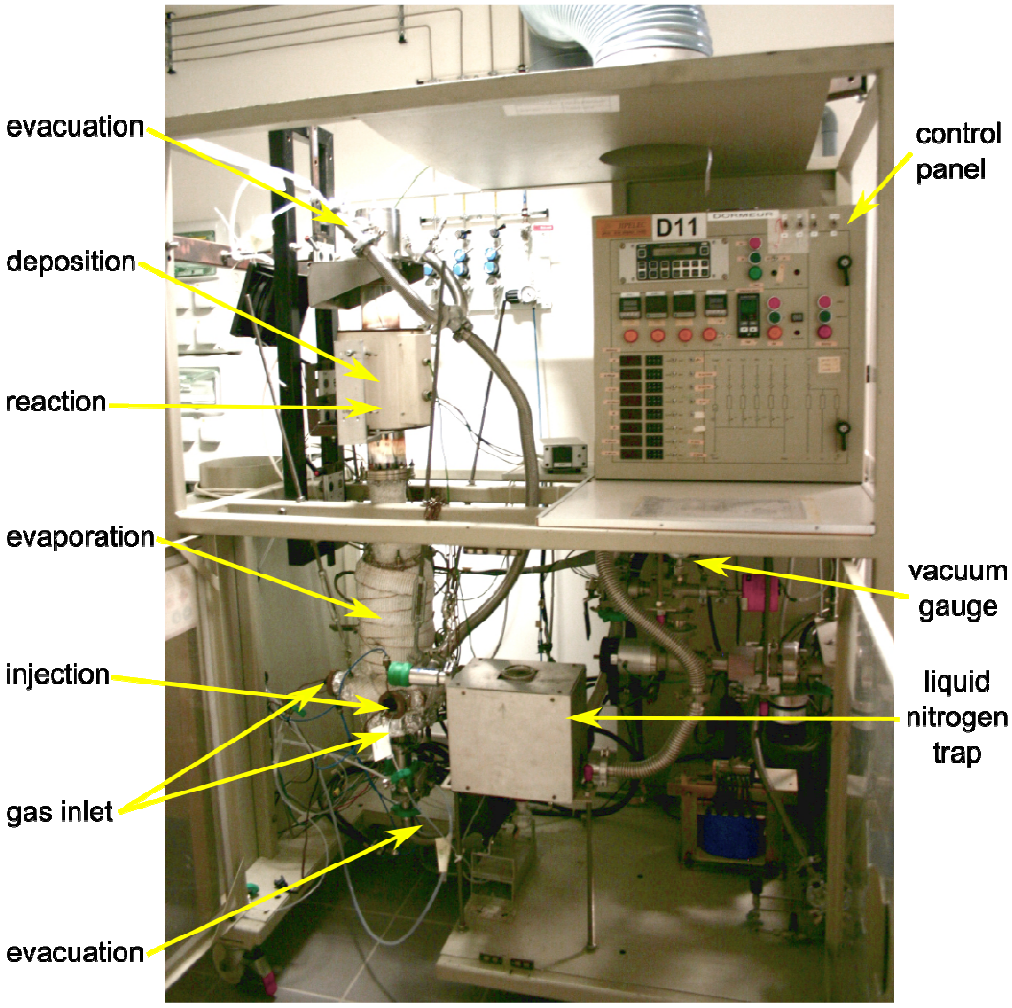

Figure II.4 Picture of the vertical PI-MOCVD setup.

The precursor solution is injected at the bottom of the reactor with the same injector type, then the solvent and the solid precursors are volatilized. The resulted gases are transported toward the reaction zone by the aid of Ar and O_2 flow which enters on the lateral sides of the injection zone. The substrate, oriented perpendicularly to the reactive flow, is heated by a resistive heater. The reaction residues resulted from the deposition are evacuated through the pumping system placed at the top part of the reactor. Another pumping output is located at the other extremity (bottom) of the reactor and is used to purge the system from top to bottom before and after deposition in order to avoid the contamination of the film surface. The pressure regulation is carried out by a

throttle valve located upstream of a vane pump. The pressure can be regulated between $7.5 \cdot 10^{-3}$ and 10 Torr.

2.1.2 Pulsed laser deposition

In order to be able to do a comparison with our chemical deposited samples, a physical deposition technique by PLD was employed for a few samples. The depositions were made at the National Institute for Laser, Plasma & Radiation Physics (INFLPR) in Laser-Surface-Plasma Interactions Laboratory (Lasers Department) in Măgurele, Bucharest, Romania.

Pulsed laser deposition [7] is a physical vapor deposition process which consists in focusing a pulsed laser onto the target material to be deposited. A typical PLD system is shown in Figure II.5.

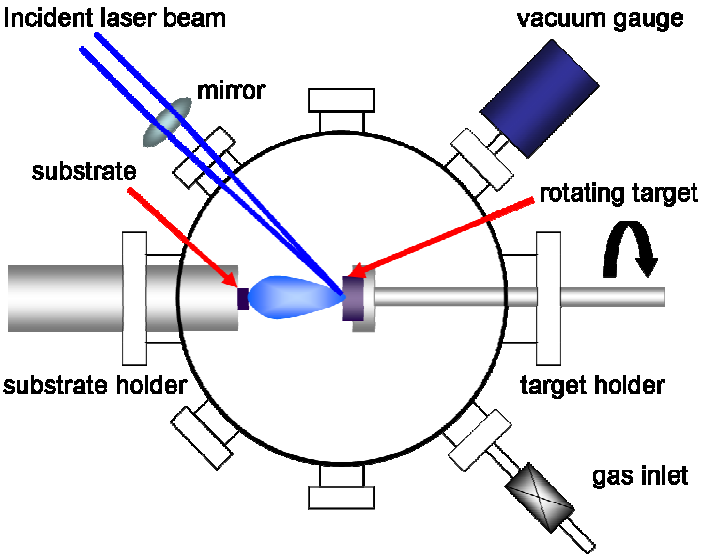

Figure II.5. PLD schematic setup [8].

Each laser pulse ablates a small quantity of the target material creating a plasma plume. The ablation plume provides the material flow for the film growth. The stoichiometry of the target is usually transferred to the film, making this technique very compelling for the deposition of complex oxides. Generally, the phase of the target does not need to be the same as that of the film (only the stoichiometry needs to be the same). As a main requirement, it is highly preferred to have very dense target materials. To ensure a homogenous ablation, the target is rotated during the deposition. Efficient ablation of the target requires the laser pulse to be short in duration, high in energy density, and well absorbed by the target material. In PLD, a background gas is often

introduced and serves, on one side, in the chemistry of the film, at the formation of reactive species (e.g., O_2 for oxides), and on the other side to reduce the kinetic energies of the ablated species as the interaction with the ambient gas slows the ablation plume expansion. Each ablation pulse typically provides an amount of material for the deposition of a submonolayer of the desired phase. However, the film growth rate (typically between 0.001 to 1 Å per pulse) will depend on multiple factors, including target–substrate separation, background gas pressure, laser spot size and laser energy density. In some cases, the control of the film growth is done in-situ using the reflection high-energy electron diffraction (RHEED) characterization.

In our experiments, a pulsed KrF excimer laser beam (λ = 248 nm, τ=25 ns and 3 Hz) is deflected, focused and guided into the vacuum chamber through a series of optical elements (mirrors, focusing lenses, windows) and then onto a rotating solid YMO target at an angle of incidence of 45° with a fluence of 2.5 J/cm^2. The substrate is stick to the holder by silver paste or by metallic clips and placed at 5 cm away from the target. The substrate temperature is set to 800 ºC during the deposition (measured by a thermocouple placed in the heater block and regulated by a PID system). The number of laser pulses, which controls the film thickness, was kept constant at 10000 pulses for all depositions. The reaction chamber was evacuated to a residual gas pressure between 10^{-4} and 10^{-5} Pa prior to deposition. During the laser ablation, followed by the vaporization of the target material and deposition onto the substrate, oxygen is introduced into the chamber.

2.1.3. Solid state reaction technique

The solid state reaction technique is the most common method used for the elaboration of polycrystalline solids. Its principle is based on the solid state diffusion, (i.e. transport of atoms in solid phases). The precursors (reagents) are solid materials which are weighed according to the required amounts and then mixed. The mixing and grinding are either done manually (for small quantities) with the aid of an agate mortar and a pestle or mechanically using a ball mill. Sometimes, acetone or ethanol are added to facilitate the homogenization, then are afterwards evaporated. The purpose of these processes is to obtain fine grain powders in order to maximize the surface contact area between particles. The quantity of crystallites in intimate contact may be increased by pelletizing the powders using a press. Diffusion is controlled by the Fick's first Law

$$J = -D\frac{\partial c}{\partial x}$$

where J is the atom diffusion flux, D is the diffusion coefficient, c is the concentration and x is the position.

The reaction containers (crucibles) must withstand the high temperatures and to be chemically inert to the reactants. They are usually made from alumina, silver, gold or platinum. The atmosphere is also critical. Depending on the nature of the compound to be synthetized, oxidative, reductive, inert, etc., a gaseous atmosphere or vacuum is needed.

The solid-state reaction route was used to prepare h-YMO samples (stoichiometric and non-stoichiometric) as references for different measurements and h-YMO targets for PLD experiments. Powder precursors of Y_2O_3 and Mn_2O_3 (99.99% purity) have been weighed out in the required amounts and manually mixed in an agate mortar. Occasionally, some amount of alcohol was added to the mixture to aid homogenization. After the complete homogenous mixing of the precursors and volatilization of the liquid the powder was pressed into pellets applying pressures up to 5 tons. Subsequently, the pellets were sintered in a furnace at 900 ºC for 72 hours and afterwards at either 1200°C or 1400°C for 48h or 96h in normal air. Black h-YMO samples have resulted which were then characterized.

2.1.4 Single crystal growth

Single crystals of h-YMO, used as reference for Raman spectroscopy and magnetic measurements, were grown previously by floating zone in LEMA laboratory at Tours.

2.2 Characterization techniques

2.2.1 Structural Characterization

2.2.1.1 X-ray diffraction

X-ray diffraction (XRD) is a non-destructive characterization tool which offers valuable information concerning the crystallinity, the nature of the crystalline phases present in the films, the preferential and epitaxial orientation, the lattice parameters, the grains size, stress, etc. The principle of XRD is well known [9] and will not be discussed here. Essentially, XRD is based on the constructive interference of a monochromatic X-ray beam scattered by a periodic

arrangement of atoms in a crystal. The interaction X-ray – sample produces a constructive interference when satisfying Bragg's Law ($2d \sin\theta = n\lambda$) thus giving rise to a peak in the XRD pattern. This peak corresponds to a family of planes, indexed by Miller indices.

A diffractometer is composed roughly of three parts: a X-ray source, a goniometer and a detector. The X-rays are generated by a cathode tube, then filtered to provide a monochromatic radiation, collimated and then directed towards the sample. The diffracted X-rays are then detected, processed and counted.

An important application of the XRD is the identification of the phases present in a sample. Each crystalline phase has a unique diffractogram because the line positions depend on the interatomic distances and the line intensities depend on the arrangement of atoms in the crystal.

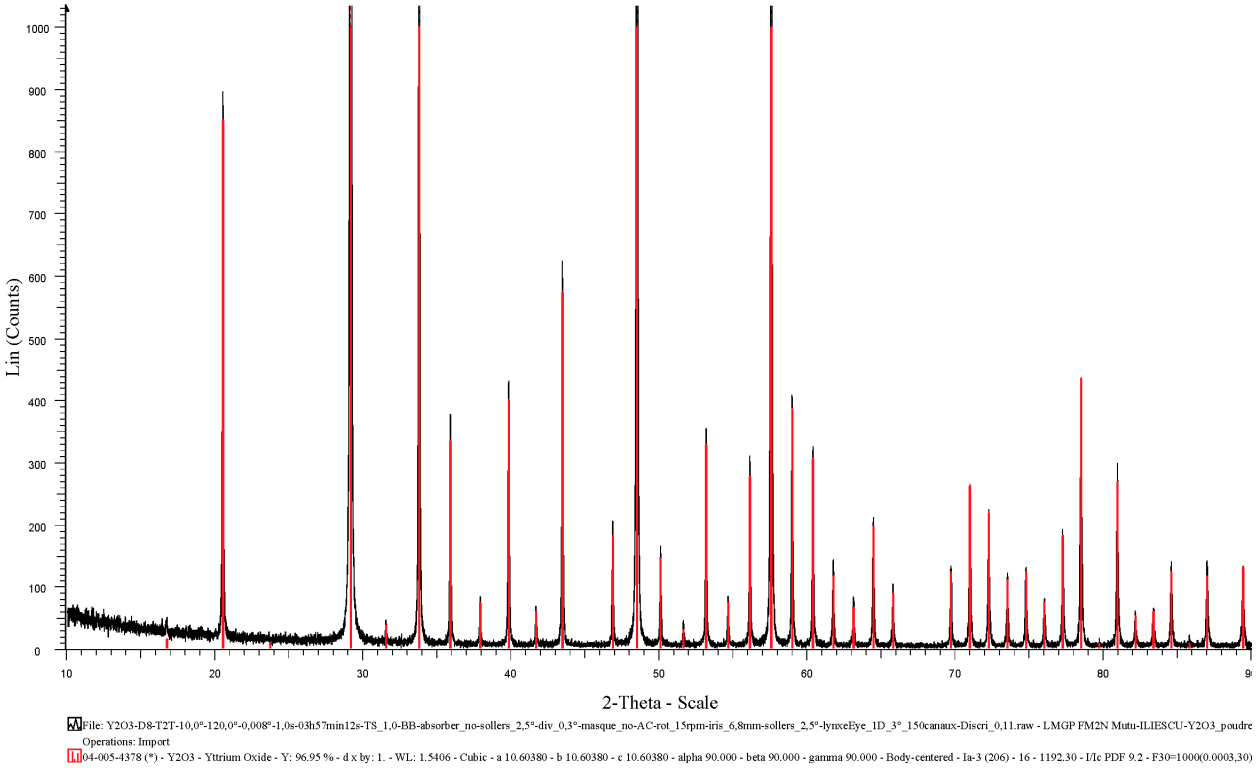

Figure II.6. XRD phase identification with EVA software.

The phase identification consists in comparing the experimental pattern, corresponding to different *d*-spacing and intensities, with a powder diffraction reference data, existing in databases (e.g. Joint Committee on Powder Diffraction Standards - JCPDS) [10]. This search was done, in our case, with the "Diffrac Plus EVA" software (17.0) from Bruker. One example of phase

identification is shown in Figure II.6. The position of the diffraction peaks in the experimental XRD pattern, marked in black, corresponds perfectly with the position of the diffraction peaks of the compound existing in the database, marked in red. Also, it can be noticed that the experimental peak intensities and those listed in the database match closely. Prior to data processing, in the case of our films, the diffractogram is calibrated in 2θ relative to the substrate peaks. This avoids any *x*-offset or sample displacement in height (*z*-offset).

Another common application of XRD is the calculation of the crystallite size based on the profile analysis of the diffraction lines. In theory, the diffraction lines should be extremely narrow, but due to the instrumental contribution (finite size and monochromaticity deviations of the X-ray source, axial divergence of the beam, etc.) and sample contribution (finite crystallite size, microstrain, defects, etc.) these profiles present usually a width characterized by the full width at half maximum (FWHM). The Scherrer equation allows the determination of the crystallite size *L* (in nm):

$$L = \frac{K\lambda}{\beta_{1/2}\cos\theta},$$

Where K is a constant (usually 0.9), λ (Å) is the radiation wavelength, $\beta_{1/2}$ is FWHM (in rad) and θ (in deg.) is the incidence angle.

Depending on the sample type and the desired information several scan types and geometries are available.

θ-2θ scan

In the θ-2θ geometry, as it is in our case, the X-ray tube is stationary, the sample moves by the angle θ and the detector simultaneously moves by the angle 2θ (see Figure II.7). The distance between the X-ray focal spot and the sample is equal to the distance from the sample to the detector. In this type of configuration only the planes parallel to the sample surface are probed (marked in green in Figure II.7). In the case of crystalline powders, by scanning the sample through the whole 2θ angle range, all diffraction planes having different Miller indices are diffracting due to the random orientation of crystallites. In the case of epitaxial or textured films, the θ-2θ scan reveals only some families of planes (i.e. those parallels to the sample surface). In this case, complementary XRD measurements (e.g. grazing incidence, rocking curve) or other techniques are necessary in order to have a complete picture of the sample.

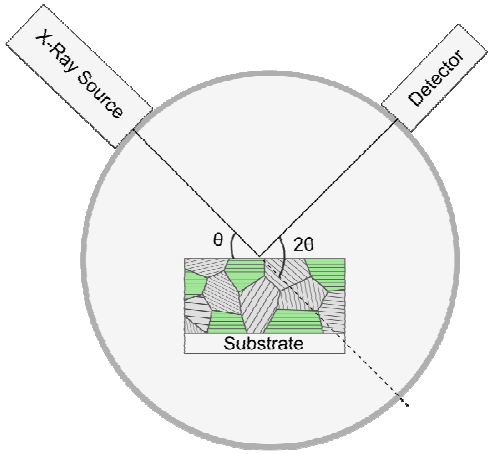

Figure II.7. Schematic diagram of θ-2θ scan setup.

The crystalline structure of the films was investigated using a Bruker D8 Advance diffractometer with monochromatic CuKα1 radiation (λ = 1.5406 Å) and a LynxEye 1 dimension detector. The measurements were done at 40 kV and 40 mA and were carried out between 10° and 90° in 2θ range with a step size between 0.011° and 0.022° and a scan speed between 1s and 2s.

Grazing incidence XRD (GIXRD)

X-ray diffraction measurements of films using conventional θ-2θ Bragg-Brentano geometry generally provides a weak signal from the film and an intense signal from the substrate especially if the film is very thin (see Figure II.8).

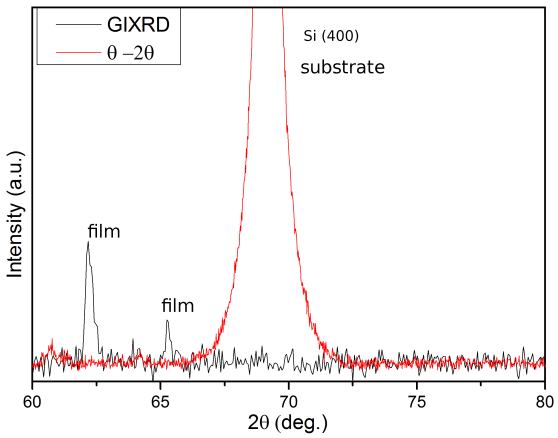

Figure II.8. Comparison between θ-2θ scan and GIXRD geometry.

To overcome this issue, a 2θ scan with a fixed grazing incidence angle (fixed θ), commonly known as grazing incidence X-ray diffraction (GIXRD) can be more useful. The value of the

fixed angle is generally chosen to be slightly above the critical angle ω_c of the film material, leading to total reflection. Besides the fact that the film/substrate signal is enhanced, this geometry allows to probe the planes non-parallel to the specimen surface. For GIXRD measurements, a 60 mm parabolic mirror was used in order to obtain a monochromatic radiation ($\lambda_{CuK\alpha}$=1.54184 Å) and a parallel incident beam (with a divergence less than 0.05° in 2θ direction). The angle of incidence (in the range 0.325° - 0.5°) was set to maximize the signal of the layer; a 2x2mm slit and a collimator (0.23° divergence) with a scintillator 0D detector were used to perform a scan in the 2θ range between 15 – 90° with a step size of 0.06° and a counting time between 47 and 87 s.

X-ray reflectivity

X-ray Reflectivity (XRR) is a technique which uses the scattering of X-rays at very small angles. It permits the measurement of film thickness, roughness and density through the characterization of the electron density profiles. For X-rays, the refractive index is slightly smaller than 1, which gives rise to the phenomenon of total reflection for angles of incidence less than a critical angle ω_c, called the angle of total reflection (in the range of a few fraction of a degree). Beyond ω_c, a part of the incident beam can penetrate into the medium and will be reflected by the different interfaces giving rise to interference fringes. The period of the interference fringes is related to the thickness of the layer (or layers in case of multilayers). The slope of the curve gives information on the roughness of the interfaces, and the value of the critical angle is related to the density of the material. The typical range for XRR measurements is between $0 < \theta < 5°$. A standard example of XRR profile and the corresponding characteristic parameters of the film is shown in Figure II.9.

The reflection of the X-rays from the surface of the sample is obtained with a Siemens D5000 X-Ray Diffractometer (Cu X-ray source with Göbel parabolic mirror and scintillation detector). The 2θ/ω XRD measurements were performed between 0° and 6° (in 2θ scale) with a step of 0.002° and 40 s by step. Δω (θ-ω) was kept at 0.044°. Using the simulation Leptos software (6.02) from Brucker for the reflectivity pattern, an accurate calculation of thickness, roughness, and layer density for both crystalline and amorphous thin films and multilayers can be obtained.

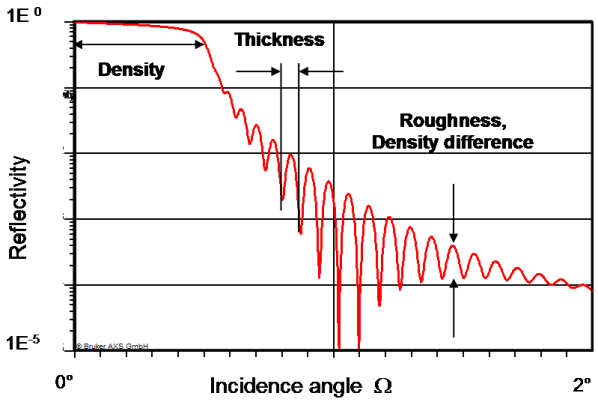

Figure II.9. Relation between the profile of the X-ray reflectivity and the corresponding parameters of the film (from [11]).

The graphical user interface automatically fits measurements using sample models input [12]. Figure II.10 shows an example of a Pt film on a Si substrate and how the thickness and roughness variation affect the simulated curve shape (in blue). By changing the fitting parameters (roughness, thickness) we can reach a good overlapping between the experimental and calculated patterns.

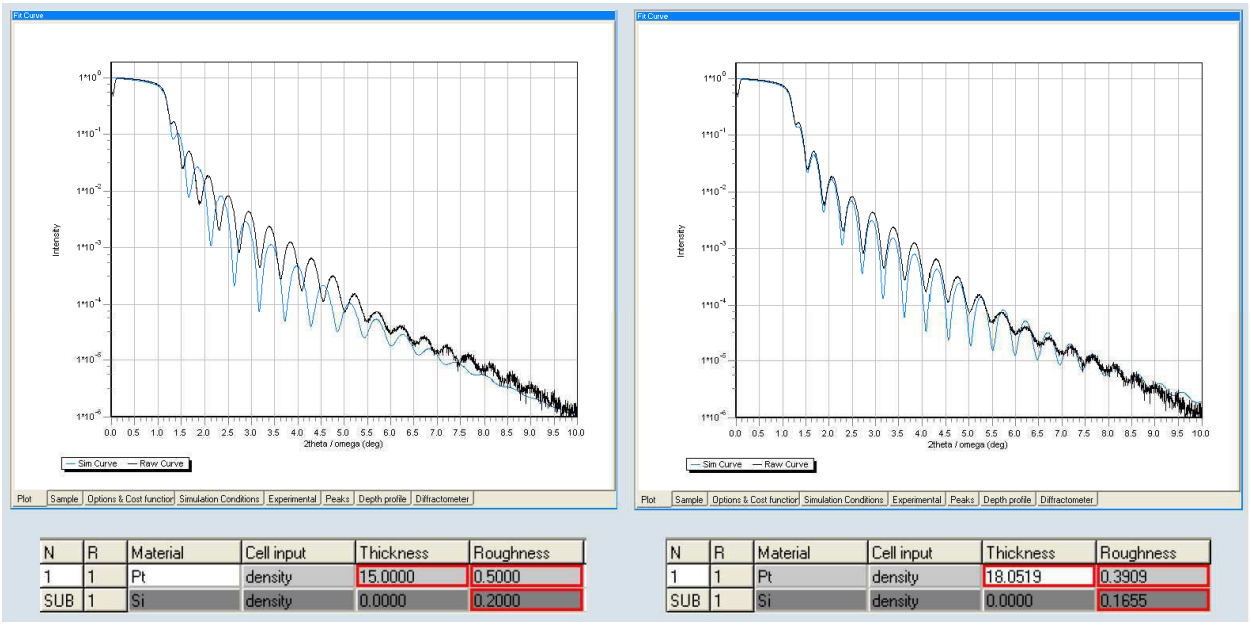

Figure II.10. Experimental XRR curves (in black) and the fitting profiles obtained using the Bruker Leptos software package for a Pt film on Si substrate [13].

Reciprocal space mapping (RSM)

High resolution XRD coupled with Reciprocal Space Mapping (RSM) provides the most complete set of information for the analysis of strained films. The resulting data is a 2D map of the reciprocal space of the sample. These maps plot the diffraction intensity distribution using multiple scans in order to observe both the film and substrate peaks. RSM were generally measured (position and shapes of the reciprocal lattice peaks) by scanning the 2θ and ω axes in the scattering plane with fixed χ and ϕ values (see Figure II.11) in symmetric and asymmetric RSM co-planar geometry.

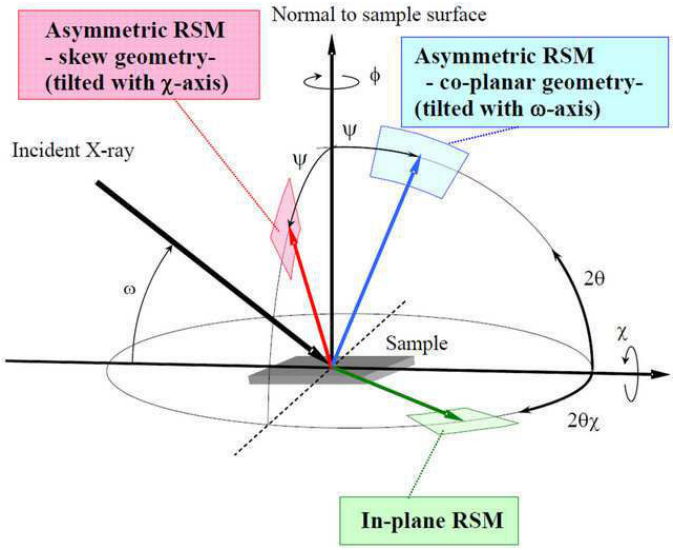

Figure II.11. Schematic of the RSM geometry (from [14]).

The RSM data were measured with a RIGAKU Smartlab diffractometer equipped with a 9kW rotating anode Cu source (45kV and 200mA). In order to obtain a monochromatic parallel x-ray beam, a particular optics is needed before the sample: a 1D parabolic mirror, a Germanium monochromator (400)-oriented with 2 reflections, a mask of 2 mm and a 0.6 mm slit. The obtained beam ($\lambda_{K\alpha1}$ =1.506 Å) dimensions are about 2 mm x 0.6 mm. During acquisition, the sample was fixed on the sample holder with a droplet of ethanol. After the interaction of the X-rays with the sample, two 1.0 mm x 10.0 mm slits, a 2.5° Sollers slit, an automatic attenuator and a point detector were used. Symmetric and asymmetric peaks were scanned as shown in Figure II.12. For example, the RSM of the 004 reflection (symmetric) was obtained from several 2θ-ω scans. These scans have different ω offsets, ranging from -1° to 1° with a step of 0.05°, from the symmetric position (ω=2θ/2).

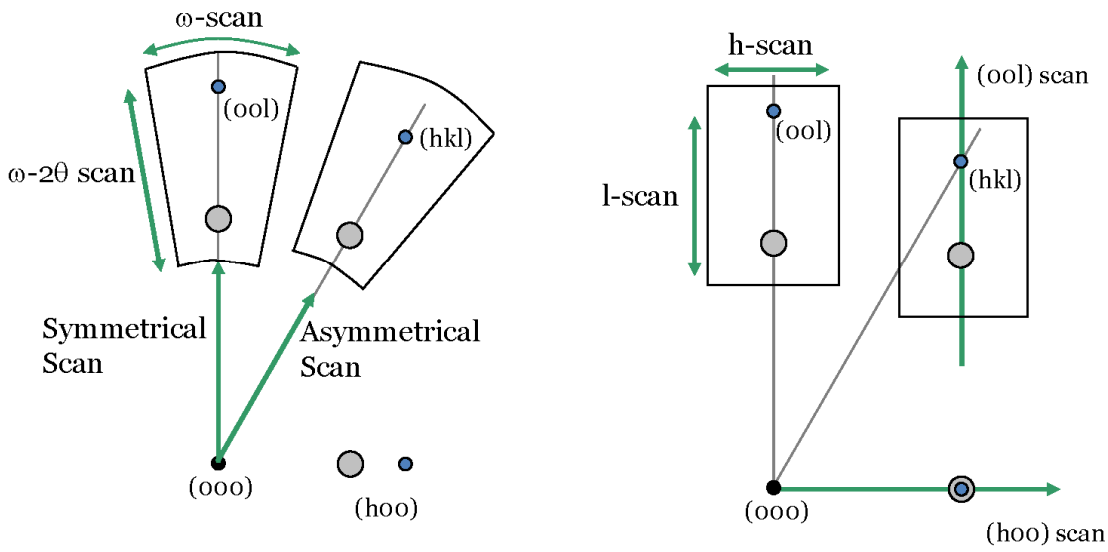

Figure II.12. Symmetrical and asymmetrical scan representation (from [15])

Rigaku 3D explore software version 3.0.1.0 was used for data processing and allows in particular to convert 2θ-ω maps in h-l maps.

2.2.1.2 Raman spectroscopy

Raman spectroscopy is a non-destructive spectroscopic analysis method. The basic principle of the Raman effect is the inelastic scattering of the light. When the light (usually monochromatic light from a laser) encounters matter, the photons are shifted in either higher (Stokes shift) or lower energy states (anti-Stokes shift), depending upon the state of the molecule under study (see Figure II.13). This shift, measured in a Raman spectrum, provides information about vibrational, rotational and other low frequency transitions in molecules. The major applications of this technique in material science are: phase identification, including distinction between polymorphic forms, crystallinity, phase transitions, stress characterization, superlattice structure, distinction between bonds etc.

The Raman spectra in the present work were collected using a Jobin Yvon/Horiba LabRam spectrometer. Experiments were conducted in the micro-Raman mode in a backscattering geometry.

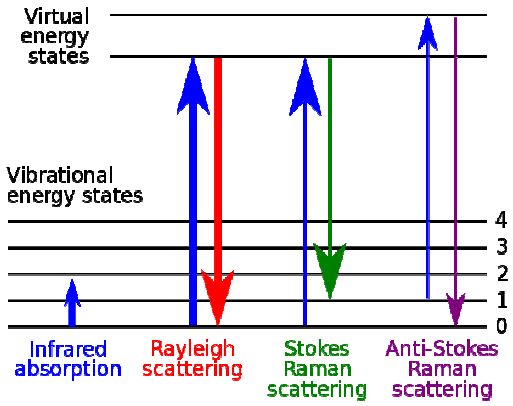

Figure II.13. Schematic diagram of the Raman effect showing the states involved in Raman signal. The line thickness is depicted depending on the intensity of different transitions (from [16]).

The Ar^+ ion laser beam (λ=514.5 nm) - giving the best ratio for the film /substrate signal - was focused on a 1 μm^2 area, with intensity close to 0.35 mW on the sample surface to avoid structural transformations due to overheating. Spectra were recorded in unpolarized mode with an instrumental resolution of 2.8 ± 0.2 cm^{-1} and were calibrated in wavenumber using the Si spectrum at room temperature. The phase identification is mainly performed by comparison with the existent data from the literature (few database are available). The Raman lines were fitted with Lorentzian profiles using Origin software after subtraction of the baseline with the Labspec software of Jobin Yvon/Horiba. The quantities fitted were: mode position, FWHM of the peak, peak area and background.

2.2.2. Microstructural and surface characterization

2.2.2.1 Scanning electron microscopy (SEM)

Scanning electron microscopy (SEM) is a powerful surface characterization technique of materials. Depending on its accessories, it can provide complementary information such as chemical composition (energy dispersive X-ray - EDX), crystalline domain (Electron backscatter diffraction - EBSD) or cathodoluminescent properties (CL-SEM). Its basic principle consists in the emission of electrons from a cathode and the detection of signals from the interaction of electrons with the sample (emission of secondary electrons, backscattered electrons and X-rays). The electrons emitted by the cathode gun are accelerated from top to bottom and focused through

a series of electromagnetic lenses and apertures to produce a convergent beam on the sample surface. To avoid any collision, which would result in a decrease in energy and beam intensity, a high vacuum is required along the path of electrons. Then the electrons bombard the sample surface and penetrate to a certain depth into the material producing different signals (electrons, photons) collected and sent to the detectors. The volume affected by the electrons depends on the average atomic number of the sample elements and the electron energy (fixed by voltage). Two signals are often used to generate SEM images: secondary electrons (SE), most valuable for morphology and topography contrast, and backscattered electrons (BSE), most valuable for composition contrasts in multiphasic samples. For SE the penetration depth is from 10 to 100 nm while the BSE are emitted from much larger depths (~ 1 μm). Another common signal is represented by the X-ray photons used for qualitative and quantitative elemental analysis (EDX).

The morphology, chemical composition and thickness of the films presented in this work were analysed in SE and BSE mode, using an environmental scanning electron microscope QUANTA FEI 250 ESEM FEG, equipped with an EDX detector.

2.2.2.2 Transmission electron microscopy (TEM)

The TEM is a destructive technique for the local study of the crystallinity, topography, morphology, and composition (EDX-TEM) of samples. Currently, TEM has the most powerful magnification of all microscopes, over one million times and a resolution close to 1 Å.

The principle, similar to optical microscopes, consists in using a high energy electron beam transmitted through a very thin sample (<100 nm) to image the materials with an atomic scale resolution. The electrons are accelerated at several hundred kV which give them a very small wavelength (at 200kV λ_e=0.025Å).

Along their passage, before and after specimen, the electrons are focused with a complex system of electromagnetic lenses and the image is captured by a CCD camera. All TEMs have two basic operation modes: image mode and diffraction mode. Other modes are available depending on the type of the microscope: high resolution TEM, bright-field/dark-field imaging (at intermediate magnification), EDX, electron energy loss spectroscopy (EELS), annular dark-field imaging (ADF) and scanning TEM (STEM).

In the diffraction mode, the electrons are scattered almost elastically by the atoms (both electrons and nuclei) of the studied material. In a way, it is similar to XRD, however, due to their small wavelength, the scattering angles are very small comparing to those of XRD ($0<\theta<2$). The obtained pattern depends on the *d*-spacing and composition of the specimen. If the sample is made of an amorphous material (Figure II.14.a), then the ED pattern consists of one bright small ring and two or three faint bigger rings (sometimes not visible at all). In the case of randomly oriented (Figure II.14.b) or textured polycrystalline (Figure II.14.c) samples, the pattern presents well-defined concentric rings or arcs respectively. For single crystals (Figure II.14.d), a regular arrangement of spots satisfying the Bragg relation will result. Whatever the crystalline structure, each ED pattern has a central bright spot representing the transmitted beam (in order to not saturate the image, a beam stopper is used when needed). Selected Area Electron Diffraction (SAED) is usually used to limit the diffracting sample volume by using diaphragms (small aperture in the image plane of the low object lens).

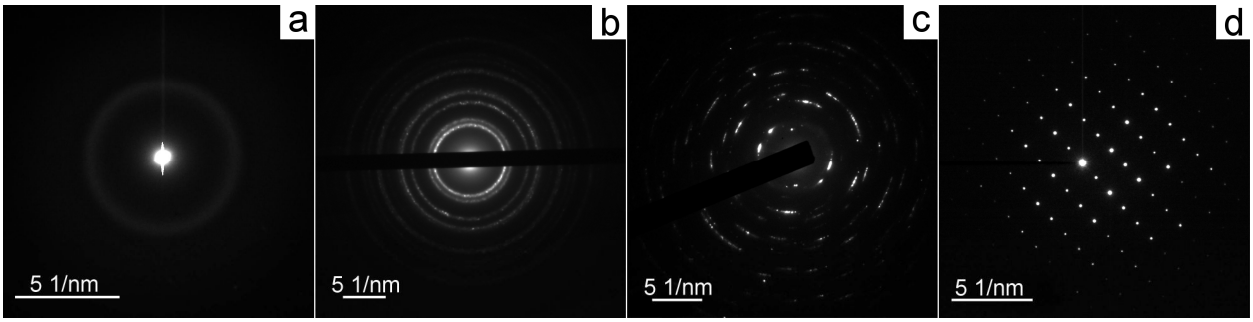

Figure II.14. Typical ED patterns obtained from: a) amorphous $YMnO_3$; b) polycrystalline Au; c) textured $YMnO_3$; d) single crystalline $Y_{4.67}(SiO_4)_3O$ grain.

In the present thesis, detailed structural characterizations of the films were carried out by TEM observations with a JEOL 2010 microscope operated at 200 kV with a beam current of 110 μA (0.19 nm resolution). The TEM was operated in several working modes: HRTEM, bright-field and dark-field and SAED (with or without precession). A coupled EDX detector was used for chemical quantification.

The Digital Micrograph software from Gatan Microscopy Suite was used for data acquisition and image processing (thickness and *d*-spacing measures, image filtering, FFTs).

Diffraction ring profiler software was used for extracting 1D ED patterns from 2D ED profiles (scattering vector or d vs. intensity) allowing direct comparison with θ-2θ XRD patterns.

CarIne software was used to compare the experimental data with simulated structures in real and reciprocal space. It offers a 3D modeling of crystalline structures and analysis modules such as: stereographic projections, XRD on powders and single crystals, reciprocal lattices in 3D and 2D, a dedicated module to electronic diffraction, interactive bond and polyhedron searching, distance indications etc.

For cross-section TEM analysis, the samples were prepared by mechanical polishing (tripode technique) perpendicular to the film, using diamond lapping films to achieve a sample thickness of around 10 μm. The final thinning was performed by the precision ion polishing system (with milling angle ±7° at 3.2 KeV) in order to obtain large electron transparent area, down to 100 nm thick.

2.2.2.3 Atomic force microscopy (AFM)

Atomic force microscopy (AFM) is a scanning microscopy which permits the topographical analysis of samples with very high resolution (in nm laterally and in Å in height). AFM operates by measuring the force between a sharp probe (tip) and a sample placed at a very short distance. The probe is situated on the end of a cantilever which acts like a spring. The movement of the probe above the sample surface is controlled using a feedback loop and piezoelectronic scanners. When the probe's tip is brought into the proximity of the sample surface, the cantilever is deflected due to the forces between the tip and the sample. The deflection is measured via a laser, reflected to a photodiode and then converted into the image. Depending on the nature of the forces between tip and sample, there are several working modes:

-contact (repulsive force)

-non contact (attractive Van der Waals force)

-tapping (short-range repulsive and long-range attractive forces)

Our measurements were carried out on an AFM Nanoscope II Digital Instruments in tapping mode with a Si_3N_4 tip probe. This has permitted us to observe the surface topography and to measure the root mean square roughness.

2.2.3 Chemical composition analysis

2.2.3.1 Energy-dispersive X-ray spectroscopy (EDX)

EDX is a chemical analysis technique used to measure (qualitatively and quantitatively) the chemical elements of a sample. It relies on the interaction of the electron beam and the sample. The EDX is performed in conjunction with Scanning Electron Microscopy (SEM) or Transmission Electron Microscopy (TEM). When the electrons strike the surface of a sample (SEM) or of a thin film (TEM), they generate X-ray emissions from the irradiated material. The energy of the X-rays (emitted photons) is characteristic to each element present in the examined material and gives an EDX spectrum characteristic of the sample.

In the case of an EDX-TEM spectrum, a special absorption correction is required due to the small specimen thickness. The EDX-TEM quantification algorithm for thin materials is based on the Cliff-Lorimer method and neglects the absorbance and fluorescence. For a bi-elemental specimen, the Cliff-Lorimer equation [17] relates the compositions of the constituent elements C_A and C_B to the measured characteristic X-ray intensities I_A and I_B as:

$$\frac{C_A}{C_B} = k_{AB} \frac{I_A}{I_B}$$

where k_{AB} is the Cliff-Lorimer factor, which can be determined both theoretically and experimentally. In this approach no reference material is needed.

Although the resolution of the EDX is around 150 eV, various factors limit the accuracy of the final quantitative result: elements with overlapping peaks (e.g. Mn K_β and Fe K_α), sum peaks (e.g. Si at 2 $K\alpha$ = 3.48 keV), sample nature (inhomogeneous or rough samples give lower quality results), etc. It is important to note that light elements ($Z < 11$) cannot be routinely analyzed by EDX.

EDX measurements were performed on either QUANTA 250 ESEM FEG (usually at 15 kV) or JEOL 2010 (at 200 kV) microscopes.

2.2.3.2. Electron probe microanalysis (EPMA)

EPMA is a specialized technique of quantitative micro analysis. It works on both bulk and film samples. Its concept, similar to EDX, consists in bombarding a few microns volume of a sample with an electron beam and collecting the X-ray photons emitted by the elemental species contained in the sample. The wavelengths of these X-rays are characteristic to each chemical

element so the sample composition can be easily identified by wavelength dispersive spectroscopy (WDS). WDS spectrometers are based on the Bragg's law of diffraction to separate the X-rays. For a quantitative analysis, standards containing the chemical elements in the samples are used. The accuracy of the EPMA technique is about 1% or in the range of ppm depending on the atomic number Z of the element. Compared to the EDX method, the resolution of the WDS system is far superior (see Figure II.15)

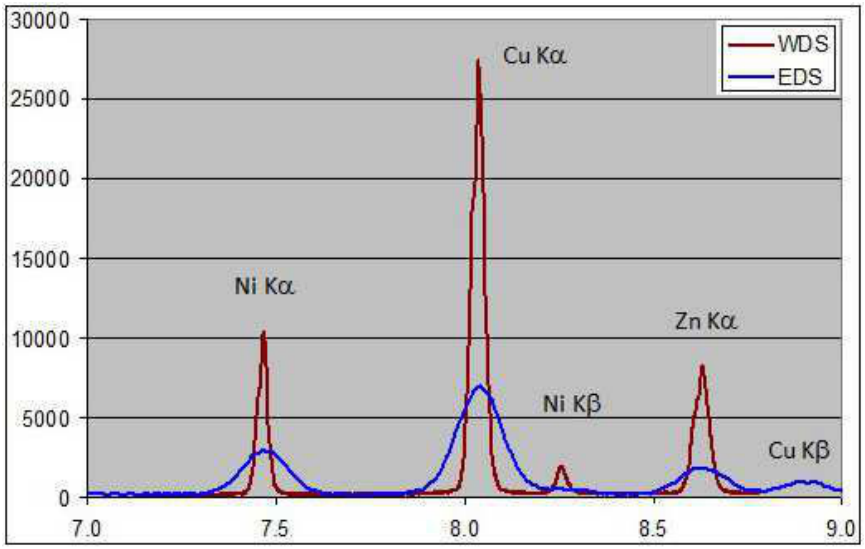

Figure II.15. Spectral resolution and sensitivity of the WDS (in red) compared to EDX (in blue).

The overall atomic compositions and the thicknesses of the films were determined using a CAMECA SX50 microprobe equipped with four WDS crystals and one EDX spectrometer from the Materials Characterization Center of Grenoble INP (CMTC). Unlike the case of EDX measurements, for which the samples do not require any preparation, in this case, the samples were previously coated with a few nanometers of C layer and stick with silver conductive adhesive on the sample holder. YPO_4 and $MnTiO_3$ references were used for quantitative analysis of Y and Mn or O respectively. Si, $SrTiO_3$, $LaAlO_3$ and $(LaAlO_3)_{0.3}(Sr_2AlTaO_6)_{0.7}$ substrate references were also used. Several areas were measured for each film at three different acceleration voltages in the range 10 to 20 kV.

The commercial software STRATAGem was used for data processing. The conversion of measured X-ray intensities to concentrations and thickness are performed by analytical (iterative) algorithms. The calculation is based on modeling of the layers architecture (stacking, estimated

thickness), previously defined by the user.

The technique requires measurements at different electron energies E and analysis of measured K-ratios (ratio of the intensity $I_{sample}/I_{standard}$) in order to eliminate instrumental parameters. For the different acceleration voltages the electrons are penetrating more or less in the sample. Then, the K-values are plotted against E and fitted by use of calculated K-values with the thickness and composition as free parameters [18]. Figure II.16 shows an example of the K-ratio vs. E plot for a Bi-Sn-Ti-Se-O thin film sample on Si calculated with STrataGEM using intensities measured at 7, 11 and 15 keV [19].

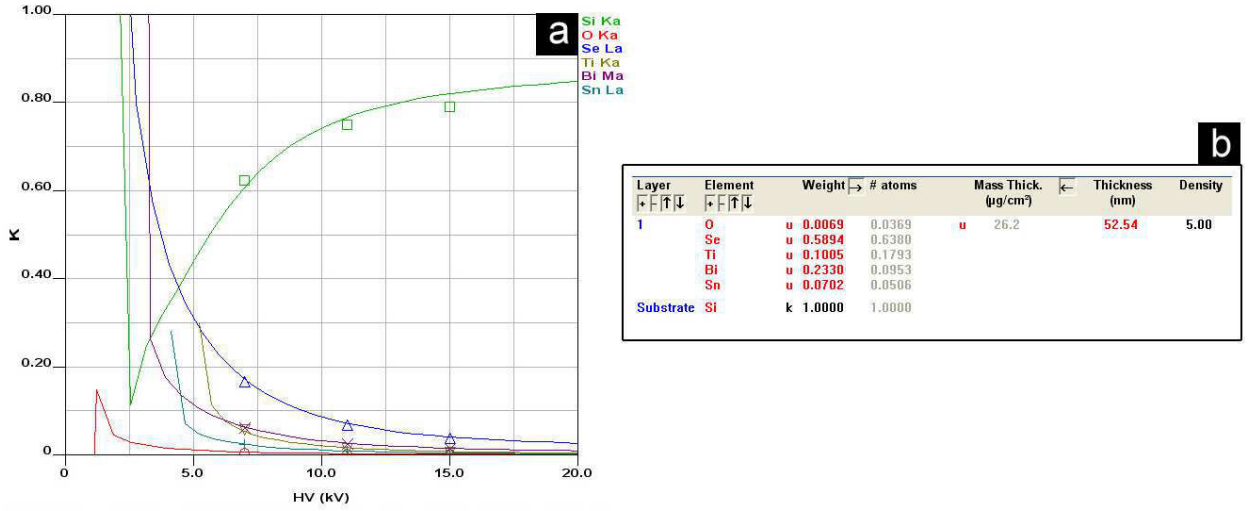

Figure II.16. a) Dependence on primary electron energy of measured K-values and b) sample description used for the iterative algorithms for the Bi-Sn-Ti-Se-O layer on Si substrate.

2.2.4 Physical characterization: SQUID magnetometry

The superconducting quantum interference device (SQUID) detects and measures the magnetic moment of the sample from which the magnetization and magnetic susceptibility can be determined. The operating principle is based on the tunnel effect of the superconducting current carriers (Josephson effect) subjected to a magnetic field through the insulating junctions. The amplitude of this current is a periodic function depending of the magnetic flux in the junction. The measurement is carried out by displacing the sample with a frequency between 0.5 and 1 Hz along the longitudinal axis around which the detection coils are located. As the sample moves through the coils, its magnetic moment generates an electric current variation (and thus an output voltage) proportional to the change in magnetic flux.

Magnetization measurements were performed at the Néel Institute (Magnetometry pole) on a SQUID MPMS magnetometer from Quantum Design. This device can measure very low magnetizations (10^{-8} emu), under external magnetic fields up to 5 Tesla and a temperature range between 2 K and 400 K. A typical prepared sample is shown in Figure II.17.

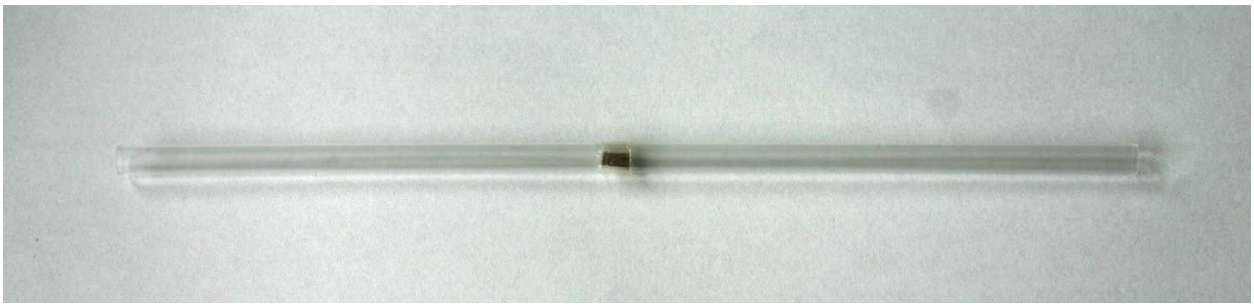

Figure II.17. Prepared sample for SQUID measurements.

The sample is initially placed in plastic wrap and then inserted through the two cuts carried out on both sides of a straw, parallel to its axis. The signal generated by the sample holder (straw and plastic film) and the substrate has been subtracted from the total measured signal (when possible). The remaining signal corresponds, thus, to the bare film. However, several precautions have to be taken when removing the substrate contribution. The data acquisition was performed as follows. The temperature dependence of the magnetization (M(T)) curves in zero-field-cooled (ZFC) and field-cooled (FC) mode was studied in the 4–300 K temperature range with an applied in-plane field of 500 Oe. The magnetization curves as a function of the magnetic field (M(H)) measurements were recorded between −50 and +50 kOe at 5 and 300 K.

References

1. Pierson, H.O., *Handbook of Chemical vapor deposition (CVD) Principles, Technology, and Applications.* William Andrew Publishing, LLC Norwich, New York, 1999.
2. Gelard, I., *Heterostructures d'oxydes multiferroiques de manganites de terre rares hexagonaux RMnO3 - Elaboration par MOCVD a injection et caracterisations structurales et physiques.* 2009.
3. J.P. Sénateur, et al., *Patent No 93/08838 PCT No FR94/00858 (Europe, U.S.A.).*
4. Sénateur, J.P., et al., *Pulsed injection MOCVD of functional electronic oxides.* Advanced Materials for Optics and Electronics, 2000. **10**(3-5): p. 155-161.
5. Iliescu, I., et al., *Growth and structural characterization of YMnO3 thin films grown by pulsed liquid injection MOCVD on Si and SrTiO3 substrates*, in *Phase Transitions*. 2013. p. 1094-1103.
6. Girardot, C., *Structures et Proprietes Physiques de Films Minces RENiO3 (RE=Sm, Nd) elabores par MOCVD*, in *LMGP*. 2009, Institut Polytechnique de Grenoble.
7. Eason, R., *Pulsed laser deposition of thin films: applications-led growth of functional material*. 2007: John Wiley & Sons.
8. Wang, K., *Laser Based Fabrication of Graphene (Chapter 4)*. Nanotechnology and Nanomaterials "Advances in Graphene Science", ed. M. Aliofkhazraei. 2013: InTech.
9. Vitalij K. Pecharsky and P.Y. Zavalij, *Fundamentals Of Powder Diffraction And Structural Characterization Of Materials*. Technology & Engineering. 2004. 713.
10. Broll, N., *Caractérisation de solides cristallisés par diffraction X* 1996.
11. Lee, H.N., Y.T. Kim, and S.H. Choh, *Comparison of memory effect between YMnO3 and SrBi2Ta2O9 ferroelectric thin films deposited on Si substrates.* Applied Physics Letters, 2000. **76**(8): p. 1066-1068.
12. Ulyanenkov, A. *LEPTOS: a universal software for x-ray reflectivity and diffraction*. 2004.
13. Lin, W. *Introduction to X-Ray Reflectometry*. 2010; Available from: http://www.phys.ncyu.edu.tw/~ccliu/index.files/xrd.files/xrr.
14. K. Inaba, et al., *High Resolution X-Ray Diffraction Analyses of (La,Sr)MnO3/ZnO/Sapphire(0001) Double Heteroepitaxial Films.* Advances in Materials Physics and Chemistry, 2013. **3** (1A): p. 72-89.
15. *Thin Film Scattering: Epitaxial Layers 6th Annual SSRL Workshop on Synchrotron X-ray Scattering Techniques in Materials and Environmental Sciences: Theory and Application*. 2012.
16. Moxfyre, b.o.w.o.U.P. *Raman energy levels* 2009; Available from: http://upload.wikimedia.org/wikipedia/commons/thumb/4/41/Raman_energy_levels.svg/784px-Raman_energy_levels.svg.png.
17. Nacucchi, M., et al., *Quantitative EDS analysis in transmission electron microscopy using unconventional reference materials.* Materials Science and Engineering, 2010. **7**(1): p. 012020.
18. Procop, M., et al., *Electron probe microanalysis (EPMA) measurement of thin-film thickness in the nanometre range.* Anal Bioanal Chem, 2002. **374**: p. 631–634.
19. Software, P. *Thin Film Acquisition and Analysis in Probe for EPMA*. 2013; Available from: http://probesoftware.com/smf/index.php?topic=111.0.

Chapter 3

$YMnO_3$ film deposition and process optimization

Summary

3.1 The choice of the substrate ……..…....66
3.2 MOCVD deposition ……..…….…….68
3.2.1 Choice of deposition temperature ……..…..70
3.2.2 Choice of Y and Mn atomic concentrations in the injected solution …….…..75
3.3 PLD deposition …….……...…78
3.4 Determination of the film thickness and chemical composition ……79
3.5 Summary and conclusions ……..83
References ……84

The growth of $YMnO_3$ films by MOCVD and PLD on Si, STO, LAO and LSAT substrates is presented in this chapter. Among the large number of experimental parameters specific to the deposition techniques, we have chosen to study in more detail the influence of the deposition temperature, the composition of the solution, the film thickness and oxygen pressure (in the case of PLD). In the purpose of optimizing the deposition conditions, the accurate determination of the parameters was necessary. The methods used are compared and discussed. The complete characterization of the $YMnO_3$ films will be studied in the following chapters.

High-quality $YMnO_3$ films are essential for the integration into new devices, but also for the fundamental study of the structural and physical properties. As seen in Chapter 1, the choice of appropriate substrates is important in the selective growth of hexagonal or orthorhombic $YMnO_3$ phases and in the film epitaxy. In the case of $YMnO_3$ films deposited by MOCVD, several additional factors are also important: the choice of deposition temperature, the composition of the injected solution, the system pressure and atmosphere, the precursors, the evaporation temperature etc. Some of them are discussed in detail in the following.

3.1 The choice of the substrate

In this thesis, the influence of the substrate on the structural and physical properties was among the studied items. Therefore, several substrates were chosen in the deposition of YMO films.

On the one hand, non-constrained films were deposited on Si. From the applications point of view, the YMO films on Si substrates have gained a particular interest since they have been reported as new candidates for nonvolatile memory devices [1]. Moreover, the Si substrates have the advantage of being low cost (compared to the perovskite-type substrates required for epitaxial growth) making them very convenient for optimizing the deposition process. For this reason they are used in a first step of elaboration. Si (100) wafers from Crystec (a= 5.43 Å) were cleaved into sections of approximately 1 cm x 1 cm and used as substrates.

On the other hand, epitaxial films with different strain values were grown on (100)-oriented $SrTiO_3$ (STO), $LaAlO_3$ (LAO) and $(LaAlO_3)_{0.3}(Sr_2AlTaO_6)_{0.7}$ (LSAT) substrates from Crystec.

These substrates, with cubic perovskite structure (except LAO which is approximated with a pseudocubic one), are widely used for growing rare earth manganese oxides and stabilizing the orthorhombic phase, as previously seen in the state-of-the-art in Chapter 1. A lattice mismatch less than 10% allows epitaxial growth with one or more domains.

The lattice constant of the substrates are 3.792 Å for LAO [2] (pseudocubic), 3.872 Å for LSAT [3] and 3.905 Å for STO [2]. The bulk lattice parameters of the o-YMO phase are: a=5.8361 Å, b=7.3571 Å and c=5.2580 Å [4]. It can be observed that even though the cell parameters of the substrates are very different from those of the o-YMO phase (direct comparison), it appears that the value of the substrate unit-cell diagonal is close to either a or c o-YMO lattice parameter and also $b/2$ o-YMO is close to the a lattice parameter of the substrates. According to these

observations and to our experimental results, several orientation relationships are possible. Three of them are illustrated in Figure III.1:

- orientation 1: $[010]_{YMO}//[100]_{STO}$, $[101]_{YMO}//[010]_{STO}$
- orientation 2: $[101]_{YMO}//[100]_{STO}$, $[10\text{-}1]_{YMO}//[010]_{STO}$
- orientation 3: $[101]_{YMO}//[100]_{STO}$, $[010]_{YMO}//[010]_{STO}$

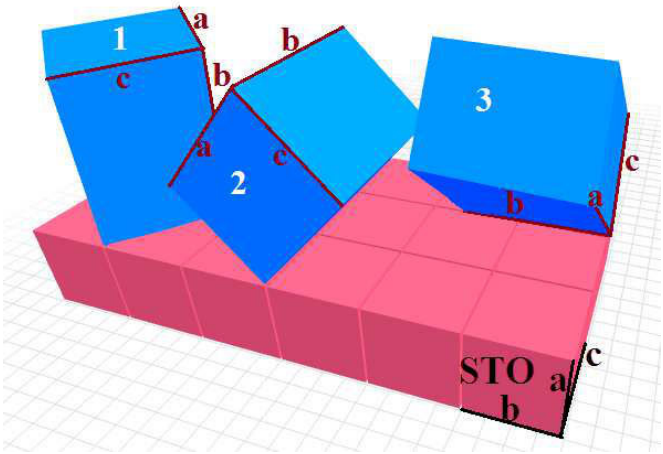

Figure III.1 Schematic 3D representation of the orientation relationships of YMO on STO.

Orientation 2 and 3 correspond to 90° in-plane rotated domains and have equivalent mismatches. Briefly, the orientations in Figure III.1 can be simplified as having $b_{o\text{-}YMO}$ in-plane (2 and 3) or out-of-plane (1). The corresponding mismatch values along a given direction is calculated as $f=100\cdot(d_{substrate}-d_{o\text{-}YMO})/d_{o\text{-}YMO}$ and are shown in Table II.1. For example, in the case of o-YMO films grown on LAO substrate the mismatch along the [010] of the film is $f_{010}=100\cdot(d_{001(LAO)}-d_{020(YMO)})/d_{020(YMO)}=100\cdot(3.792-3.6785)/3.6785=3.08\%$. It seems that the growth along *b*-axis (*b* out-of-plane) is well accommodated for the STO substrate, while for the LAO substrate, the *b*-axis within the in-plane direction is more favorable.

Substrate	**Lattice parameter [Å]**	**Substrate diagonal (011) [Å]**	**Mismatch (%)**			
			***b* in-plane**		***b* out-of-plane**	
			f_{010}	f_{101}	f_{100}	f_{001}
LAO	3.792* [2]	5.362	3.08	-2.93	-8.12	+1.98
LSAT	3.872 [3]	5.475	5.26	-0.88	-6.19	+4.13
STO	3.905 [2]	5.522	6.15	-0.03	-5.38	+5.02

*Table III.1 Lattice mismatch between the STO, LAO (*pseudocubic) and LSAT substrates and orthorhombic YMO phase (see definitions in the text).*

Several attempts have been made on cubic MgO and yttria-stabilized zirconia Y_2O_3 (15%): ZrO_2 (111) (YSZ(111)) substrates from Crystec. These substrates are suitable for epitaxial growth of hexagonal YMO phase (a=6.1453 Å, c= 11.3714 Å [5]). Indeed, YSZ(111) (a=5.12 Å), has a good lattice agreement with YMO (f_{001}=2.4%) with the following epitaxial relations [6]: $(0001)_{YMO}//(111)_{YSZ}$ and $(1\text{-}100)_{YMO}//(1\text{-}10)_{YSZ}$. In the same manner, YMO(0001) was grown on MgO(100) (a=4.21 Å) with a strain factor of -0.29% [7]. The results are shown in Appendix A.

The experimental protocol followed for all deposition processes involves the cleaning of substrates with acetone and ethanol in an ultrasonic bath for 10 minutes each, and subsequently their drying using a nitrogen flow. Note that after this step, a native oxide layer of SiO_x exists on the Si substrate. Because of the large lattice mismatch, which does not allow an epitaxial growth of the YMO phase on Si, the removal of the native SiO_x layer was not considered necessary. The substrates thus prepared were glued with silver paste in order to ensure the thermal conductivity with the sample holder. Because of the high temperatures used in the deposition chamber, silver contamination, particularly on Si substrates, was sometimes detected by XRD, EPMA and EDX analysis. All of these samples were generally disregarded for further characterizations.

3.2 MOCVD deposition

In this section, the influence of the deposition conditions on the quality of the YMO films grown by PI-MOCVD has been studied, with regard to the parameters optimization. A particular interest is given to the YMO films on Si substrates.

The previous theses conducted in our laboratory on the rare earth manganites [6] have allowed us to conserve or adapt certain parameters. From the work of I. Gelard [6] we have preserved the type of precursors and solvent as well as their total concentration, the total pressure in the reactor and the injection parameters (injector opening time and injection frequency). From the work of C. Girardot [8] on the horizontal reactor, we have retained the evaporation temperature and the in-situ annealing parameters (time and atmosphere). Other parameters have been changed between the horizontal and vertical reactor and will be discussed later.

The metal-organic precursors were $Y(tmhd)_3$ and $Mn(tmhd)_3$, where tmhd=2,2,6,6-tetramethyl-3,5-heptane-dionate, with formula $YC_{33}H_{57}O_6$ and $MnC_{33}H_{57}O_6$, respectively. The $Y(tmhd)_3$ and $Mn(tmhd)_3$ precursors were solid white and black powders respectively at room temperature and

were dissolved in monoglyme solvent (1,2-dimethoxyethane with formula $C_4H_{10}O_2$), in concentration of 0.02 mol/L. Both precursors were mixed in a unique solution and sealed into the injector reservoir. The solid metal-organic precursors of tmhd-type are often preferred due to their stability at room temperature and non-toxicity compared to other liquid precursors or with solid acac-type (acetylacetonate hydrate) precursors. Moreover, they are chemically compatible between each other and with the solvent. The typical deposition conditions used in this work for the elaboration of films are summarized in Table III.2. Each film growth in the horizontal PI-MOCVD reactor was followed by an in-situ annealing at the same temperature as the deposition, during 30 minutes in air with a supplementary O_2 flow to fully oxygenate the film. In the case of the vertical PI-MOCVD device, no annealing was performed.

Parameter	Horizontal PI-MOCVD	Vertical PI-MOCVD
Substrates (100-oriented)	Si, STO, LAO, MgO, YSZ*	Si, STO, LAO, LSAT, MgO
Substrate temperature (°C)	600 − 850	600 − 800
Evaporation temperature (°C)	230	250
Deposition time (min)	10 − 40	10 − 80
Metalorganic precursors	$Y(tmhd)_3$ and $Mn(tmhd)_3$	$Y(tmhd)_3$ and $Mn(tmhd)_3$
Y/Mn in the injected solution	0.5 − 2	0.25 − 1.33
Solution concentration (mol/l)	0.02	0.02
Transport gas	$Ar + O_2$	$Ar + O_2$
Ar flow rate (cm^3/min)	300	300 − 1700
O_2 flow rate (cm^3/min)	300	220 − 400
Deposition total pressure (Torr)	5	5
Number of injections	450 − 2030	500 − 4000
Injection frequency (Hz)	1	1
Injection time (ms)	2	2
Annealing temperature (°C)	600 − 850	−
Annealing time (min)	30	−

Table III.2. Typical deposition conditions used for YMO thin films grown by PI-MOCVD ((111)-oriented).*

It was found that the substrate temperature and the Y/Mn atomic ratio in the injected solution play a key role in the film crystallinity. Different number of injections and deposition times were used in order to achieve various film thicknesses. Based on the several attempts to vary the argon and oxygen flow rate as well as their proportion, we have concluded that at high flow rates the films are highly inhomogeneous. An example of such film is shown in Figure III.2.

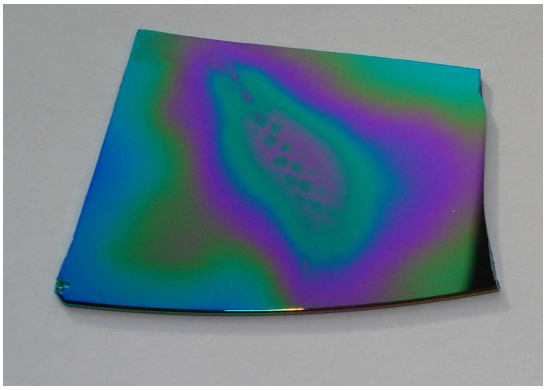

Figure III.2. An inhomogeneous $YMnO_3$/Si film deposited at high flow rate.

Therefore, the main parameters that were varied during our depositions were the substrate temperature and the Y/Mn atomic ratio in the injected solution.

3.2.1 Choice of deposition temperature

3.2.1.1 Horizontal PI-MOCVD setup

Series of films were deposited on Si(100) substrates at different deposition temperatures and different Y/Mn compositions in the injected solution. The dependence of the crystalline structure (as found by XRD) with these two parameters is displayed in Figure III.3.

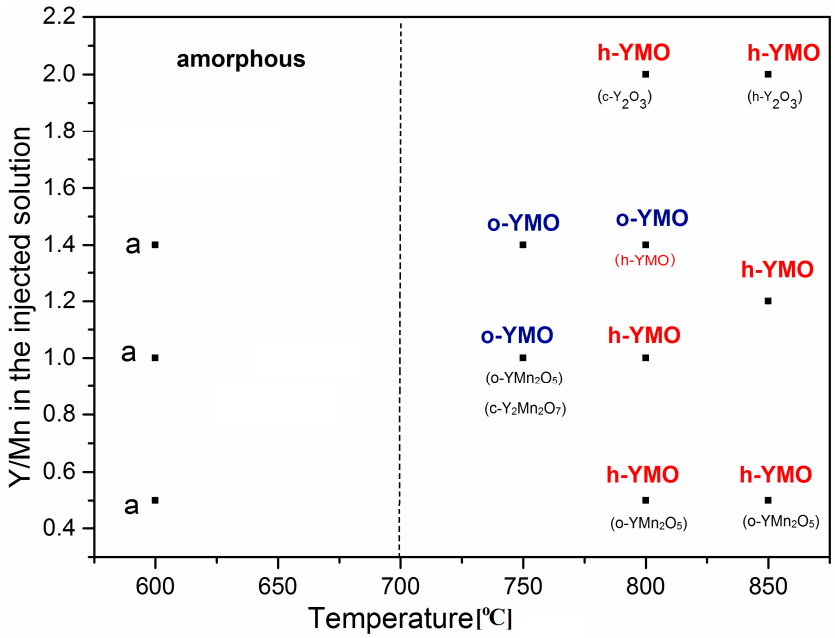

Figure III.3. Crystalline structure dependence on the temperature and Y/Mn atomic ratio in the injected solution for the horizontal PI-MOCVD setup. See text for labels.

The results show that the films deposited below 700 °C are amorphous (label **a** in Figure III.3), those deposited at 750 °C are o-YMO, and finally, above 800 °C the h-YMO phase is present in most of the films. Secondary phases were also observed mainly when the atomic ratio Y/Mn in the injected solution is either Y/Mn < 1 or Y/Mn > 1.4. In the region where Y/Mn > 1.4, Y_2O_3 is formed to compensate the Y excess, while in the region where Y/Mn < 1, Mn-rich phases (e.g. YMn_2O_5) are formed.

Figure III.4a shows the XRD patterns of the YMO films deposited on Si substrate with Y/Mn=1 at deposition temperatures between 600 and 850°C. The effect of deposition temperature on the phases present in the films can be clearly seen: at 600°C the film is amorphous (very narrow peak near 2θ=33° in the XRD pattern is due to Si), at 700°C the film is o-YMO while at 800 and 850°C the films are mainly h-YMO (a secondary YMn_2O_5 phase is present in the film deposited at 850°C)

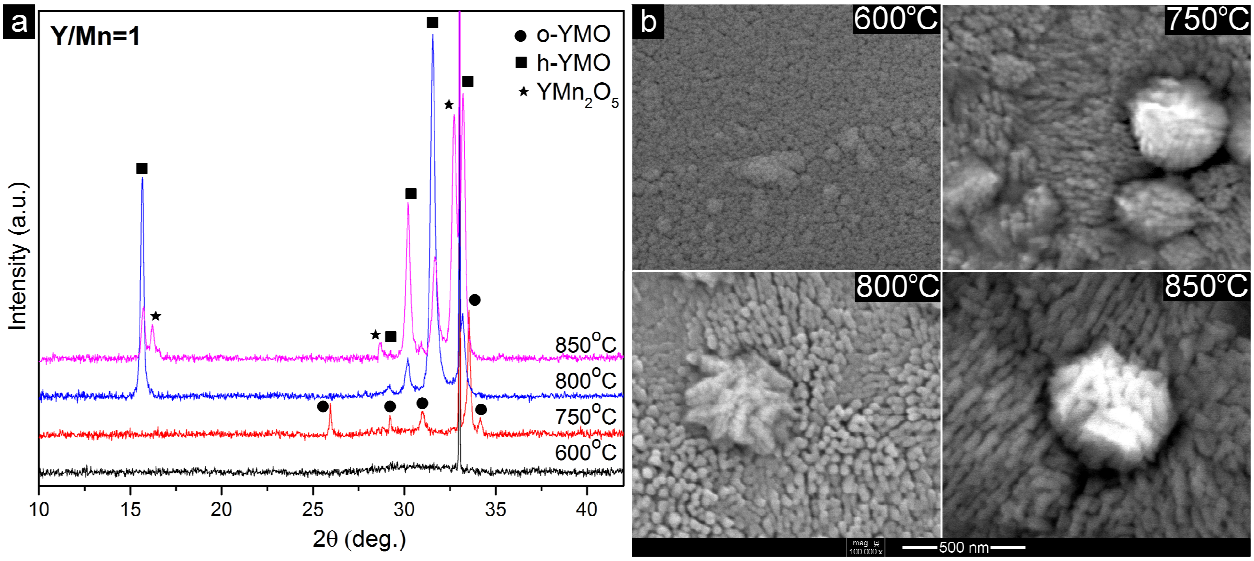

Figure III.4. YMO films deposited with Y/Mn=1 in the injected solution and temperatures between 600-850°C: a) XRD patterns and b) SEM top-view images.

The morphology of the YMO films for a given composition is dependent on the deposition temperature. In Figure III.4b the corresponding top view SEM images in SE mode show distinct morphologies. At 600°C, for the amorphous Y-Mn-O phase, the SEM image does not display any sign of crystallization. At 750°C, the o-YMO film displays a dense structure with two types of morphology: one corresponds to dome-capped grains and the other to dendritic aggregates of grains.

At 800 and 850°C, the two YMO films, mainly of h-YMO phase present similar morphologies with star-shaped grains on a regular matrix of dome-capped grains. Also, for the films deposited between 750 and 850°C the grains tend to be oriented along certain preferential directions, indicating a texture. The morphological features are compatible with an island growth type which generates columns within the film (for further details see Chapter 4).

3.2.1.2 Vertical PI-MOCVD setup

In the case of the vertical PI-MOCVD setup, the crystalline structure depending on the temperature and atomic ratio Y/Mn in the injected solution for Si substrate is displayed in Figure III.5. It can be noticed that below 750°C the films are amorphous, while at 800°C the h-YMO phase dominates. The same tendency of forming secondary phases was seen when working in the Y-rich or Mn-rich regions. It must be pointed out that the depositions have been performed at different pressure and growth rates by varying the gas flow, and thus, an accurate comparison with the results from Figure III.3 is impossible. The unexpected result that at 750°C no crystallized phase of either orthorhombic or hexagonal YMO structure is formed is certainly due the nonstoichiometry of the Y/Mn ratio in the film, which is different from that of the Y/Mn in the injected solution and which can block the crystallization (see section 3.3.1.2).

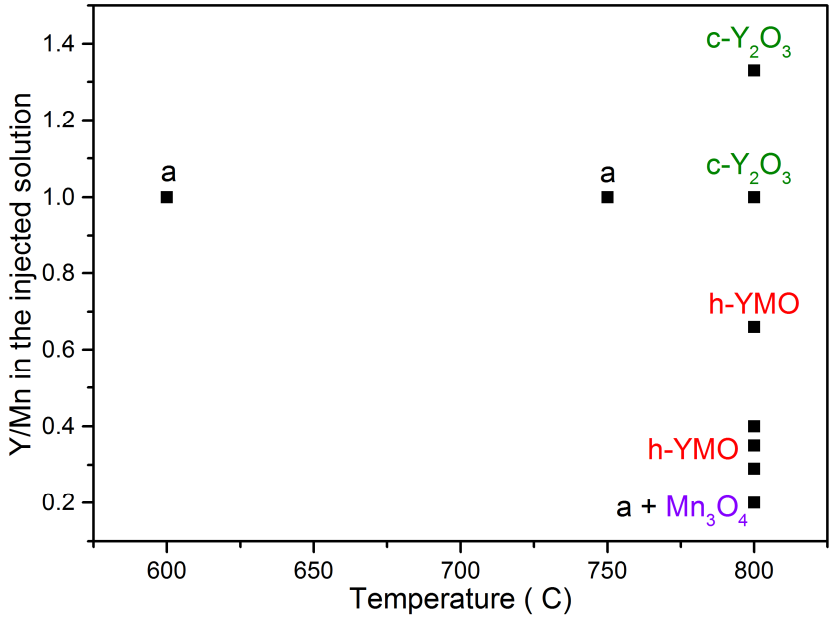

Figure III.5. Phase formation depending on the Si substrate temperature and atomic ratio Y/Mn in the injected solution in the vertical PI-MOCVD setup.

The films morphology depends mainly on the temperature and, to a lesser extent, on the composition. Figure III.6 shows the typical morphological features of the YMO films deposited on Si substrate in the horizontal (left side of each figure) and vertical (right side) PI-MOCVD device, depending on the crystalline structure. The results show that the amorphous YMO films, independently of the MOCVD device used, have very similar morphologies, with small grains and smooth surfaces as it can be seen in Figure III.6a. The crystalline YMO phase of hexagonal symmetry (Figure III.6b) is characterized by two types of morphological features: one corresponding to columnar grains and the other to dendritic aggregates of grains. This usually happens in thick deposits where a uniform structure is more difficult to obtain [9]. In the Y-rich region (Figure III.6c), the Y_2O_3 phase is formed in the bulk of the film (left side of Figure III.6c) or as white precipitates (right side of Figure III.6c). A distinctive surface morphology is observed for the Mn-rich films in Figure III.6d. Different shapes and types of grains are shown, which arise from YMn_2O_5 or Mn_3O_4 phase. Other examples are shown in Appendix B.

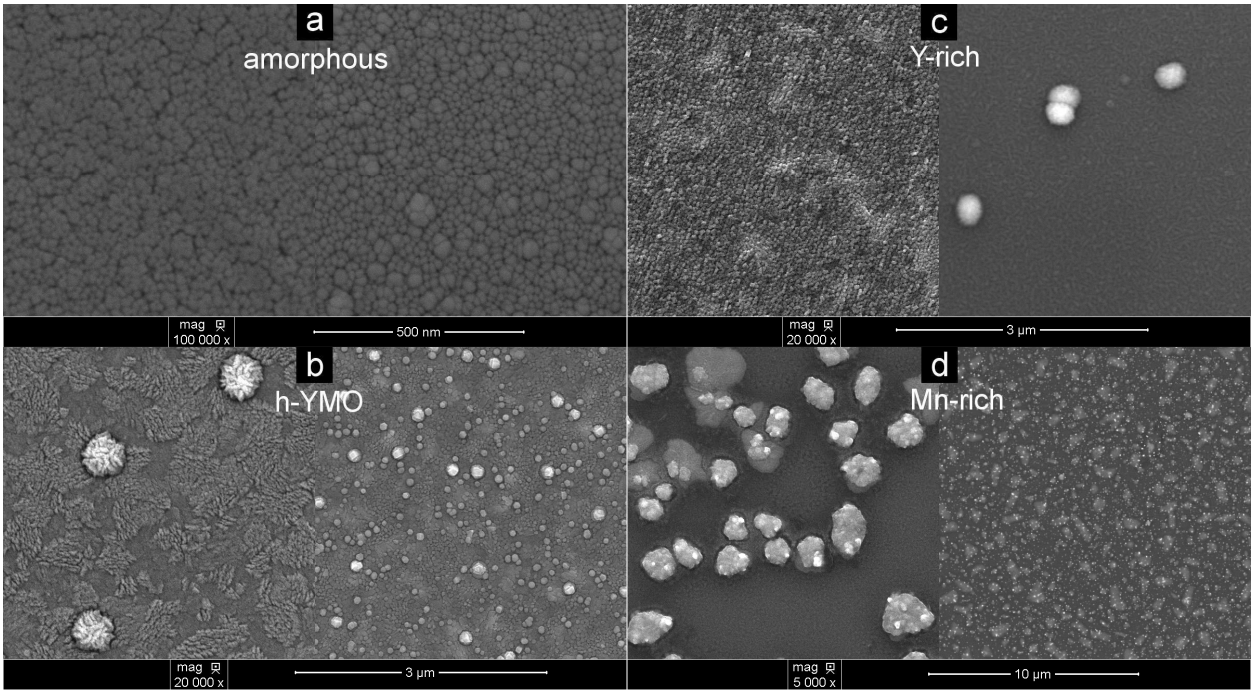

Figure III.6. *Morphology of the YMO films deposited on Si substrate: a) amorphous; b) h-YMO phase; c) Y-rich region; d) Mn-rich region. The films on the left side of each figure were elaborated in the horizontal PI-MOCVD device while those on the right side in the vertical PI-MOCVD device.*

Surface morphologies of the YMO films deposited on STO and LAO substrates are shown in Figure III.7. The images display homogenous and smooth surfaces, independent of the substrate or MOCVD setup used for the depositions. Dome-capped columnar grains of small size are typical for all YMO films (a-d). Compared to YMO/Si films, no precipitates or different types of microstructure are observed. On the areas probed by AFM, the samples have a relatively smooth surface with an average roughness of 4 Å, which is less than a monolayer as illustrated in Figure III.7e. Our results suggest that this type of morphology is associated to the epitaxial film growth.

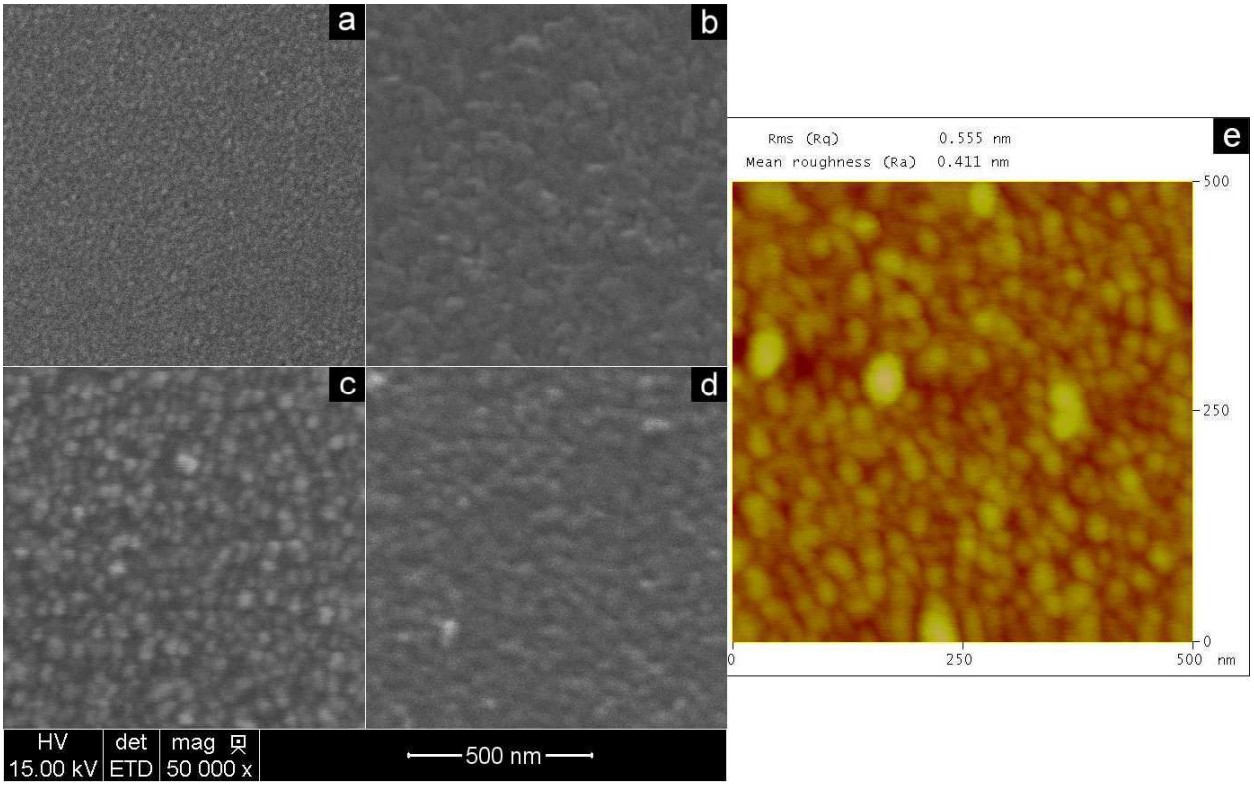

Figure III.7. Morphology of the epitaxial YMO films deposited on STO (a and b) and LAO (c and d) substrates in the horizontal (a and c) and vertical (b and d) MOCVD device; e) an example of sample roughness as measured by AFM.

These results show that it is thus possible to control the nature of a MOCVD film structure by carefully manipulating the deposition parameters such as the substrate temperature and Y/Mn ratio.

3.2.2 Choice of Y and Mn atomic concentrations in the injected solution

One of the difficulties of the MOCVD growth of complex oxide is the control of the film stoichiometry. In principle, the composition of the films is determined by the composition of the precursor solution. However, in some cases, the composition of the film can be very different from that of the solution. Since the precursors do not have the same decomposition rate at a given temperature (see Table III.3) and, moreover, the different elements do not have the same incorporation efficiency in the crystal lattice, it is necessary to find, for each compound, the adequate composition of the liquid solution. The $Y(tmhd)_3$ and $Mn(tmhd)_3$ precursors are decomposing between 250 °C and 290 °C [10] with the total degradation of organic fragment a few degrees below 600 °C [11] [12].

	Melting point (°C) [10]	Boiling point (°C) [10]
$Y(tmhd)_3$	173 - 175	290
$Mn(tmhd)_3$	165	255
monoglyme	-69	85

Table III.3. Physical properties of the precursors and solvent used for MOCVD deposition.

Throughout our experiments, various syntheses have been performed varying the stoichiometry in the precursor solution. Y/Mn ratios between 0.5 and 2 were used for the horizontal PI-MOCVD setup and between 0.2 and 1 for the vertical PI-MOCVD setup. Structural characterizations were carried out in order to investigate the effect of the stoichiometry on the phases and crystalline quality of the films. The composition of films deposited on Si substrates was analyzed by EDX and EPMA techniques. It has been observed that on thick samples (submicronic) the chemical quantification by EDX overestimates the Y/Mn ratio by ~ 10-20% compared to the EPMA technique. This is mainly due to the fact that the EDX technique is not adapted to quantify thin films because absorption and thickness corrections are not considered.The results are presented in the next subsections depending on the used reactor type.

3.2.2.1 Horizontal PI-MOCVD setup

Figure III.8 compares the Y/Mn ratios in the injected solution of precursors against those measured by EPMA in the films, at a deposition temperature of 800°C. A linear behavior is

observed, which demonstrates the capability to control the film composition by optimizing the cationic ratio of Y and Mn in the injected solution.

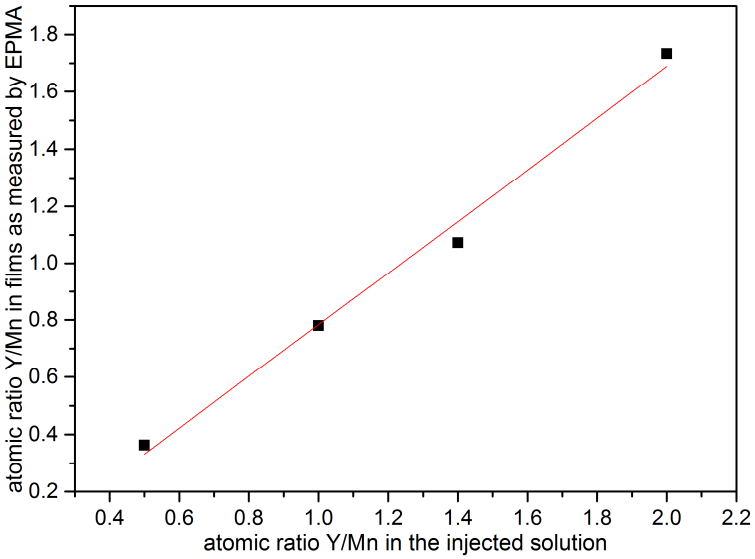

Figure III.8. Relation between atomic ratios Y/Mn in the injected solution (x-axis) and in the films (y-axis) grown at 800°C as measured by EPMA.

The optimal composition of the injected solution needed to obtain a stoichiometric ratio Y/Mn=1 in the film is close to 1.2 when working at 800°C. This difference leads to the conclusion that the deposition rate of the $Y(tmhd)_3$ is lower than that of $Mn(tmhd)_3$ under the experimental conditions used for the growth. When considering different deposition temperatures, an important data dispersion was observed, suggesting that the optimal ratio is temperature dependent. A similar behavior was observed when growing $PbTiO_3$ on $LaAlO_3$ substrates [13].

3.2.2.2 Vertical PI-MOCVD setup

For the depositions in the vertical PI-MOCVD reactor, we have tried to keep the growth conditions previously used in the horizontal reactor, including the atomic ratios Y/Mn in the injected solution. Surprisingly, the composition of the films deposited with a ratio Y/Mn=1 in the injected solution was very different from the stoichiometry (see Figure III.9). This parameter required, therefore, a new search and revaluation. Figures III.9a and b summarize the EDX results on YMO films deposited on Si (a) and on STO, LAO and LSAT (b) substrates, respectively.

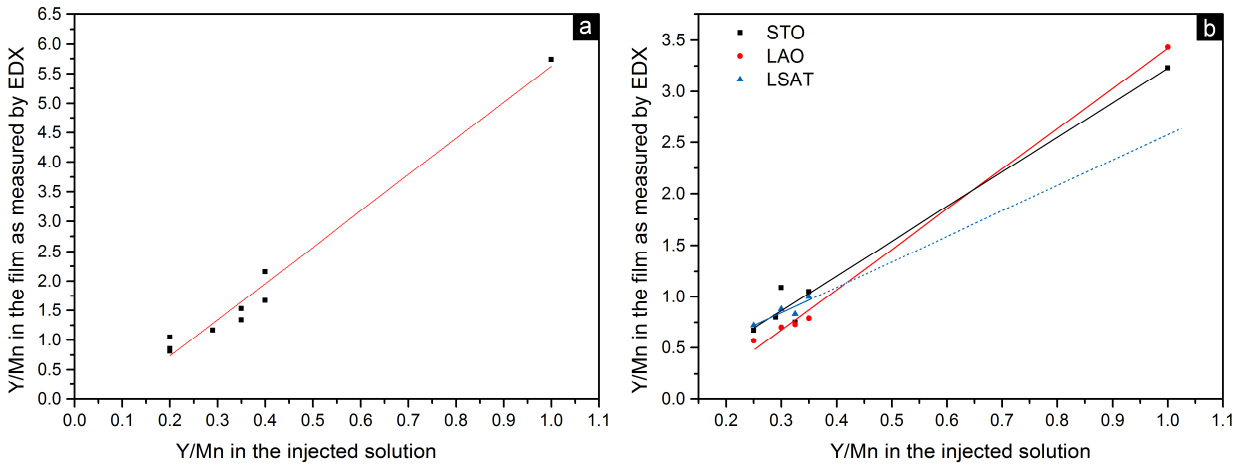

Figure III.9. Atomic ratios Y/Mn in the film as measured by EDX vs. Y/Mn in the injected solution for the depositions at 800 °C on a) Si substrate and b) STO, LAO or LSAT substrates.

An almost linear behavior, observed for all substrates, shows that the film composition can be tuned by optimizing the composition of the injected solution. According to EDX results the optimal Y/Mn value necessary to obtain a stoichiometric film is close to 0.3, presenting, however, small deviations when working with the different substrates. This value suggests that the deposition rate of the $Y(tmhd)_3$ precursor is much higher than that of the $Mn(tmhd)_3$, contrary to previous results from Figure III.8. This indicates a strong influence of the reactor geometry (horizontal vs. vertical) and, in particular, of the different transport pathways of the precursors (mechanically-carried vs. gas-carried).

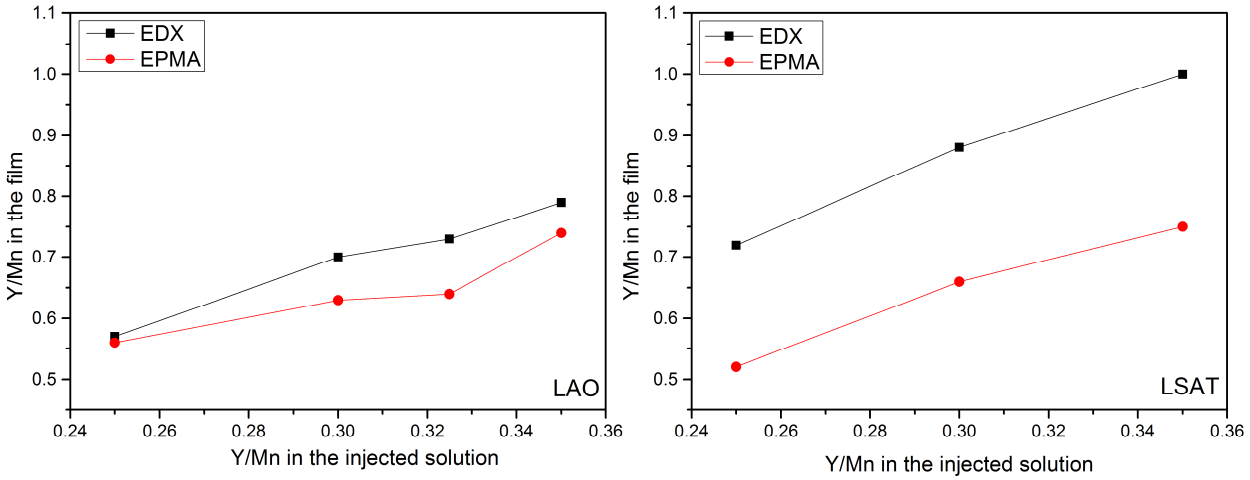

Figure III.10. Atomic ratios Y/Mn in the film as measured by EDX and EPMA vs. Y/Mn in the injected solution for samples deposited at 800°C on a) LAO and b) LSAT substrates.

When comparing the EDX and the EPMA results from selected samples of YMO on LAO and LSAT films (see Figure III.10) it appears that the values obtained by EDX are systematically overestimated. The Y/Mn ratio in the injected solution, required to obtain a ratio Y/Mn=1 in the film, is closer to 0.5 rather than the value of 0.3 obtained previously. Despite this, orthorhombic $YMnO_3$ films were obtained in the entire range of compositions (see Chapter 6).

3.3 PLD deposition

The deposition temperature and atmosphere are among the most important parameters in the oxide growth by PLD. To study the influence of a single parameter, we kept all values constant between depositions, including the deposition temperature and we drastically varied the O_2 pressure with a range of three orders of magnitude. Table III.4 summarizes the data regarding the deposition conditions of the films prepared by PLD.

Parameter	PLD deposition conditions
Substrates (100-oriented)	Si, STO, LAO, LSAT
Substrate temperature (°C)	800
Laser	KrF 248 nm
Fluence (J/cm^2)	2.5
$d_{target\text{-}substrate}$ (cm)	5
O_2 pressure (Torr)	0.105 −225
Preliminary pressure (Torr)	$7.5\ 10^{-3}$ −$7.5\ 10^{-2}$
Number of laser pulses	10000
Pulse rate (Hz)	3
Pulse duration (ns)	25
Annealing temperature (°C)	800
Annealing time (min)	30

Table. III. 4. PLD deposition conditions

The dependence of the crystalline structure (as found by XRD) on the O_2 pressure and Y/Mn ratio in the film (measured by EDX) is shown in Figure III.11. This representation is equivalent to those in Figure III.3 and Figure III.5 for MOCVD (crystalline structure vs. temperature and Y/Mn in the injected solution). In the case of PLD the composition plays a minimal role (the target composition does not vary) despite the EDX results which indicate that the composition in the film depends on the P_{O2} (see dotted line).

It is obvious that on perovskite-type substrate, the stabilization of the o-YMO phase is achieved independently of the O_2 pressure or the film composition. On the contrary, the crystallinity of the YMO films on Si substrate is influenced by the oxygen pressure. At low O_2 pressure the h-YMO

is formed, in the intermediate O_2 pressure range (0.01 – 0.1 mbar) an amorphous phase dominates, while at high O_2 pressure the o-YMO phase is stabilized.

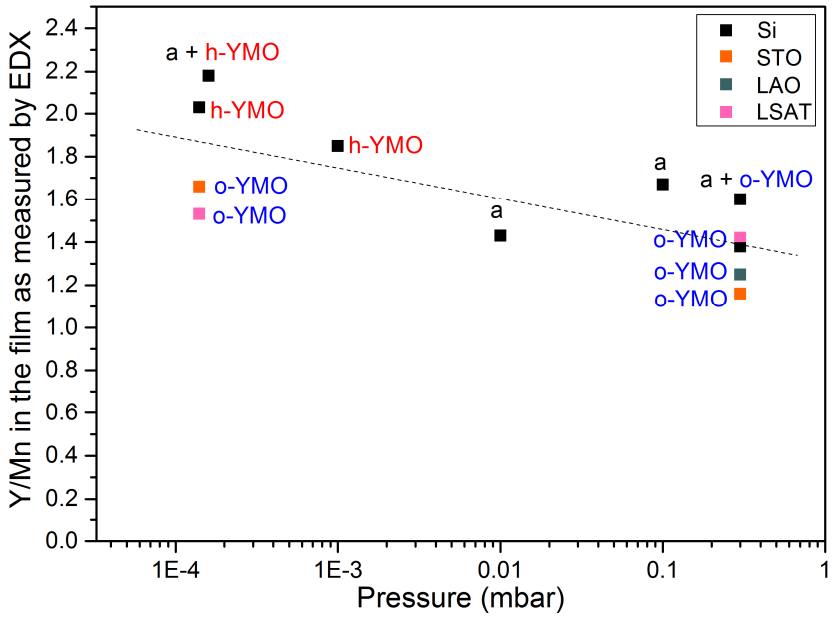

Figure III.11. Phase formation dependence on the O_2 pressure and atomic ratio Y/Mn in the films deposited by PLD on different substrates at 800°C.

These results, comparable to those obtained by MOCVD, show that a selective growth of amorphous, hexagonal or orthorhombic $YMnO_3$ phase can be achieved by the suitable choice of O_2 pressure during the deposition.

3.4 Determination of the film thickness and chemical composition

In order to better optimize the deposition process, an accurate determination of the film composition and thickness is necessary. As discussed in Chapter II, the thickness of the film can simply be controlled by the number of injections in the case of MOCVD or by the number of laser pulses in the case of PLD growth. The determination of the thickness value has been made by several techniques and compared. Cross-section SEM and TEM observations were used to directly measure the films thickness, while EPMA and XRR data were employed to estimate it by simulation algorithms. The XRR technique was employed when the size and the roughness of the samples were in measurable ranges (small samples or rough and thick films over 50 nm cannot be easily measured).

Thicknesses with accuracy better than 1-5 % can be routinely obtained. The values obtained from EPMA are comparable to those found by direct measurement (TEM, SEM). An example of measurements obtained by SEM and TEM and calculated by EPMA on a YMO/Si film is given in Figure III.12. Direct measurements by both SEM and TEM techniques show that the film is 369 nm thick. The EPMA estimation gives 355 nm, which is in good agreement with the direct measurements.

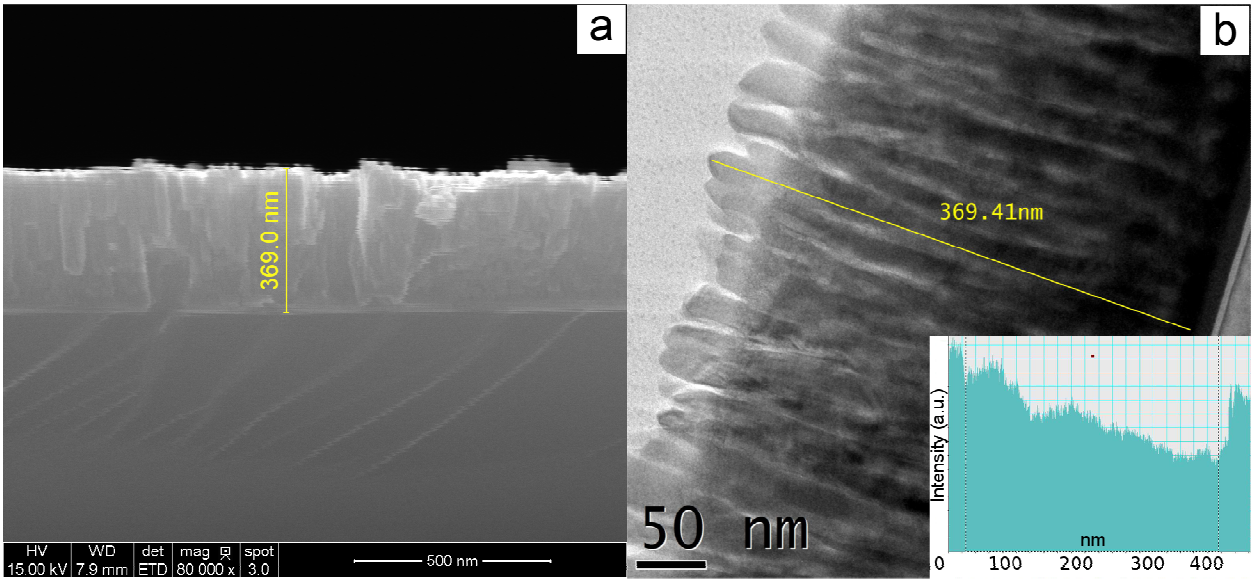

Figure III.12. Cross section of YMO/Si films measured by SEM (a) and TEM (b). Inset of b): Intensity histogram depending of the film thickness (yellow line) obtained with Digital Micrograph.

Another example of the thickness determination by EPMA is shown in Figure III.13.

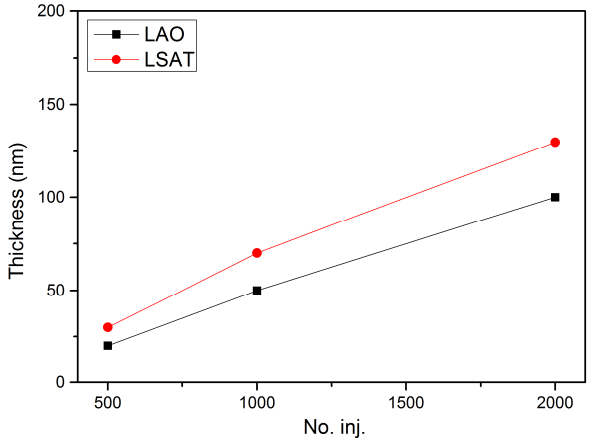

Figure III.13. The film thickness (determined by EPMA) vs. the number of injections for the YMO films deposited on LAO and LSAT substrates.

The YMO films deposited on LAO and LSAT substrates with the same Y/Mn ratio in the injected solution (Y/Mn=0.325) and with a different number of injections (500, 1000 and 2000) have similar thicknesses. Moreover, the thickness evolution with the number of injection presents an almost linear behavior, which means that the film thickness can be controlled by varying the deposition parameters. Regarding the thickness distribution across the films, this appears to be very homogenous relative to the sample dimensions. An example of such distribution is shown in Figure III.15a. The SEM determination of thickness in cross section gives an average thickness of 82 ± 7% nm.

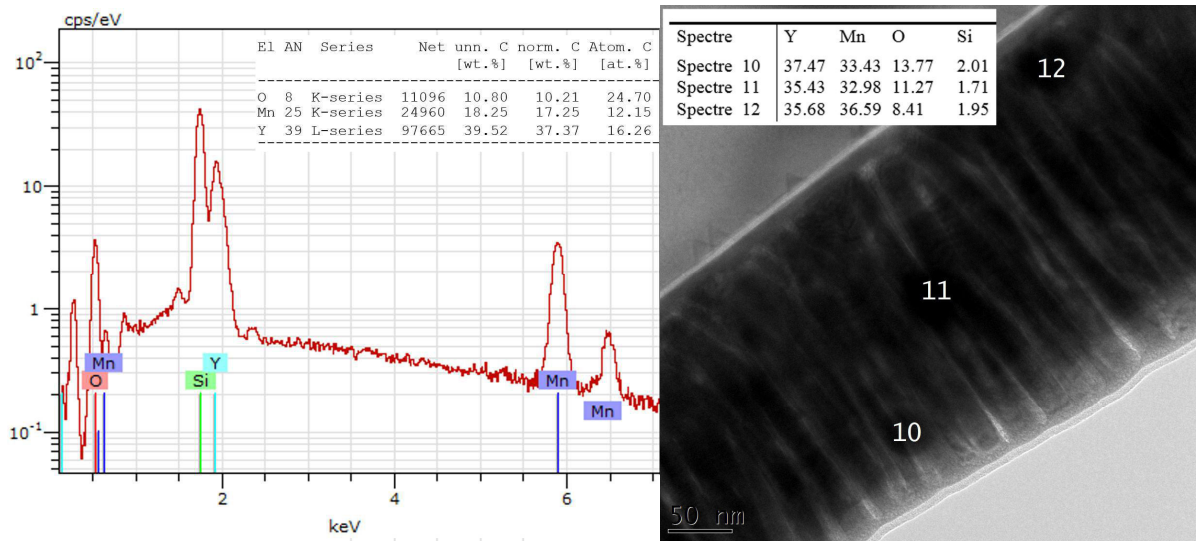

Figure III.14. Average EDX-SEM (left panel) and local EDX-TEM (right panel) results of chemical composition in a YMO/Si film. EDX-TEM composition of the three probed regions labeled 10, 11 and 12 are given in the inset.

The chemical composition of the films was measured by EDX-SEM, EPMA or/and EDX-TEM (see Figure III.14 for EDX-SEM and EDX-TEM examples). When comparing these techniques, it was found that whereas EPMA give accurate results, EDX-SEM give more approximate values, especially when the film thickness is small. One of the major drawback for the precise chemical quantifications in our YMO/Si films was due to the presence of an amorphous layer or secondary phases (see chapter 4, section 4.1). The EDX-TEM method provides in general reliable results, however in some cases the quantifications were not very accurate.

Figure III.14 shows the EDX-SEM and EDX-TEM quantification for a YMO film on Si substrate with an initial ratio Y/Mn=1.4 in the precursor solution. The Y/Mn ratio in the film was

1.33 and 1.05±0.07 as measured by EDX-SEM and EDX-TEM, respectively. The EPMA estimation was Y/Mn=1.09, which is close to the EDX-TEM. EDX-TEM also shows that the chemical composition distribution is quite homogenous across the films (see Figure III.14b and its inset indicating three probed regions marked with 10, 11 and 12).

A final example in Figure III.15 shows that good quality and homogenous films (regarding the thickness, the composition and the surface smoothness) can be obtained by MOCVD. We present on the one side SEM-EDX results of different probed regions as depicted in Figure III.15b (green crosses). The values of the Y/Mn ratio (marked on the figure for each measured point) present very small spread with respect to the average value that gives 1.33 ± 3%. On the other side, Figure III.15a shows a very homogeneous thickness distribution along the black line measured in cross section after cleavage of the sample.

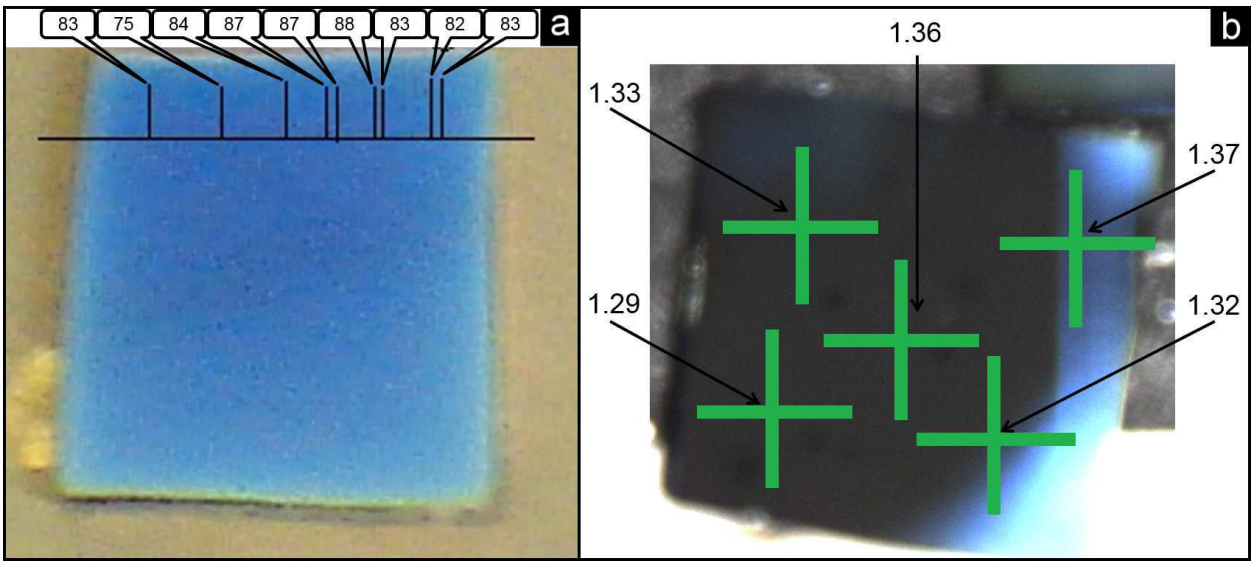

Figure III.15. YMO film on Si substrate: a) thickness distribution (the values are given in nm) as measured by SEM in cross-section (not shown); b) Y/Mn ratio distribution as measured by EDX-SEM (top view).

3.5 Summary and conclusions

The growth conditions of YMO films deposited on Si, STO, LAO and LSAT substrates by **MOCVD** and **PLD** have been optimized leading to films of high-quality showing no significant gradients in either thickness or composition and almost stoichiometric.

Two main deposition parameters were optimized for **MOCVD**: the deposition temperature and the Y/Mn ratio of the precursors in the injected solution.

- Under the experimental conditions used, the $Y(tmhd)_3$ precursor does not react in the same manner as the $Mn(tmhd)_3$ one. As a consequence:

  -there is a difference of the Y/Mn ratio in the injected solution and in the film.

  -the control of the film composition (one of the main challenges in the MOCVD growth of oxides) is strongly influenced by the geometry of the experimental MOCVD device

  -to a minor extent this composition is affected by the deposition temperature.

- Varying the two main parameters leads to a selective growth of YMO/Si film:

  Samples near the optimized Y/Mn ratio deposited at 600°C are amorphous, those deposited at 750°C are orthorhombic and finally those deposited in the range 800-850°C are hexagonal.

A similar selective growth is found as a function of O_2 pressure (with a fixed temperature) for the **PLD**. At low pressure the h-YMO is formed, in the intermediate O_2 pressure range an amorphous phase dominates, at high pressure the o-YMO phase is stabilized.

On perovskite type substrates the deposition parameters (temperature, Y/Mn ratio, oxygen pressure) have almost no influence and the orthorhombic YMO phase is stabilized by a strain mechanism.

The structural, morphological and magnetic characterizations performed in order to investigate the effect of the deposition parameters on the existing phases and the crystalline quality of the films are discussed in the following chapters.

References

1. Fujimura, N., et al., *Epitaxially grown YMnO3 film: New candidate for nonvolatile memory devices.* Applied Physics Letters, 1996. **69**(7): p. 1011-1013.
2. Chen, J., et al., *Tuning of transport and magnetic properties in epitaxial LaMnO3+x thin films.* Advances in Condensed Matter Physics, 2014. **2014**: p. 5.
3. Lei, D.Y., et al., *Spectroscopic ellipsometry as an optical probe of strain evolution in ferroelectric thin films.* Optics Express, 2012. **20**(4): p. 4419-4427.
4. Uusi-Esko, K., et al., *Characterization of RMnO3 (R = Sc, Y, Dy-Lu): High-pressure synthesized metastable perovskites and their hexagonal precursor phases.* Materials Chemistry and Physics, 2008. **112**(3): p. 1029-1034.
5. Malo, S., et al., *Structural and magnetic properties of the solid solution (0<x<1) YMn1−x(Cu3/4Mo1/4)xO3.* Solid State Sciences, 2005. **7**(12): p. 1492-1499.
6. Gelard, I., *Heterostructures d'oxydes multiferroiques de manganites de terre rares hexagonaux RMnO3 - Elaboration par MOCVD a injection et caracterisations structurales et physiques.* 2009.
7. K. H. Wu, H.J.C., Y. T. Chen, C. C. Hsieh, C. W. Luo, T. M. Uen, J. Y. Juang, J. Y. Lin, T. Kobayashi, M. Gospodinov, *Marked enhancement of Néel temperature in strained YMnO3 thin films probed by femtosecond spectroscopy* Europhysics Letters, 2011. **94**(2): p. 280.
8. Girardot, C., *Structures et Proprietes Physiques de Films Minces RENiO3 (RE=Sm, Nd) elabores par MOCVD*, in *LMGP*. 2009, Institut Polytechnique de Grenoble.
9. Pierson, H.O., *Handbook of Chemical vapor deposition (CVD) Principles, Technology, and Applications.* Second Edition William Andrew Publishing, LLC Norwich, New York, U.S.A., 1999.
10. Inc., C. *Chemical Book*. 2008; Available from: http://www.chemicalbook.com/.
11. O. Nilsen, H.F., A. Kjekshus, *Inexpensive set-up for determination of decomposition temperature for volatile compounds.* Thermochimica Acta, 2003. **404**: p. 187–192.
12. A.Y. Kovalgin, F.C.-R., M.L. Hitchman, S.H. Shamlian and S.E. Alexandrov, *A study by In Situ FTIR Spectroscopy of the Decomposition of Precursors for the MOCVD of High Temperature Superconductors.* JOURNAL DE PHYSIQUE IV 1995. **5**(Colloque C5, supplement au Journal de Physique II): p. 357-364.
13. Bartasyte, A., *Stress effects and phase transitions in PbTiO3 thin films deposited by MOCVD*. 2007, INP Grenoble and Vilnius University.

Chapter 4

Structural and magnetic characterization of $YMnO_3$ films on Si (100) substrates

Summary

4.1 Characterization of amorphous as-deposited YMO films ……86
4.1.1 Structural characterization of amorphous as-deposited YMO films ……...86
4.1.2 Magnetic characterization of amorphous as-deposited YMO films ……91
4.2 Characterization of hexagonal as-deposited YMO films ……..……..93
4.2.1 h-YMO films elaborated in the horizontal PI-MOCVD setup ……..…...93
4.2.2 h-YMO films elaborated in the vertical PI-MOCVD setup ……...100
4.2.3 h-YMO films elaborated by PLD ……..103
4.2.4 Magnetic characterization of h-YMO films ……...106
4.3 Characterization of orthorhombic as-deposited YMO films ……111
4.3.1 o-YMO films elaborated by PI-MOCVD ……..111
4.3.2 o-YMO films elaborated by PLD ……..119
4.3.3 Magnetic characterization of o-YMO films ……...122
4.4 Summary and conclusions ……123
References ……...126

In this chapter, the structural characterization and magnetic properties of $YMnO_3$ films grown on (100)-oriented Si substrates by MOCVD and PLD techniques are presented. The chapter has been divided into three parts that treat separately amorphous, hexagonal and orthorhombic $YMnO_3$ phase, which have been grown under different conditions. A short analysis of the magnetic properties is given for each section individually.

4.1 Characterization of amorphous as-deposited YMO films

At low deposition temperature, i.e. 600 °C, all as-deposited YMO films grown by MOCVD (mainly in the horizontal setup) on Si(100) substrate were amorphous whatever the Y/Mn atomic ratio used in the injected solution. Table IV.1 summarizes the main characteristics of these films and the growth conditions. The thickness was measured based on the SEM or/and TEM cross-section images and EPMA estimations. A good agreement was obtained between these techniques. The chemical composition of the films was measured by EPMA.

Label	T_s (°C)	$Y/Mn_{solution}$	$Y/Mn_{film\ (EPMA)}$	Thickness (nm)
YMO-600-0.5	600	0.5	0.38	150
YMO-600-1	600	1	0.85	300
YMO-600-1.4	600	1.4	1.06	260
YMO-600-1-v	600	1	1.04*	100

*Table IV.1. The main characteristics of the amorphous Y-Mn-O films. *this value was measured by EDX and then extrapolated to EPMA in a sample that was deposited in the vertical PI-MOCVD reactor.*

4.1.1 Structural characterization of amorphous as-deposited YMO films

The deposition at 600 °C did not lead to any crystal phase detectable in the film by classical θ-2θ XRD or GIXRD, as illustrated in Figure IV.1. None of the samples deposited at 600 °C present diffraction peaks in the θ-2θ patterns except those of the Si substrate. A typical θ-2θ diffractogram is shown in Figure IV.1a for the YMO-600-1-v sample. In addition, the GIXRD patterns, providing an enhanced film signal without the Si substrate peaks, present two broad peaks, characteristic of amorphous materials. An example of a typical GIXRD pattern is illustrated in Figure IV.1b (red line) for the YMO-600-1 sample. This pattern has been superimposed on the 1D electron diffraction (ED) pattern (intensity vs. 2θ) of the YMO-600-1.4 sample. The 1D ED pattern is deduced from a SAED image (see Figure IV.2d) using the Diffraction Ring Profiler software. Both diffraction patterns (X-ray and electrons) contain two broad diffuse maxima centered at the same position (to be able to compare them, the background of both patterns was subtracted and the GIXRD was smoothed). The maxima correspond to a distance of d=2.8 Å, which is similar for both amorphous samples.

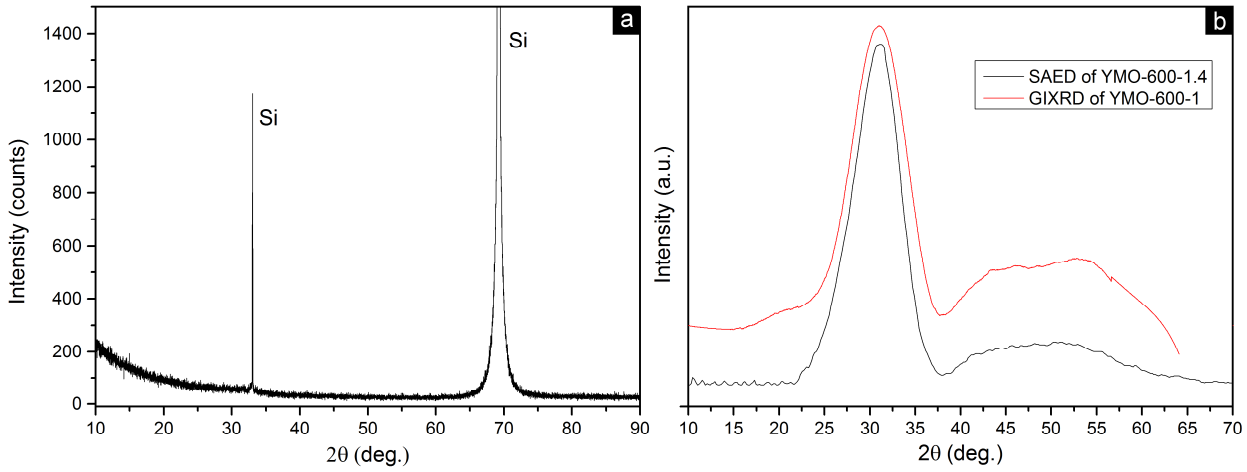

Figure IV.1. a) θ-2θ XRD pattern of YMO-600-1-v sample; b) GIXRD pattern of YMO-600-1 sample overlapped with the transformed ED pattern into 2θ range of the YMO-600-1.4 sample.

The amorphous character of the YMO films deposited on Si(100) at 600 °C was confirmed by TEM observations. An example of a TEM cross-section image is shown in Figure IV.2a for the YMO-600-1.4 film. The measured thickness corresponds to 260 nm, in agreement with SEM observations and EPMA calculation, and is homogenous with regard to the TEM measurement range. A relative smooth interface, between the film and the Si substrate (covered by a 3 nm of native SiO_x) is observed in the inset of Figure IV.2a. The columnar structure observed for all amorphous samples appears to be a distinctive feature of the YMO films grown on Si substrate 攝含 MOCVD. This indicates that during the deposition, the films exhibit a 3D-island growth mode. In this case, the adatom-adatom interactions are stronger than adatom-substrate interactions leading to the formation of 3D islands. The adatoms are incorporated gradually into the nuclei and thus form the columns. The diameter of the columns, marked with dotted lines in Figure IV.2b, ranges between 15-20 nm. The HRTEM image in Figure IV.2c confirms that the film exhibits a disordered atomic structure. The corresponding SAED pattern in Figure IV.2d shows a circular halo (the second one almost invisible here, but visible in Figure IV.1b) which is characteristic to amorphous materials.

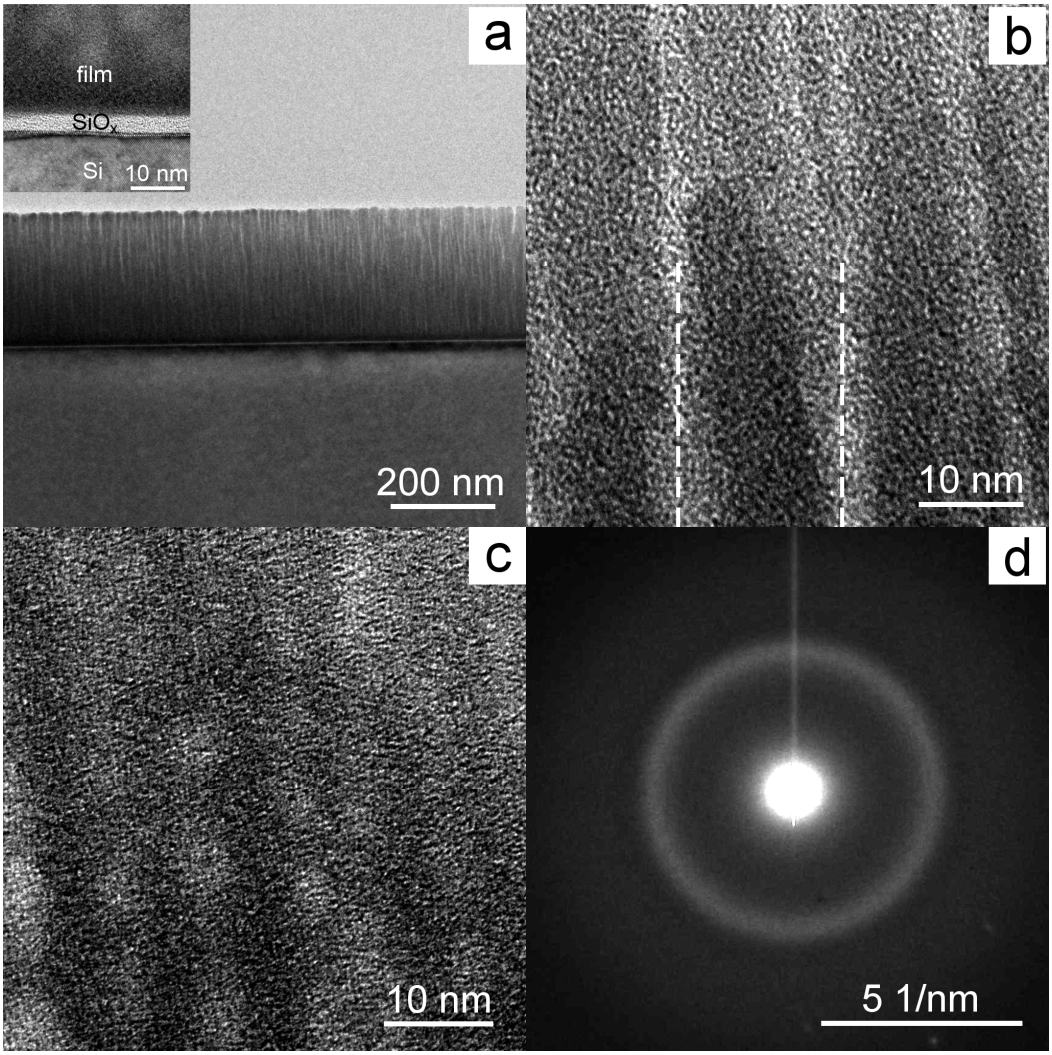

Figure IV.2. Cross-section TEM observations of the YMO-600-1.4 film: a) low magnification TEM showing the columnar structure (in the inset the substrate-film interface with the SiO_x layer in between); b) HRTEM image of the individual columns; c) typical HRTEM of amorphous YMO structure d) corresponding SAED pattern of c).

The SEM top view images of the amorphous YMO films shown in Figure IV.3 present a regular morphology (except some aggregates) with the features of a structure, which we will call in the following, cauliflower. The surface morphology of these films does not change when modifying the Y/Mn ratio and is a consequence of the MOCVD growth mechanism. This corresponds to the columnar growing morphology (viewed from the top), shown previously in the TEM images of Figure IV.2. The columns diameter ranges from 15 to 30 nm, in agreement with TEM measurements. No sign of crystallization is observed, consistent with XRD and TEM characterizations.

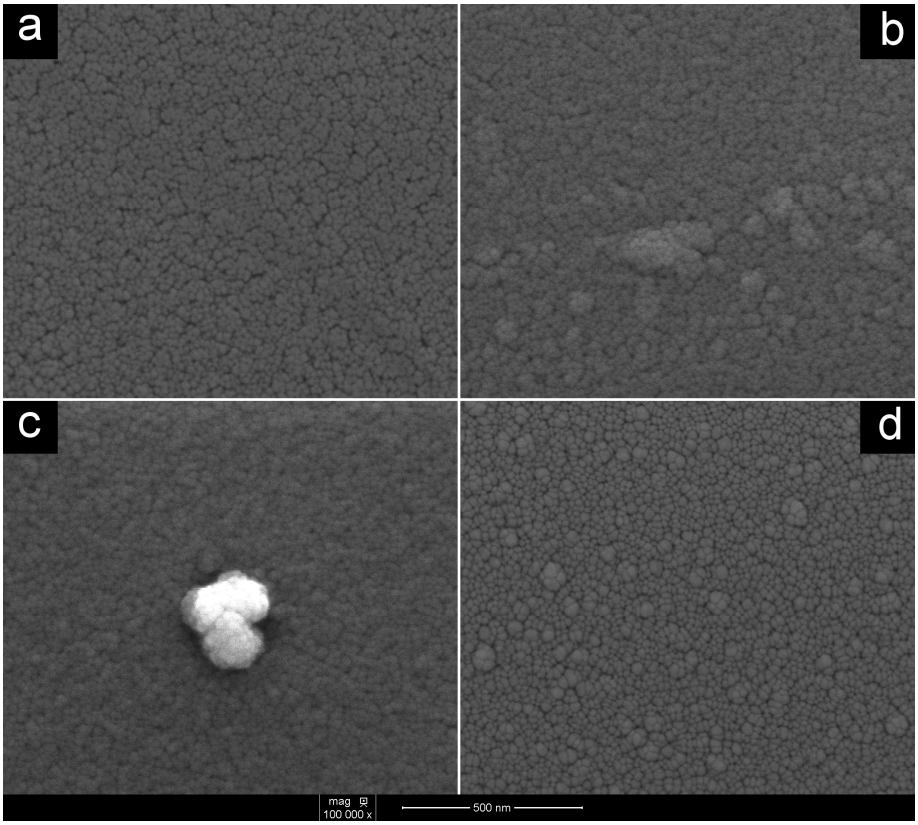

Figure IV.3. Typical top view SEM morphologies of: a) YMO-600-0.5; b) YMO-600-1; c) YMO-600-1.4 and d) YMO-600-1-v films.

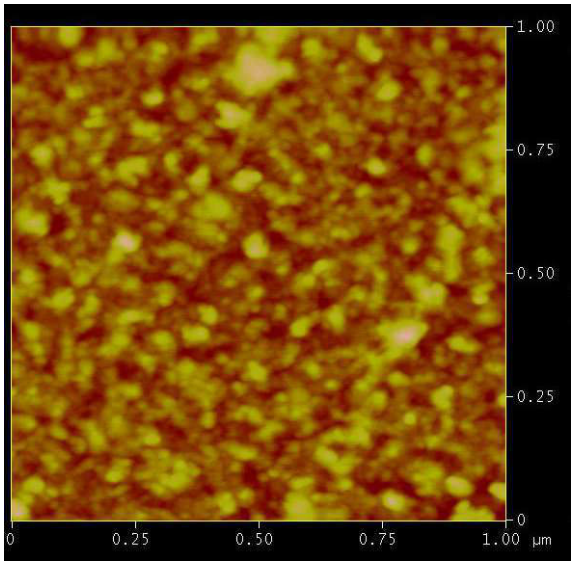

Figure IV.4. AFM image of the YMO-600-0.5 film surface

The morphology observed using the AFM scans is similar to the previous one shown in Figure IV.3, so-called cauliflower. Figure IV.4 shows the AFM image of the YMO-600-0.5 film which presents a relatively smooth surface, with an average roughness of 2 nm.

Complementary characterizations of the films were performed by Raman spectroscopy. The resulting spectra are shown in Figure IV.5a (the reference spectrum of the Si substrate is shown in Figure IV.5b).

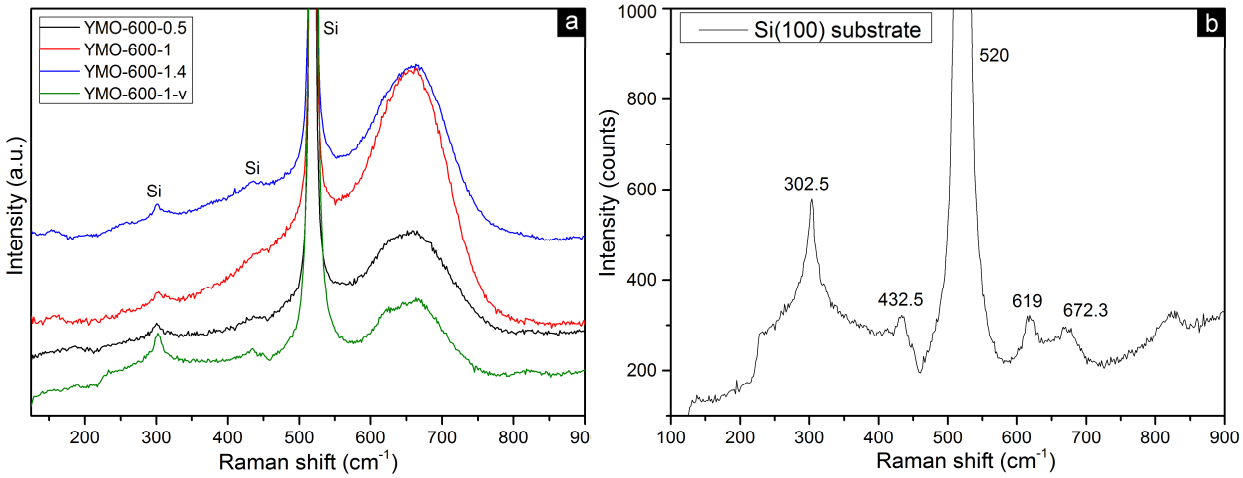

Figure IV.5.a) Raman spectra of amorphous YMO films deposited with a different Y/Mn ratio in the injected solution; b) Raman spectrum of the Si(100) substrate.

The main characteristic of the films is the presence of a broad peak located at ~ 650 cm^{-1}. An amorphous material usually displays this kind of feature: a strong broadening of the Raman mode which corresponds to the disordered state of the amorphous sample. The position of the broad peak is close to the most intense peak for the crystalline h-YMO (681 cm^{-1}) and o-YMO (618 cm^{-1}) phases. Except this broad peak, no other peaks are observed; the other modes are originating from the Si substrate, in accordance with its Raman spectrum shown in Figure IV.5b. In order to elucidate the detailed local structure or to assign a phonon vibration to the broad Raman mode supplementary analyses (e.g. EXAFS) are required.

The presence of an amorphous phase at low deposition temperatures (below ~ 700°C) was already observed for YMO thin films. Kim et al. [1] show that YMO films grown by MOCVD on SiO_2/Si substrates are amorphous in the deposition temperature range 450-650°C. Choi et al. [2] confirmed by XRD that Bi(3-10%):$YMnO_3$ films grown on Y_2O_3/Si(100) substrates by PLD are amorphous below 670°C. Similarly, $YMnO_3$ films grown on Pt/TiO_2/SiO_2/Si by PLD were

amorphous at 650°C [3]. Amorphous YMO/Si(001) films deposited by rf sputtering [4] (Figure IV.6a) have TEM and SAED patterns comparable to our images from Figure IV.2.

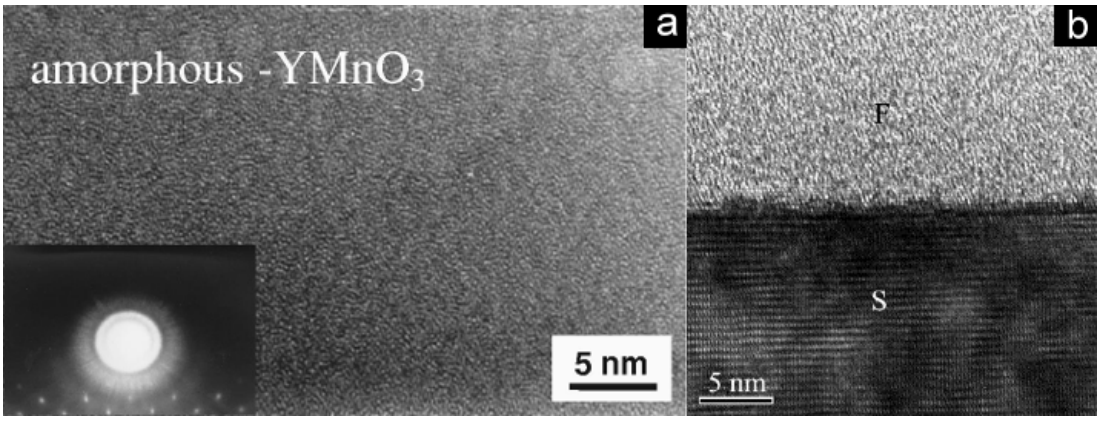

Figure IV.6. HRTEM image of amorphous $YMnO_3$ film grown on top of a) Si (from [4]) and GaN (from [5]).

Furthermore, Balasubramanian et al. [5] have demonstrated by HRTEM images (Figure IV.6b) that in the case of the PLD growth of YMO/GaN films, no crystalline phase could be obtained below 700°C. ALD depositions between 250-300°C on Si, STO and LAO substrate have produced amorphous films regardless of the substrate or their composition [6]. Also, amorphous YMO powder was obtained at 200°C, based on glycine-nitrate method and crystallized between 600°C and 700°C [7]. YMO ceramics prepared by co-precipitation and sintered at 600°C was also amorphous [8].

All these results demonstrate that the same amorphous YMO phase can be obtained in film or bulk form. Except θ-2θ XRD patterns and cross-section TEM images, no other technique was reported in the characterization of amorphous Y-Mn-O films.

4.1.2 Magnetic characterization of amorphous as-deposited YMO films

The magnetization vs. temperature (M(T)) in the field-cooled (FC) and zero-field-cooled (ZFC) modes, measured under a magnetic field of 500 Oe, for the amorphous YMO-600-0.5 and YMO-600-1 films, is shown in Figure IV.7. The ZFC curve exhibits a maximum (T_f) at 19 K and 11 K for YMO-600-0.5 and YMO-600-1 films, respectively, while the FC curve increases gradually with decreasing temperature. Below these temperatures, the ZFC and FC curves are obviously splitting, although no complete overlapping is present for the temperatures above T_f either. These results indicate that a spin-glass behavior is present in the films with a possible superimposed paramagnetic contribution.

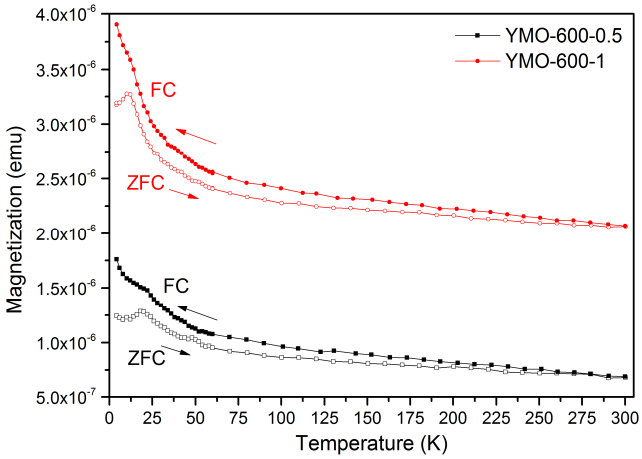

Figure IV.7. Temperature dependence of zero-field-cooled (ZFC, open symbols) and field-cooled (FC, solid symbols) magnetization measured under a magnetic field of 500 Oe for the amorphous YMO samples (film and Si substrate).

A similar spin-glass behavior was reported by Nakamura et al. [9] for $BiFeO_3$ amorphous films. It appears that a local clustering of spins occurs at low temperatures (< 220 K). The spins undergo antiferromagnetic interaction with random bond angles resulting in a net magnetic moment for each spin cluster, which therefore behave as a superparamagnet. The authors have reported that as the temperature goes down, the fluctuation of the spin clusters becomes slower and is finally frozen around 20 K. In this state, all spins are frozen into random directions with a short-range antiferromagnetic (speromagnetic) order. The spin freezing state is very similar to that of the spin glass.

Summary

The YMO films deposited at 600°C are amorphous, indicating that the amorphous phase is easily formed and stable for the **MOCVD** growing conditions in a large range of compositions. This phase forms prior to the crystallization of either o-YMO or h-YMO phases even if appropriate substrates (STO, LAO, GaN) would favor the crystalline phases [5], [6]. Furthermore, the formation of the amorphous YMO phase is independent of the synthesis method, initial composition of the precursors or oxygen pressure.

The as-deposited MOCVD films follow a 3D columnar growth mode with columns diameter between 15 and 20 nm and a cauliflower-like morphology. The Raman spectra present only a large mode at around 650 cm^{-1}. The magnetization measurements suggest a spin-glass behavior with a maximum in the ZFC curve between 11 and 19 K.

4.2 Characterization of hexagonal as-deposited YMO films

This section is devoted to the characterization of h-YMO films grown on Si(100) substrates by MOCVD or PLD. The characterization results are grouped according to the experimental deposition device used for the film growth.

4.2.1 h-YMO films elaborated in the horizontal PI-MOCVD setup

Different h-YMO films have been grown on Si substrates by MOCVD (Figure III.3 summarizes the optimal conditions for which the h-YMO phase is obtained). In the following we present only those who have the most detailed characterization. The XRD results of these films are shown in Figure IV.8 (see their label in Table IV.2).

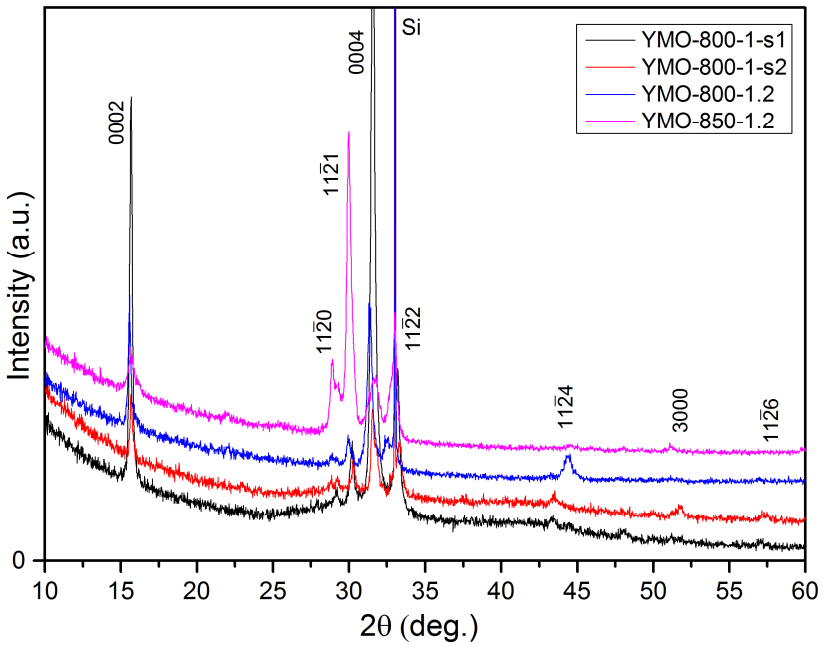

Figure IV.8. XRD patterns of h-YMO films. The reflections of the hexagonal $YMnO_3$ phase (JCPDS card No. 11-9577) are marked for each peak.

All peaks have been indexed with the h-YMO phase and are pure as far as the XRD is concerned. The θ-2θ patterns indicate that the films are textured (see Miller indices in Figure IV.8 and powder reference pattern in Appendix C). In the case of the YMO-800-1-s1, YMO-800-1-s2 and YMO-800-1.2 samples, the h-YMO film is *c*-axis textured, i.e. most of the grains grow with the (000l) planes parallel to the Si surface. For the YMO-850-1.2 film, the growth of the h-YMO phase along [11-21] is preferred.

Regarding the literature results, for h-YMO films deposited by MOCVD on Si(100), Si(111), SiO_2/Si(100), Y_2O_3/Si(111), YSZ(111) and Pt/Ti/SiO_2/Si substrates it was found that, in general, a *c*-axis orientation is favorable to the growth of h-YMO phase, independently of the substrate. It has been argued that the preferential orientation of the films depends on the substrate temperature and oxygen concentration [1]. A change in the preferential orientation and a shift of the peaks was observed when varying the Y/Mn ratio in the neighboring region of stoichiometry, while in the Y-rich or Mn-rich regions, secondary phases, such as Y_2O_3 and YMn_2O_5, respectively, were formed. These results are in agreement with our experiments.

The lattice parameters of the h-YMO phase, derived from XRD patterns, present some differences when compared to the JCPDS card No. 11-9577. Table IV.2 summarizes the *a* and *c* cell parameters of h-YMO values as well as the composition of the films.

Label	T_s [°C]	Y/Mn solution	Film composition (EPMA)	Film composition (EDX)	a* [Å]	c* [Å]	Thick-ness [10]
YMO-800-1-s1	800	1	$Y_{0.95}Mn_1O_{2.60}$	$Y_{1.18}Mn_1O_{5.66}$	6.129(5)	11.353(3)	350
YMO-800-1-s2	800	1	$Y_{0.83}Mn_1O_{2.48}$	$Y_{1.06}Mn_1O_{5.78}$	6.111(4)	11.343(3)	300
YMO-800-1.2	800	1.2	-	$Y_{1.46}Mn_1O_{8.31}$	6.189(5)	11.422(3)	325
YMO-850-1.2	850	1.2	-	$Y_{1.92}Mn_1O_{5.21}$	6.183(5)	11.343(4)	350

*Table IV.2. The main characteristics of the h-YMO films (label, main deposition parameters, composition, lattice parameters, thickness; * a = 6.1453 Å and c = 11.3714 Å as in the JCPDS card No. 11-9577).*

As it can be seen, the film composition differs considerably from that of the YMO stoichiometric phase. However, it is impossible to attribute a composition for the h-YMO phase present in the samples because of the existence of an interfacial amorphous layer (see Figure IV.11). This layer, of unknown composition, found between the h-YMO film and the Si/SiO_x substrate is included in the average formula given by EPMA or EDX. This amorphous layer has variable thickness: 50-60 nm for the YMO-800-1-s1 sample and 25-35 nm for the YMO-800-1-s2 sample. As the EDX-TEM analysis indicates, it contains Y-Mn-Si-O, but the exact quantification could not be achieved.

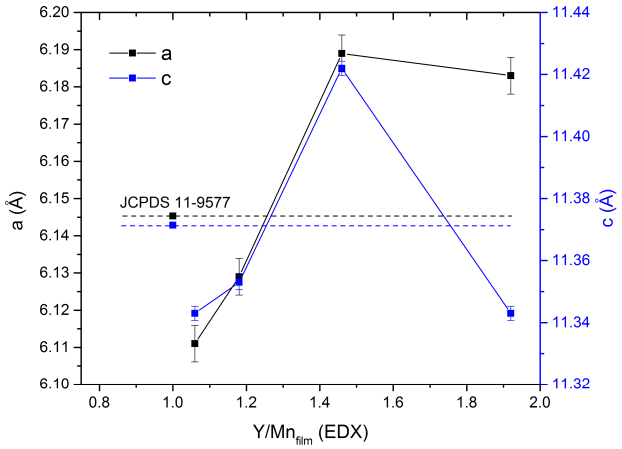

Figure IV.9. The lattice parameters a and c of the h-YMO phase vs. the Y/Mn ratio (measured by EDX) in the film (dotted lines represent the values from the JCPDS card No. 11-9577).

A representation of the *a* and *c* parameters variation with the composition Y/Mn in the film is shown in Figure IV.9. It is observed that the *a* and *c* values increase with the increasing Y/Mn ratio in the film except for the film with Y/Mn_{film}=1.92. These values are higher and lower respectively than the reference values from the JCPDS card No. 11-9577 (see dotted lines). We may believe that the films are sub- and over-stoichiometric but the scattering of the data in the literature avoids further comparison (e.g. $YMnO_3$: a = 6.138(4), c = 11.407(3) [11] ; a = 6.1542(3), c = 11.4031(2) [12]; $YMnO_{2.91}$: a = 6.137(9), c = 11.411(2) [11]; $YMnO_{2.95}$: a = 6.1728(2), c = 11.4509(4) [12];$YMnO_{2.85}$: a = 6.1806(1), c = 11.4545(4) [12]). Finally, what is evident is the fact that the h-YMO phase can be obtained in a large range of non-stoichiometry of the injected solution and the overall composition of the film.

A typical SEM image of the *c*-axis textured h-YMO film (see Figure IV.8) is displayed in Figure IV.10a for the YMO-800-1-s1 sample. The top-view micrograph displays a dense structure with two types of morphology: one corresponds to columnar grains (zone 1 in Figure IV.10a) and the other to dendritic aggregates of grains (zone 2 in Figure IV.10a). They indicate two different growing modes: columnar and dendritic. The column (individual grain) diameter is around 30 nm, while the total diameter of the aggregates ranges between 200 and 400 nm. It can be observed that on small regions the columns seem to be tilted in the same direction (see zone 1 from Figure IV.10a). No difference in the chemical composition was observed for these two morphologies of the h-YMO phase. The morphology of the YMO-850-1.2 film (see Figure IV.10b), mainly [11-21]-oriented is different compared to the *c*-axis oriented films from Figure

IV.8. However, one of their main features is present: the dendritic aggregates of grains. No evidence of columnar growth and oriented grains is seen. This is in agreement with the XRD results. It seems that a radial growth or a recrystallization process may have occurred in this case. It is supposed that the observed differences in texture and morphology are mainly due to the deposition temperature (850 °C), which is higher than the deposition temperature of the three other samples (800 °C).

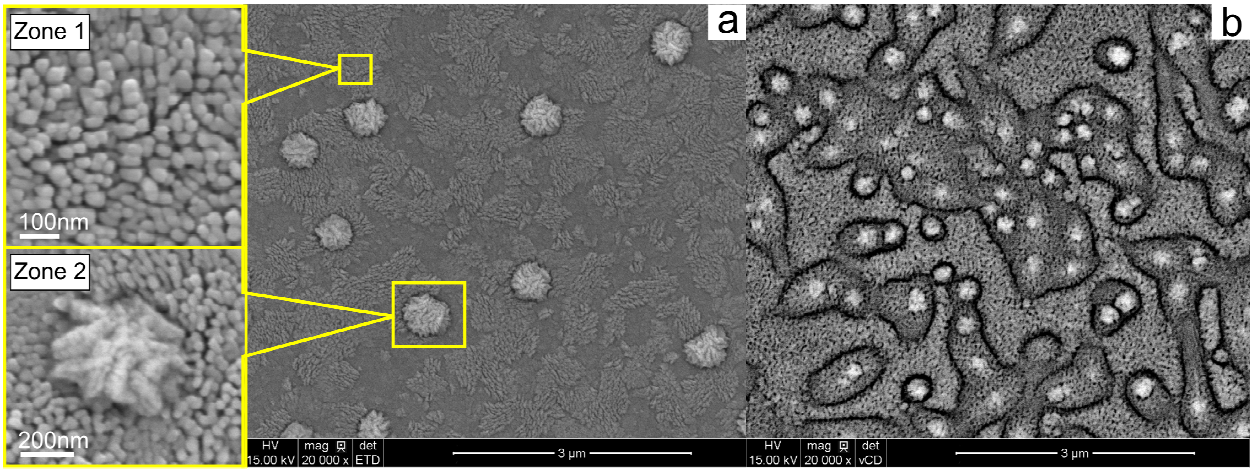

Figure IV.10. Top view SEM images of h-YMO films: a) YMO-800-1-s1 sample. Zone 1 shows a columnar morphology, zone 2 displays a dendritic-like feature; b) YMO-850-1.2 sample.

Further microstructural characterizations using TEM were carried out on the cross-section of the YMO films. The corresponding images for the YMO-800-1-s1 sample are presented in Figure IV.11. The low magnification image of the h-YMO film (Figure IV.11a) shows three different layers on top of the Si. From top to bottom they can be identified as follows: the uppermost one (~300 nm thick) corresponds to the crystalline h-YMO film grown in the form of columns, in agreement with the previous morphological results obtained by SEM. The intermediate layer (~50-60 nm thick), in gray color in Figure IV.11a is amorphous and is observed between the columnar grains in the YMO film (top layer) and the native amorphous SiO_x oxide of the Si substrate (bottom layer, 8 nm thick, with white color in Figure IV.11a).

The amorphous SiO_x layer is commonly found when deposited on Si substrates even when a chemical HF cleaning is performed. The oxygen atmosphere and also the organic precursors favor the formation of this layer. It seems, thus, impossible to grow the $YMnO_3$ phase directly on Si substrate by MOCVD.

Concerning the intermediate amorphous layer, the precise identification of this layer was not possible in the present work, it appears that similar amorphous layers were previously observed when growing oxides on silicon substrate and were reported either as a silicate [1] [13] or as amorphous YMO phase [14]. Considering these findings and our results, we have reason to believe that this layer forms as a compensation mechanism for the non-stoichiometry. It is uncertain if the amorphous layer forms during the deposition or as a result of the annealing. Our attempts to crystallize this layer under the TEM electron beam were unsuccessful.

A typical selected area electron diffraction (SAED) pattern of a small region of Figure IV.11a containing several columnar grains is shown in Figure IV.11b.

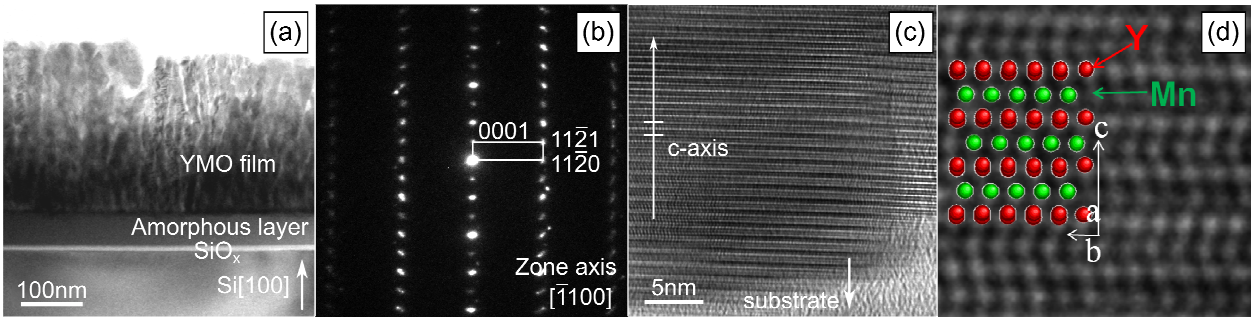

Figure IV.11. TEM images of the YMO-800-1-s1 film deposited by MOCVD: (a) low magnification cross-section TEM image showing three different layers on top of the Si film; (b) SAED pattern of a small region of (a) containing several columnar grains; (c) HRTEM image of a columnar grain c-axis oriented; (d) enlargement of (c) overlapped with structure simulation.

This pattern corresponds to a [-1100]-zone axis. It presents an alignment of 000l diffraction spots along the vertical direction of the figure (i.e. out of plane direction with respect to the Si substrate) and thus the columnar grains extend vertically along the $[0001]_{h\text{-}YMO}$ (*c*-direction of h-YMO). This result is consistent with previous XRD results indicating a textured sample with grains preferentially oriented (i.e. $[0001]_{h\text{-}YMO}$ is parallel to $[100]_{Si}$). The splitting of some diffraction spots in Figure IV.11b indicates a misorientation of a few degrees between columnar grains. A good agreement is observed between the corresponding cell parameters (a = 6.11(3) Å and c = 11.31(4) Å) measured from Figure IV.11b and the results obtained by XRD (see Table IV.2). The high resolution TEM (HRTEM) micrograph of a single columnar grain of the h-YMO film is shown in Figure IV.11c and a partial enlargement is represented in Figure IV.11d. It has the same orientation as the SAED in Figure IV.11b, corresponding to a [-1100]-zone axis. The white dots aligned horizontally can be identified with the (000l) atomic planes perpendicular to

$[0001]_{h\text{-}YMO}$. The *c*-axis of the columnar grain, extending along the vertical direction of the figure, is normal to the Si surface. The distance indicated by horizontal white lines in Figure IV.11c represents the unit cell along the *c*-axis, corresponding to an interplanar spacing of around 11.35(4) Å of the (0001) planes. The projected structure (according to [15]) along the [-1100]-zone axis superimposed to the image in Figure IV.11d shows a good agreement between the white dots from the HRTEM image and the arrangements of Y (red) and Mn (green) atoms derived from the structural model.

Complementary structural characterizations have been carried out by Raman spectroscopy. For the h-YMO phase (space group $P6_3cm$) the theoretical results for Γ-point phonon modes give a total of 60 Γ-point modes ($10A_1 + 5A_2 + 10B_1 + 5B_2 + 15E_1 + 15E_2$) among which 38 ($9A_1 + 14E_1 + 15E_2$) are Raman active [16]. Depending on the measuring polarization configuration and the crystal/film orientation, the number of the measured Raman active modes can be reduced. The unit cell of the ferroelectric $P6_3cm$ structure and the Y, Mn and O atoms label is illustated in Figure IV.12. The corresponding vibration motion of each mode is given in Table IV.3. The A_1 Raman line at 681 cm^{-1}, which is dominant in the spectra, corresponds to stretching vibrations of O1 and O2 atoms along the *c* direction.

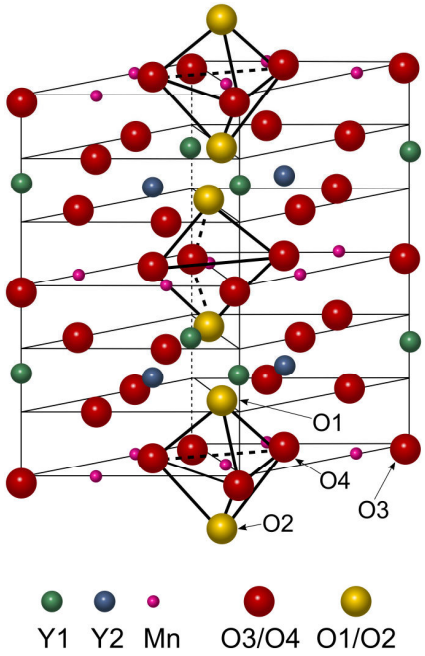

Figure IV.12. The unit cell of the ferroelectric $P6_3cm$ structure and the Y, Mn and O atoms label (adapted from [17]).

The position of the Raman modes of the h-YMO films shown in Figure IV.13 are in good agreement with the previous measurements reported by Iliev et al. [17], and with our experiments performed on h-YMO single crystals (last column in Table IV.3).

Mode symmetry	**Assignment**	**Iliev et al. (single crystal)**	**Our data**	
			single crystal	**ceramic**
E_2	+x,y (Y1) - x,y (Y2)	135	137	137
A_1	+z(Y1) – z(Y2)	148	152	153
A_1	$Rot._{x,y}$ (MnO_5)	190	188	189
E_2	+x,y(O2,Mn) –x,y(O1,O3)	215	222	221
A_1	+z(Y1, Y2) – z(Mn)	257	258	
A_1	X(Mn), z(O3)	297	298	
E_2	z(O2)-z(O1), x,y(O4)	302	304	305
E_1	+x,y (O1) - x,y (O2)	376	375	376
E_1	+x,y (O1) - x,y (O2)	408	408	405
A_1	z(O4,O3) – z(Mn)	433	437	439
A_1	x,y(O1,O2) –x,y(Mn)	459	458	461
E_1	x,y(O3) –x,y(O4)	632	639	639
A_1	z(O1)-z(O2)	681	681	684

Table IV.3. Experimental values of Raman mode frequencies for h-YMO single crystal from [17] compared to our data. The mode symmetries and the assigned vibrations are given in the first two columns.

Small shifts in the mode position are observed when comparing to the single crystal data from Table IV.3. The shift of the A_1 mode centered at ~ 684 and 685 cm^{-1} for YMO-800-1-s1 and YMO-800-1-s2 films is likely caused by the oxygen vacancies or Mn non-stoichiometry as this mode corresponds to the O vibration in the MnO_5 bypyramid. The hypothesis is in agreement with the EPMA results.

Furthermore, the spectra of the YMO-800-1-s1 film acquired in the two morphologically different regions (corresponding to the *c*-axis oriented film and to aggregates formed by randomly oriented grains) shown in Figure IV.10a, are almost identical. However, a difference in the intensity is observed for the lines at 641 cm^{-1} (see inset Figure IV.13): E_1 mode is more intense in the aggregate zone and barely visible in the textured region of the film. Due to symmetry reasons, the E_1 mode cannot be observed for the *c*-axis oriented films in the backscattering configuration used in our experiment (laser propagation along the *c*-axis; see Fig. 2 in [17] for the polarized scattering configurations).

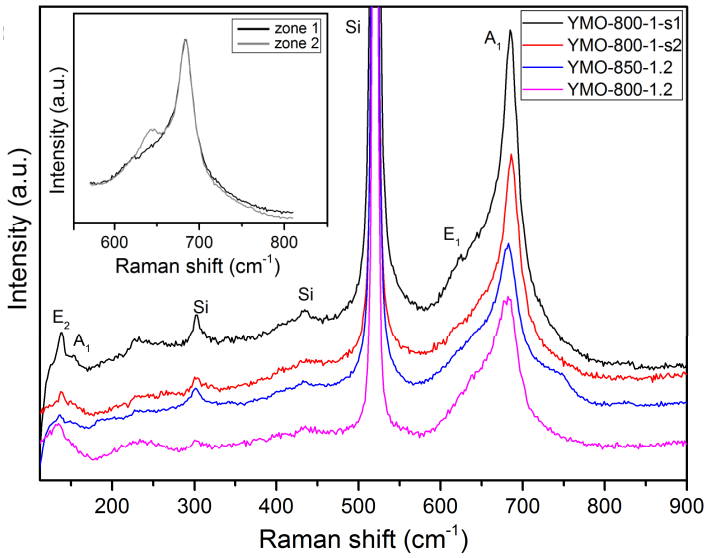

Figure IV.13. Raman spectra of h-YMO films elaborated in the horizontal PI-MOCVD device. Inset: A part of the Raman spectra collected in the two morphologically different regions (zone 1 and zone 2) of the YMO-800-1-s1 sample.

This clearly confirms that aggregates are formed by randomly oriented grains of the h-YMO phase, in agreement with the EDX measurements.

The Raman frequencies of the YMO-800-1.2 and YMO-850-1.2 films are closer to the single crystal values, indicating that these samples are close to the stoichiometric hexagonal $YMnO_3$ phase.

Mode symmetry	YMO-800-1-s1-zone1	YMO-800-1-s1-zone2	YMO-800-1-s2	YMO-800-1.2	YMO-850-1.2
E_2	138	138	138.5	133.5	136
A_1	153	153			148.5
E_1		641			
A_1	684.5	684.5	685.5	680.5	681

Table IV.4. Experimental values of Raman mode frequencies for h-YMO films (zone 1 and 2).

4.2.2 h-YMO films elaborated in the vertical PI-MOCVD setup

The characterization results of h-YMO films grown on Si substrates by PI-MOCVD using the vertical setup (Figure III.5 summarizes the optimal conditions for which the h-YMO phase is obtained) are shown in the following. The representative samples and their principal characteristics are given in Table IV.5. For this study, the only variable deposition parameters is the Y/Mn ratio in the injected solution, all others being constant.

Label	T_s (°C)	$Y/Mn_{solution}$	Y/Mn_{film} (EDX)	a (Å)	c (Å)	Thickness (nm)
YMO-800-0.29-v	800	0.29	1.05	6.063(4)	11.296(3)	85
YMO-800-0.35-v	800	0.35	1.22	6.090(4)	11.306(3)	100
YMO-800-0.4-v	800	0.4	1.57	6.131(4)	11.326(3)	62

Table IV.5. The main characteristics of the h-YMO films (label, main deposition parameters, composition, lattice parameters, thickness)

The XRD patterns of the h-YMO films (see their label in Table IV.5) are shown in Figure IV.14a. The diffraction peaks are indexed on the basis of h-YMO phase (see indices in Figure IV.14a). Their intensity indicates a growth mainly along the *c*-axis. The lattice parameters (*a* and *c*) derived from the XRD peaks increase almost linearly with the increase of the Y/Mn ratio in the film as measured by EDX (see Figure IV.14b).

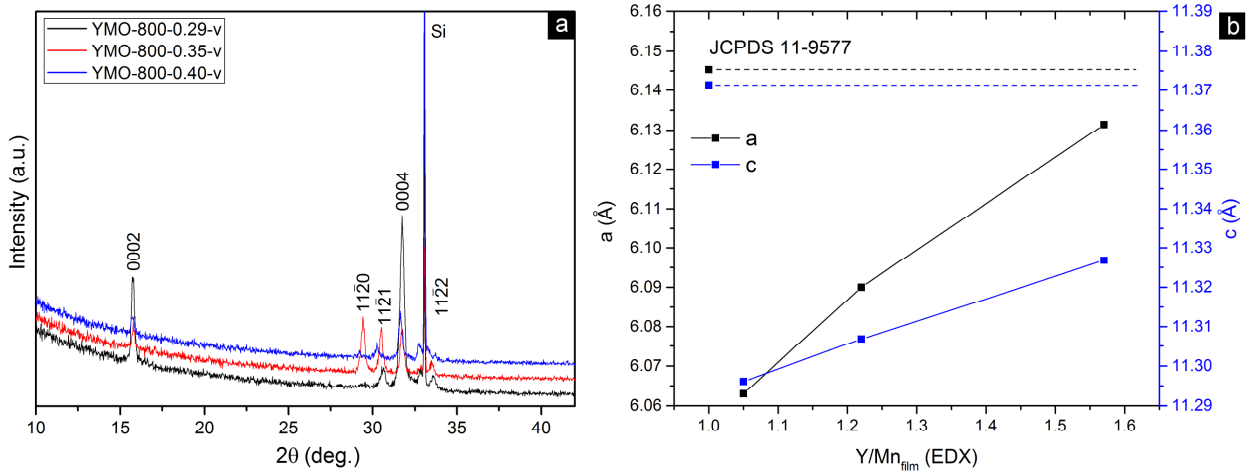

Figure IV.14. a) XRD patterns of YMO films indexed with the h-YMO phase (JCPDS card No. 11-9577); b) The lattice parameters a and c of the h-YMO phase vs. the Y/Mn ratio (measured by EDX) in the film (dotted lines represent the values from the JCPDS card No. 11-9577).

They show a significant difference when compared to those from the literature (see JCPDS card No. 11-9577) for the stoichiometric YMO. The cell parameters of the YMO-800-0.4-v film are the closest to the reference data, suggesting that this sample is almost stoichiometric.

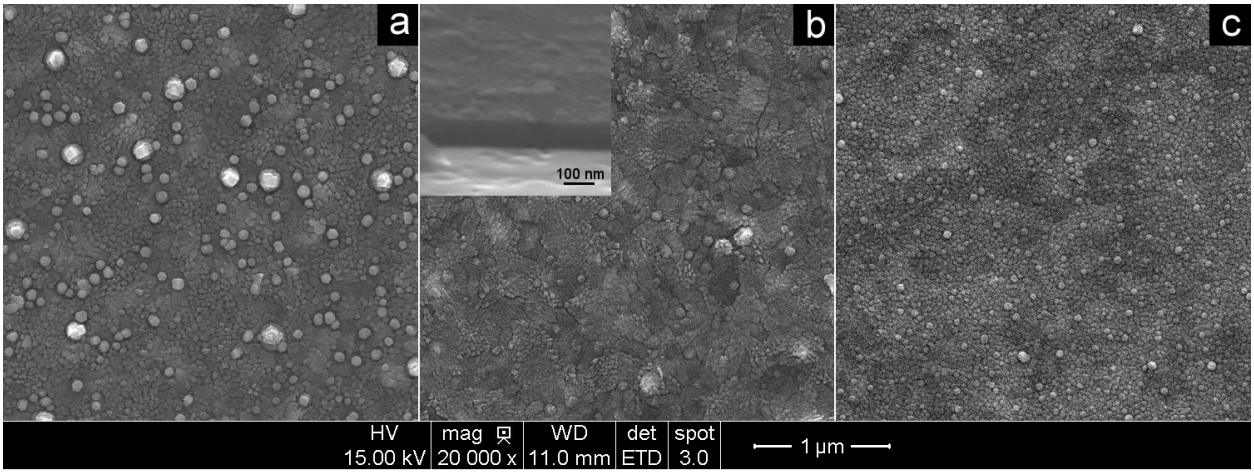

Figure IV.15. Top-view SEM images of h-YMO films.

The SEM top-view images of the h-YMO films are shown in Figure IV.15. They reveal a dense matrix microstructure and low porosity with an average grain diameter of 40 nm. This can correspond to a columnar growth, although from the cross-section SEM image shown in the inset of Figure IV.15 it is difficult to distinguish the type of growth. Many grains agglomerate in aggregates of particles ranging from 100 to 200 nm. These morphologies are very similar to those shown in Figure IV.10 for the h-YMO films grown in the horizontal MOCVD reactor. The same growth mechanism is, thus, occurring.

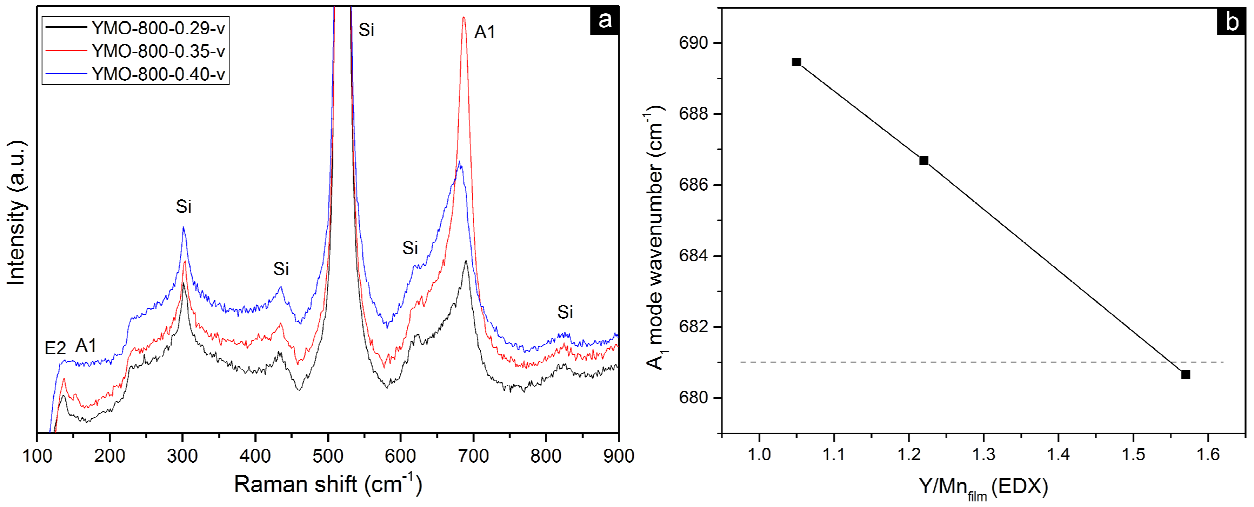

Figure IV.16. a) Raman spectra of h-YMO films; b) A_1 Raman mode evolution with the Y/Mn ratio in the film (the dotted line represent the reference value of the single crystal).

The Raman spectra of the YMO films are characterized by the intense A_1 mode of the h-YMO phase, whose intensity is related to the film thickness. As previously mentioned, this mode is associated with the vibration of the apical oxygen atoms in the MnO_5 bypyramids along the *c*-axis and should be very sensitive to any distortion (e.g. different bond lengths) or disorder in the oxygen atom sublattice. As shown in Figure IV.16b, the position of the mode shows a linear dependence with the Y/Mn ratio in the film (measured by EDX). The position of the A_1 mode at ~681 cm^{-1} corresponding to the YMO-800-0.4-v film is almost identical with that in the single crystal (see Table IV.3), suggesting that this sample is the closest one to the stoichiometric formula. Indeed, as we move away from the stoichiometric $YMnO_3$ composition, due to the MnO_5 bipyramidal distortions, the vibration modes become more energetic and a shift toward high wavenumbers is observed. These results are in agreement with the previous XRD results of cell parameter determination, which may be related to the presence of oxygen vacancies and/or the Y/Mn substitutional disorder (cation vacancies).

4.2.3 h-YMO films elaborated by PLD

Two representative samples, deposited at different O_2 pressures (see labels in Table IV.6), have been chosen for characterization in this section.

Figure IV.17 shows the θ-2θ XRD patterns of the two films. The intense peaks correspond to the (11-20) and (11-21) reflections of the h-YMO phase. No other peaks are appearing, which indicates that the films are textured.

When measuring the GIXRD pattern of the YMO-Si-1 film (see inset of Figure IV.17), a relatively different pattern come out: beside the intense (11-21) and (11-21) peaks observed in the θ-2θ XRD pattern, other peaks, indexed as (0004), (11-22) and (30-30) appear. Using the Scherrer's equation to determine the crystallite size from the peak FWHM (see section 2.2.1.1), we found crystallite sizes close to 20 and 37 nm for YMO-Si-1 and YMO-Si-6 respectively.

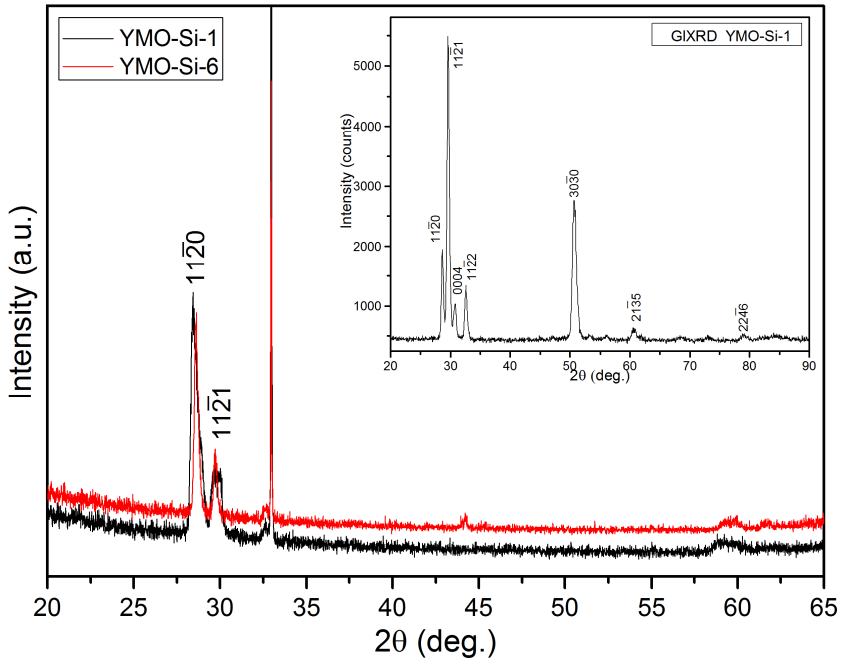

Figure IV.17. θ-2θ XRD patterns of h-YMO films deposited by PLD at different O_2 pressures. The Miller indices correspond to the reflections of the hexagonal $YMnO_3$ phase (JCPDS card No. 11-9577. Inset: The GIXRD pattern of the YMO-Si-1 sample.

The cell parameters deduced from θ-2θ XRD and GIXRD patterns are summarized in Table IV.6. It can be observed that the values of the *a* parameter are close between each other and higher than those obtained for both types of MOCVD films (Table IV.2 and 5) and in JCPDS card No. 11-9577. In contrast, the *c* parameter is either higher or lower than the c parameter given in the reference card or obtained for MOCVD films. This shows that a drastic variation in the oxygen pressure during the PLD growth greatly affects the lattice parameters of the h-YMO phase.

Label	**T (°C)**	**PO2 (bar)**	**Composition EDX**	**a (Å)**	**c (Å)**	**$D_{Scherrer}$ (nm)**
YMO-Si-1	800	10^{-3}	$Y_{1.85}Mn_1O_{2.93}$	6.226(3)	11.612(4)	20
YMO-Si-6	800	$1.4\ 10^{-4}$	$Y_{1.98}Mn_1O_{3.58}$	6.233(3)	11.205(5)	37

Table IV.6. The main deposition parameters of h-YMO films grown by PLD (label, main deposition parameters, composition, lattice parameters, correlation length).

Figure IV.18 compares the *a* and *c* parameter values obtained for all the h-YMO films deposited by MOCVD and PLD as function of the Y/Mn ratio in the film.

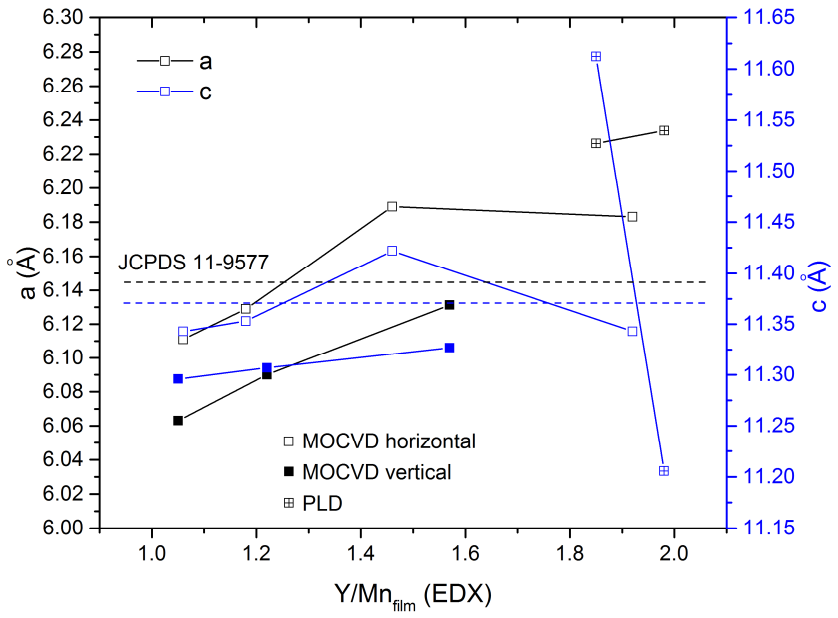

Figure IV.18. The values of a and c parameters obtained for the h-YMO films deposited by MOCVD and PLD as function of the Y/Mn ratio in the film.

The SEM top-view images of the two PLD films are shown in Figure IV.19. The films surfaces present a very dense microstructure, without cracks or aggregates. The grains are uniform and tightly packed of about 90-150 nm in size, which is much higher than the crystallite size obtained by Scherrer formula.

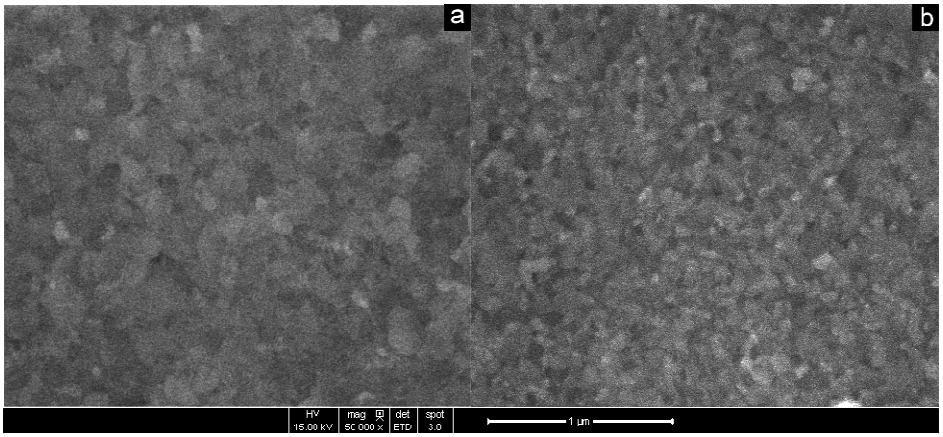

Figure IV.19. Top-view SEM images of h-YMO films deposited by PLD.

The existence of the h-YMO phase was confirmed by the Raman results shown in Figure IV.20. Only the most intense A_1 mode of the h-YMO phase is present, together with several Raman lines of the Si substrate. The values of the Raman shift for the A_1 mode are 681 and 675 cm^{-1} for the YMO-Si-1 and YMO-Si-6 films, respectively. The first value is identical to the bulk value in

agreement with a stoichiometric film, but in disagreement with the XRD and EDX results. For the YMO-Si-6 film, the position of the mode is shifted toward lower energy at 675 cm^{-1}, suggesting strong vibrations of the MnO_5 bipyramid which implies a non-stoichiometry in the Mn or O atoms. The Raman mode dependence of the experimental conditions (Y/Mn ratio, oxygen pressure, deposition temperature etc.) is lacking in the existing publications.

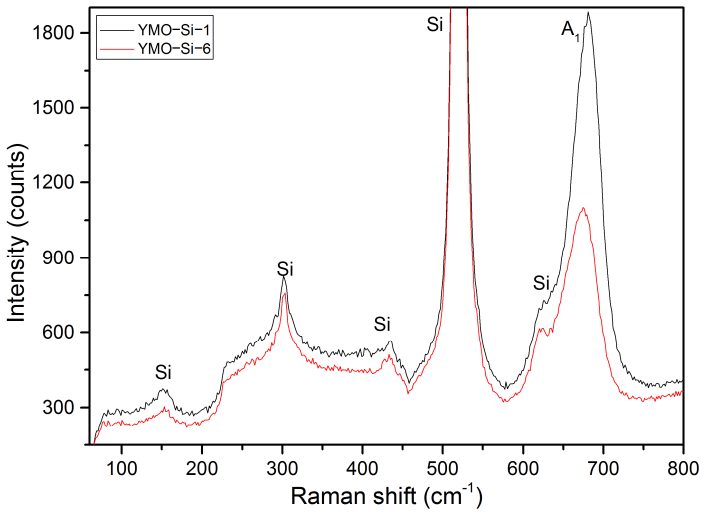

Figure IV.20. Raman spectra of YMO films deposited by PLD.

4.2.4 Magnetic characterization of h-YMO films

In addition to the structural investigations, magnetization M(T) and M(H) measurements were performed for the h-YMO films. In order to compare them to their bulk counterpart, the same type of measurements were performed on hexagonal YMO ceramic powders and single crystal. The similarities and differences are discussed in the following.

A typical example of temperature dependence of the magnetization (M(T)) is shown in Figure IV.21a for YMO-800-1-s1 sample. A splitting of ZFC-FC curves, with a maximum in the ZFC curve at the freezing temperature $T_f = 20$ K, indicates a spin glass-like behavior.

As shown in the Figure IV.21b, an almost linear variation in the M(H) curve is observed at room temperature for the h-YMO film as expected for a paramagnetic behavior. At low temperature, a small hysteresis loop is observed, indicating an additional weak ferromagnetic contribution.

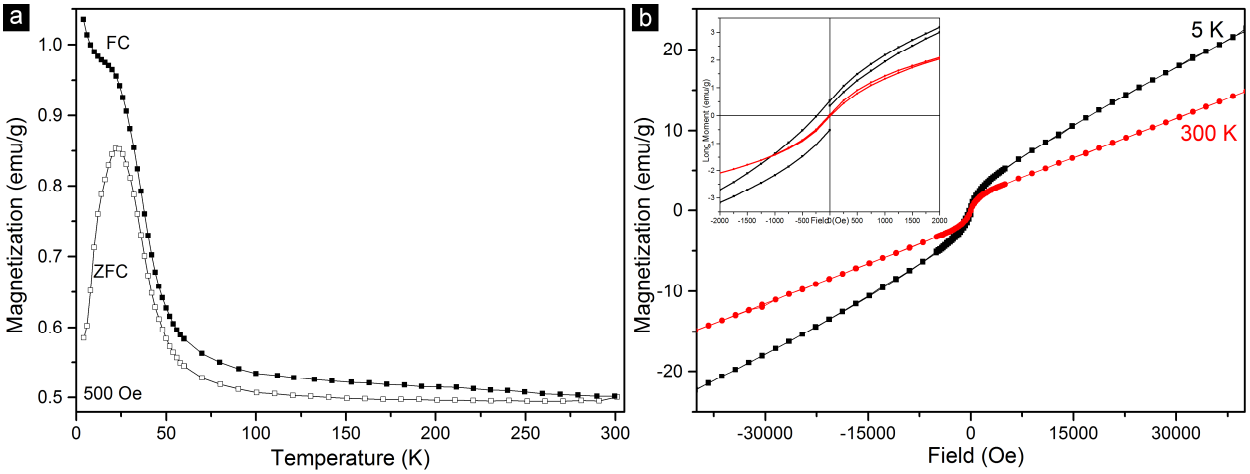

Figure IV.21. a) Temperature dependence of the magnetization (M(T)) for YMO-800-1-s1 film. Open (solid) symbols represent the M(T) taken in the ZFC (FC) mode; b) Field dependence of the magnetization (M(H)) at 5 and 300 K. Inset: enlargement of the M(H) curve in the low magnetization values.

The magnetization of hexagonal $YMnO_3$ films has been studied to a lesser extent. Fujimura et al. [18] have reported a Néel temperature of 130 K in h-YMO grown on Pt/sapphire, which in our opinion seems unlikely, especially as the authors do not have enough experimental results to explain why the Néel point was so high. Other reports show the existence of a similar spin-glass state for the bulk h-YMO phase [19], although it was found at different freezing temperatures (11 K and 56 K).

Our M(T) magnetization results in ZFC and FC mode on h-YMO single crystal, shown in Figure IV.22, is dominated by an antiferromagnetic ordering with Néel temperature T_N= 70 K. The ZFC and FC curves are overlapping, as expected for a proper antiferromagnetic behavior. Furthermore, the inverse magnetic susceptibility ($1/\chi$) (see inset of Figure IV.22a) in the linear region is fitted in order to obtain (by extrapolation) the Curie-Weiss temperatures. The negative value is obtained for the Curie-Weiss constant (θ_{CW}=-640 K) which indicates dominant antiferromagnetic interactions between Mn^{3+} spins.

These results, typical for hexagonal YMO crystals are in agreement with those in the literature ([20], [21], [22], [23], [11]). The Néel ordering temperature reported in all of these cases ranges from 70 K to 75 K, in agreement with our results. Furthermore, the M(H) field magnetization dependence, displayed in Figure IV.22b, shows a paramagnetic behavior at room temperature,

which is above T_N, as expected. At low temperature (T=5 K), a linear dependence, characteristic of antiferromagnetic materials can be observed, despite the fact that our data is a bit noisy.

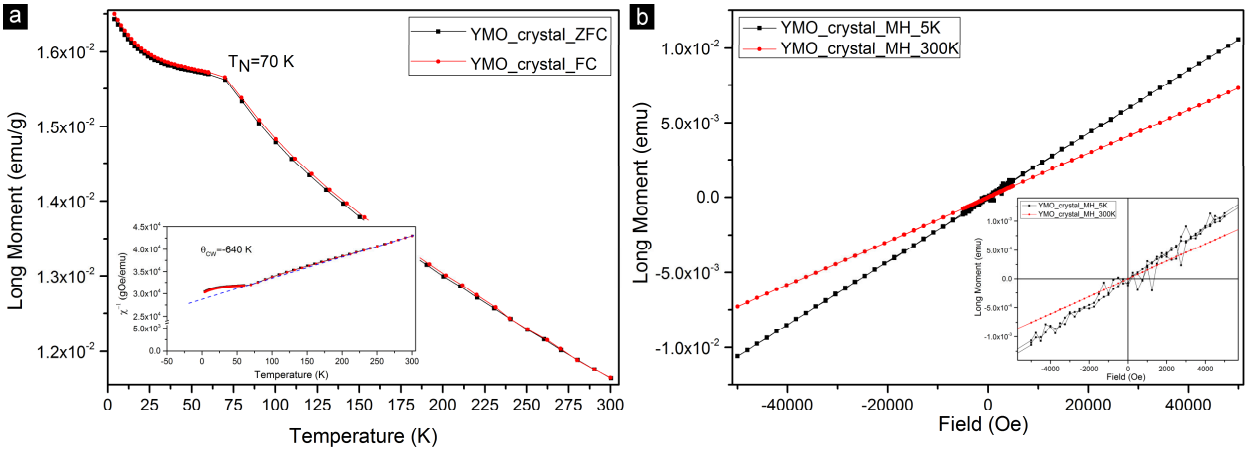

Figure IV.22. Magnetization measurements of h-$YMnO_3$ single crystal: a) M(T) magnetization in ZFC-FC mode. In the inset Curie-Weiss plot (χ^{-1} vs. T); b) M(H) at 5 and 300 K. In the inset: enlargement of the M(H) curve in the low magnetization values.

However, when observing the magnetization of hexagonal YMO ceramics, the picture appears a bit different. Three different ceramic samples were elaborated with the following compositions: $Y_1Mn_{0.95}O_3$, $Y_{0.95}Mn_1O_3$ and $Y_1Mn_1O_3$. The temperature dependence of the magnetization for these samples in an applied magnetic field of 500 Oe and between 2 and 300 K are shown in Figure IV.23.

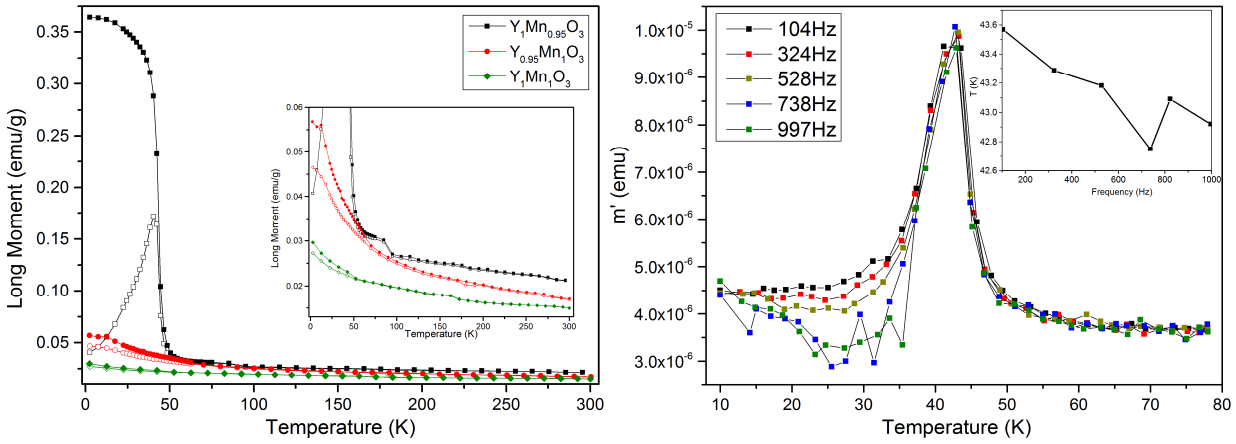

Figure IV.23. a) Temperature dependence of the magnetization for $Y_{1-x}Mn_{1-y}O_3$ powder samples. Open (solid) symbols represent the M(T) taken in the ZFC (FC) mode. Inset: enlargement of the figure in the low magnetization values; b) Temperature dependence of ac magnetic susceptibility for the $Y_1Mn_{0.95}O_3$ sample. Inset: T vs. frequency of the maxima from b) (from A. Schulman).

$Y_1Mn_{0.95}O_3$ sample shows a different behavior when compared to the $Y_{0.95}Mn_1O_3$ and $Y_1Mn_1O_3$ samples. A split of the ZFC-FC curves occurs at T=40 K. This may indicate a spin-glass transition. To further characterize the SG behavior of the $YMn_{0.95}O_3$ sample, we have performed frequency dependent susceptibility measurements. Figure IV.23b shows the temperature dependence of a.c. magnetic susceptibility at different frequencies (104, 324, 528, 738 and 997 Hz) in an applied field of 100 Oe for the $Y_1Mn_{0.95}O_3$ sample. The peak position of the a.c. susceptibility versus the temperature corresponding to the spin freezing (T_f) is almost unchanged (however, a very small shift of 0.5 K toward lower temperatures is observed with increasing frequency – see inset of Figure IV.23b). This behavior is not expected for a spin-glass, suggesting that another type of interaction (e.g. superparamagnetic) may be responsible for the trends of the M(T) curves. A similar behavior of the M(T) dependency is well known for Mn_3O_4 ceramics at 42 K [24]. Therefore, it is possible that small quantities of Mn_3O_4 impurity are contained in the $Y_1Mn_{0.95}O_3$ sample, although it was not detected in our analysis (Rietveld refinement of XRD pattern and Raman spectroscopy – see Appendix C). A kink in both ZFC and FC curves is observed at around T= 85 K (see black symbols in the inset of Figure IV.23a), which is close to the Néel temperature of the $YMnO_3$ phase.

The $Y_{0.95}Mn_1O_3$ and $Y_1Mn_1O_3$ samples also show a splitting in the ZFC-FC curves at 70 and 65 K, respectively without a decrease in the ZFC magnetization curve as previously observed for the film. This indicates a possible spin-glass behavior but further measurements are required.

Summary

The h-YMO films, grown by **MOCVD** or **PLD** have been characterized by several techniques and the following characteristics are resulting:

- Orientation:
  - the **MOCVD** films are mainly *c*-axis textured, strongly influenced by the deposition temperature and to a minor extent the Y/Mn ratio in the solution
  - the **PLD** films are mainly (11-20) and (11-21) oriented independently of the oxygen pressure (basically, the *c*-axis texture is completely suppressed comparing to the MOCVD films).
- Cell parameters

- Large variations in the cell parameter values are produced by the variation of the Y/Mn ratio in the film (both XRD and Raman are sensitive to these variations). As a consequence the h-YMO phase can be grown in a large range of non-stoichiometry.

- Microstructure
  - The **MOCVD** h-YMO films present a columnar growth, which is typical for the MOCVD process with grain diameter between 20-40 nm.
  - The **PLD** growth produces dense grains, mainly polygonal-shaped, between 90-150 nm in size
  - An amorphous layer (10-50 nm) forms between the h-YMO films and the Si substrate independently of the temperature or Y/Mn ratio.
- Magnetism
  - A spin-glass behavior characterized by a splitting of the ZFC-FC curve and a maximum in the ZFC curve at T_f=20 K was observed for the h-YMO films. A weak ferromagnetic contribution is present at 5 K in the M(H) curve. A splitting of the ZFC-FC curves was observed for polycrystalline powders at ~ 65 ($Y_1Mn_1O_3$) and 70 K ($Y_{0.95}Mn_1O_3$), without maximum in the ZFC. On the contrary, the h-YMO single crystal shows in both M(T) and M(H) curves a pure antiferromagnetic ordering at T_N=70 K.

4.3 Characterization of orthorhombic as-deposited YMO films

This part describes the structural characterizations of the o-YMO films grown on (100)-oriented Si substrates by PI-MOCVD and PLD. They confirm that two parameters are important in the stabilization of the o-YMO phase on Si substrates: the temperature in the case of the PI-MOCVD and the O_2 pressure in the case of PLD.

4.3.1 o-YMO films elaborated by PI-MOCVD

A detailed structural analysis will be presented for two films deposited with the optimized MOCVD parameters (horizontal device) as follows:

- a film deposited at T = 750°C, Y/Mn = 1 (hereafter YMO-750-1)
- a film deposited at T = 750°C, Y/Mn = 1.4 (hereafter YMO-750-1.4).

The XRD patterns of the o-YMO films are shown in Figure IV.24. They clearly indicate that the o-YMO phase is present, as far as XRD is concerned, but the presence of amorphous or nanocrystalline phases cannot be ruled out (see next paragraphs for TEM results). They also indicate that the o-YMO film grows on the Si substrate without any particular orientation, having the characteristics of a polycrystalline powder (see phase indexation). This confirms the importance of the temperature as the main parameter for selective growth mechanism when using PI-MOCVD.

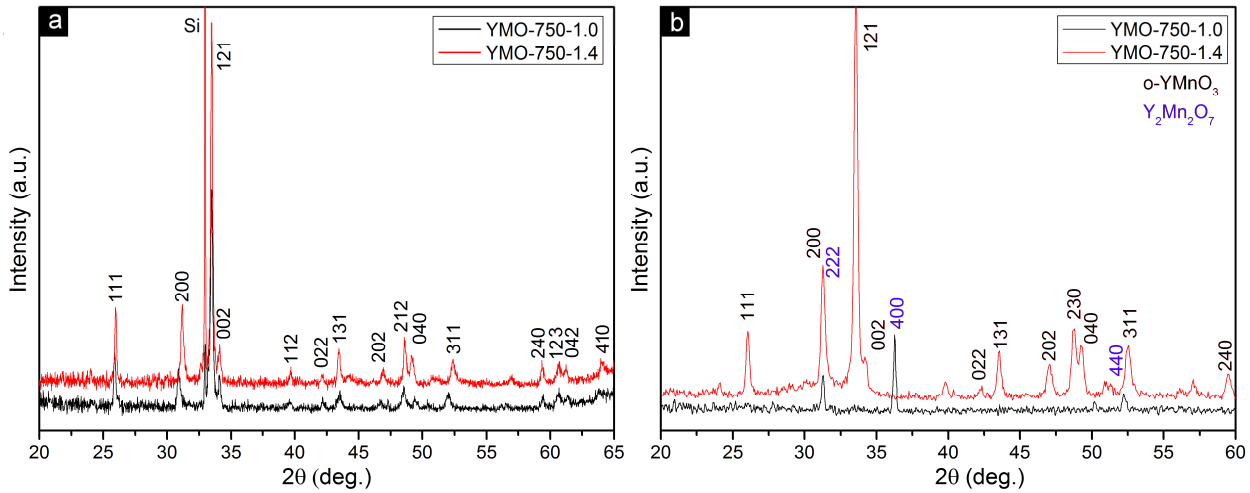

Figure IV.24. XRD patterns of o-YMO films: YMO-750-1 (black line) and YMO-750-1.4 (red line): a) θ-2θ patterns indexed with the o-YMO phase; b) GIXRD patterns indexed with the $Y_2Mn_2O_7$ phase for the YMO-750-1 film and with o-YMO phase for the YMO-750-1.4 film.

In addition to θ-2θ scans, corresponding GIXRD patterns are shown in Figure IV.24b. The patterns of the two samples are very different: the YMO-750-1.4 film contains only the o-YMO phase, while the YMO-750-1 film exhibits only the $Y_2Mn_2O_7$ pyrochlore phase. Since this phase appears only in the GIXRD pattern, it can be assumed that it is found in a too small quantity to be detectable by classical θ-2θ geometry and/or it is not in a Bragg diffraction position. No clear explanation is found for this point (a possible problem of texture may be inferred). It is interesting to note that $Y_2Mn_2O_7$ phase is metastable under normal synthesis conditions. The formation of the $Y_2Mn_2O_7$ was reported by several authors (Chen et. al. [25], Fujinaka et al. [26] and Subramanian et al. [27]) under high oxygen pressure (3–4 GPa) and at high temperatures (1000–1100 °C) or under hydrothermal conditions. These authors claim that after heating this phase at 900 °C, it decomposes into $YMnO_3$.

Sample	**Composition**	**a [Å]**	**b [Å]**	**c [Å]**
JCPDS 16-1775	$YMnO_3$	5.8361	7.3571	5.2580
YMO-750-1	$Y_{0.82}Mn_1O_{2.39}$	5.780(2)	7.375(3)	5.253(4)
YMO-750-1.4	$Y_{1.24}Mn_1O_{3.20}$	5.732(2)	7.402(4)	5.252(3)

Table IV.7. XRD lattice parameters of o-YMO films compared to a reference bulk sample (JCPDS card)

The film lattice parameters obtained from the XRD pattern (*Pnma* setting) shown in Table IV.7 present differences when compared to a powder diffraction standard (JCPDS card No. 16-1775 stoichiometric o-YMO phase), mainly on the *a* and *b* lattice parameters. This can be due to differences in sample composition but further comparison is not possible because of the scarce data in the literature and the presence of the amorphous interfacial layer (and $Y_2Mn_2O_7$) which prevents the precise determination of the o-YMO phase composition in our films. The EPMA measurement provides an average chemical formula of $Y_{0.82}Mn_1O_{2.39}$ for the YMO-750-1 film and of $Y_{1.24}Mn_1O_{3.20}$ for the YMO-750-1.4 film (atomic values are normalized such that Mn atomic ratio is 1). Note that the compositions given in Table IV.7 correspond to the average composition of the films, including the amorphous interfacial layer and the $Y_2Mn_2O_7$ phase (see details in next paragraphs for TEM results).

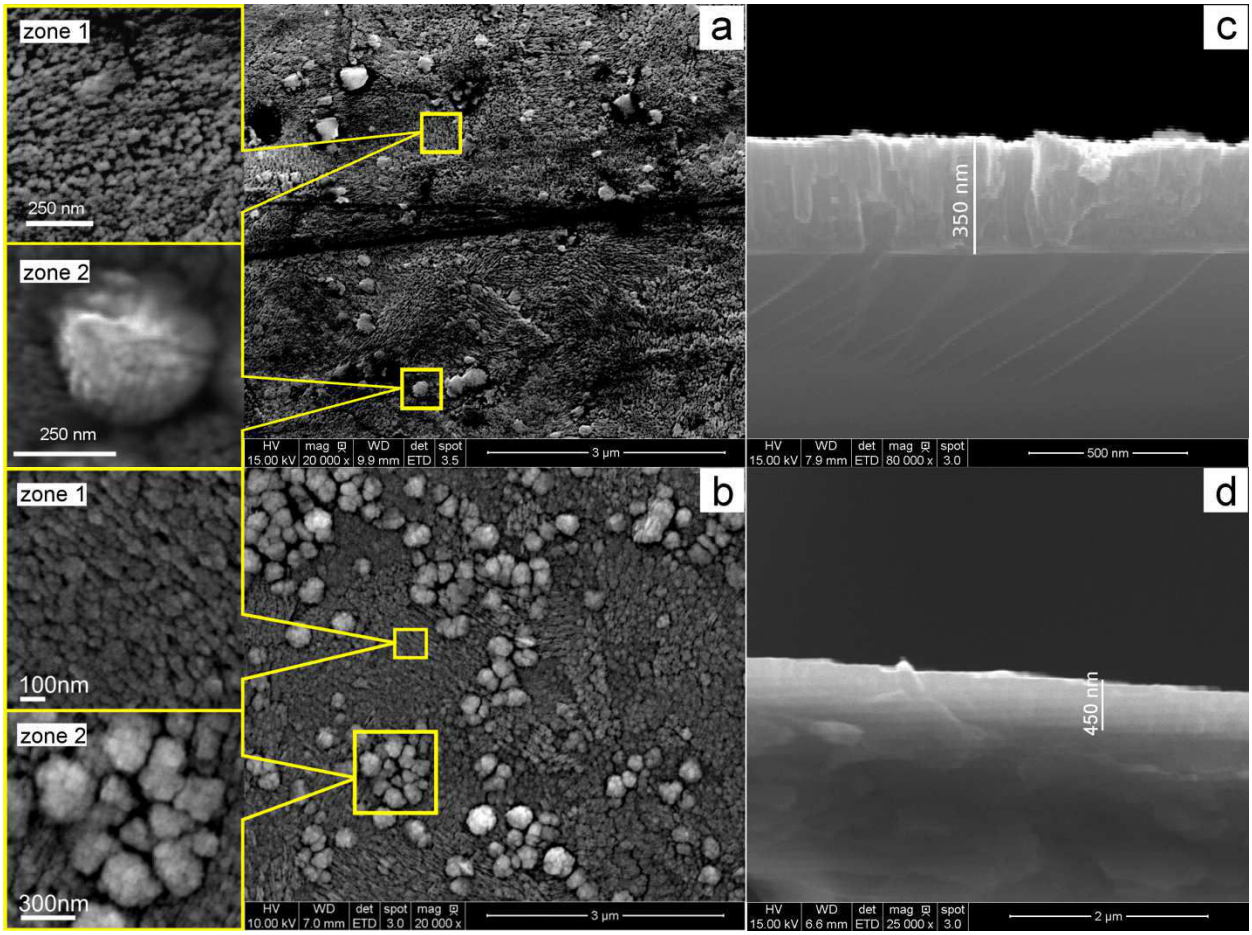

Figure IV.25. Top view SEM images of: a) YMO-750-1 film; b) YMO-750-1.4 film. Two types of morphologies can be identified: columnar (zone 1 in (a) and (b)) and dendritic-like (zone 2 in (a) and (b)). Cross-section SEM images of c) YMO-750-1 film; d) YMO-750-1.4 film.

The top-view scanning electron microscopy (SEM) micrographs of the o-YMO films are shown in Figure IV.25a and b. For both films, the images display a dense structure with two types of morphology: one corresponds to columnar grains (zone 1 in Figure IV.25a and b) and the other to dendritic aggregates of grains (zone 2 in Figure IV.25a and b). They indicate two different growing modes: columnar and dendritic, similar to the h-YMO films presented in section 4.2. The column (individual grain) diameter is around 30 nm, while the total diameter of the aggregates ranges between 200 and 400 nm. Cross-section SEM images (Figure IV.25c and d) show a thickness of 350 nm (resp. 450 nm) for the YMO-750-1 (resp. YMO-750-1.4) films. No difference in the chemical composition was observed for these two morphologies, indicating that they correspond to the same o-YMO phase.

Further microstructural characterizations using TEM were carried out on the cross-section of the YMO films. The corresponding images are presented in Figures IV.26-28 (YMO-750-1) and Figure IV.29 (YMO-750-1.4) and are discussed separately.

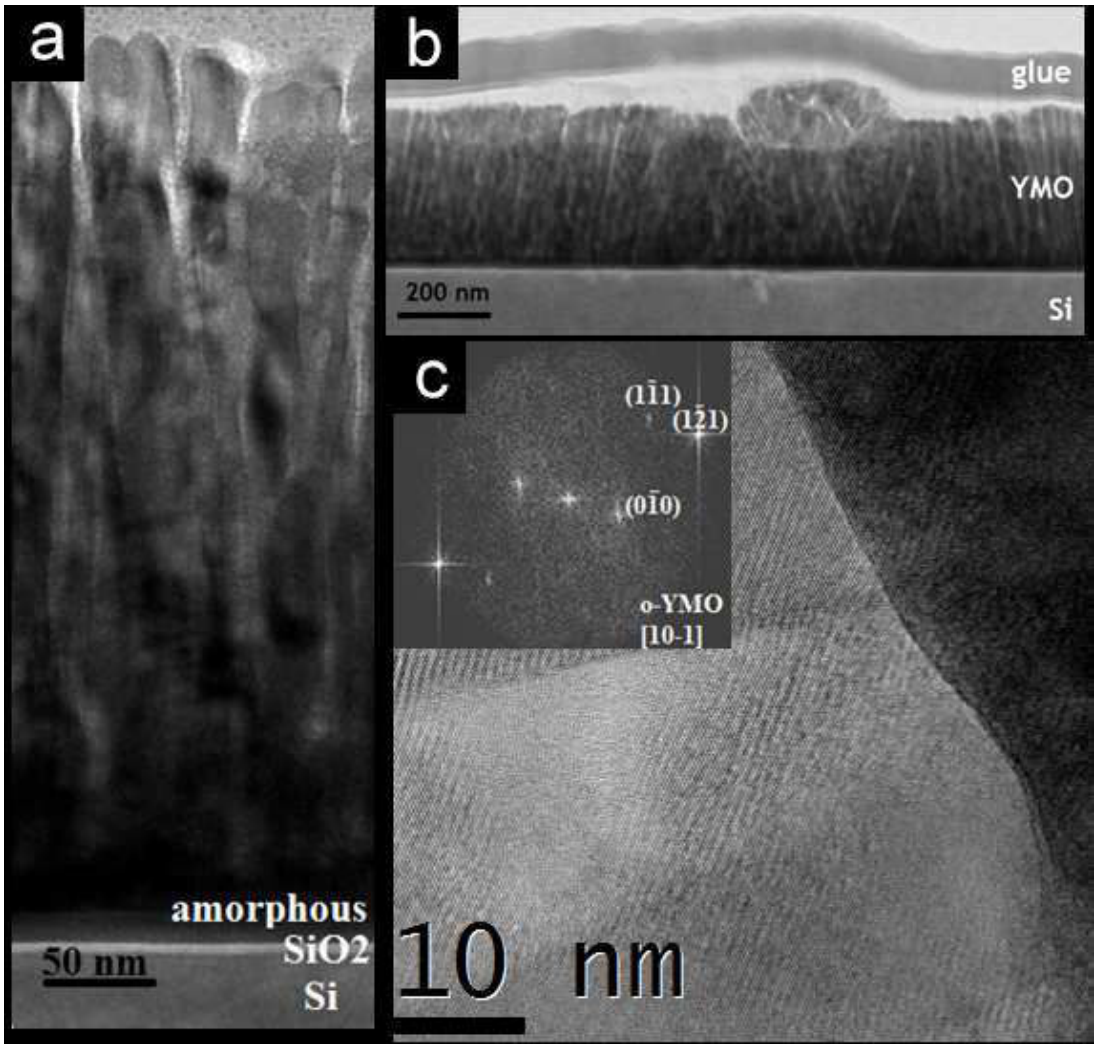

Figure IV.26. Cross section TEM observations for YMO-750-1 film: a) medium resolution image showing the different layers on top of the Si substrate and the columnar growth morphology b) low resolution image showing the general aspect of the film with two types of morphologies; c) high resolution image of an enlarged region of a) and the associated FFT (inset) indicating the same growing orientation for two neighboring columns corresponding to o-YMO [10-1] zone axis.

YMO-750-1 film

From the medium and low resolution TEM images in Figure IV.26a and b, it can be observed a columnar growth of the YMO film, in agreement with the previous morphological results

obtained by SEM. The diameter of the columns ranges between 20 nm and 30 nm and corresponds to the small grains observed by SEM in zone 1 of Figure IV.25a. In addition, grain aggregates of around 300 nm in diameter, are observed on the top part of the film, near its surface. This corresponds to the morphology shown in zone 2 of Figure IV.25a.

Three different layers on top of the Si substrate are observed in Figure IV.26a, identified as follows: the upper layer (~ 350 nm thick) corresponds to the crystalline o-YMO films grown in the form of columns. The intermediate layer (~10 nm thick) is amorphous and is observed between the columnar YMO film (top layer) and the bottom layer represented by the native amorphous SiO_x (5 nm thick). As for the h-YMO films, this layer forms as a compensation mechanism of the non-stoichiometry in the o-YMO film.

The columnar grains of the o-YMO phase shown in Figure IV.26a and b can present similar (preferential) orientation. An example of preferential orientation is shown in Figure IV.26c corresponding to an enlarged region of Figure IV.26a. From the fast Fourier transform of the crystalline zone (inset of Figure IV.26c), we have deduced that the adjacent columns are composed of o-YMO phase with similar zone axis [10-1] (*Pnma* setting). The {121} planes are shown by the black/white contrast in Figure IV.23c. The interplanar spacing d_{121} measured on the high resolution TEM image is 2.67 Å, which is close to the theoretical bulk value (2.678 Å) and to XRD measure (2.668(4) Å). The value of $b_{o\text{-}YMO}$ (deduced from the FFT of Figure IV.26c) is equal to 7.350(1) Å, also close to the theoretical bulk value ($b_{o\text{-}YMO}$ =7.357 Å) and to the measured XRD value (7.375(3) Å).

These observations by HRTEM images showing that, on small regions, the grains have in general the same orientation, are in agreement with the regular arrangements of columns seen in the SEM images (zone 1 Figure IV.25a).

A close look at the interface between two adjacent columns (Figure IV.27a and b) shows the presence of small misorientations. The same atomic planes observed on two or more columns can have misalignments ranging from a few degrees (see Figure IV.27a) to tens of degrees (see Figure IV.27b).

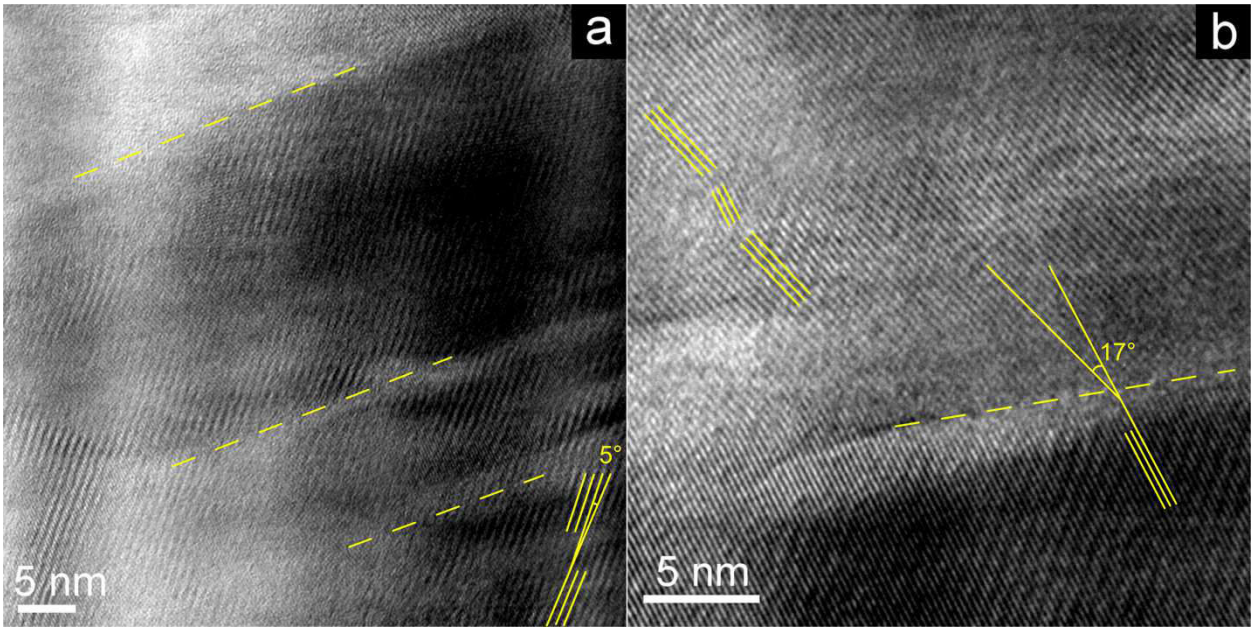

Figure IV.27. High-resolution transmission electron microscopy image of o-YMO columns showing different misalignments between neighboring columns.

These results were additionally characterized by bright-field and dark-field TEM images, shown in Figure IV.28. The SAED image (inset of Figure IV.28a) displays the selected beam for the resultant image: the direct beam is used to form the bright-field image, while a diffracted beam is needed to form the dark-field image. Both selected spots are shown surrounded by red circles. The diffraction spot corresponds to (121) planes. Thus, the dark-field image from Figure IV.28a reveals all reflections of {121} planes coming from several grains, which appear as white areas. It is seen that on regions of about 100 nm the grains have the same 121-orientation. However, it seems that this orientation is not maintained all along the film section. Grains with different textures are found at the film-substrate interface. Isolated regions of 121-orientation are spread within the film. This confirms that the film is polycrystalline in average, with nanoscale preferred-oriented zones, in agreement with previous SEM and TEM observations.

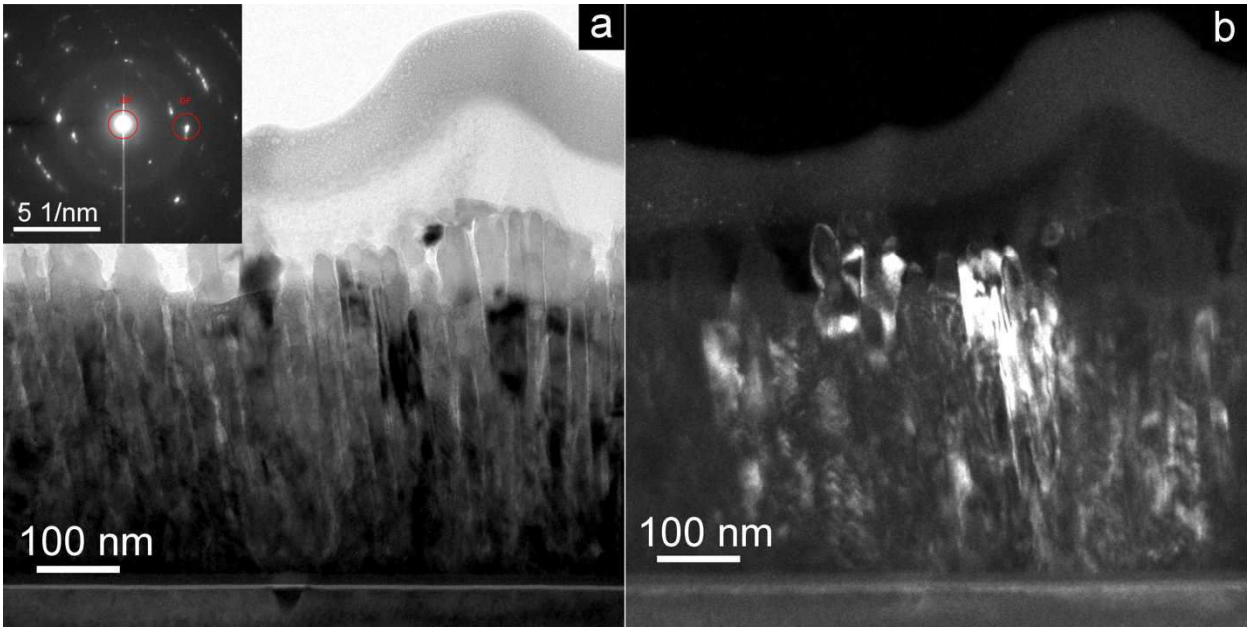

Figure IV.28. Cross section TEM images of YMO-750-1 film: a) dark field mode; b) bright field mode. Inset: Corresponding SAED pattern showing the transmitted beam and the 121 reflection.

In the bright-field image from Figure IV.28b, thick areas appear with dark contrast. It is observed that the film is thicker at the interface, while it is thin near the surface. This effect is due to the sample preparation, and in particular to the ion milling.

No observation of the $Y_2Mn_2O_7$ phase could be made from the TEM images, but this is probably because the analyzed regions are limited and, in addition, the presence of this phase is scarce.

YMO-750-1.4 film

The low magnification image of the YMO-750-1.4 film (Figure IV.29a) shows three different layers on top of the Si. From top to bottom the layers in Figure IV.29a can be identified as follows: the top layer (~450 nm thick) corresponds to the crystalline o-YMO films grown in the form of columns (dashed lines are given as guide for the eye), in agreement with the previous morphological results obtained by SEM. An intermediate amorphous layer (~10 nm thick) is observed between the columnar YMO film (top layer) and the native amorphous Si oxide of the Si substrate (bottom layer) which is 4 nm thick. A typical SAED pattern of the o-YMO film is shown in Figure IV.29b. One can clearly identify the regular array of intense reflections originating from the Si substrate (highlighted by yellow rhombus in the figure). In addition, less intense reflections originating from the columnar grains of o-YMO film are seen in Figure IV.29b. These reflections appear to be distributed along certain circles corresponding to a

polycrystalline o-YMO phase. Even if the intensity does not form a continuous and homogeneous distribution along each circle – as expected for completely randomly oriented distribution – it has a particular arrangement indicating several different orientations of the grains (white arcs in Figure IV.29b).

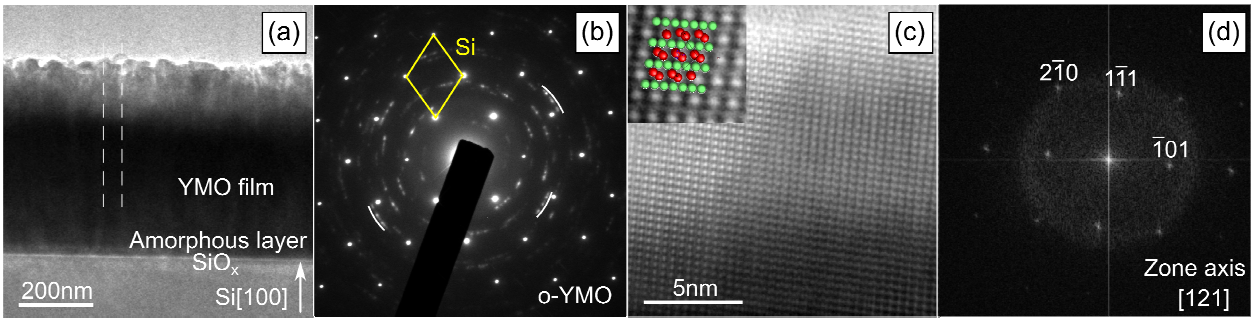

Figure IV.29. TEM results of the o-YMO film deposited by MOCVD: a) low magnification cross-section image showing three different layers on top of the Si substrate; b) SAED pattern of a region of (a) containing several columnar grains and the Si substrate; c) HRTEM image of the o-YMO film in a particular [121]-zone axis orientation. In the inset an enlargement overlapped with the structure simulation; d) FFT of the HRTEM image from (c) showing that the orientation corresponds to [121]-zone axis.

The HRTEM image of a columnar grain with a particular orientation (corresponding to [121]-zone axis) is shown in Figure IV.29c and its enlargement is represented in the inset. The projected structure (according to [28]) along the [121]-zone axis superimposed to the image in this inset shows a good agreement between the HRTEM image and the arrangements of Y (red) and Mn (green) atoms derived from the structural model : the most intense white dots superimpose with Y atoms. The fast Fourier transform (FFT) image of Figure IV.29c shown in Figure IV.29d indicates that the grain orientation is such that $[1\text{-}11]_{o\text{-}YMO}$ is almost parallel to the $[100]_{Si}$ (vertical direction in the figure).

Complementary structural characterizations have been carried out by Raman spectroscopy. According to [16], there are 24 active Raman modes ($7A_g + 5B_1g + 7B_{2g} + 5B_{3g}$) for the o-YMO (*Pnma* group) among which the most intense are given in Table IV.8. The position of the Raman modes of both o-YMO films (see Figure IV.30) are in good agreement with the reference values reported for powder o-YMO [16] and only small shifts are observed. These shifts are due to the non-stoichiometry of the films.

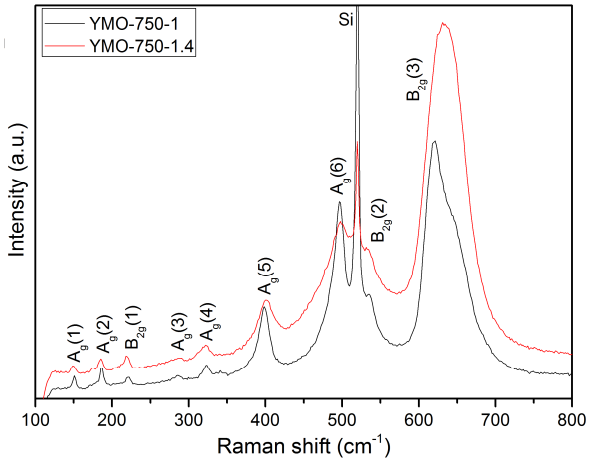

Figure IV. 30. Raman spectra of the o-YMO phase for YMO-750-1 and YMO-750-1.4 films.

Mode	Assignment	YMO-750-1	YMO-750-1.4	Iliev et al. [16]
A_g(1)	x(Y)	150.8	149.3	151
A_g(2)	z(Y)	186.4	185.2	188
B_{2g}(1)	x(Y)	220.7	219.3	220
A_g(3)	Rot. y(MnO_6)	285.5	288.1	288
A_g(4)	x(O1)	323.1	321.3	323
A_g(5)	Rot. x(MnO_6)	398.6	401.0	396
A_g(6)	Bend(MnO_6)	497.0	499.0	497
B_{2g}(2)	Bend(MnO_6)	534.9	532.5	537
B_{2g}(3)	Strec. xz(MnO_6)	620*	618*	616
?		652*	651*	653

Table IV.8. Wavenumbers of the o-YMO Raman modes for YMO-750-1 and YMO-750-1.4 films and for a ceramic pellet reference. The A_g and B_{2g} modes are numbered following their order of appearance with increasing wavenumbers in the spectrum (uncertain values due to the modes overlapping).*

4.3.2 o-YMO films elaborated by PLD

A representative o-YMO film grown by PLD on Si(100) substrate (at 800 °C and P_{O2}=0.3 bar) was chosen for the following characterizations.

Figure IV.31 shows the θ-2θ XRD and GIXRD scans. Both patterns show only the peaks of the o-YMO phase. No reflections of other phases were detected. The XRD peaks of the o-YMO phase and their intensity suggest that the film has the characteristic of an almost randomly oriented polycrystalline sample. The cell parameters derived from both XRD techniques

(*a*=5.791(3) Å, *b*=7.338(4) Å, *c*=5.2370(4) Å) are in relatively good agreement with those reported in the JCPDS card No. 16-1775, although differences exist mainly when comparing the *a* parameter.

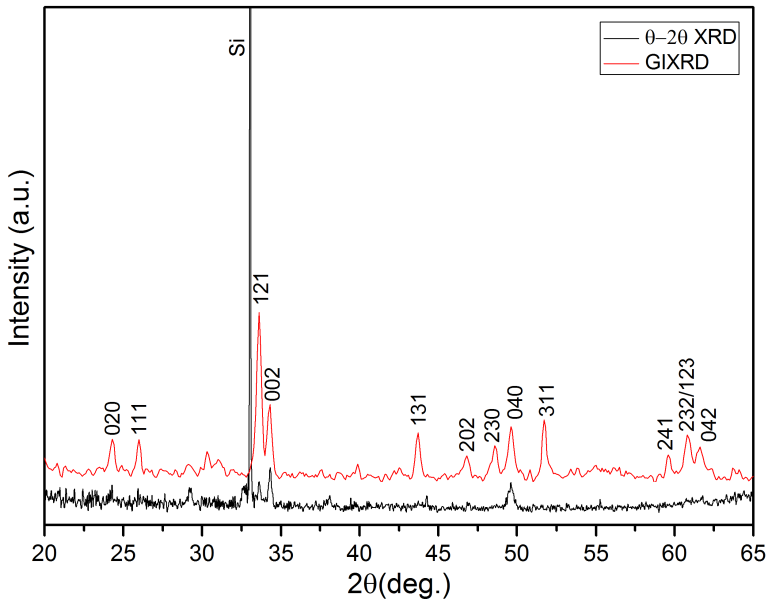

Figure IV.31. θ-2θ XRD (black line) and GIXRD (red line) patterns of the o-YMO film grown by PLD (P_{O2}=0.3 bar, T=800 °C).

A top-view SEM image of the o-YMO film grown on Si substrate is shown in Figure IV.32.

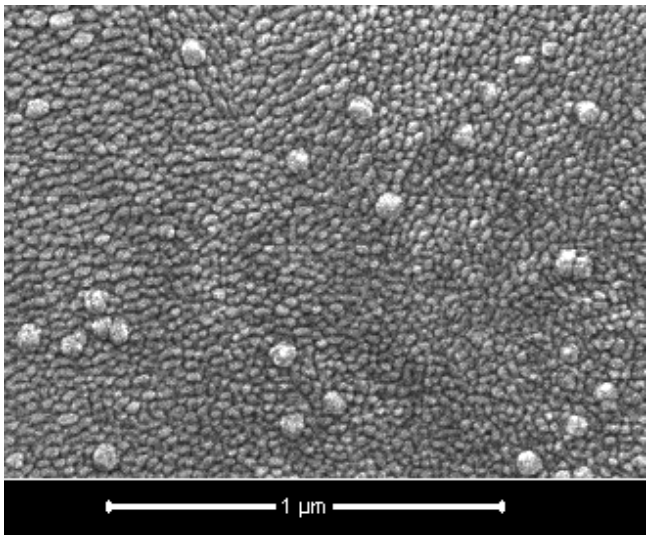

Figure IV.32. Top-view SEM image (secondary electrons) of the o-YMO film deposited on Si(100) by PLD. Two types of morphologies can be identified: granular and dendritic-like.

As in the case of o-YMO films elaborated by MOCVD (Figure IV.25), two types of morphologies can be identified: granular and dendritic-like. The grains are around 20-30 nm in diameter while the aggregates are ranging between 65 and 75 nm. The 20-30 nm grains may be related to a columnar growth, but without further cross-section SEM or TEM observation, it cannot be confirmed. The chemical composition measured by EDX gives the formula $Y_{1.36}Mn_1O_{3.11}$. Similarly to the MOCVD YMO films, an intermediate amorphous layer between the film and the Si substrate is expected. Complementary TEM observations are needed to clarify this issue. Finally, the Raman results confirm the presence of the o-YMO phase. A typical Raman spectra of this o-YMO film is presented in Figure IV.33. All experimental peaks can be assigned to the modes of the o-YMO phase and the modes of the Si substrate, which were used to calibrate the spectrum (the Si mode at 520 cm^{-1} was the reference). The line positions of the o-YMO phase are indicated on the graph. They match very well with those reported by Iliev et al. [16] for a ceramic pellet.

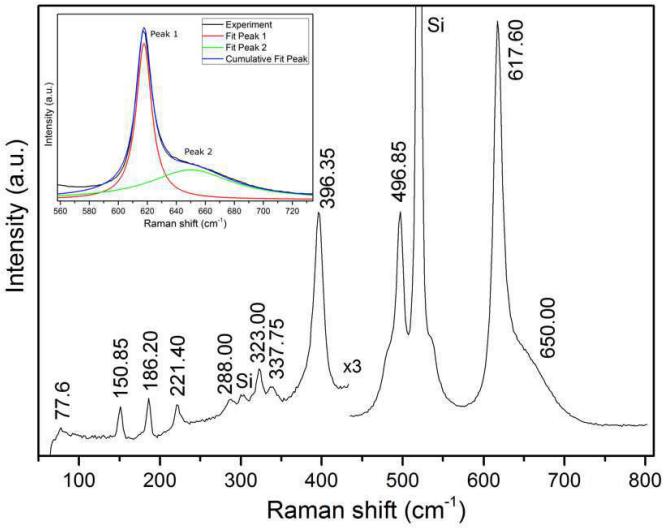

Figure IV.33. Raman spectra of o-YMO film elaborated by PLD. The left part of the spectrum was multiplied by 3 in order to have a better visibility when comparted with the right part. Inset: in red, respectively green, the Lorentzian line shapes used to fit the B_{2g} and "650 cm^{-1}" modes. In blue, the resulting fit.

Experimental Raman peaks are fitted using Lorentzian profiles. The peak positions, the full width at half maximum (FWHM), the peak area and the baseline are the free varying parameters. Inset of Figure IV.33 shows an example of such a fit, in the 560-730 cm^{-1} range. A perfect

agreement between the experimental (in black) and simulated (in blue) spectrum has been achieved. The fitted values are displayed in Table IV.9.

	Peak 1	**Peak 2**
Peak center (cm^{-1})	617.60	650.00
FWHM (cm^{-1})	13	70
Area	375305	383558
Background (counts)	600	600

Table IV.9. Simulated Lorentzian peak parameters for the experimental Raman spectrum in the 560-730 cm^{-1} range.

4.3.3 Magnetic characterization of o-YMO films

Figure IV.34a shows the M(T) curves for the o-YMO film (sample YMO-750-1.4). A splitting of the ZFC-FC curves, with a maximum in the ZFC curve at the freezing temperature T_f= 20 K, indicates a spin glass-like behavior. Previous reports show the existence of a similar spin-glass state for either bulk [29] or film [30] o-YMO phase, although different freezing temperatures are reported (11 K and 40 K). As shown in the Figure IV.34b, a linear variation in the M(H) curve is observed at room temperature, as expected for a paramagnetic behavior. At low temperature, a small hysteresis loop is observed in the inset of Figure IV.34b, indicating an additional weak ferromagnetic contribution.

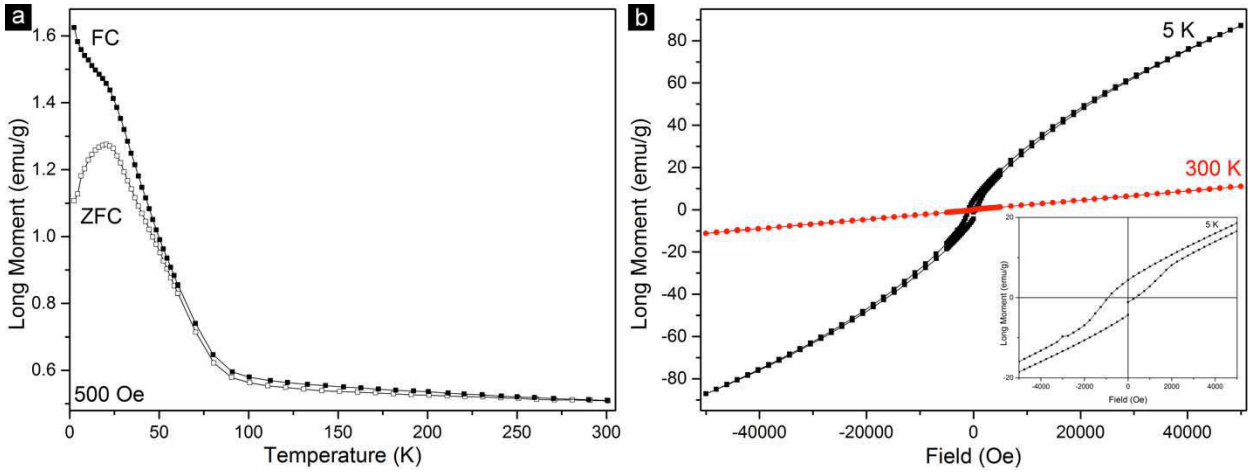

Figure IV.34. Temperature dependence of the magnetization (M(T)) for YMO-750-1.4 film. Open (solid) symbols represent the M(T) taken in the ZFC (FC) mode; b) Field dependence of the magnetization (M(H)) at 5 and 300 K. Inset: enlargement of the M(H) curve in the low magnetization values.

Summary

o-YMO films have been grown on Si(100) substrate by both **MOCVD** and **PLD** techniques without any strain stabilization mechanism and free of the h-YMO phase ($Y_2Mn_2O_7$ secondary phase was obtained due to the nonstoichiometry of the precursor solution).

The main characterization results of the o-YMO films, grown by **MOCVD** or **PLD** are the following:

- Orientation
  - The films are mainly polycrystalline.
  - Regions of textured grains are observed at nanometrical scale by top view SEM.
- Cell parameters
  - Some variations in the cell parameter values are produced by the variations of the Y/Mn ratio in the **MOCVD** film and of the PO_2 in the **PLD** film: from 5.732 to 5.791 Å for *a*, from 7.338 to 7.402 Å for *b* and from 5.237 to 5.253 Å for *c*. As a consequence the o-YMO phase can be grown in a relatively large range of non-stoichiometry.
- Microstructure
  - A columnar growth is observed for the **MOCVD** o-YMO films with columns between 15-30 nm and aggregates ranging from 200 to 400 nm. Similarly, the **PLD** growth produces grains of 20-30 nm in size and aggregates of grains between 65 and 75 nm.
  - An amorphous layer of about 10 nm is formed at the o-YMO film-Si substrate interface independently of the **MOCVD** initial Y/Mn composition.
- Magnetism
  - Magnetic measurements indicate a spin-glass behavior, characterized by a splitting of the ZFC-FC curves, with a maximum in the ZFC curve at T_f= 20 K. A weak ferromagnetic contribution is observed at 5 K.

4.4 Summary and conclusions

To remind the reader the conclusions derived from each section, we reproduce below the individual summaries:

4.1 Characterization of amorphous as-deposited films:

The YMO films deposited at 600°C are amorphous, indicating that the amorphous phase is easily formed and stable for the **MOCVD** growing conditions in a large range of compositions. This phase forms prior to the crystallization of either o-YMO or h-YMO phases even if appropriate substrates (STO, LAO, GaN) would favor the crystalline phases [5], [6]. Furthermore, the formation of the amorphous YMO phase is independent of the synthesis method, initial composition of the precursors or oxygen pressure.

The as-deposited MOCVD films follow a 3D columnar growth mode with columns diameter between 15 and 20 nm and a cauliflower-like morphology. The Raman spectra present only a large mode at around 650 cm^{-1}. The magnetization measurements suggest a spin-glass behavior with a maximum in the ZFC curve between 11 and 19 K.

4.2 Characterization of hexagonal as-deposited YMO films

The h-YMO films, grown by **MOCVD** or **PLD** have been characterized by several techniques and the following characteristics are resulting:

- Orientation:
  - the **MOCVD** films are mainly *c*-axis textured, strongly influenced by the deposition temperature and to a minor extent by the Y/Mn ratio in the solution
  - the **PLD** films are mainly [11-20] and [11-21] oriented independent of the oxygen pressure (basically, the *c*-axis texture is completely suppressed comparing to the MOCVD films).
- Cell parameters
  - Large variations in the cell parameter values are produced by the variation of the Y/Mn ratio in the film (both XRD and Raman are sensitive to these variations). As a consequence the h-YMO phase can be grown in a large range of non-stoichiometry.
- Microstructure
  - The **MOCVD** h-YMO films present a columnar growth, which is typical for the MOCVD process with grain diameter between 20-40 nm.
  - The **PLD** growth produces dense grains, mainly polygonal-shaped, between 90-150 nm in size
  - An amorphous layer (10-50 nm) forms between the h-YMO films and the Si substrate independent of the temperature or Y/Mn ratio.
- Magnetism

- A spin-glass behavior characterized by a splitting of the ZFC-FC curve and a maximum in the ZFC curve at T_f=20 K was observed for the h-YMO films. A weak ferromagnetic contribution is present at 5 K in the M(H) curve. A splitting of the ZFC-FC curves was observed for polycrystalline powders at ~ 65 ($Y_1Mn_1O_3$) and 70 K ($Y_{0.95}Mn_1O_3$), without maximum in the ZFC. On the contrary, the h-YMO single crystal shows in both M(T) and M(H) curves a pure antiferromagnetic ordering at T_N=70 K.

4.3 Characterization of orthorhombic as-deposited YMO films

o-YMO films have been grown on Si(100) substrate by both **MOCVD** and **PLD** techniques without any strain stabilization mechanism and free of the h-YMO phase ($Y_2Mn_2O_7$ secondary phase was obtained due to the nonstoichiometry of the precursor solution).

The main characterization results of the o-YMO films, grown by **MOCVD** or **PLD** are the following:

- Orientation
  - The films are mainly polycrystalline.
  - Regions of textured grains are observed at nanometrical scale by top view SEM.
- Cell parameters
  - Some variations in the cell parameter values are produced by the variation of the Y/Mn ratio in the film (**MOCVD**) and P_{O2} (**PLD**): from 5.732 to 5.791 Å for *a*, from 7.338 to 7.402 Å for *b* and from 5.237 to 5.253 Å for *c*. As a consequence the o-YMO phase can be grown in a relatively large range of non-stoichiometry.
- Microstructure
  - A columnar growth is observed for the **MOCVD** o-YMO films with columns between 15-30 nm and aggregates ranging from 200 to 400 nm. Similarly, the **PLD** growth produces grains of 20-30 nm in size and aggregates of grains between 65 and 75 nm.
  - An amorphous layer of about 10 nm is formed at the o-YMO film-Si substrate interface independently of the **MOCVD** initial Y/Mn composition.
- Magnetism
  - Magnetic measurements indicate a spin-glass behavior, characterized by a splitting of the ZFC-FC curves, with a maximum in the ZFC curve at T_f= 20 K. A weak ferromagnetic contribution is observed at 5 K.

References

1. Kim, D., et al., *C-Axis Oriented MOCVD YMnO3 Thin Film and Its Electrical Characteristics in MFIS FeTRAM.* Integrated Ferroelectrics, 2004. **68**(1): p. 75-84.
2. Choi, T., et al., *Ferroelectric Bi Modified YMnO3 Thin Films Grown on Si(001) Using Y2O3 Buffer Layer for Metal-Ferroelectric-Insulator-Semiconductor Structure.* Integrated Ferroelectrics, 2002. **45**(1): p. 23-29.
3. Zhou, L., et al., *Structure and ferroelectric properties of ferroelectromagnetic YMnO3 thin films prepared by pulsed laser depositon.* physica status solidi (a), 2004. **201**(3): p. 497-501.
4. Kim, Y.T., et al., *Atomic structure of random and c-axis oriented YMnO3 thin films deposited on Si and Y2O3/Si substrates.* Journal of Applied Physics, 2003. **94**(8): p. 4859-4862.
5. Balasubramanian, K.R., et al., *Growth and structural investigations of epitaxial hexagonal YMnO3 thin films deposited on wurtzite GaN(001) substrates.* Thin Solid Films, 2006. **515**(4): p. 1807-1813.
6. Uusi-Esko, K., J. Malm, and M. Karppinen, *Atomic Layer Deposition of Hexagonal and Orthorhombic YMnO3 Thin Films.* Chemistry of Materials, 2009. **21**(23): p. 5691-5694.
7. Alqat, A., et al., *Synthesis of hexagonal YMnO3 from precursor obtained by the glycine–nitrate process.* Ceramics International, 2013. **39**(3): p. 3183-3188.
8. Muneeswaran, M., C. Mascovani, and N.V. Giridharan, *Structural and multiferroic properties of YMnO3 ceramics synthesized by co-precipitation method.* AIP Conference Proceedings, 2013. **1512**(1): p. 1270-1271.
9. Shin Nakamura, S.S., Naoshi lkeda, Midori Tanaka, *Spin-glass behavior in amorphous BiFeO3.* J. Appl. Phys. , 1993. **74**(9): p. 5652-5657.
10. Jin, Z., et al., *Ultrafast dynamics of the Mn3+ d-d transition and spin-lattice interaction in YMnO3 film.* Applied Physics Letters, 2012. **100**(2): p. 021106-021106-4.
11. Chen, D.P., et al., *Oxygen-vacancy effect on structural, magnetic, and ferroelectric properties in multiferroic YMnO3 single crystals.* Journal of Applied Physics, 2012. **111**(7): p. -.
12. Overton, A.J., et al., *Influence of Topotactic Reduction on the Structure and Magnetism of the Multiferroic YMnO3.* Chemistry of Materials, 2009. **21**(20): p. 4940-4948.
13. Durand, C., et al., *Microstructure and electrical characterizations of yttrium oxide and yttrium silicate thin films deposited by pulsed liquid-injection plasma-enhanced metal-organic chemical vapor deposition.* Journal of Applied Physics, 2004. **96**(3): p. 1719-1729.
14. Yoo, D.C., et al., *Effects of post-annealing on the microstructure and ferroelectric properties of YMnO3 thin films on Si.* Journal of Crystal Growth, 2001. **233**(1–2): p. 243-247.
15. Malo, S., et al., *Structural and magnetic properties of the solid solution (0<x<1) YMn1−x(Cu3/4Mo1/4)xO3.* Solid State Sciences, 2005. **7**(12): p. 1492-1499.
16. Iliev, M.N., et al., *Raman spectroscopy of orthorhombic perovskitelike YMnO3 and LaMnO3* Physical Review B, 1998. **57**(5): p. 2872-2877.
17. Iliev, M.N., et al., *Raman- and infrared-active phonons in hexagonal YMnO3: Experiment and lattice-dynamical calculations.* Physical Review B, 1997. **56**(5): p. 2488-2494.

18. Fujimura, N., et al., *Multiferroic behaviour of YMnO3 and YbMnO3 epitaxial films.* Philosophical Magazine Letters, 2007. **87**(3-4): p. 193-201.
19. Liu, S.-H., et al., *Structural transformation and charge transfer induced ferroelectricity and magnetism in annealed YMnO3.* AIP Advances, 2011. **1**(3): p. -.
20. Van Aken, B.B., et al., *Asymmetry of electron and hole doping in YMnO3.* Physical Review B, 2001. **63**(12): p. 125127.
21. Katsufuji, T., et al., *Dielectric and magnetic anomalies and spin frustration in hexagonal RMnO3 (R =Y, Yb and Lu).* Physical Review B, 2001. **64**(10): p. 104419.
22. Sharma, P.A., et al., *Thermal Conductivity of Geometrically Frustrated, Ferroelectric YMnO3: Extraordinary Spin-Phonon Interactions.* Physical Review Letters, 2004. **93**(17): p. 177202.
23. Nugroho, A.A., et al., *Enhancing the magnetoelectric coupling inYMnO3 by Ga doping.* Physical Review B, 2007. **75**(17): p. 174435.
24. Wang, L., et al., *Composite structure and properties of Mn3O4/graphene oxide and Mn3O4/graphene.* Journal of Materials Chemistry A, 2013. **1**(29): p. 8385-8397.
25. Chen, M., B. Hallstedt, and L.J. Gauckler, *Thermodynamic assessment of the Mn–Y–O system.* Journal of Alloys and Compounds, 2005. **393**(1–2): p. 114-121.
26. H. Fujinaka, N.K., M. Koizumi, Y. Miyamoto, S. Kume, *Syntheses and physical properties of pyrochlore-type A2B2O7 (A=Tl,Y; B=Cr,Mn).* Mater. Res. Bull., 1979. **14**(9): p. 1133.
27. M. A. Subramanian, C.C.T., D. C. Johnson, J. Pannetier, A. W. Sleight *Ferromagnetic R2Mn207 Pyrochlores (R = Dy-Lu, Y).* Journal of Solid State Chemistry, 1988. **72**: p. 24-30.
28. Uusi-Esko, K., et al., *Characterization of RMnO3 (R = Sc, Y, Dy-Lu): High-pressure synthesized metastable perovskites and their hexagonal precursor phases.* Materials Chemistry and Physics, 2008. **112**(3): p. 1029-1034.
29. Muñoz, A., et al., *The magnetic structure of YMnO3 perovskite revisited.* Journal of Physics: Condensed Matter, 2002. **14**(12): p. 3285.
30. Li, S.Z., et al., *Preparation of epitaxial orthorhombic YMnO3 thin films and the current–voltage rectifying effect.* Applied Physics A, 2009. **94**(4): p. 975-980.

Chapter 5

Phase transformations and thermal stability studies in $YMnO_3$ films on Si (100) substrates

Summary

5.1 Phase transformations in amorphous as-deposited YMO films ……129
5.1.1 Ex-situ heat treatments on as-deposited amorphous YMO films ……129
5.1.2 In-situ Raman experiment on as-deposited amorphous YMO film ……..134
5.1.3 In-situ TEM experiment on as-deposited amorphous YMO film ……138
5.2 Stability of the as-deposited o-YMO phase ……140
5.2.1 In-situ Raman experiment on as-deposited o-YMO film ……140
5.3 Magnetic characterization ……..143
5.4 Discussion and summary ……..…….146
References ……...148

As we saw in the previous chapter, we have succeeded in stabilizing the o-YMO phase on Si substrate without a particular stabilization mechanism. We are now interested in the thermal stability of this phase. Therefore, this chapter covers the phase transformations and the stability of the o-YMO phase in the amorphous as-deposited films and o-YMO as-deposited films, respectively. In-situ and ex-situ experiments have been performed in order to investigate the transformation of amorphous as-deposited YMO films into the o-YMO phase and the behavior of the o-YMO film when increasing the temperature. Finally, the magnetic behavior before and after the heat treatments was investigated.

The structural changes resulted from the phase transformation have been studied by XRD, SEM, TEM and Raman spectroscopy. Three samples were analyzed for this purpose: they are labelled YMO-600-1 (T_s=600 °C and Y/Mn=1), YMO-600-1.4 (T_s=600 °C and Y/Mn=1.4) and YMO-750-1.4 (T_s=750 °C and Y/Mn=1.4). A detailed characterization of these samples was already presented in Chapter 4, section 4.1 and 4.2.1. We present here only the phase transformation and phase stability studies performed by various heat treatments. On the one hand, the films were subsequently heated (*ex-situ*) at different constant temperatures (750, 800, 850 and 900 °C) for a short period of time (1h) under air atmosphere in a muffle furnace. On the other hand, *in-situ* experiments were carried out as follows:

- Raman spectroscopy: a Linkam High Temperature Stage System (TS1500) was used in the temperature range RT – 1100 °C under an Ar flow (RT= room temperature). The temperature was increased in stages at a rate of 25 °C/min up to 600 °C and at 10 °C/min above this temperature. Each stage was maintained for 5 min before the measurement was done in order to achieve thermal stability. The data processing consisted in the fitting of each spectrum using Lorentzian profiles after the subtraction of the baseline in order to find the mode positions.
- TEM: the sample was heated by using the electron beam of the transmission electron microscope.

5.1 Phase transformations in amorphous as-deposited YMO films

5.1.1 Ex-situ heat treatments on as-deposited amorphous YMO films

As-deposited YMO-600-1 and YMO-600-1.4 films are characterized by an amorphous phase as demonstrated by the previous structural characterization results in Chapter 4:

-the XRD patterns of the films (Figure IV.1a) contain no diffraction lines except those of the Si substrate.

-the GIXRD pattern of the YMO-600-1 film (Figure IV.1b) contains a main broad peak characteristic of amorphous materials.

-the HRTEM image of the YMO-600-1.4 film (Figure IV.2) does not present any evidence of crystalline order; its SAED pattern is composed of circular halos characteristic of an amorphous phase.

- The Raman spectra (Figure IV.5a) of both films contain only a broad band partially superimposed on the Si Raman line.

During the film heating, the crystallization of the amorphous phase takes place; an estimation of the onset of the crystallization was obtained from XRD and SEM observations of the samples after each intermediate *ex-situ* heat treatment at 750, 800, 850 and 900 °C.

Figure V.1 compares the XRD patterns of the YMO-600-1 (Figure V.1a) and YMO-600-1.4 (Figure V.1b) films annealed at different temperatures in the 750-900°C range. The first clear diffraction peaks, indicating the crystallization, are observed at 750 °C for YMO-600-1 and at 800 °C for YMO-600-1.4. At 800 °C, both samples present rather similar XRD patterns corresponding mainly to the polycrystalline o-YMO phase (marked by full circles in Figure V.1) which remains stable up to 900 °C. This temperature was the highest tested in these *ex-situ* experiments. In addition to the formation of the o-YMO phase, a Si diffusion with the subsequent formation of a $Y_{4.67}(SiO_4)_3O$ phase (pointed by full squares in Figure V.1) was observed: in particular, an intense peak corresponding to the 200 reflection of the silicate phase emerges at $2\theta=21.5°$ for both samples after heating at 900 °C.

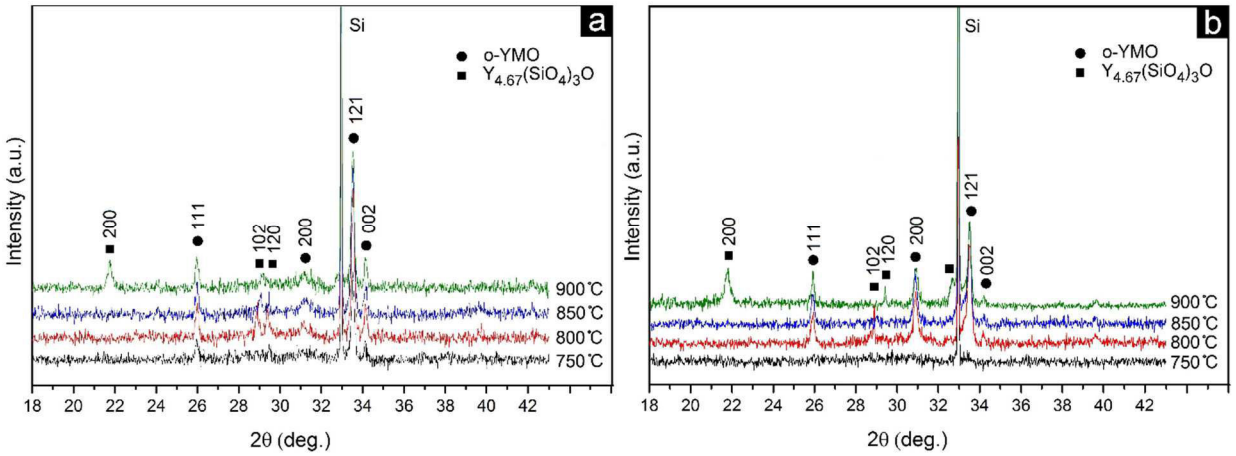

Figure V.1. XRD patterns of the annealed YMO-600-1 (a) and YMO-600-1.4 (b) films under air atmosphere for 1h at each step. The annealing temperature is indicated on each pattern.

The cell parameters calculated from the XRD reflections are: a=5.736(3) Å, b=7.376(4) Å, c=5.248(3) Å for the YMO-600-1 film and a=5.786(2) Å, b=7.360(4) Å, c=5.243(3) Å for the YMO-600-1.4 film after annealing at 900 °C. These parameters do not present significant changes during the annealings (see Figure V.1). This indicates that the o-YMO phase was formed in the first stages of annealing and it is stable during the temperature increase. The stability of the o-YMO phase was further confirmed in Figure V.2a which shows the temperature dependence of the $(121)_{o\text{-}YMO}$ reflection (the most intense in both XRD patterns). In the 750-900 °C temperature range

for the YMO-600-1 film and 800-900 °C for the YMO-600-1.4 film, the value of the interatomic distance d_{121} is constant and close to 2.670(3) Å and 2.672(3) Å, respectively, which is a bit lower than the bulk value (d_{121}=2.678 Å). The small difference between these distances and the bulk reference is due to a compositional effect (different Y/Mn ratio used). The correlation length (or crystallite size) calculated using the Scherrer formula for the (121) reflection at each temperature is represented in Figure V.2b. For both samples the crystallite size ranges from 50.5 to 52.5 nm. Compared with the as-deposited o-YMO film (YMO-750-1.4), the correlation length is smaller (~ 50 vs. 150 nm). When taking a closer look, we can see that these values increase slightly during the annealing process between 750 and 850°C, which indicates a small improvement of the film crystallinity. Then, between 850 and 900°C a decrease is observed, related to the observed silicate impurity and to the degradation of the morphology (see Figure V.3 below).

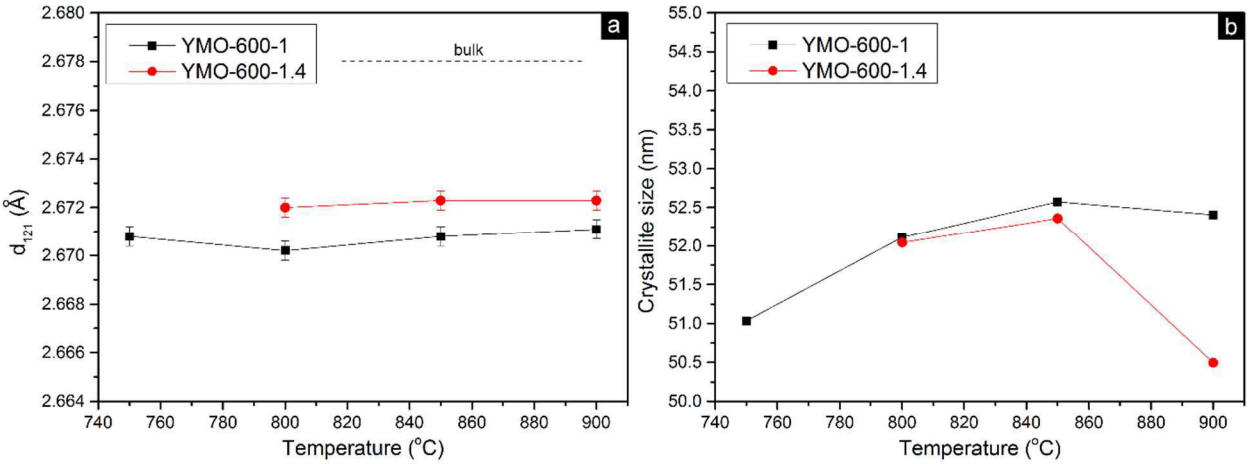

Figure V.2. Temperature dependence of a) the d_{121} distance and b) the crystallite size for the YMO-600-1 (in black) and YMO-600-1.4 (in red) films.

The SEM observations in Figure V.3 indicate more precisely that the crystallization has already started at 750 °C in both samples. Indeed, when compared to the as-deposited sample, they present new crystalline grains with larger sizes. They have grown radially around several nucleation centers spread over the films, resulting in the disk shape morphologies observed in the SEM images. These disks are around 2-2.5 µm in diameter and each individual crystal is 40-80 nm in width and 650-900 nm in length. The width of the individual crystals is in agreement with the crystallite size found by XRD. Almost no change in the disk shape is observed as the temperature increases indicating a quasi-complete transformation at 750 °C.

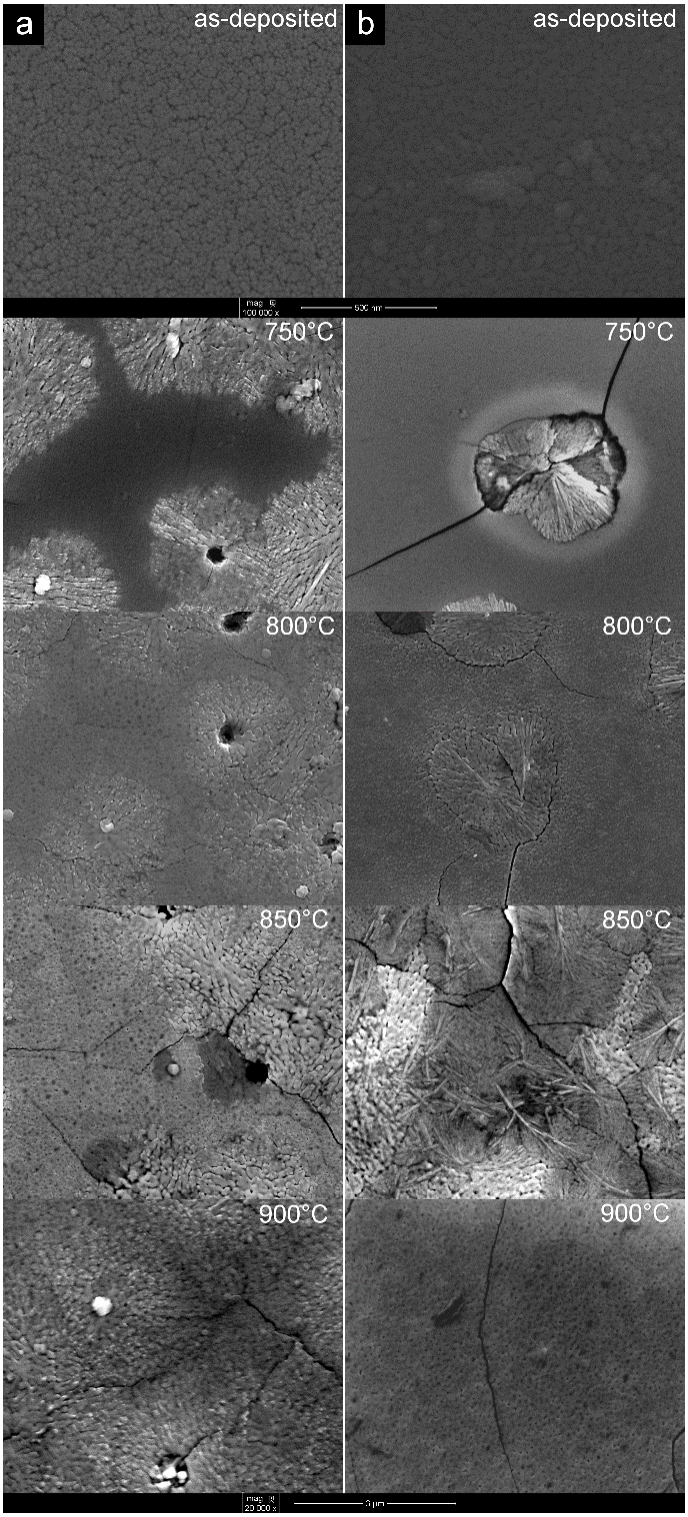

Figure V.3. SEM images showing the morphology evolution of the as-deposited films with annealing temperatures of 750 °C, 800 °C, 850 °C and 900 °C: YMO-600-1 (a) and YMO-600-1.4 (b).

Some minor changes are observed in-between the disks where crystals with similar sizes to those present in the disk are formed (see SEM observations at 800 °C). They probably correspond to crystals nucleating from a center located in the bulk of the film. At higher temperatures (850 and 900 °C), the surface is damaged and cracks appear in the films due to the thermal stress induced by the heat treatment. This fact and the presence of the $Y_{4.67}(SiO_4)_3O$ impurity phase identified by XRD prevent any further SEM analysis at 900 °C.

Complementary Raman measurements for the YMO-600-1 and YMO-600-1.4 films were made at room temperature, after the *ex-situ* annealings at 900°C under air atmosphere. The spectra are displayed in Figure V.4.

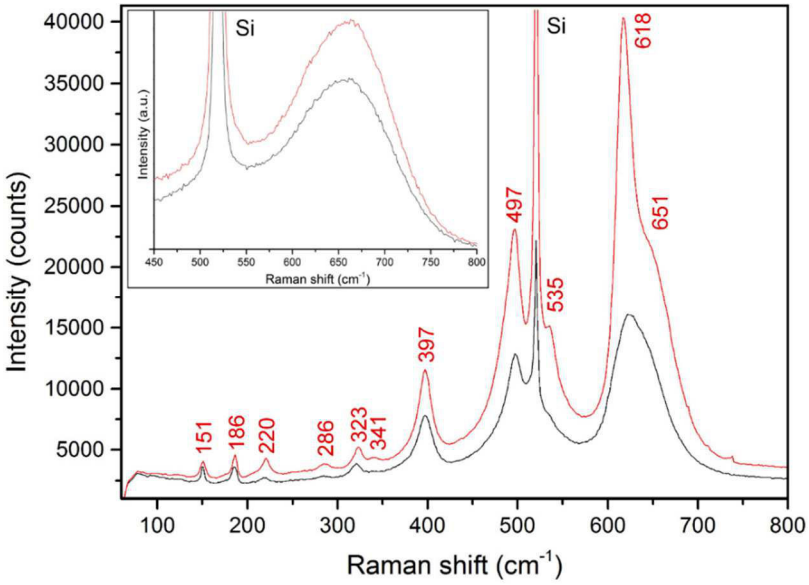

Figure V.4. RT Raman spectra of the YMO-600-1 (black line) and YMO-600-1.4 (red line) films annealed at 900 °C. Inset: Raman spectra of the as-deposited YMO-600-1 (black line) and YMO-600-1.4 (red line) films (see Figure IV.5 for complete spectra).

All the Raman lines are assigned to the o-YMO phase (see vibrations assignments in Table IV.8) except the line at 520 cm^{-1} originating from the Si substrate. The comparison of the Raman spectra of the as-deposited film (inset of Figure V.4) and of the films annealed at 900 °C indicates that the transformation from the amorphous to the o-YMO phase took place, as shown from the XRD and SEM observations. The Raman modes of the crystalline phase are in good agreement with those reported by Iliev et al. [1] for o-YMO (see Table.V.1). Both spectra are almost similar and only very small shifts in the line positions are observed, intensity differences being mainly due to different thicknesses and orientations of the probed micro-regions.

Mode	YMO-600-1	YMO-600-1.4	Iliev et al. [1]
$A_g(1)$	151	151	151
$A_g(2)$	186	186	188
$B_{2g}(1)$	219	220	220
$A_g(3)$	285	286	288
$A_g(4)$	322	323	323
$B_{2g}(2)$	-	341	341
$A_g(5)$	397	397	396
$A_g(6)$	497	497	497
$B_{2g}(3)$	534	535	537
$B_{2g}(4)$	620	618	616
?	652	651	653

Table V.1. RT Raman wavenumbers of the o-YMO phase for YMO-600-1 and YMO-600-1.4 films annealed at 900°C (this work) and for an o-YMO ceramic pellet [1]. The A_g and B_{2g} modes are numbered following their order of appearance with increasing wavenumbers in the spectrum.

No Raman signal of the impurity phase could be detected. Note that the line at ~ 652 cm^{-1} is not a proper vibration mode of the o-YMO phase although it was already observed in Iliev's spectra [1]. Concerning its origin, different possibilities were considered: defects [2], contributions from zone-boundary phonons [3] and on-site Jahn-Teller mode [4]. The Raman results indicate that the o-YMO phase formed in the two films have similar composition.

5.1.2 In-situ Raman experiment on as-deposited amorphous YMO film

The onset of the amorphous to crystalline phase transformation was investigated *in-situ* for the YMO-600-1 sample by Raman spectroscopy (Figure V.5). When heating from RT to 675 °C under Ar atmosphere, the broad band characteristic of the amorphous sample shifts gradually from ~ 650 cm^{-1} at RT to ~ 637 cm^{-1} at 675 °C with a simultaneous intensity decrease and line broadening, as expected from thermal expansion. A sudden change relative to the phase transformation is observed in the spectrum with further temperature increase to 700 °C (see red spectrum in Figure V.5 and Figure V.6). Indeed, at 700 °C, three Raman lines occur at ~ 306, 381 and 609 cm^{-1}; they are assigned to the $A_g(4)$, $A_g(5)$ and $B_{2g}(4)$ Raman modes of the o-YMO phase reported in Table V.1, respectively, taking into account Raman shifts due to thermal expansion. Their temperature dependence in the RT-900°C range is shown in Figure V.6.

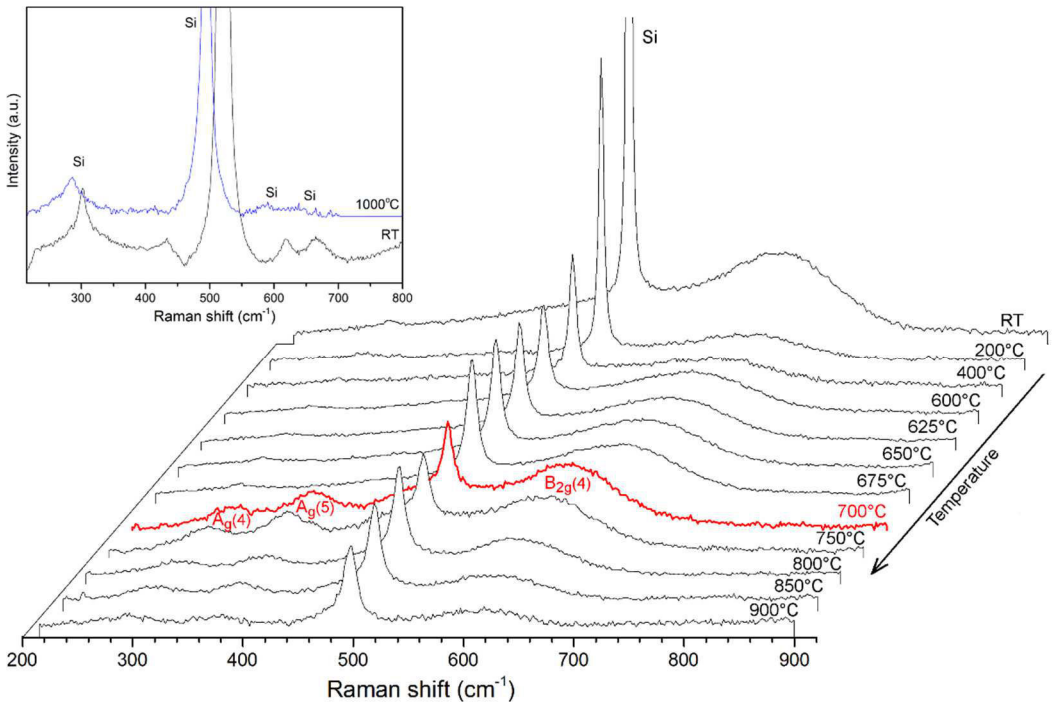

Figure V.5. Temperature-dependent Raman spectra of the YMO-600-1 film in the temperature range RT-900°C. The red spectrum marks the crystallization of the amorphous phase into the o-YMO phase. Inset: spectra at 1000°C and after cooling down to room temperature.

It is observed that a continuous temperature dependency of the o-YMO modes occurs after the transition at 700°C. This confirmed that no other phase transition takes place up to 900°C. The thermal dependence of the E_g mode at ~ 520 cm^{-1} of the Si substrate from our data is in very good agreement with the one reported in [5].

From 900 °C up to 1100 °C, the modes of the o-YMO phase disappear and only an enhancement of the Si line intensity is observed (see blue spectrum in the inset of Figure V.5). The spectrum remains unchanged when cooling down to RT as seen on the black spectrum in the inset of Figure V.5. This indicates an irreversible change in the sample. It is related to the formation of a new phase due to the Si diffusion in the film at high temperature.

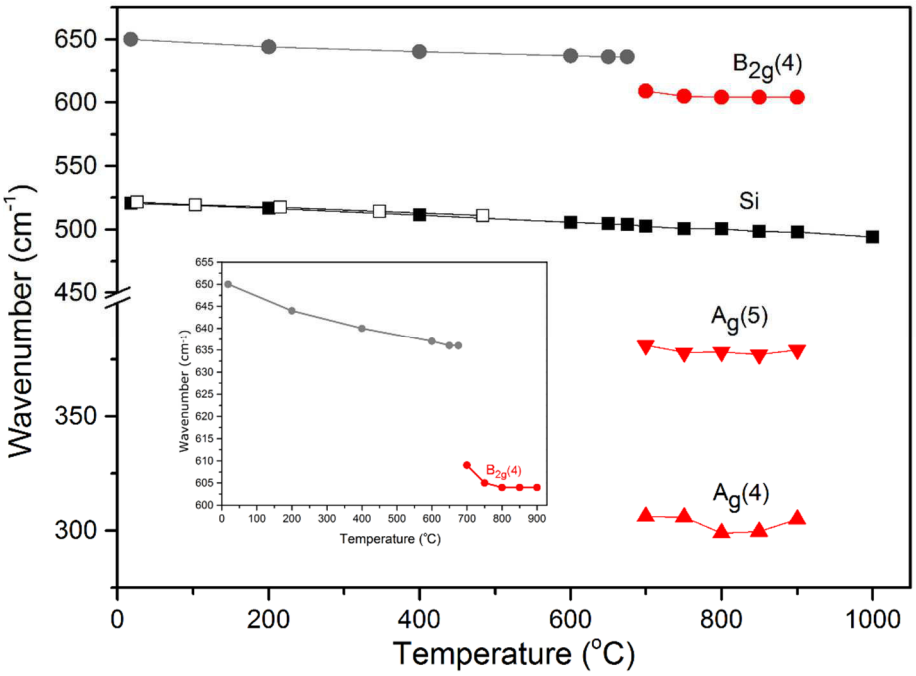

Figure V.6. Temperature dependence of the $A_g(4)$, $A_g(5)$ and $B_{2g}(4)$ mode wavenumbers of the o-YMO phase for the YMO-600-1 film. The thermal dependence of the E_g mode of the Si substrate ~ 520 cm^{-1} from our data (close symbol) and that reported in [5] (open symbol) is also given. Inset: enlargement of the $B_{2g}(4)$ wavenumber evolution.

In order to obtain structural information about the phase formed during Raman investigation above 1000 °C, complementary XRD, SEM and TEM analyses of the film were performed after cooling down to RT (Figure V.7). They reveal the formation of a silicate phase from the Si diffusion into the film, as mentioned above.

More precisely, the hexagonal $Y_{4.67}(SiO_4)_3O$ phase (JCPDS card No. 30-1457) can be identified by both XRD (square symbols in the pattern of Figure V.7a) and TEM observations: the HRTEM micrograph of the $Y_{4.67}(SiO_4)_3O$ phase and the corresponding SAED pattern in [011]-zone axis are shown in Figure V.7b and its inset. The $Y_{4.67}(SiO_4)_3O$ projected structure along the [011] direction is superimposed in Figure V.7c on an enlargement of the HRTEM micrograph of Figure V.7b. CarIne software was used with the $Y_{4.67}(SiO_4)_3O$ structural parameters given in the JCPDS card No. 30-1457 as input. A good agreement between the white dots from the HRTEM image and the arrangements of Y atoms (yellow) of the structural model is observed (Figure V.7c).

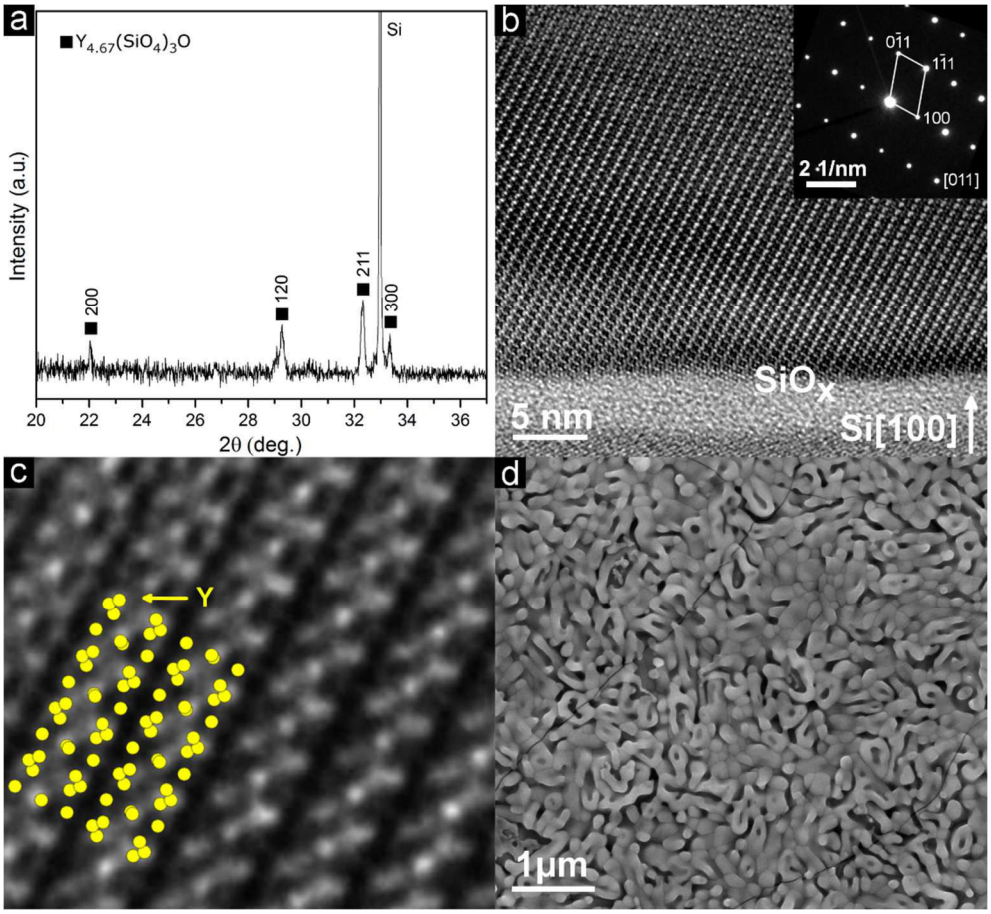

Figure V.7. Structural characterizations of the YMO-600-1 film annealed in-situ (Raman experiment) at 1100°C under Ar atmosphere and cooled down to RT: (a) XRD pattern indicating the hexagonal $Y_{4.67}(SiO_4)_3O$ silicate phase (JCPDS card No. 30-1457); (b) Cross-section HRTEM image of the film showing the $Y_{4.67}(SiO_4)_3O$ phase in the [011]-zone axis on top of the Si substrate and its SiO_x native oxide layer (3nm); the corresponding SAED pattern is given in the inset; (c) enlargement of HRTEM image of the $Y_{4.67}(SiO_4)_3O$ phase overlapped with the projected structure along the [011] direction; (d) SEM top view of the YMO film surface.

The SEM image in Figure V.7d indicates that the film morphology has been modified when compared to that of the as-deposited film and that of the film annealed at 900°C shown in Figure V.3b. Much larger grains are observed for the silicate (up to 500 nm) and the resulting surface is very rough with a high porosity between individual grains. Cracks due to thermal stress are also visible.

5.1.3 In-situ TEM experiment of as-deposited amorphous YMO film

TEM was used to study the local heating effect of the electron beam irradiation on the amorphous phase, which allowed us to have a closer look in the first stages of crystallization.

The HRTEM cross-section micrograph of the as-deposited YMO-600-1.4 film shown in Figure V.8a and its corresponding SAED pattern given in the inset are characteristic of an amorphous phase: no periodic arrangement related to a crystalline material is observed in the image and the SAED pattern presents circular halos. One can notice the columnar growth of the film (~15 nm column diameter). The power density of the electron beam was increased by varying the focus on the sample surface in order to induce a local recrystallization of the amorphous phase by heating. The *in-situ* transformation was carried out in several regions and similar results were obtained (see Figure V.8b-d). Whereas no change is observed in the image when a low power density is used, the amorphous film starts to crystallize as independent nucleation centers growing simultaneously after 3 min of electron irradiation when using a more focused beam (Figure V.8b). The irradiated region consists of several crystallites of 10-20 nm average size formed simultaneously with the disappearance of the as-deposited columnar structure. The corresponding Fast Fourier Transform (FFT) shown in the inset of figure V.8b presents distinct diffraction spots typical of polycrystalline samples. Increasing the irradiation time from 3 to 8 min (Figure V.8c) does not result in any significant change in the crystalline and amorphous regions and the *d*-spacings from the FFT pattern (inset of Figure V.8c) remain constant. The *d*-spacings can be assigned to the o-YMO phase which gives evidence of the transformation of the amorphous phase into a nano-crystalline o-YMO phase by heating under the electron beam for a short period of time.

The projected atomic structure of o-YMO (CarIne software, with minor modifications of the lattice parameters of the JCPDS card No. 16-1775) locally well agrees with the HRTEM image in Figure V.8d as shown in its top inset (*d*-spacings are indexed as d_{100}). The regions of agreement are relatively small due to the presence of a large quantity of defects probably related to the irradiation. Indeed, the beam impact can be observed on the irradiated surface, as shown in the bottom inset of Figure V.8d.

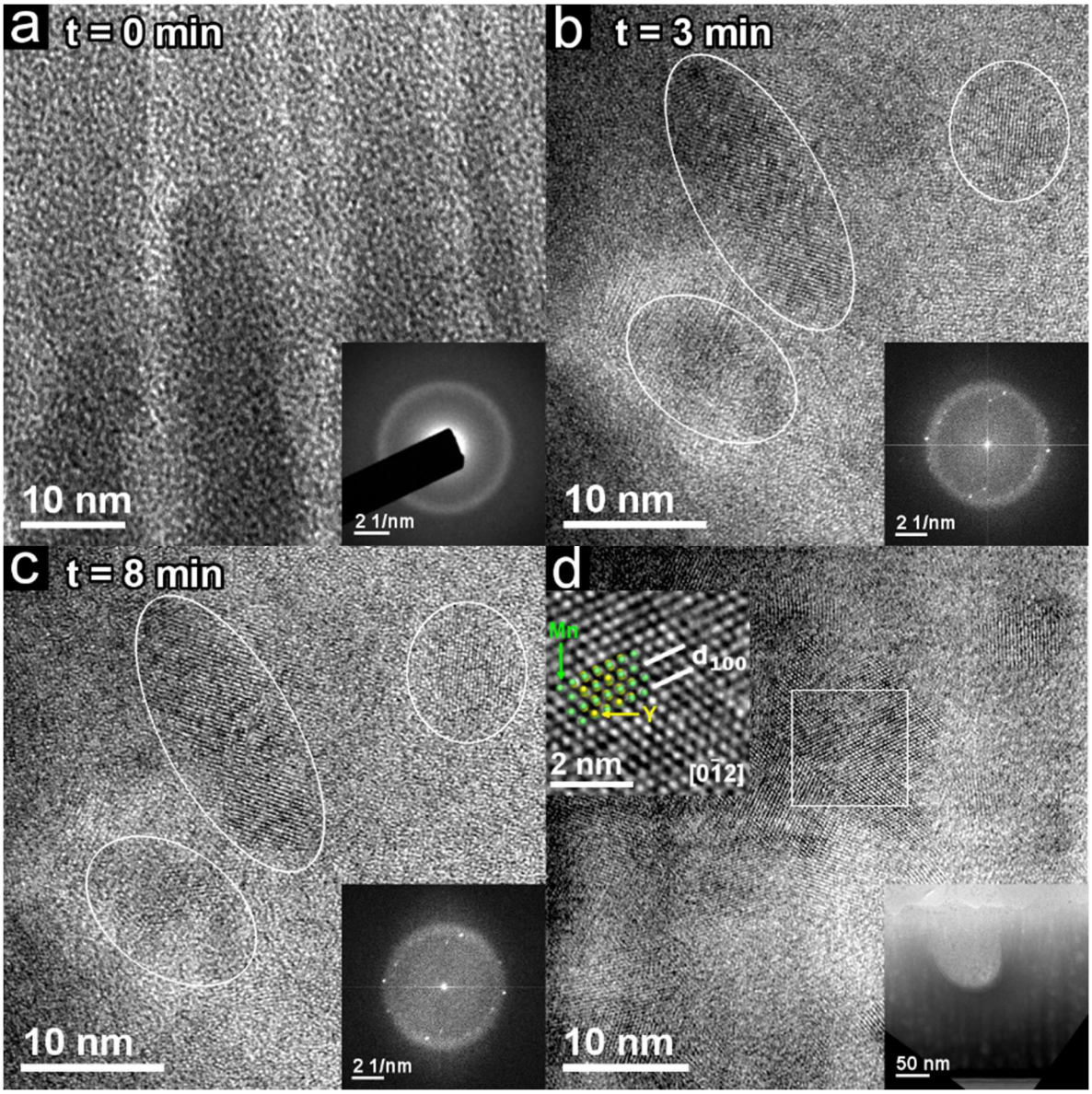

Figure V.8. In-situ TEM experiment on the YMO-600-1.4 film: (a) HRTEM cross-section image of the amorphous as-deposited film (t=0 min), the corresponding SAED is given in the inset; (b) HRTEM cross-section image after 3 min of heating by the electron beam irradiation showing the crystallization of some amorphous regions into the o-YMO phase. Inset: corresponding FFT with distinct diffraction spots with d-spacings matching the o-YMO phase; (c) same as (b) after 8 min of heating. No change compared to (b) is observed; (d) HRTEM image after 3 min beam irradiation in a different zone. Top inset: enlargement of an o-YMO nanocrystal (square box in (d)) in a particular $[0\bar{1}2]$*-zone axis orientation overlapped with the simulated o-YMO structure; bottom inset: low resolution TEM image of the film showing the beam impact.*

5.2 Stability of the as-deposited o-YMO phase

5.2.1 In-situ Raman experiment on as-deposited o-YMO film

The stability of the o-YMO phase was investigated *in-situ* by Raman spectroscopy from RT up to 900 °C using the YMO-750-1.4 film. As shown in the Chapter 4 (see section 4.3), the use of the corresponding deposition parameters (T_s=750 °C, Y/Mn=1.4) led to the deposition of the o-YMO phase on Si (100) substrate. Figure V.9 shows the temperature dependence of the Raman spectrum of the o-YMO film in the temperature range RT - 900 °C: all Raman modes except the Si line can be assigned to the o-YMO phase throughout the whole temperature range. Lineshifts toward low wavenumbers, intensity decrease and line broadenings are observed with increasing temperature for all lines, as expected from thermal expansion. The temperature dependence of the $A_g(5)$ and $B_{2g}(4)$ modes as well as the Si substrate is given in Figure V.10. The abnormal decrease in wavenumber observed above ~ 750 °C for the $A_g(5)$ mode can be related to the difficult fitting of the corresponding weak broadened line at such high temperatures.

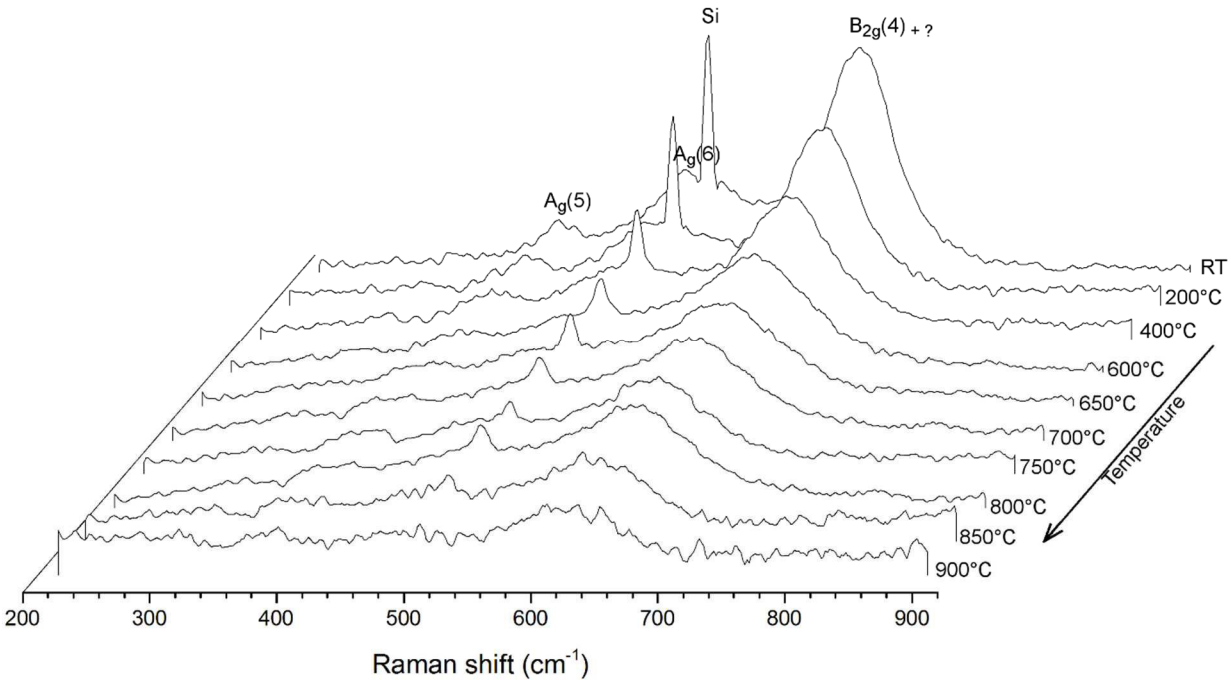

Figure. V.9. In-situ Raman experiment on the as-deposited YMO-750-1.4 film: temperature-dependent Raman spectra in the RT-900 °C temperature range under Ar atmosphere.

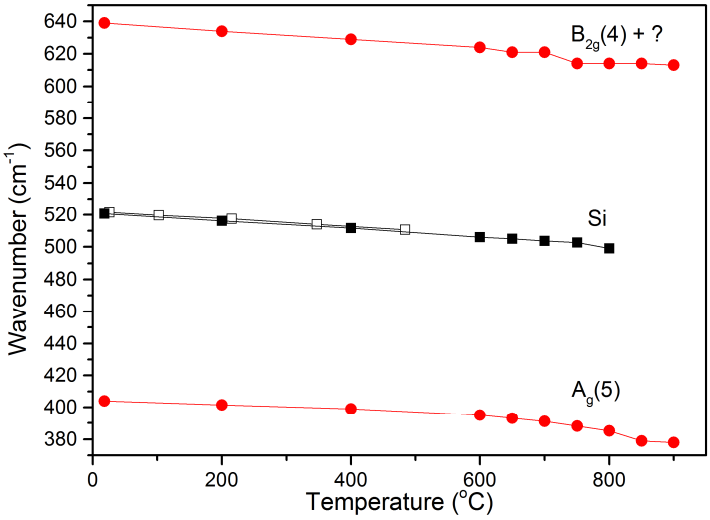

Figure V.10. Temperature dependence of the $A_g(5)$ and $B_{2g}(4)$ modes of the o-YMO phase for the YMO-750-1.4 film. The thermal dependence of the E_g mode of the Si substrate ~ 520 cm^{-1} from our data (closed symbol) and that reported in [5] (open symbol) is given as reference.

No other change occurs, indicating that the o-YMO film is stable and undergoes no phase transition in the investigated temperature range. Spectra measured during the cooling are identical to those measured at the same temperature during the heating (see Figure V.11a); it is especially confirmed by the spectra measured at RT before (i.e. as-deposited) and after the *in-situ* temperature experiment in Figure V.11b (note that these spectra are measured outside the cell temperature which explains the higher intensity than in spectra of Figure V.11a).

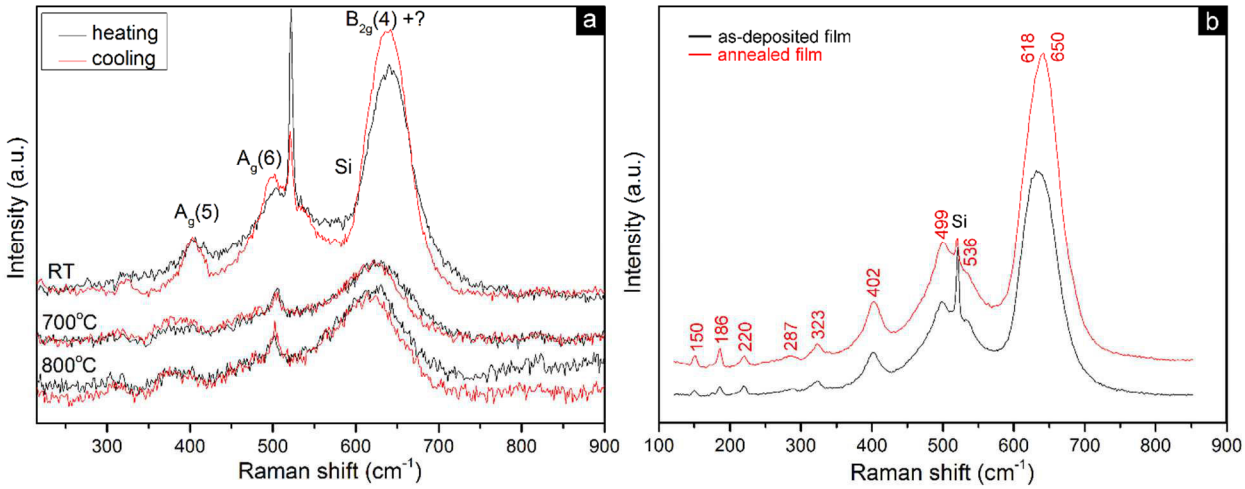

Figure V.11. a) Raman spectra measured during the heating (red line) and those measured during the subsequent cooling at RT, 700 °C and 800 °C; b) RT Raman spectra of the as-deposited film and of the film annealed at 900 °C and cooled down to RT.

XRD and SEM analyses of the YMO-750-1.4 film before and after annealing at 900°C confirm the stability of the o-YMO phase. XRD patterns in Figure V.12 confirm the o-YMO phase for both films (as-deposited in black, after *in-situ* annealing in red) in agreement with Raman experiment. However, the annealed film presents additional peaks corresponding to an impurity phase probably due to the diffusion of silicon, as previously observed for the YMO-600-1 and YMO-600-1.4 samples, although it does not correspond to the previously identified silicate phase.

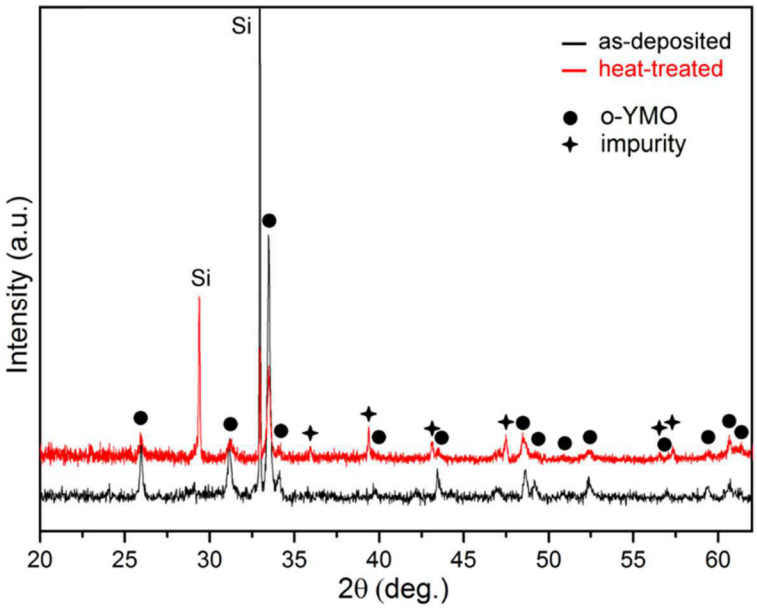

Figure V.12. XRD patterns of the as-deposited YMO-750-1.4 film (black line) and of the film after in-situ annealing at 900°C under Ar atmosphere. Full circles and crosses indicate the o-YMO and an impurity phase, respectively.

Figure V.13 shows the surface morphology of the annealed YMO-750-1.4 film. It exhibits a granular structure with a single family of grains strongly intertwined with nanometer-sized pores between them. They are distributed across the film as shown by the tilted top view image on the border of the sample in the inset of Figure V.13a. The grain size increases from 15-30 nm in the as-deposited film (Figure V.13b) up to 60-100 nm in the annealed film (Figure V.13a). Some aggregates, generally round-shaped, can also be observed on top of the films (Figures V.13a and V.13b).

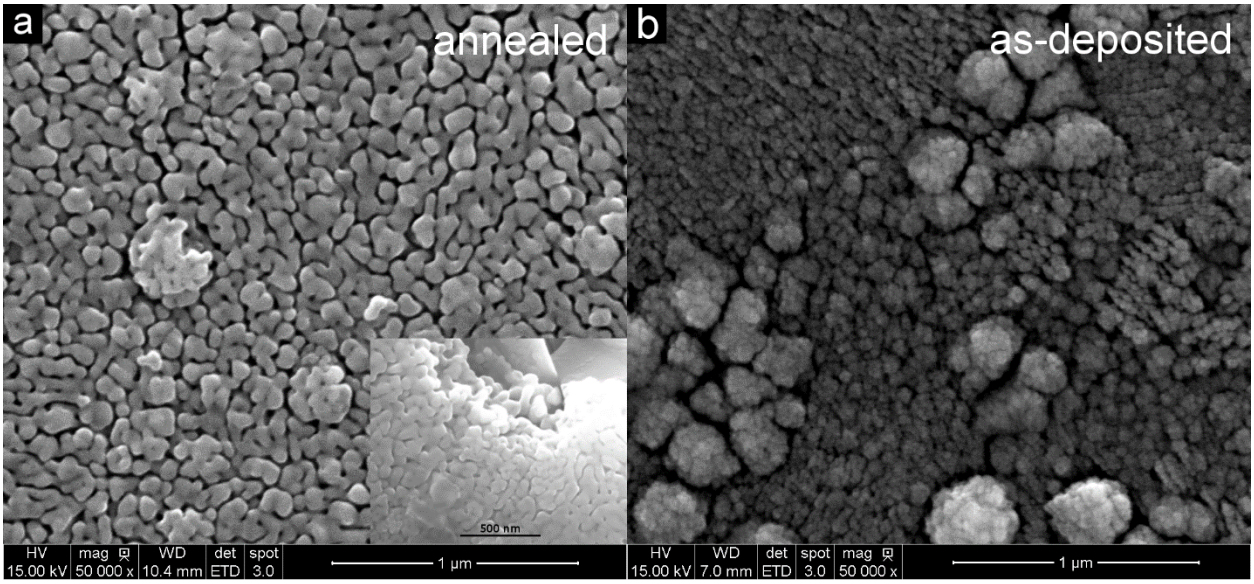

Figure V.13. Top view SEM images of YMO-750-1.4 film showing the morphology evolution of the film after in-situ annealing (a), of the as-deposited film (b). An enlargement showing the edge of the annealed film is shown in the inset in (a).

5.3 Magnetic characterization

The magnetic properties of the samples annealed by *in-situ* and *ex-situ* experiments are discussed briefly in the following. The temperature dependence of the magnetization was measured at a field of 500 Oe in both the zero field cooled (ZFC), and field cooled (FC) modes.

YMO-600-1 sample

Figure V.14a displays the temperature dependence of the magnetization of the YMO-600-1 film annealed at 900 °C in both the ZFC and FC modes. The result corresponding to a similar measurement on the as-deposited sample is shown in the inset of Figure V.14a (see section 4.1 from Chapter 4 for the complete description).

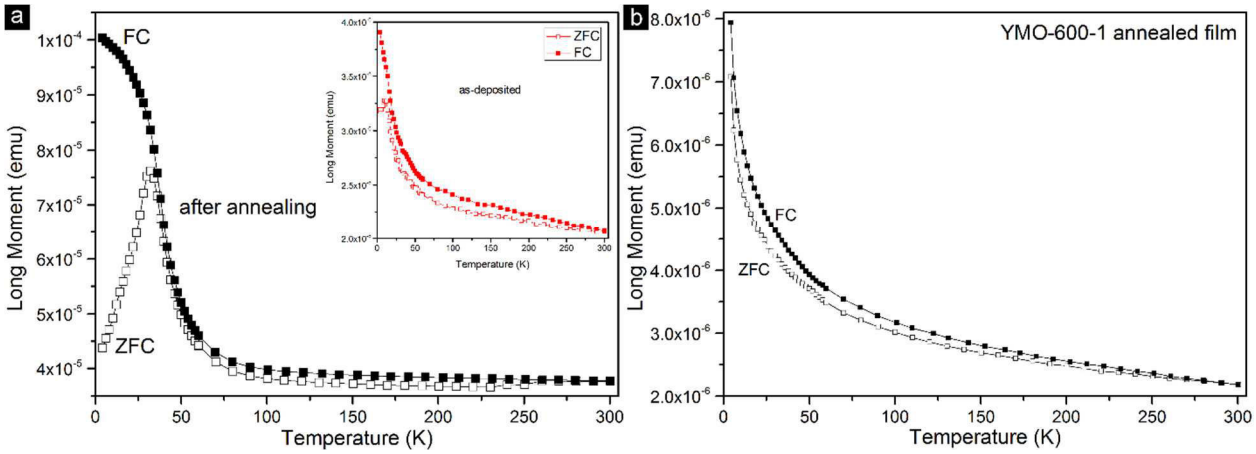

Figure V.14. Temperature dependence of the magnetization in both the ZFC (open symbol), and FC (filled symbol) modes for YMO-600-1 sample annealed a) ex-situ at 900°C; b) in-situ at 1100°C. Inset of a): temperature dependence of the magnetization for the as-deposited film.

The YMO-600-1 film annealed *ex-situ* at 900 °C exhibits a paramagnetic increase with the decreasing temperature down to 32 K (Figure V.14a). At this temperature, a splitting in the ZFC-FC curves takes place. Compared to the as-deposited film, for which T_f=11 K, the ZFC-FC splitting temperature is higher in the annealed film. This behavior can be related to the formation of the crystalline o-YMO phase during the annealing in the 750-900 °C temperature range.

The M(T) magnetization curve of the YMO-600-1 film annealed in-situ at 1100 °C is shown in Figure V.14b. The magnetization values of both ZFC and FC curves increase when decreasing the temperature without other change. This is a typical paramagnetic behavior and suggests that the silicate $Y_{4.67}(SiO_4)_3O$ phase is paramagnetic in the 5-300 K temperature range.

YMO-600-1.4 sample

The YMO-600-1.4 film annealed *ex-situ* at 900 °C shows a similar behavior in the temperature dependence of the magnetization curves (Figure V.15a). The ZFC-FC curves increase with the decreasing temperature down to 32 K as for a paramagnetic material. At T_f= 35 K a splitting is observed between the curves, similarly to the YMO-600-1 film annealed at 900 °C. However, a second increase in the magnetization occurs in the ZFC curve below 10 K.

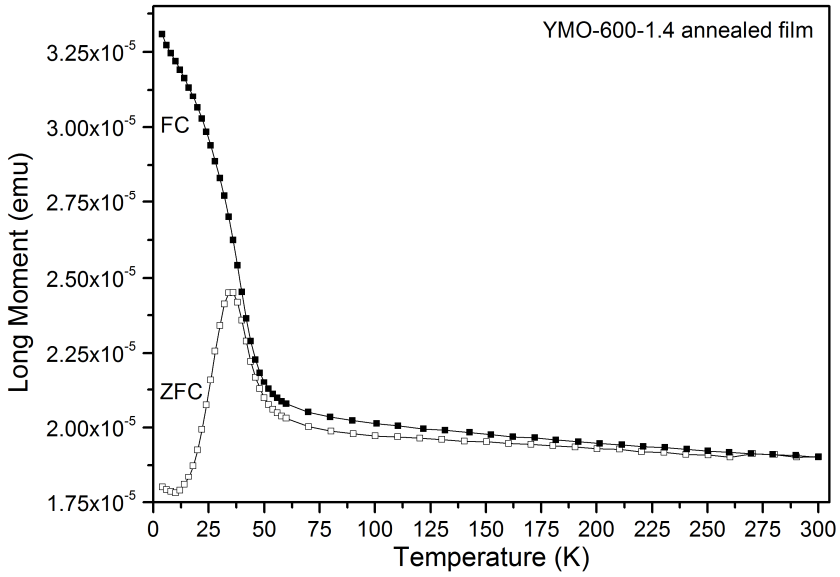

Figure V.15. Temperature dependence of the magnetization in both the ZFC (open symbol), and FC (filled symbol) modes for YMO-600-1.4 sample annealed ex-situ at 900 °C.

YMO-750-1.4 sample

Figure V.16 displays the temperature dependence of the magnetization in the ZFC and FC modes of the YMO-750-1.4 film before (in black) and after annealing at 900 °C (in red).

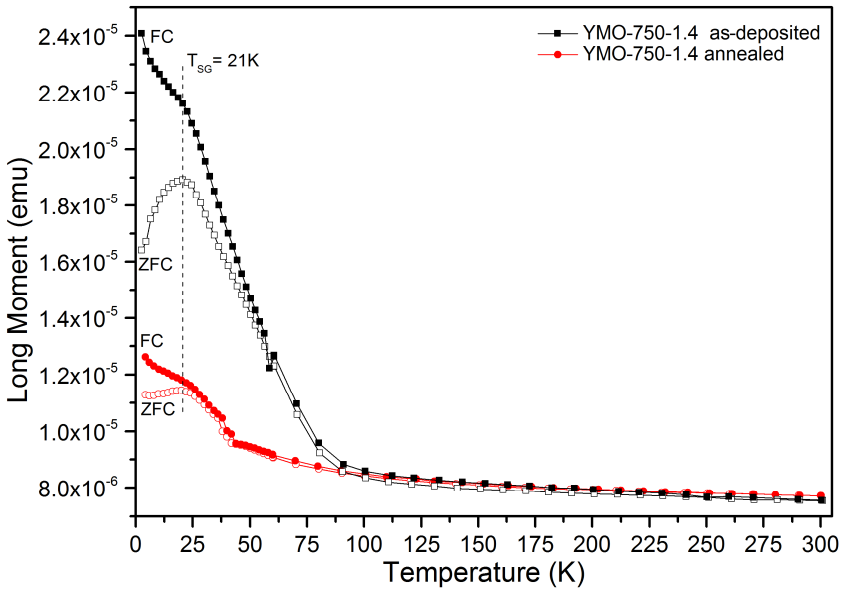

Figure V.16. Temperature dependence of the magnetization in both the ZFC (open symbols), and FC (filled symbols) modes for the as-deposited (in black) and annealed ex-situ at 900 °C (in red) YMO-750-1.4 sample.

Both as-deposited and annealed states of the film exhibit a pronounced irreversibility in the ZFC-FC curves. The observed splitting in the ZFC and FC curves at low temperatures (T_f =21 K) is a hallmark of spin-glass-like transition of the o-YMO phase. In addition to this, we have also observed a sharp cusp at around 42 K in the ZFC and FC curves of the annealed film. This transition is close to the transition temperature of the ferromagnetic Mn3O4 and can be due to the presence of this phase as small quantity impurity in our films. However, no indication from any of the characterization techniques used could confirm the presence of this phase. In conclusion, a spin-glass like behavior was observed for the annealed o-YMO phase, independently of the as-deposited phase.

5.4 Discussion and summary

The transformation from the amorphous to the o-YMO phase and its stability were studied in detail using XRD, SEM, TEM and Raman spectroscopy. Amorphous as-deposited YMO-600-1 and YMO-600-1.4 films transform irreversibly to o-YMO phase in the temperature range 675-700 °C. Once the o-YMO phase was formed, it remained stable when heating up to 900 °C. The stability of the o-YMO phase in the RT-900°C range (during heating and cooling) was also confirmed by performing a temperature *in-situ* Raman experiment using the o-YMO as-deposited sample (YMO-750-1.4).

The present results explain the **MOCVD** selective growth mechanisms previously reported in Chapters 3 and 4: films deposited on Si substrate below 700 °C are amorphous; they crystallize in the pure orthorhombic phase when deposited in the 750-800 °C range, and in the hexagonal structure for depositions above 800 °C. The amorphous YMO phase is the stable phase below 700 °C in agreement with the results from bulk samples prepared by a solution-based procedure via complexation by citrates reported in [6]. In such a way, an inorganic amorphous oxide carbonate has been obtained (final firing at 350–450 °C). This amorphous phase crystallizes mainly into the o-YMO phase in the temperature range 700–900 °C in air or O_2 atmosphere. Under N_2 or CO_2 atmosphere, the h-YMO phase is dominant, suggesting that the oxygen partial pressure has a large influence on the yield of o-YMO. These results seem very close to our MOCVD results and attest that the growing mechanisms and process conditions to obtain the o-YMO phase are rather similar: formation of an intermediate amorphous phase, low temperature annealing and oxidizing

atmosphere. The small differences in temperature can be due to different amorphous states prior to crystallization [6].

The parameters used in our work appear particularly interesting as no h-YMO phase is present in the whole investigated temperature range, which improves the selectivity of the growing process.

We finally note that the expected transition of o-YMO into the stable high temperature phase h-YMO was reported to occur near 1100 °C [6, 7]. This explains why no indication of this transition has been obtained in our study, which was limited to 900 °C annealing, due to Si diffusion.

In conclusion, *in-situ* and *ex-situ* thermal annealings gave evidence of the crystallization of the amorphous as-deposited films into the o-YMO phase at ~700 °C in a short period of time and confirm the stability of this phase up to at least 900 °C. The o-YMO as-deposited film presents a similar behavior: it is stable from RT up to 900 °C. At higher temperature, a Si diffusion from the substrate into the film leads to the formation of a silicate phase. These results allow to consider a **MOCVD** selective growth (amorphous, orthorhombic or hexagonal) of YMO films by adapting the deposition temperature according to the temperature stability region of the different phases.

References

1. Iliev, N., et al., *Raman active phonons in orthorhombic YMnO3 and LaMnO3.* Journal of Physics and Chemistry of Solids, 1998. **59**(10–12): p. 1982-1984.
2. Iliev, M.N., et al., *Raman spectroscopy of orthorhombic perovskitelike YMnO3 and LaMnO3.* Physical Review B, 1998. **57**(5): p. 2872-2877.
3. Iliev, M.N., et al., *Structural, transport, magnetic properties and Raman spectroscopy of orthorhombic Y 1− x Ca x MnO 3 (0≤ x ≤0.5).* Journal of Physics: Condensed Matter, 2005. **17**(21): p. 3333.
4. Laverdière, J., et al., *Raman study of orbital mediated multiphonons in RMnO3 (R = Pr,Sm,Eu,Tb,Y).* The European Physical Journal B - Condensed Matter and Complex Systems, 2006. **54**(1): p. 67-72.
5. Chiashi, S., et al., *Cold wall CVD generation of single-walled carbon nanotubes and in situ Raman scattering measurements of the growth stage.* Chemical Physics Letters, 2004. **386**(1–3): p. 89-94.
6. H. W. Brinks, H.F., A. Kjekshus, *Synthesis of Metastable Perovskite-type YMnO3 and HoMnO3.* JOURNAL OF SOLID STATE CHEMISTRY 1997. **129**: p. 334-340
7. Liu, S.-H., et al., *Structural transformation and charge transfer induced ferroelectricity and magnetism in annealed YMnO3.* AIP Advances, 2011. **1**(3): p. -.

Chapter 6

Epitaxial orthorhombic $YMnO_3$ films grown on (100)-perovskite substrates ($SrTiO_3$, $LaAlO_3$ and $(LaAlO_3)_{0.3}(Sr_2AlTaO_6)_{0.7}$)

Summary

6.1 Structural study of epitaxial o-$YMnO_3$ thin films ……151
6.2 Magnetic characterization of epitaxial o-$YMnO_3$ thin films ……160
6.3 Structural study of non-stoichiometric o-$YMnO_3$ films ……...172
6.4. Magnetic characterization of non-stoichiometric o-$YMnO_3$ films ……..181
6.5 Summary and conclusions ……182
References ……...184

In this chapter we report on the structural and magnetic characterization of epitaxial o-YMO films grown on perovskite substrates (STO, LAO, LSAT). For nearly stoichiometric films, the epitaxial character and its evolution with thickness are analyzed in details. At the end of the chapter the influence of the non-stoichiometry is studied.

For most technological applications, it is desired that the deposited multiferroic material form a single-oriented crystalline layer.

Based on the free-energy increase due to the structural coherence at the film-substrate interface, the epitaxial phase stabilization in which the nucleation process is controlled during the film growth by the appropriate choice of the substrate, is a useful tool to stabilize new phases, despite their instability in the bulk form.

In this way, extreme conditions (e.g. high pressure) commonly used for the stabilization of metastable phases, are avoided. This method has been commonly used to stabilize hexagonal $RMnO_3$ phase for large rare earths or orthorhombic $RMnO_3$ phase for smaller ones.

We have seen in the previous chapters that an epitaxial growth was not possible in the case of Si substrates for either hexagonal or orthorhombic YMO (o-YMO) phases. In the case of the o-YMO phase, the STO and LAO were the main substrates reported (see section 1.6.2 from Chapter 1) for the epitaxial growth. Here, additionally to these substrates, we explore the synthesis of the o-YMO phase on LSAT substrates.

6.1 Structural study of epitaxial o-YMO thin films

Table VI.1 summarizes different possible mismatches between the perovskite substrates used in this chapter and the o-YMO phase obtained using high pressure synthesis. This o-YMO phase ([1], JCPDS card No. 16-1775) has been considered as the bulk reference to estimate the mismatch corresponding to different orientation relationships between the film and the substrate. In Table VI.1 the lattice mismatch along a given direction is calculated as $f\ (\%)=100\cdot(d_{substrate}-d_{o\text{-}YMO})/d_{o\text{-}YMO}$. The values of the interplanar distances for the substrates ($d_{substrate}$) are calculated considering the following values of cubic (pseudocubic for LAO) cell parameters: 3.792 Å for LAO [2], 3.872 Å for LSAT [3] and 3.905 Å for STO [2]. The values of the interplanar distances of the o-YMO ($d_{o\text{-}YMO}$) are calculated along different directions considering the *Pnma* setting with *a*=5.8361 Å, *b*=7.3571 Å and *c*=5.2580 Å cell parameters.

			$d_{o\text{-}YMO}$ [Å]			
			d_{100} =5.8361	d_{020}= 3.6785	d_{001}= 5.2580	d_{101}= 3.9064
$d_{Substrate}$ [Å]	LAO	d_{100} =3.792		+3.08		-2.93
		d_{011}= 5.362	-8.12		+1.98	
	LSAT	d_{100} =3.872		+5.26		-0.88
		d_{011} =5.475	-6.19		+4.13	
	STO	d_{100} =3.905		+6.15		-0.03
		d_{011}=5.522	-5.38		+5.02	

Table VI.1 Lattice mismatches, f (in %), between STO, LAO and LSAT substrates and the o-YMO phase.

According to the mismatch values shown in Table VI.1, domains with different orientations are possible. Some examples are represented in a schematic way in Figure VI.1.

The orange domains from Figure VI.1 have the *b* axis out-of-plane with respect to the substrate surface (STO is represented in blue and the direction out-of-plane, i.e. perpendicular to the surface, is $[100]_{STO}$) and corresponds to two domains, 90° in-plane rotated, with the following orientation relationships:

- $[010]_{YMO}//[100]_{STO}$ and $[100]_{YMO}//[011]_{STO}$
- $[010]_{YMO}//[100]_{STO}$ and $[100]_{YMO}//[0\text{-}11]_{STO}$

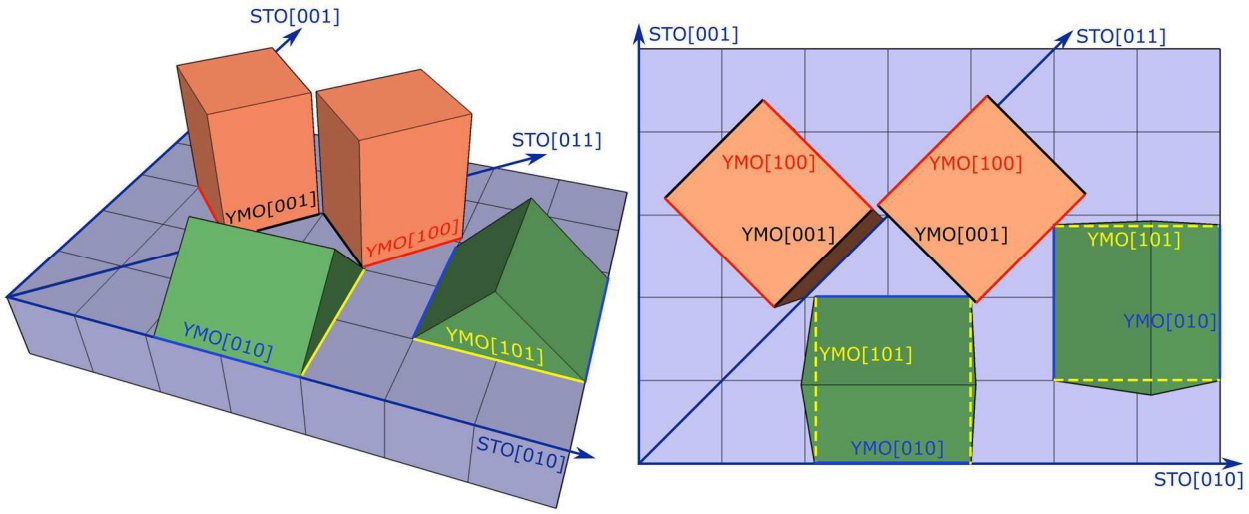

Figure VI.1 Schematic 3D representation of the YMO domain structure on STO substrate (left part of the figure: side view, right part: top view). In blue, the STO substrate (several cells) is represented by cubes; in orange and green, YMO (individual cells) is represented by parallelepiped.

These domains correspond to misfits of -2.93% (LAO), -0.88% (LSAT) and -0.03% (STO) along the $[101]_{YMO}$. The misfit is relatively small in the case of the STO substrate (the YMO cell is represented by the orange parallelepiped in Figure VI.1.

The green domains in Figure VI.1 have the *b* axis in the plane of the substrate and correspond to two domains, 90° rotated, that have the following orientation relationships:

- $[10\text{-}1]_{YMO}//[100]_{STO}$ and $[010]_{YMO}//[010]_{STO}$
- $[10\text{-}1]_{YMO}//[100]_{STO}$ and $[010]_{YMO}//[001]_{STO}$

These domains correspond to misfits of +3.08% (LAO), +5.26% (LSAT) and +6.15% (STO) along $[010]_{YMO}$.

Considering the misfit values obtained in these examples, one would expect to have mainly *b* out-of-plane domains for the films grown on LSAT and STO, whereas both *b* in- and out- of-plane domains should be equally present in the films grown on LAO substrate.

In the following part, we will focus on the characterization of epitaxial o-YMO films grown on top of STO, LSAT and LAO substrates by either MOCVD or PLD techniques using different experimental conditions. The main characteristics of the MOCVD films and the experimental growing condition are summarized in Table VI.2 and Table VI.5.

T_s (°C)	$Y/Mn_{solution/target}$	P_{O2} (bar)	No. inj.	Y/Mn_{film}/Thickness (nm)	
				STO	LAO
750	1	$3.33 \cdot 10^{-3}$	1000	0.99†/12	-
			1400	?/23	?/20

Table VI.2. Experimental conditions and main characteristics of the MOCVD YMO films on (100) STO and LAO substrates (†EDX-TEM, ?unmeasured).

o-YMO films grown on STO substrates by MOCVD

Figure VI.2 shows the θ-2θ XRD patterns corresponding to the two YMO films obtained by PI-MOCVD and grow on STO substrate. In both cases, all peaks can be indexed with the (0k0) reflections of the o-YMO phase.

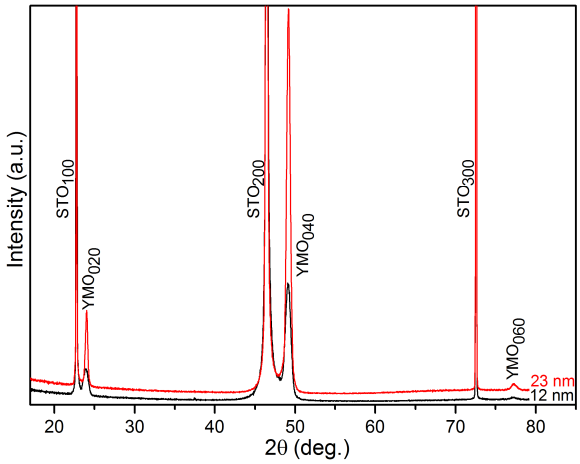

Figure VI.2. θ-2θ XRD pattern of two o-YMO films grown on STO substrate by PI-MOCVD, 12 nm (in black) and 23 nm (in red) of thickness.

The films are textured with the out-of-plane direction $[010]_{YMO}$ parallel to $[100]_{STO}$. This is compatible with epitaxial domains having $[100]_{YMO}//[011]_{STO}$ and/or $[100]_{YMO}//[0\text{-}11]_{STO}$ (orange domains in Figure VI.1). No other reflections corresponding to either different domains or traces of impurity phases have been detected.

The out-of-plane interplanar distances derived from the $0k0_{YMO}$ peaks positions are d_{010}=7.409(3) for the 12 thick film and d_{010}=7.402(3) for the 23 nm thick film and are respectively ~ 0.71% and 0.61% larger than the bulk value (*b*=7.3571 Å). These values observed for our MOCVD films are close to those obtained by Marti et al [4] for YMO films deposited by PLD on STO(100) substrates.

These authors show that depending on the oxygen pressure, the *b* parameter (i.e. d_{010}) can be almost constant or present a small decrease (from 7.409 Å (30 nm) to 7.389 Å (120 nm)) with the increasing thickness whereas the increase of *a* parameter is the most important variation (*c* parameter being almost constant). In our case, the relatively small decrease of *b* parameter (comparable to sample grown with P_{O2}= 0.3 mbar in [4]) gives an indication of the strain relaxation with thickness.

A detailed investigation of the thickness of these films was carried out by XRD, XRR, and/or TEM. The XRD FWHMs of the $040_{o\text{-}YMO}$ Bragg peaks in Fig. VI.2 are equal to 0.8434° and 0.5236° and correspond to correlation lengths of 12 nm and 23 nm respectively (calculated from the Scherrer's formula). Considering that the epitaxial growth is maintained from the bottom to the top interface of the film, these values can be associated with the film thickness. An excellent agreement is obtained when comparing this value of the correlation length with the thickness found by XRR and TEM (see below) in the case of the 12 nm thick YMO film. Figure VI.3 shows the corresponding XRR results. A good overlapping between the experimental curve (in black) and the simulated pattern (in blue) was obtained. The fitting parameters (thickness, roughness, density) used in the simulated pattern are displayed in the inset of Figure VI.3.

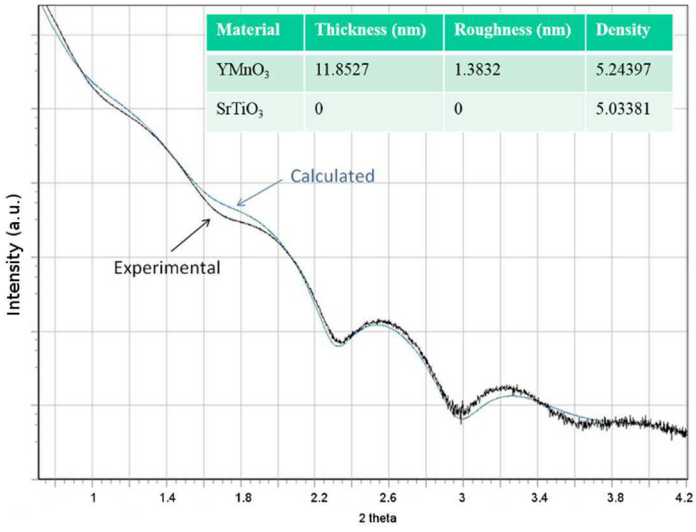

Figure VI.3. Experimental XRR curve (in black) and simulated pattern (in blue) for the 12 nm thick YMO film. Inset: the results of the fitted parameters (thickness, roughness, density).

The film roughness is around 1.38 nm and matches the results by AFM (see further Figure VI.13). The density is 5.24 g/cm^3, which is smaller than the reported bulk value of 5.64 g/cm^3 form JCPDS

card No. 16-1775. The calculated film thickness is equal to 11.85 nm and is in perfect agreement with results obtained by other techniques (XRD, TEM). The thickness of the second film deposited by MOCVD on STO was deduced from the correlation length and by comparing the XRD peaks (integrated intensity in counts/s and FWHM) and the SEM-EDX counting rates for both films. These estimations give 12 nm and 23 nm thicknesses for the two films and were in qualitative agreement with the number of injections of the precursor solution used for the depositions.

Reciprocal space mapping (RSM) measurements have been performed on these two o-YMO films grown on STO by MOCVD in order to access quantitative measurement of the in-plane strain state by measuring both in-plane and out-of-plane cell parameters.

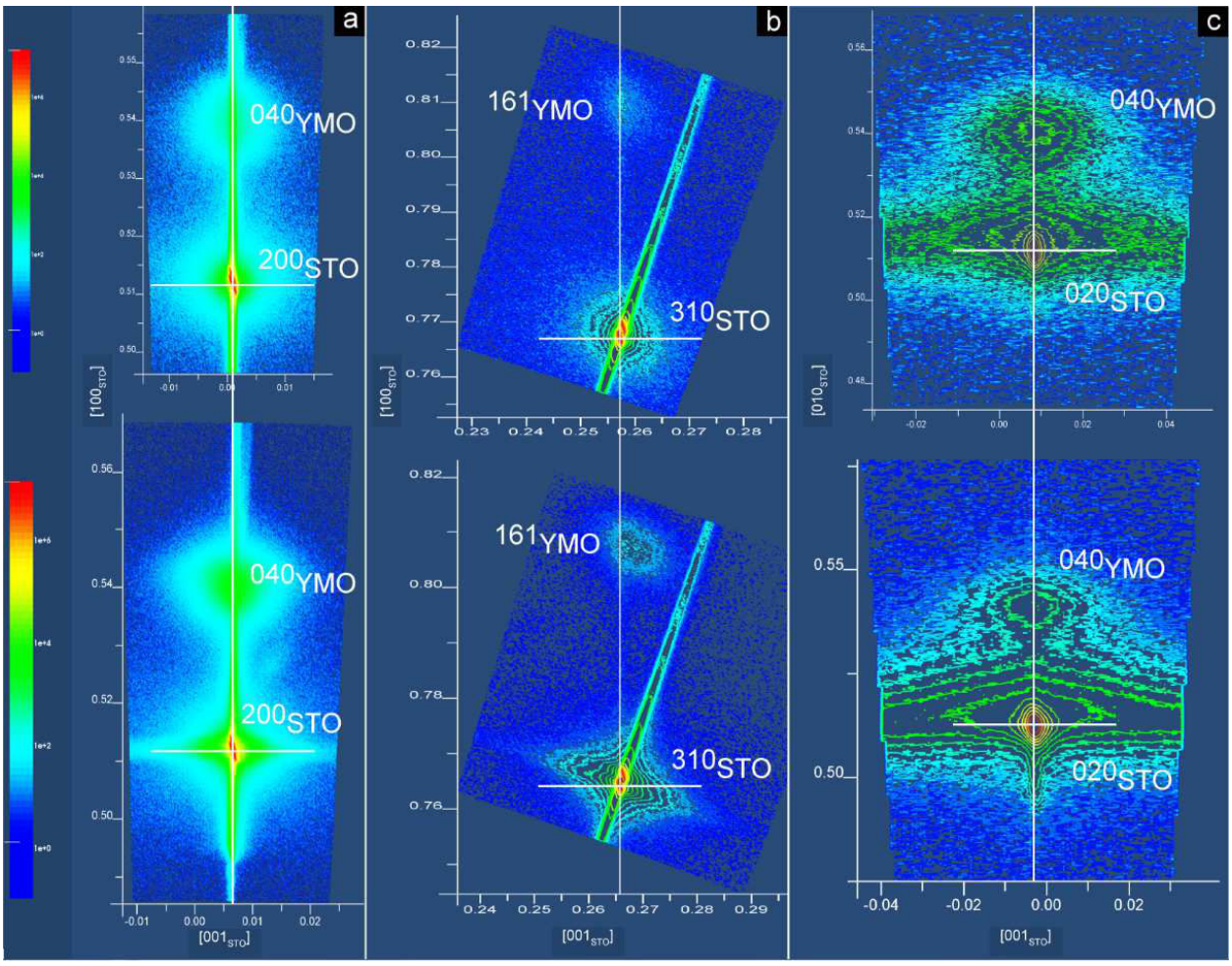

Figure VI.4. RSM for 12 nm (top part) and 23 nm (bottom part) thick YMO films: a) symmetric reflection around 200_{STO}; b) asymmetric reflection around 310_{STO}; c) in-plane around 020_{STO} reflection.

Two dimensional reciprocal space maps near the symmetric 040_{YMO} and 200_{STO} (Figure VI.4a) and asymmetric 161_{YMO} and 310_{STO} (Figure VI.4b) Bragg reflections of the YMO film and STO substrate have been collected. The corresponding results are presented in Figure VI.4a and b. The vertical axis corresponds to the out-of-plane direction (parallel to $[010]_{YMO}$ and $[100]_{STO}$), and the horizontal axis correspond to an in-plane direction (parallel to $[101]_{YMO}$ and to $[010]_{STO}$). The values are expressed in 1/d units. The in-plane component of the 161 reflection represents the d_{101} distance of the YMO film. All measurements are referred to the bright intense spots corresponding to the STO substrate marked by white vertical and horizontal lines. This procedure was kept for all RSM map analysis. The top spots on each map correspond to the Bragg reflections of the YMO films, whereas the intense bottom spots correspond to the substrate.

The out-of-plane interplanar distances derived from the symmetric 040_{YMO} peak positions are: d_{010}=7.409(3) and d_{010}=7.401(3) for the 12 and 23 nm thick films, respectively. These values are very close (equal within the error bar) to those measured by θ-2θ XRD scans.

From the position of the 161_{YMO} spot of the 12 nm thick film shown in Figure VI.4b, it can be observed that its horizontal component (along $[101]_{YMO}$ direction) is the same than that of the 310_{STO} Bragg reflection of the substrate i.e. both spots are perfectly aligned along the $[100]_{STO}$ direction (white line in the figure). This means that the film is fully strained along the direction $[101]_{YMO}$ (parallel to $[010]_{STO}$). This is expected as the misfit along this direction is very small (f_{101}= -0.03%) and thus clamping on the substrate cost relatively small energy. Contrariwise, for the 23 nm thick film, the 161_{YMO} spot is shifted toward the right side of the panel compared to the STO substrate. This shift corresponds to a slight decrease of the YMO d_{101} distance. The in-plane interplanar distances obtained from the 161_{YMO} reflection are d_{101}=3.905(3) Å and d_{101}=3.862(3) Å for the 12 and 23 nm thick films, respectively. The value for the 23 nm film is slightly smaller than that of the bulk (3.906 Å) and of the STO substrate (3.905 Å). This indicates that the relaxation could occur toward a value slightly different than our choice of reference bulk value. As it will become evident in next section one cannot, however, exclude an overestimation of the variation of YMO d_{101} due to the presence of 90° rotated out-of-plane domains.

To additionally clarify the distribution of domains in the MOCVD grown YMO/STO films, in-plane RSMs have been realized on both YMO films around the 020_{STO} diffraction spot of the substrate (labeled in Figure VI.4c). The vertical direction of Figure VI.4c corresponds to $[010]_{STO}$

and the horizontal direction corresponds to $[001]_{STO}$. The interplanar distances derived from the two spots of the YMO films are d=1.850(3) Å and d=1.849(3) Å. This distances can be identified with d_{040} of o-YMO corresponding to in-plane *b*-oriented domains. The corresponding d_{010} gives respectively $b_{o\text{-}YMO}$=7.400(3) Å and $b_{o\text{-}YMO}$=7.396(3) Å for the 12 and 23 nm thick films.

Further characterization of the domain structure was carried out by radial in-plane scans along the $[010]_{STO}$, $[011]_{STO}$, $[001]_{STO}$, $[0\text{-}11]_{STO}$ and $[0\text{-}10]_{STO}$ directions of the substrate. The obtained patterns for the 12 and 23 nm YMO films are shown in Figure VI.5a and b.

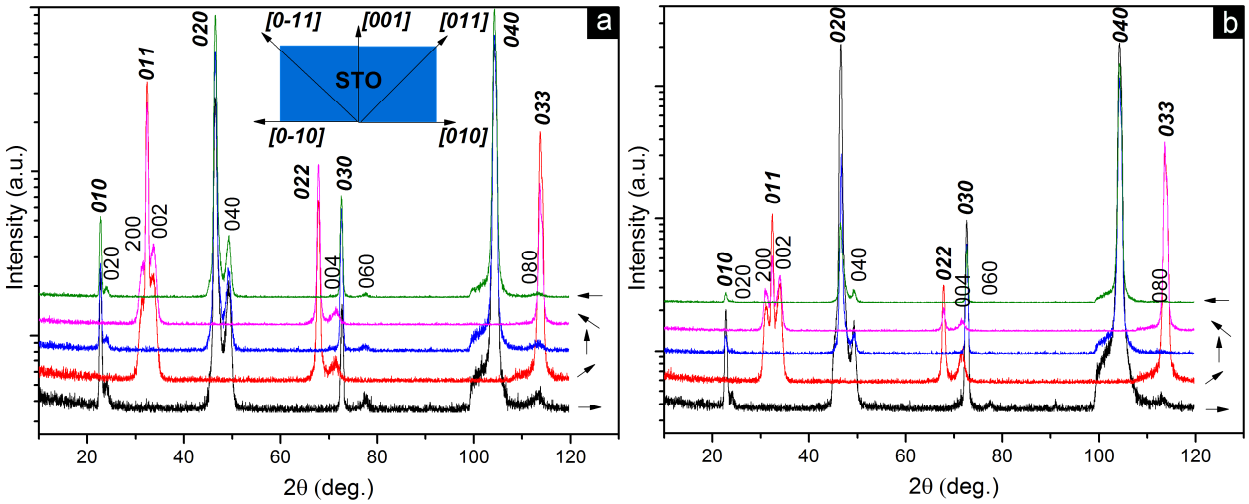

Figure VI.5. In-plane scans of 12 nm (a) and 23 nm (b) YMO films along the $[010]_{STO}$, $[011]_{STO}$, $[001]_{STO}$, $[0\text{-}11]_{STO}$ and $[0\text{-}10]_{STO}$ directions. Directions are schematically indicated by arrows for each scan and its orientation with respect to the STO substrate is given in the inset of (a). For figure clarity the Bragg peaks of the substrate are marked in bold and only for $[010]_{STO}$ and $[011]_{STO}$ scans. The YMO peaks are marked by normal font.

It can be observed from Figure VI.5 that both films have similar patterns along the corresponding measured $[hkl]_{STO}$ directions of the substrate. This means that the in-plane domain structure is similar. Four different domains orientations could have been discerned by this type of scans. They are schematically represented in Figure VI.6. The orientation relationships, as they have been discussed at the beginning of the chapter are the following:

- $[010]_{YMO}//[100]_{STO}$ and $[100]_{YMO}//[011]_{STO}$
- $[010]_{YMO}//[100]_{STO}$ and $[100]_{YMO}//[0\text{-}11]_{STO}$
- $[10\text{-}1]_{YMO}//[100]_{STO}$ and $[010]_{YMO}//[010]_{STO}$
- $[10\text{-}1]_{YMO}//[100]_{STO}$ and $[010]_{YMO}//[001]_{STO}$.

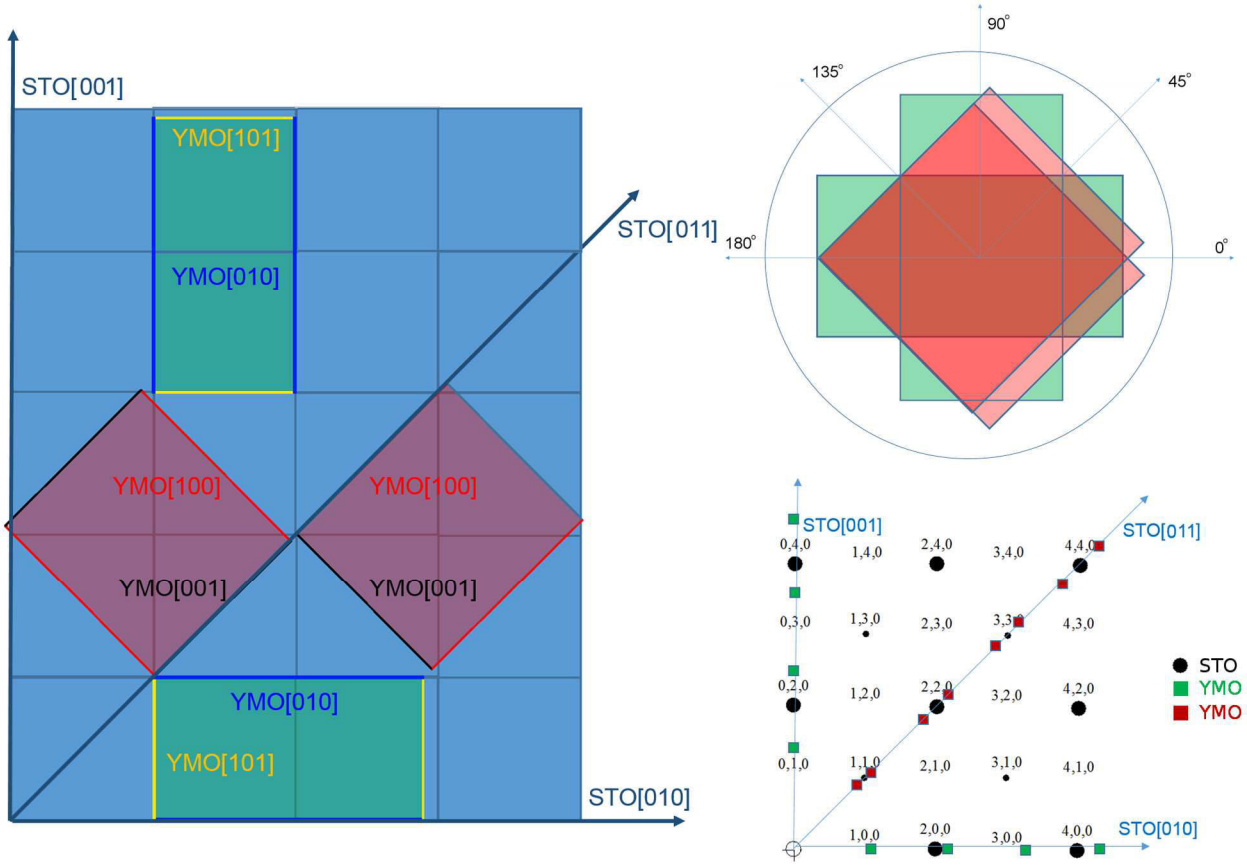

Figure VI.6. Schematic representation of the domain structure: a) direct space showing the STO substrate (blue squares) and the different YMO domains of the film (red and green rectangles); b) direct space showing the angles between the domains from a); c) configuration of the domains shown in a) in the reciprocal space (for clarity some YMO reflections have been omitted, the corresponding distances of the YMO exaggerated and the planes indexation is given only for STO).

In order to compare the in-plane cell parameters of the two films, enlargements of the scans along the $[011]_{STO}$ (around the Bragg reflection 011_{STO} and 200_{YMO} and 002_{YMO}) and along the $[001]_{STO}$ (around the Bragg reflection 001_{STO} and 040_{YMO}) are shown in Figure VI.7. It is clearly seen that the *c* parameter is decreasing while the *a* parameter is increasing with the increasing of the film thicknesses from 12 to 23 nm (almost no variation is observed for the *b* parameter).

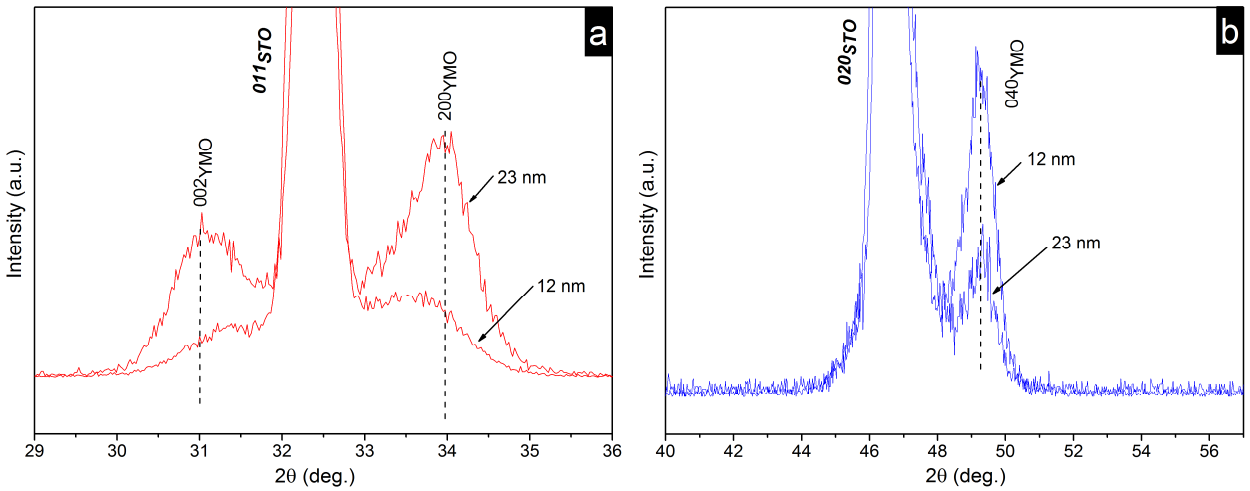

Figure VI.7. Enlargement of the in-plane scans from Figure VI.5 along the a) $[011]_{STO}$ and b) $[001]_{STO}$.

The values of the corresponding cell parameters derived from the experiments are listed in Table VI.3 and their evolution is represented in Figure VI.8. The in-plane *a*, *b* and *c* lattice parameters are measured from the 200_{YMO}, 040_{YMO} and 002_{YMO} peaks respectively in the different geometries used. It can be observed that all values are tending toward the bulk values. This indicates strained films with a thickness-dependent relaxation mechanism.

Film thickness	**12 nm**				**23 nm**			
Parameter	**a**	**b**	**c**	**d_{101}**	**a**	**b**	**c**	**d_{101}**
b out-of-plane domains	5.690	7.409	5.289	3.905	5.735	7.401	5.268	3.862
b in-plane domains		7.400				7.398		

Table VI.3. Cell parameters derived from the in-plane radial scans and RSM of 12 and 23 thick YMO films.

Our results are comparable with those reported by Marti et al. [4] on PLD grown YMO films at different oxygen pressures and with various thicknesses on top of STO (100). The authors observed the existence of two crystal domains, 90° in-plane rotated with the same out-of plane parameter:

$[010]_{YMO}//[100]_{STO}$ and $[100]_{YMO}//[011]_{STO}$

$[010]_{YMO}//[100]_{STO}$ and $[100]_{YMO}//[0\text{-}11]_{STO}$.

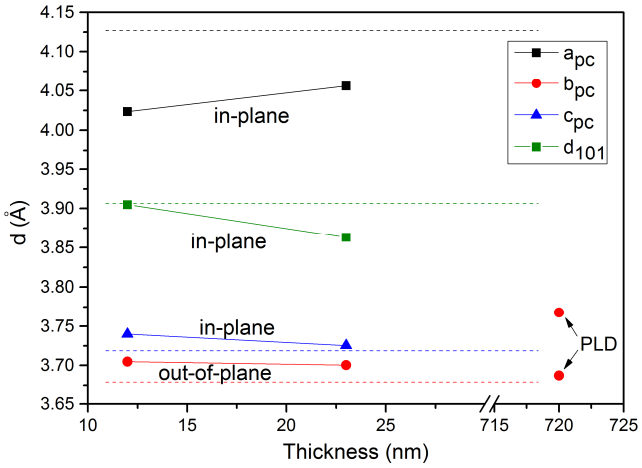

Figure VI.8. In-plane and out-of-plane lattice parameters ($a_{pc}=a/\sqrt{2}$, $b_{pc}=b/2$, $c_{pc}=c/\sqrt{2}$,) as a function of the film thickness (12 and 23 nm) for samples grown by MOCVD on STO substrate. The thick YMO films (720 nm) grown by PLD on STO substrates at two different oxygen pressures are included. Horizontal dashed lines mark the bulk values for a, b and c cell parameter of o-YMO [1].

They observed that only one in-plane distance varies (d_{100}) while the other one (d_{001}) is almost constant. Their results also show that the variation of the *a*-axis with the oxygen pressure is smaller than the variation due to the film thickness. We reproduce below Figure 2 from [4] which summarizes their findings.

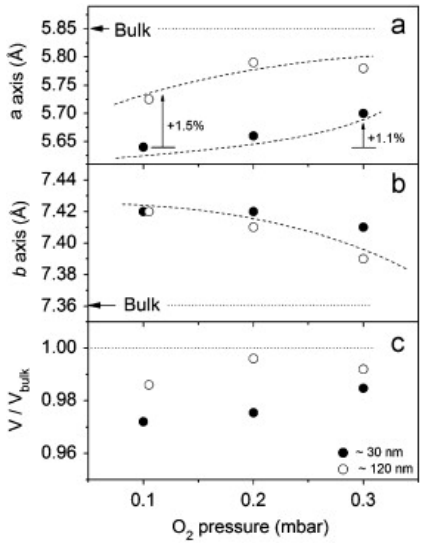

Figure VI.9. Lattice parameters of films grown at different pressures, ~30 nm thick (closed symbols) and ~120 nm thick (open symbols): (a) a-axis, (b) b-axis and (c) unit cell volume. Horizontal dashed lines correspond to the bulk values (from [4]).

Although the results obtained by Marti et al. [4] are very similar to our results, they do not show the presence of the two other domains with the *b*-axis in-plane that we have observed. We believed that this is due to the fact that the reciprocal space zone chosen for the RSM measurements does not permit to see the other types of domains.

Our PLD YMO films (see characterization details further) grown at two different oxygen pressures and very thick (720 nm) can alternatively be used as bulk references. The *b* cell parameter is represented in Figure VI.8. For the film deposited at $3 \cdot 10^{-1}$ bar, the *b* parameter is very close to the bulk value (*b*=7.374 Å), while at $1.4 \cdot 10^{-4}$ bar the *b* parameter has a larger value (7.535 Å).

Complementary TEM microstructural characterization was performed on the thinnest YMO film (12 nm) grown by MOCVD on STO. The cross section images show a dense thin film presenting a columnar growth (see Figure VI.10) with the diameter of columns (marked between dotted lines) ranging from 10 to 20 nm. These values are similar to those obtained for the YMO films on Si substrates, indicating that the columnar growth is characteristic of the MOCVD process, independently of the substrate used. From the images in Figure VI.10a and b it can observed that the columns have the same orientation starting from the bottom interface through to the top interface. Neighboring columns can have the same crystal orientation, the inter-reticular planes continuing for over two or more columns or may have different orientations as shown in Figure VI.11. This indicates a 3D growth mode with the formation of the individual columns from the same nucleating center. A relative smooth interface between film and substrate is observed (see Figure VI.10b) without amorphous or discontinuous layer as previously shown for YMO/Si films. The atomically sharp interface indicates good initial growth conditions resulting in formation of a thin and dense epitaxial layer. The measured thickness of the film was 12 nm in agreement with the values obtained by XRR, XRD and AFM. The value of the roughness is between 1.59 nm and 3.70 nm (amorphization due to sample preparation makes the estimation of the exact value of roughness difficult).

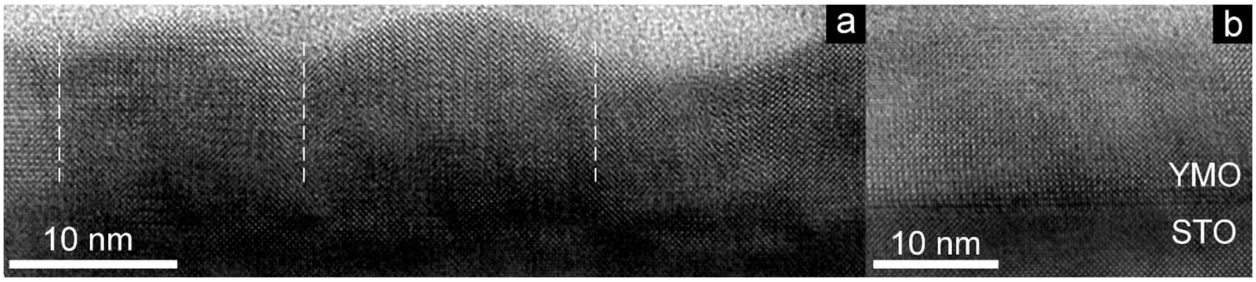

Figure VI.10. Cross section high resolution TEM images of the 12 nm thick YMO film showing: a) the columnar growth and b) the interface film-substrate.

Regarding the epitaxial domains, the TEM characterization confirms the previous XRD and RSM results: most of the domains observed in HRTEM images for the o-YMO phase have the *b*-axis oriented out-of-plane and same additional orientations are found with the *b*-axis in-plane oriented.

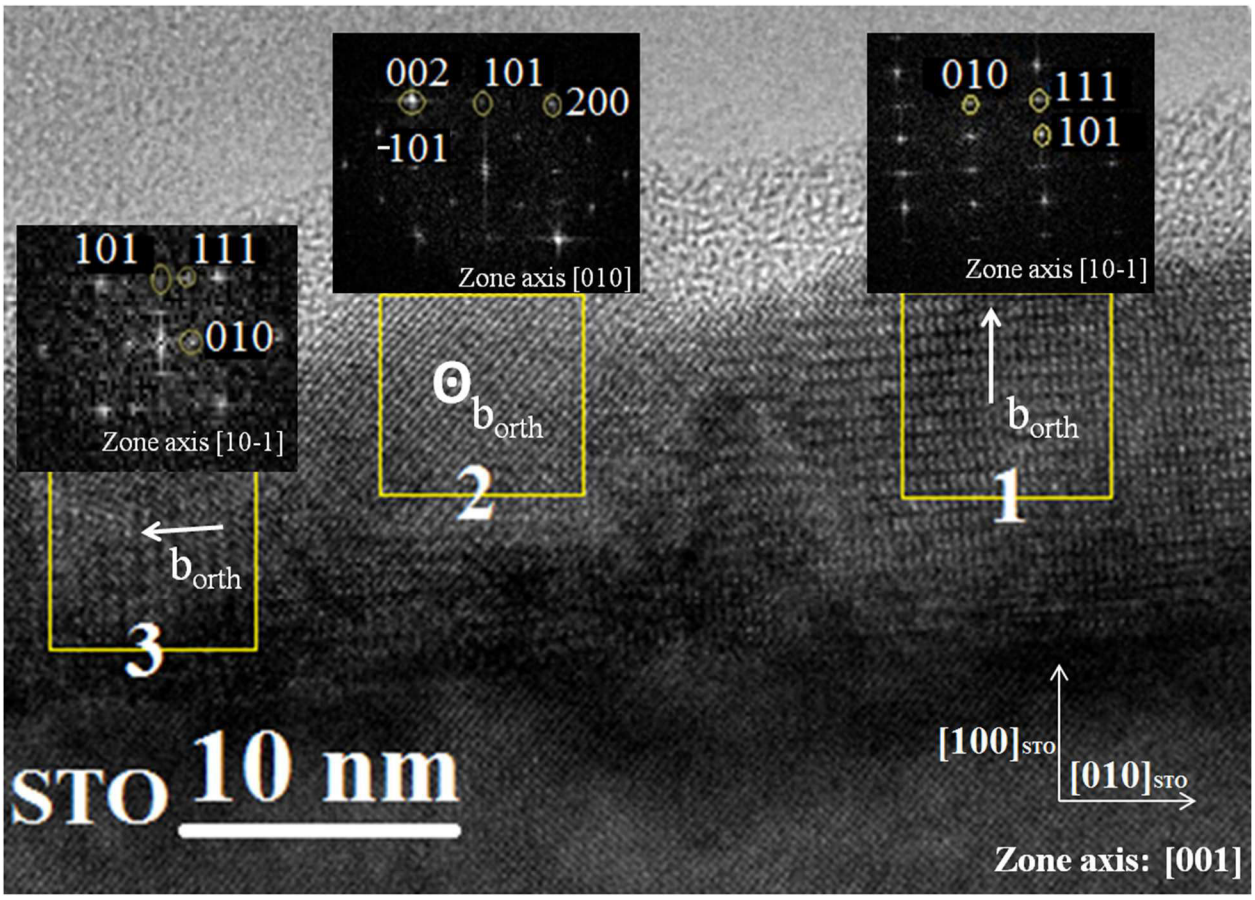

Figure VI.11. Cross-section high resolution TEM image showing three domain orientations (in the inset the corresponding FFTs).

By analyzing the HRTEM image from Figure VI.11 and the corresponding FFTs for each region marked in squares, we have determined that the o-YMO film exhibits three different orientations that corresponds to different contrasts, as follows:

region 1: $[010]_{YMO}//[100]_{STO}$, $[101]_{YMO}//[010]_{STO}$;

region 2: $[101]_{YMO}//[100]_{STO}$, $[10\text{-}1]_{YMO}//[010]_{STO}$;

region 3: $[101]_{YMO}//[100]_{STO}$, $[010]_{YMO}//[010]_{STO}$.

The orientation in the region 1 is seen in the θ-2θ XRD pattern form Figure VI.2. Note that from the TEM images and the corresponding FFTs, we cannot distinguish between [101] and [-101] directions (corresponding to a 90° in-plane rotation of *ac*-orange domains in Figure VI.1). Therefore, we have arbitrarily chosen the [101] in the following interpretations. The other two domain orientations, less abundant, could not be detected in the θ-2θ scans probably due to slight misorientations. In region 2 and 3 the *b*-axis is in-plane, i.e. perpendicular and parallel, respectively, to the plane of the paper. In region 2, the [101] and [-101] directions could be distinguish ([101] is out-of-plane and [-101] is in-plane with $d_{101}=d_{-101}=3.88(6)$ Å) and we found the value of the angle between them of 85°, which is close with the value from JCPDS card No. 16-1175 of 84°. The domains in region 2 and 3 are 90° rotated compared from one to the other.

From the three regions in Figure VI.11, the out-of-plane and the in-plane lattice parameters as well as the out-of-plane and the in-plane strain values have been obtained (see Table VI.4). The strain in the films along a given direction could be expressed by the formula $\varepsilon = (d - d_0)/d_0$, where d and d_0 are the strained and unstrained (bulk) lattice parameters, respectively, of the YMO phase.

Region	**a (Å)**	**b (Å)**	**c (Å)**	**d_{101} (Å)**	**Out-of-plane (†) misfit (%)**	**In-plane (//) misfit (%)**
1		7.46(6) †		3.85(6) //	1.40	-1.46
2	5.75(6) †		5.28(3) †	3.88(6) //	-1.48 and 0.42	-0.69
3		7.56(6) //		3.82(6) †	-2.23	2.76

Table VI.4.The in-plane and out-of-plane cell parameters derived from the TEM images for the 12 nm thick YMO film and the corresponding misfits.

Although the strain values for the in-plane d_{101} parameter in region 1 and 2 given in Table VI.4 are negative (-1.46% and -0.69%), which corresponds to a compressive strain, they are in agreement within the error bar with those measured by RSM. The *b* parameter suffers a tensile

strain (2.76%) in order to accommodate to the substrate ($2 \cdot a_{STO}$=7.81 Å). A closer look on several zones of the sample, similar to region 3, shows that at the substrate-film interface the domain is fully strained and the *b*-axis of the o-YMO phase perfectly matches the $2 \cdot a_{STO}$ value of STO substrate. This can be observed in Figure VI.12a: at the interface, the substrate and film atoms are aligned (yellow vertical lines are guides for the eyes), meaning that the growth is fully strained.

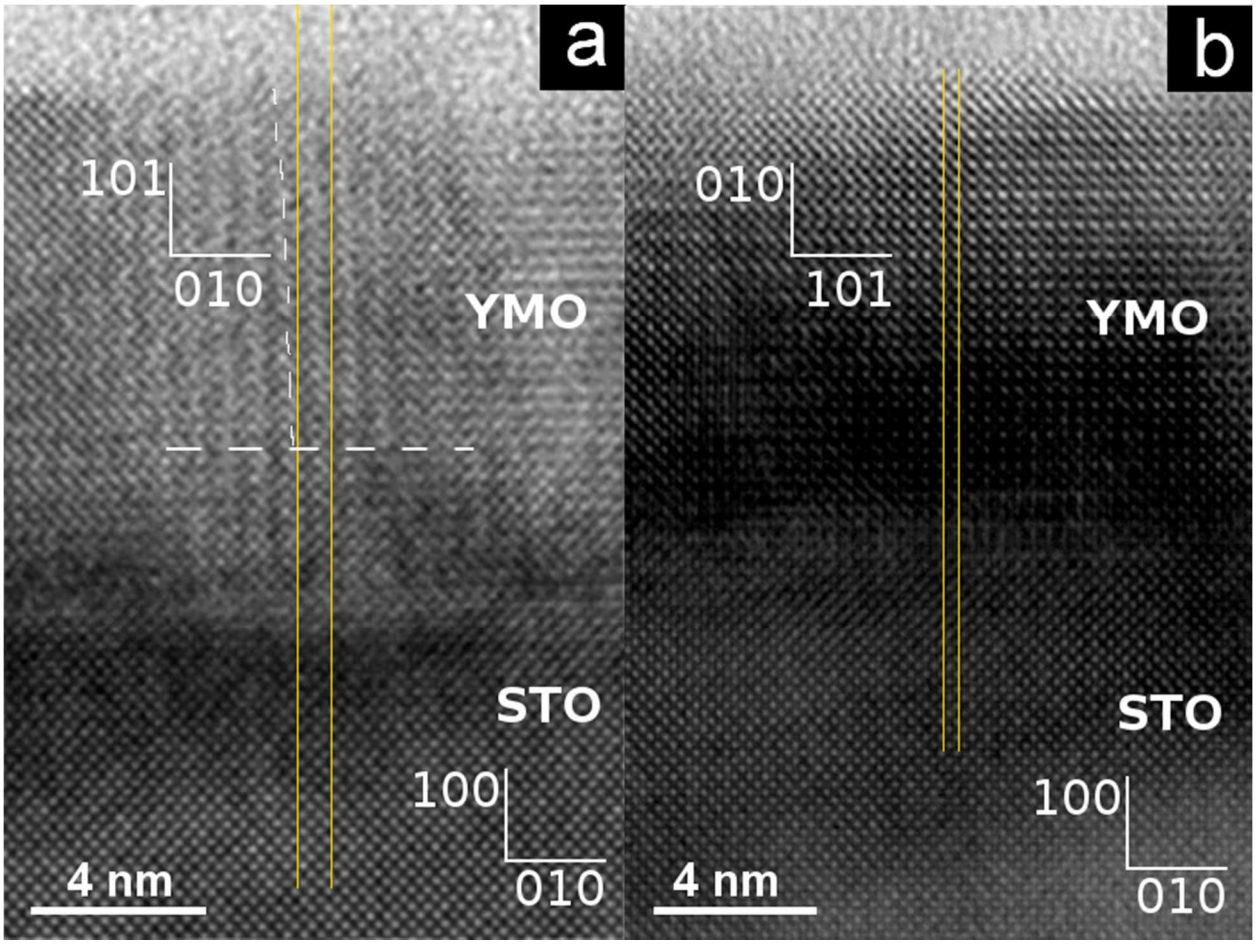

Figure VI.12. Cross-section high resolution TEM image at the interface for different domains with different strain state: (a) rapid relaxation of the b-axis when moving away from the interface with the STO substrate for domains similar to those of region 3 (dashed horizontal line indicates the critical thickness of about 3.5 nm) (b) domains similar to region 1 show no relaxation and remain fully strained (critical thickness equal to the thickness of the film). Yellow lines are guides for the eyes.

As we move away from the substrate, the atom rows become distorted and the film interplanar distance corresponding to *b*-axis increases, tending to the bulk value. The critical thickness, up to

which the film is fully strained, is close to 3.5 nm (mark by a horizontal white dashed line). Above this value, the film is progressively relaxing (the deviation from the vertical direction marked by yellow lines is indicated by the white dashed line).

For domains similar to those contained in the region 1, the strain relaxation is not occurring (see Figure VI.12b): the substrate and film atoms are vertically aligned throughout the entire film thickness (the yellow vertical lines are guide for eyes) indicating a fully strained domain in agreement with RSM results (see Figure VI.4 along $[001]_{STO}$ direction, equivalent to $[010]_{STO}$ direction in Figure VI.12b).

The chemical composition of the 12 nm thick film was investigated by EDX-TEM. The value of the Y/Mn ratio was Y/Mn=0.99. This result suggests that the film is stoichiometric. However, as the quantification of the oxygen was not possible, an oxygen excess/deficit cannot be ruled out.
The SEM images of the o-YMO films in Figure VI.13 show that the samples have an homogenous surface, with nanostructured grains with an average size of 20 nm (compatible with previous TEM results) and 40 nm for the 12 and 23 nm films, respectively. The morphology observed for the two films is consistent with a columnar growth. The difference in the grain size may be due to the film thickness and nucleation of different domains. The inset image from Figure VI.13a displays a top view AFM scan of the 12 nm film.

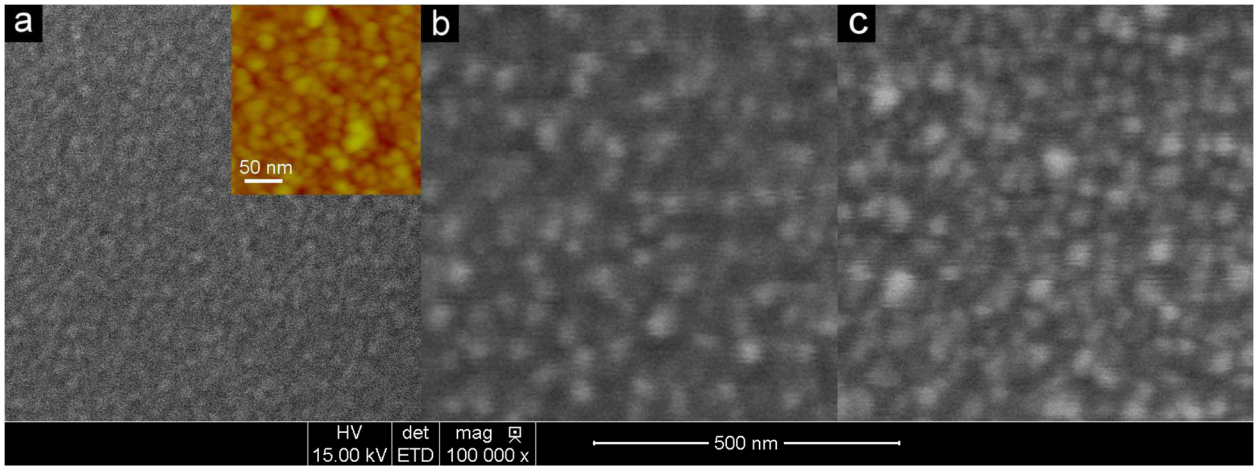

Figure VI.13. Top-view SEM images of o-YMO films on STO substrate with a thickness of: a) 12 nm (inset: the corresponding AFM image) and b) 23 nm; c) on LAO substrate with a thickness of 20 nm.

The grain size determined by AFM was between 18 and 28 nm which is in agreement with the value obtained by SEM and TEM (10-20 nm). In addition, the roughness deduced from AFM (4 nm) is close to the XRR result (1.38 nm).

o-YMO films grown on LAO substrates by MOCVD

Preliminary investigations were carried out on a 20 nm thick YMO film deposited on LAO substrate by MOCVD (see Table VI.2). Figure VI.14 shows the corresponding θ-2θ XRD pattern. All peaks can be indexed with the 202 reflections of the o-YMO phase and h00 reflections of the LAO substrate ($[101]_{YMO}//[100]_{LAO}$) indicating that *b* in-plane domains are dominant in this case, contrary to what was observed previously for the YMO films on STO substrate. The interplanar distance d_{101} of the o-YMO phase derived from the 202 reflection is d_{101}=3.886(4) Å, which is smaller than the bulk value (d_{101}=3.906 Å).

The Raman modes of the 20 nm YMO film on LAO substrate are shown in Figure VI.14 (see Appendix D for bare LAO). They are in a good agreement with the reference values (see Table VI.6), except for the A_g mode at 186.5 cm^{-1}, B_{3g} at 341 cm^{-1}, A_g at 398 cm^{-1} and B_{2g} at 620.5 cm^{-1} for which the bulk values are 188, 336, 396 and 616 cm^{-1}. This indicates slight changes in the vibration properties, in particular comparable to our previous finding for YMO films when using Si substrate (see Table IV.8 –MOCVD results, and Fig IV.30 –PLD results, in Chapter 4).

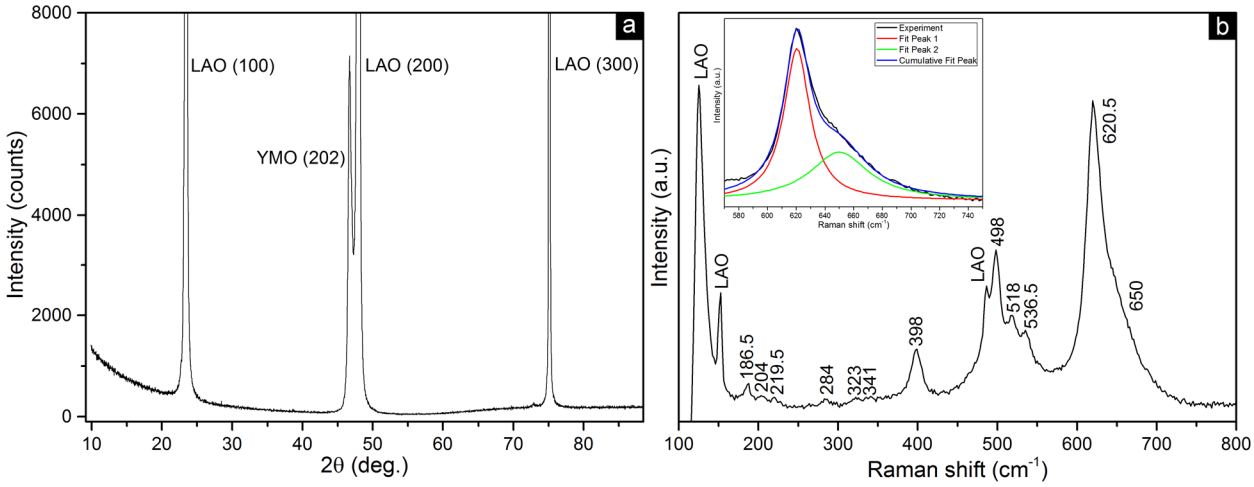

Figure VI.14. 20 nm thick o-YMO film grown on LAO substrate by PI-MOCVD: a) θ-2θ XRD pattern; b) Raman spectrum. The deconvolution of the two Raman modes in the 620-650 cm^{-1} range is shown in the inset.

These changes could be related to the particular configuration of domains (mainly *b* in-plane), non-stoichiometry of the o-YMO etc. A possible strain effect was not investigated (TEM, RSM) for this sample and further detailed investigation is necessary to fully understand these differences.

The morphology of the film, shown in the SEM image from Figure VI.13c is homogenous, with a granular surface (the average size of the grains is ~ 20 nm) consistent with a columnar growth. This morphology is very similar to that of the 23 nm YMO film on STO substrate (see Figure VI.13b).

o-YMO films grown on STO, LSAT and LAO substrates by PLD

PLD elaborations were made at two different oxygen pressures with a strong variation between the values: $1.4 \cdot 10^{-4}$ bar and $3 \cdot 10^{-1}$ bar which should permit to clearly see the effect of the oxygen on the structural properties. Four films were deposited on STO, LSAT and LAO substrates (see Table VI.5).

T_s (°C)	Y/Mn_{target}	P_{O2} (bar)	No. pulses	Y/Mn_{film}/Thickness (nm)		
				STO	LSAT	LAO
800	1	$1.4 \cdot 10^{-4}$	10000	?/?	1.14††/720	
		$3 \cdot 10^{-1}$		?/?		?/?

Table VI.5. Experimental conditions and main characteristics of the PLD YMO films on (100) STO, LAO and LSAT substrates (††EPMA, ?unmeasured).

At low oxygen deposition pressure the θ-2θ XRD patterns showed that on STO substrate the o-YMO film is purely (010)-oriented while on LSAT substrate it is (101)-oriented with a secondary (010)-orientation (see Figure VI.15a). Similar values of the *b*-axis, deduced from the *020* Bragg peaks were found for the films on STO and LSAT substrates (7.535(3) Å and 7.538(3) Å, respectively). The interplanar distance d_{101} corresponding to the 101-oriented domains on LSAT substrate is d_{101}=3.902(3) Å. At high oxygen deposition pressure the θ-2θ XRD patterns showed that the films are purely (010) and (101)-oriented for STO (not shown) and LAO substrates (see Figure VI.15b), respectively, with the corresponding spacings of 7.374(3) Å and 3.897(3) Å.

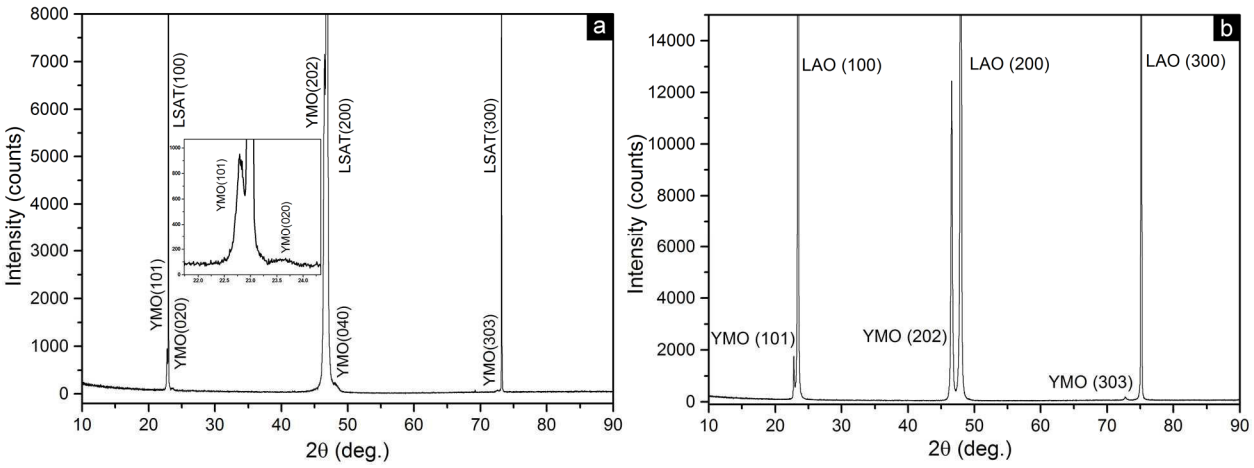

Figure VI.15. θ-2θ XRD patterns of the PLD o-YMO films deposited on: a) LSAT substrate at $1.4 \cdot 10^{-4}$ bar (inset: enlargement between 22°< 2θ<24° showing both b in-plane and out-of-plane domains) and b) LAO substrate at $3 \cdot 10^{-1}$ bar.

Fig. VI.16 summarizes the cell parameters of the films grown by PLD. Almost all the values are close to the bulk values as expected for thick samples. However, a significant difference is observed for the *b* lattice parameter obtained from the XRD patterns of the high and low P_{O2} deposited YMO films on STO substrates.

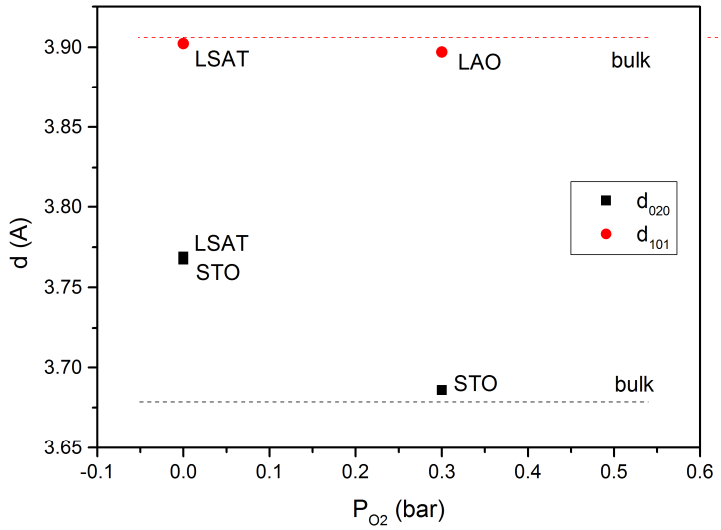

Figure VI.16. Cell parameters for the YMO films grown by PLD on STO, LAO and LSAT substrates at different oxygen pressures.

The $b_{o\text{-}YMO}$ value obtained from the film deposited at $P_{O2}= 3 \cdot 10^{-1}$ bar is very close to the bulk value (*b*=7.3571 Å), while it is 2.42 % larger when obtained from the film deposited at $P_{O2}= 1.4 \cdot 10^{-4}$ bar

(see Figure VI.16). Such an increase of the *b*-axis should lead the Raman modes to shift in wavenumber, especially the B_{2g} mode at 616 cm^{-1} which corresponds to vibrations of the octahedra along the *b*-axis. This is in agreement with the Raman observations. Indeed, for the YMO film deposited on STO substrate at P_{O2}= $3 \cdot 10^{-1}$ bar, the *b*-axis is close to the bulk value and the B_{2g} Raman mode is observed at 617 cm^{-1}, which is close to the bulk position (616 cm^{-1}). Contrariwise, for the films deposited at low oxygen pressure (P_{O2}= $1.4 \cdot 10^{-4}$ bar), the B_{2g} mode shifts toward higher wavenumbers (620.5 and 619.5 cm^{-1} for YMO/STO and YMO/LSAT, respectively). Table VI.5 summarizes the experimental data for the four films (see Appendix D for the spectra of bare substrates).

	P_{O2}=1.4·10^{-4}		**P_{O2}=3·10^{-1} bar**		**Iliev et al. [5]**
	YMO/STO	**YMO/LSAT**	**YMO/STO**	**YMO/LAO**	
Ag/B2g			150.5	150.5	151
Ag		183	185.7	185	188
B2g		219.2		219.7	220
Ag/ B1g		284.4		285	284/288
Ag		323		322.3	323
B3g		-		337	336
Ag		397.3	396	396	396
Ag	492	494.6	496	496	497
Ag			517.7	517.7	518
B2g	532	533	536	536	537
B2g	620.5	619.5	617	617	616
				650	653

Table VI.6. Raman wavenumbers of the o-YMO phase for various YMO films deposited by PLD and of the bulk o-YMO phase [5].

The microstructure and surface topography of YMO films prepared by PLD was investigated by SEM. At both deposition pressures, the films generally have very smooth and homogenous surfaces, except for a few isolated regions where spherical shaped particles are found (droplets from the target as indicated in [6]). The morphology of the YMO films deposited at $1.4 \cdot 10^{-4}$ bar on STO and LSAT substrates (Figure VI.17a and c) presents polygonal shaped grains of around 30 nm in size, very dense with grain boundaries almost invisible. The YMO films deposited at $3 \cdot 10^{-1}$ bar on STO and LAO substrates (Figure VI.17b and d) exhibit the characteristics of a columnar microstructure with well-defined round-shape grains with a diameter between 20 and 30

nm. On small regions in the 100-200 nm range (marked by the dotted zones in Figure VI.17b), the grains are aligned according to certain directions.

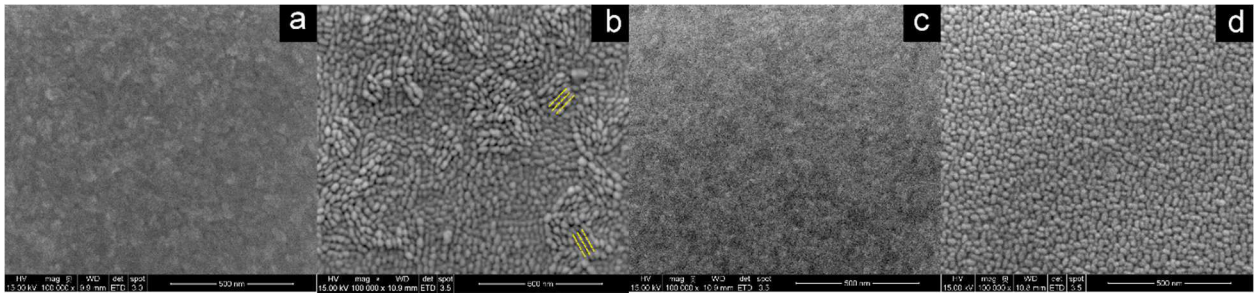

Figure VI.17. Top view SEM images of the PLD deposited films on STO ((a)- $1.4 \cdot 10^{-4}$ bar and (b) $3 \cdot 10^{-1}$ bar), LSAT ((c)- $1.4 \cdot 10^{-4}$ bar) and LAO ((d)- $3 \cdot 10^{-1}$ bar) substrates.

6.2 Magnetic characterization

Figure VI.18 shows the M(T) curve in the ZFC and FC mode for the o-YMO film deposited by MOCVD on STO substrate with a thickness of 12 nm (see Figure VI.2). A kink in the ZFC curve at T=50 K, followed by a drop in the magnetization indicate an antiferromagnetic behavior.

As shown in the Figure VI.18b, a linear variation in the M(H) curve (although not complete) is observed at room temperature, as expected for a paramagnetic behavior. At low temperature the M(H) curve is linear and confirms the antiferromagnetic ordering resulted from M(T) (the negative slope is due to the diamagnetic contribution of the STO substrate - see Appendix D -, which was not subtracted from the raw data).

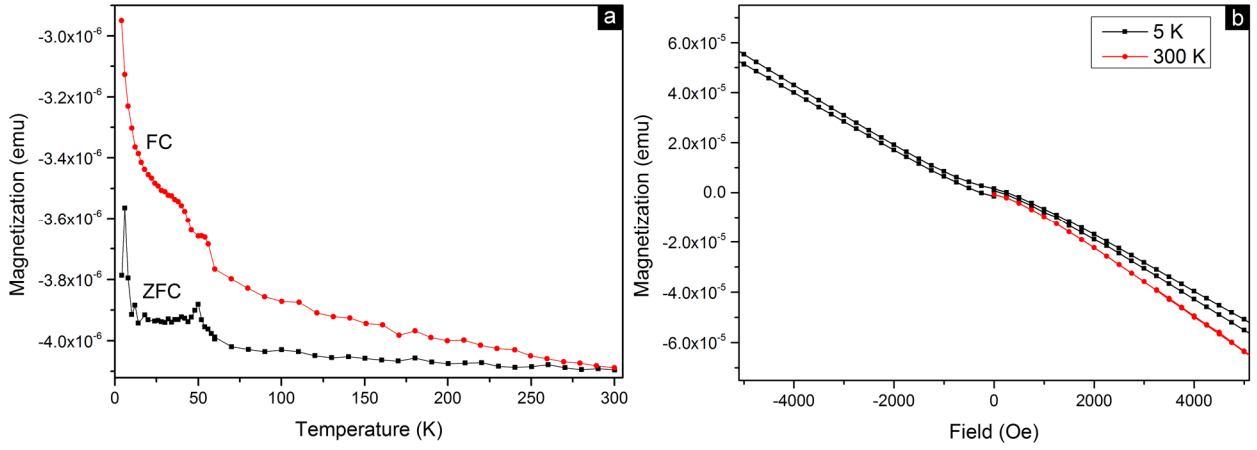

Figure VI.18. Temperature dependence of the magnetization (M(T)) for 12 nm thick YMO/STO film. b) Field dependence of the magnetization (M(H)) at 5 and 300 K (enlargement of the M(H) curve in the -5000 to 5000 Oe range).

Figure VI.19 shows the M(T) and M(H) curves for the YMO/STO films deposited by PLD at two different P_{O2}: $1.4 \cdot 10^{-4}$ bar (YMO-STO-6 film in black) and $3 \cdot 10^{-1}$ bar (YMO-STO-7 in red). A splitting of the ZFC-FC curves, with a maximum in the ZFC curve at T_f= 28 K (YMO-STO-6) and T_f= 42 K (YMO-STO-7), indicates a spin glass-like behavior. The differences in the ordering temperatures are probably due to the different oxygen pressures during the elaboration. A nonstoichiometry in the O_2 generates Mn^{4+} cations, beside the Mn^{3+} cations. The coupling between the Mn^{3+} and Mn^{4+} is ferromagnetic (double exchange coupling).

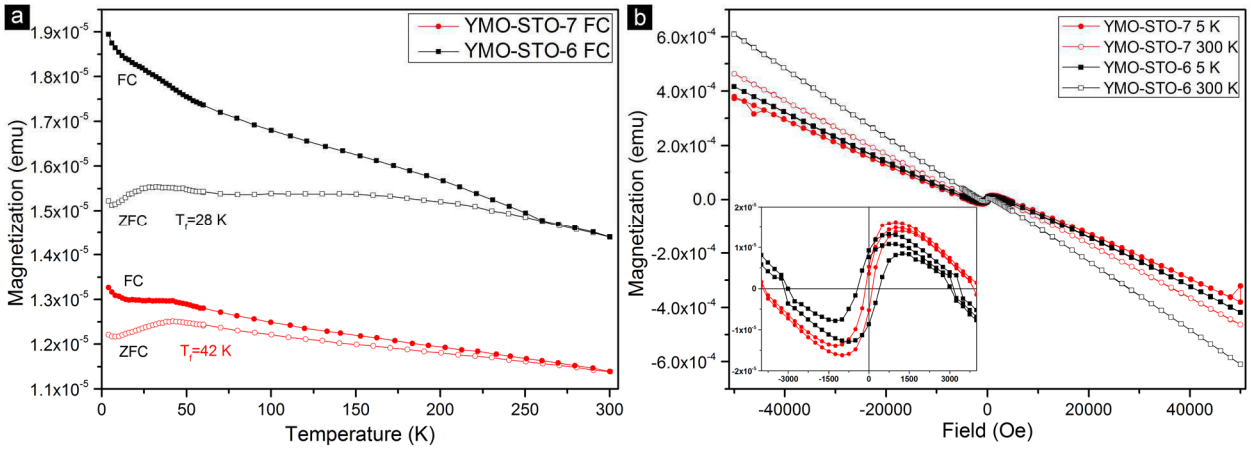

Figure VI.19. a) Temperature dependence of the magnetization (M(T)) for the YMO/STO films deposited by PLD at two different P_{O2}: $1.4 \cdot 10^{-4}$ bar (YMO-STO-6 film in black) and $3 \cdot 10^{-1}$ bar (YMO-STO-7 in red); b) Field dependence of the magnetization (M(H)) at 5 and 300 K (in the inset: enlargement of the M(H) curve in the -5000 to 5000 Oe range).

Figure VI.19b shows the M(H) curves for the two films at 5 and 300 K. It is observed that a hysteresis loop is present at 5 K (see inset of Figure VI.19b) for both films, which indicates a ferromagnetic contribution.

Figure VI.20 shows the M(T) and M(H) curves for the YMO/LSAT film deposited by PLD at $P_{O2}=1.4 \cdot 10^{-4}$ bar (YMO-LSAT-6). Contrarily to the corresponding YMO film on STO substrate (YMO-STO-6), the magnetization M(T) in the ZFC mode (see Figure VI.20a) does not show any decrease and the signal is mostly negative indicating that the contribution of the film is negligible compared to that of the LSAT substrate (see Appendix D).

The M(H) curves at 5 and 300 K shown in Figure VI.20b display negative slopes, characteristic of diamagnetic materials. A very small loop in the M(H) curve at 5 K indicates a small ferromagnetic contribution.

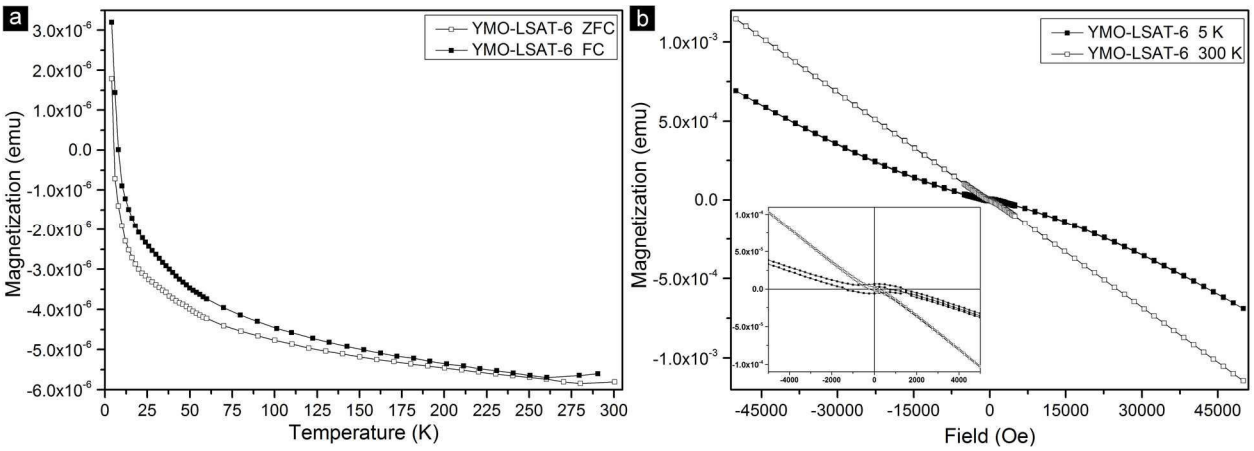

Figure VI.20. Magnetization behavior of the YMO-LSAT-6 film deposited by PLD at P_{O2} = $1.4 \cdot 10^{-4}$ bar: a) temperature dependence of the magnetization (M(T)) and b) field dependence of the magnetization (M(H)) at 5 and 300 K (in the inset: enlargement of the M(H) curve in the -5000 to 5000 Oe range).

6.3. Structural study of non-stoichiometric YMO films

We analyze hereafter the effect on structural properties of non-stoichiometric YMO films grown by MOCVD on (100)-oriented STO, LSAT and LAO substrates. Non-stoichiometry was obtained by using different Y/Mn ratios in the initial solution of precursors. A potential thickness effect on structural properties and/or chemical compositions was also investigated. For this purpose, films with different thicknesses were grown by using a variable number of injections at a fixed Y/Mn ratio in the initial solution. Table VI.7 summarizes the experimental conditions and the main characteristics of these films.

EPMA experiments show that samples deposited with increasing Y/M ratio in the injected solution and with a fixed number of injections (4000) have a ratio Y/Mn_{film} increasing from 0.52 to 0.75 and an average thickness of about 285 ± 45 nm (if non reliable data is excluded). For the samples with increasing number of injections (500 to 4000) and with a fixed Y/Mn ratio in the solution, thicknesses increase from 20 to 370 nm and Y/Mn in the films has an average value of about 0.59 ±0.1 (excluding non-reliable data). Figure VI.21 summarizes these results (this analysis was

previously presented in Chapter III when discussing the optimization of the MOCVD growing conditions; see Figure III.9 and 10).

T_s (°C)	**$Y/Mn_{solution}$**	**No. inj.**	**P_{O2} (bar)**	**Y/Mn_{film}**			**Thickness (nm)**		
				STO	LSAT	LAO	STO	LSAT	LAO
800	0.25	4000	$3.33 \cdot 10^{-3}$	?	0.52	0.56	?	320	240
	0.3	4000		?	0.66	0.63	?	260	120
	0.35	4000		?	0.75	0.74	?	330	290
	1	4000		?	-	?	?	-	?
800	0.325	500	$3.33 \cdot 10^{-3}$	?	0.46	0.61	15	30	20
		1000		?	0.59	0.65	?	70	50
		2000		?	0.65	0.74	?	130	100
		4000		?	?	0.64	?	?	370

Table VI.7. Experimental conditions and main characteristics of the YMO films grown by MOCVD in the vertical geometry on (100)-oriented STO, LSAT and LAO substrates. Top: films obtained with different Y/Mn ratios in the injected solution and fixed number (4000) of injections. Bottom: films obtained from a variable number of injections and a fixed Y/Mn ratio (0.325) in the injected solution. From left to right columns: MOCVD deposition temperature (T_s), Y/Mn ratio used in the injected solution of precursors ($Y/Mn_{solution}$), number of injections used in the deposition (No. inj.), deposition oxygen pressure used in the reactor (P_{O2}) (mixture of 50 % O_2 and 50 % Ar), Y/Mn ratio measured in the film by EPMA (Y/Mn_{film}) and thickness of the film deduced from EPMA. Green values correspond to reliable EPMA results while black values correspond to unsatisfactory results (bad agreement in EPMA analysis). Question marks correspond to unmeasured samples.

It can be observed from Figure VI.21a that the Y/Mn in the film increases with the increasing Y/Mn in the solution. A variation of 40% of the Y/Mn in the solution generates almost the same variation in the film. This indicates that a good control over the film composition can be achieved by varying the Y/Mn in the initial solution. Similarly, the film thickness estimated from EPMA increases with the number of injections (see close symbols in Figure VI.21b). This variation deviates from a linear behavior at high number of injections. Although the Y/Mn in the injected solution is constant (Y/Mn=0.325), the Y/Mn in the films shows a dependence with the films thickness (see open symbols in Figure VI.21b). A similar dependence is observed for all the

measured samples (on top of LSAT and LAO substrates). As the samples with a same thickness (LAO, STO and LSAT) are grown at the same time, it appears that the composition variation is related to either an experimental artifact or an imprecision of our EPMA analysis.

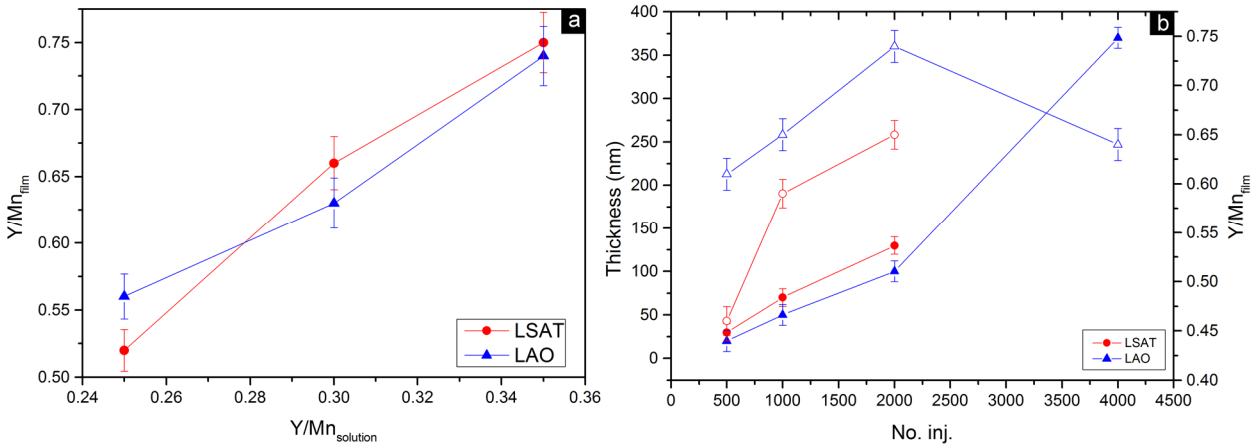

Figure VI.21. EPMA results for YMO films on LAO and LSAT substrates. a) Variation of the Y/Mn_{film} as a function of the increasing $Y/Mn_{solution}$; and b) Evolution of the film thickness (close symbols) and the Y/Mn_{film} (open symbols) as a function of the number of injections in the precursor solution.

The variation in composition is relatively high and comparable to that obtained for fixed number of injections and varying the Y/Mn ratio. This behavior clearly shows that it will be very difficult to discriminate between the thickness effect and the composition effect on the structural and physical properties of the films deposited with injections between 500 and 4000. For this reason they will not be analyzed in detail (only their composition dependence will be included) in the following. Our analyses will be focused on the films obtained by varying the Y/Mn ratio in the injected solution with a fixed number of injections. For these samples, the thickness presents some variations which can be related to experimental artifacts (different batch of samples for each ratio, different positions in the reactor, etc). However, this variation is relatively small and no systematic errors are expected.

It can be observed in Table VI.7 that the average composition Y/Mn_{film} shows very large variations from the stoichiometric formula $YMnO_3$, which is a strong indication that secondary phases may be present in the films. Indeed XRD, RSM and GIXRD results have identified two phases e.g. for the films deposited with $Y/Mn_{solution} \leq 0.35$ o-YMO and YMn_2O_5 are present (see Figure VI.22); for the films deposited with $Y/Mn_{solution}=1$, o-YMO and Y_2O_3 are observed. These results are in

agreement with the ideal composition discussed in Chapter 3 ($Y/Mn_{solution}$ to obtain pure o-YMO films is close to 0.5 for the vertical MOCVD reactor) from which it was expected that rich Mn phase (as YMn_2O_5) will be present when $Y/Mn_{solution} < 0.5$ and rich Y phase (as Y_2O_3) will be present when $Y/Mn_{solution} > 0.5$.

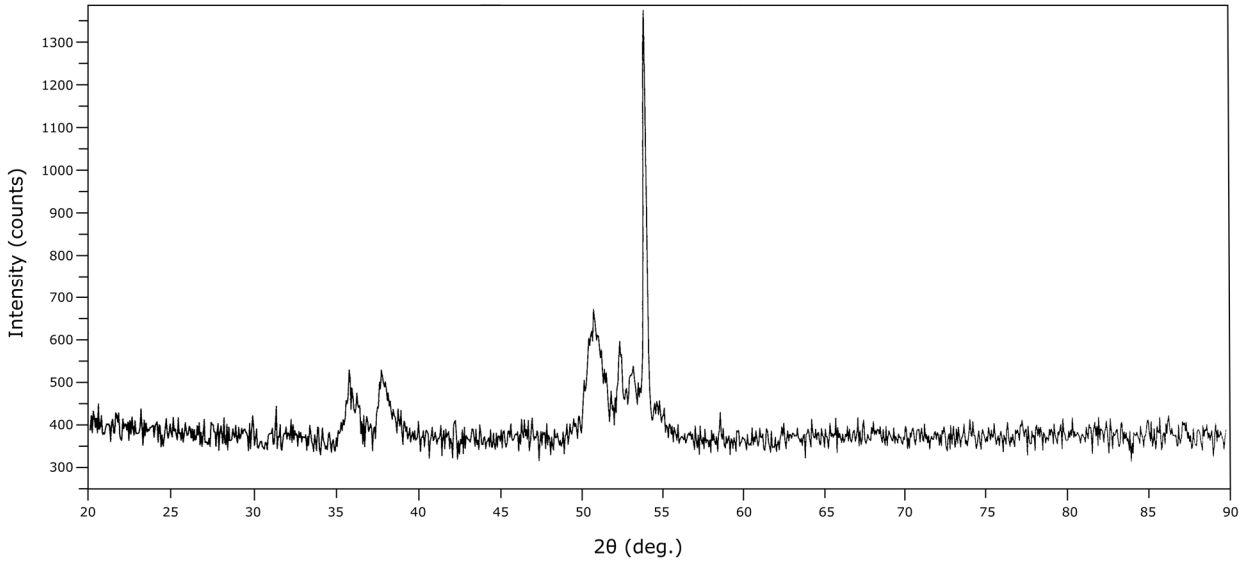

Figure VI.22. GIXRD pattern of YMO film deposited on STO substrate (Y/Mn=0.325 and no. inj.= 2000). The main peaks are indexed with the YMn_2O_5 phase (the narrow peak at $2\theta \approx 54°$ originates from multiple diffractions of the STO substrate).

As shown in the Figure VI.22 the identification of YMn_2O_5 secondary phase is clear when using GIXRD (for film with Y/Mn=0.325 and no. inj.=2000). However, the corresponding θ-2θ XRD pattern (Figure VI.23a, bottom part Y/Mn=0.325, no. inj.=2000) performed on the same sample do not show any evidence of secondary phase and reveals only the presence of epitaxial $(010)_{YMO}$ domains, showing the limitation of the θ-2θ XRD for identifying secondary phases. Indeed, only scarce secondary phases are seen in these patterns. A few samples present additional peaks at 2θ=31° and/or 2θ=38° but they could be indexed with the 200 and 112 reflections of the o-YMO phase (see Figure VI.23a and b). A secondary phase can be identified in the films deposited with Y/Mn=0.35 and 1 on STO substrate and with Y/Mn=1 on LAO substrates (see additional peaks in Figure VI.23a and c): it is the Y_2O_3 phase obtained by epitaxial growth on top of LAO substrate ($[100]_{Y2O3}//[100]_{LAO}$, see Figure VI.23c). The presence of Y_2O_3 is expected as an excess of Y is present in the injected solution (the optimum ratio being around 0.5). The peaks observed for films

on top of STO substrate (Y/Mn=0.35 and 1) were also assigned to this phase (as 222 and 433 reflections).

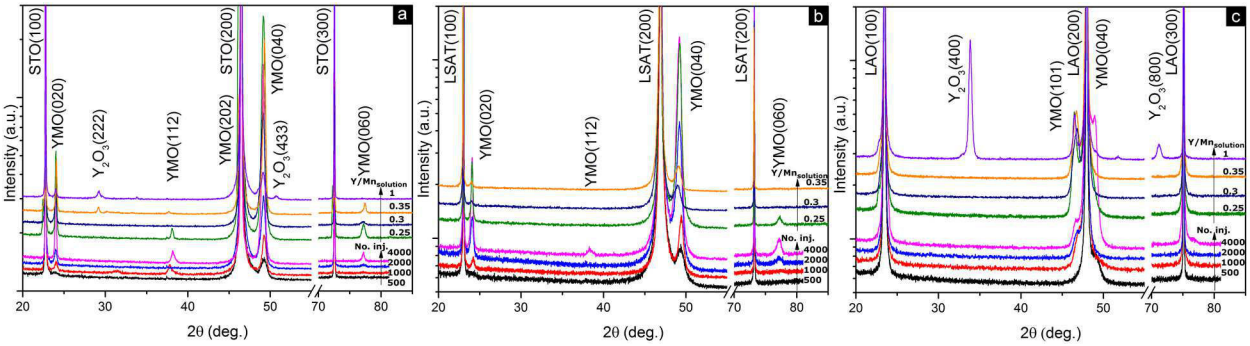

Figure VI.23. θ-2θ XRD patterns of o-YMO films grown on top of STO (a), LSAT (b) and LAO (c) substrates. The patterns represented in the bottom part correspond to thickness varying samples (Y/Mn=0.325 and No. inj. from 500 to 4000) and those in the top part to the varying composition (0.25 < $Y/Mn_{solution}$ < 1, No. inj. 4000) – see Table VI.7 for thicknesses and Y/Mn_{film}.

The θ-2θ XRD patterns performed on all YMO films on STO, LSAT and LAO substrates show the o-YMO phase with an epitaxial growth representing a fraction of the film. This fraction of o-YMO phase grows mainly with $(010)_{YMO}$ domains for STO and LSAT substrates ($[010]_{YMO}$//$[100]_{STO/LSAT}$) and mainly with (101) domains for LAO substrate ($[101]_{YMO}$//$[100]_{LAO}$).

	No. inj.	**500**	**1000**	**2000**	**4000**
YMO/LSAT	**Thickness (nm)/Y/Mn$_{film}$** (EPMA)	30	70	130	?
		0.46	0.59	0.65	
	Thickness XRR (nm)	15			
	Thickness from I$_{Net\ Area}$ (nm)	8	20	50	80
	Fraction o-YMO (%)	27	29	38	

Table VI.8. Estimation of the fraction of o-YMO phase present in the film based on thickness evaluation from XRD peaks net area ($I_{Net\ Area}$), EPMA and XRR.

From the net area of the diffraction peaks of the o-YMO films grown on top of LSAT substrate ($Y/Mn_{solution}$=0.325 and no. inj. from 500 to 4000, see Table VI.7), the thickness of the fraction of o-YMO phase was roughly evaluated and is represented in Table VI.8 together with the thickness deduced by EPMA (XRR measurement, slightly different from EPMA results, on one sample is also included).

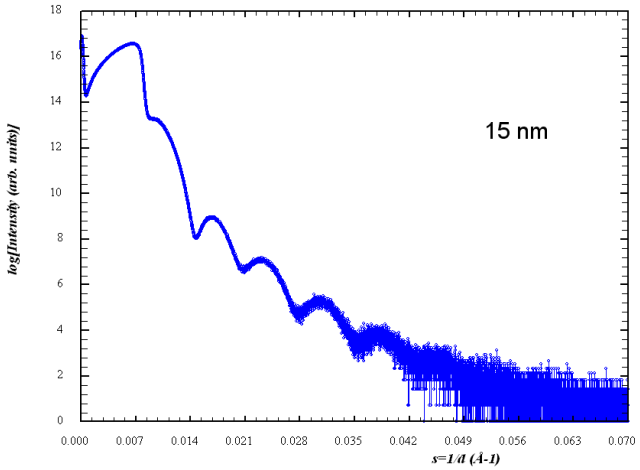

Figure VI.24. XRR pattern of the YMO film deposited on LSAT substrate ($Y/Mn_{solution}$=0.325, no.inj.= 500) showing the thickness.

It can be deduced that about 27 to 38 % of the films is made of o-YMO phase. Note that this evaluation is consistent when considering an average ratio of Y/Mn_{film} (EPMA) close to 0.6 (deduced for reliable data from the thickness series). The composition of the film can be decomposed considering the presence of YMn_2O_5 as secondary phase as $Y_{0.6}Mn_1O_x$ = $0.2YMnO_y$ + $0.4YMn_2O_z$ that is 33% of $YMnO_3$ and 66% of YMn_2O_5. One should keep in mind that these evaluations are limited by the fact that EPMA analysis was performed by considering a uniform composition (i.e. single phase or phases with same composition) and in particular the exact composition determination of the o-YMO phase is not possible without further investigations.

Despite these limitations we present in the following a characterization of the fraction of o-YMO present in the non-stoichiometric films. Note that the chemical composition of the YMO films obtained by EPMA and used in the following in our analyses, represents the average composition of the films, including the secondary phases.

The out-of-plane lattice parameters or d-spacings (d_{020} for the films on STO and LSAT substrates and d_{101} for LAO substrate) deduced from the Bragg peaks in Figure VI.23 are represented in Figure VI.25 as function of the Y/Mn_{film} (the open symbols represent the films deposited at constant $Y/Mn_{solution}$ and variable number of injections, the closed symbols represent the films with constant number of injections and variable $Y/Mn_{solution}$).

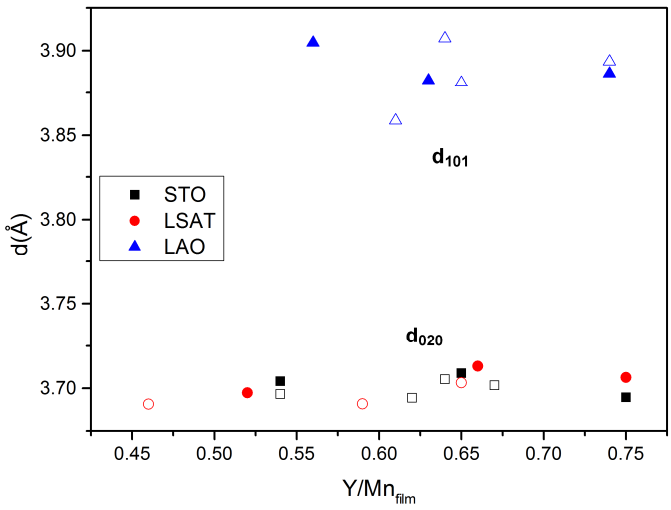

Figure VI.25. Out-of plane d_{020} and d_{101} spacings for films on STO (open and closed black square), LSAT (open and closed red circle) and LAO (open and closed blue triangles) substrates as a function of composition. Close symbols (resp. open symbols) are for films which present mainly a composition dependence (resp. both a thickness and composition dependence).

It can be observed that the out-of-plane d_{020} distance for the YMO films on STO and LSAT substrates ranges from 3.690 Å (*b*=7.380 Å) to 3.713 Å (*b*=7.426 Å). This range of values, groups together films which present mainly a composition dependence and films which present both a thickness and composition dependence without any particular tendency. A similar behavior is observed for the d_{101} distance for YMO films on LAO substrate (ranges from 3.860 to 3.907 Å). These results are not surprising considering the presence of secondary phases. Indeed, the composition Y/Mn_{film} is an average composition and not the composition of the o-YMO phase and, thus, no direct correlation could be made. The small variations of the d_{020} and d_{101} distances indicate that a similar o-YMO phase, with regard to the stoichiometry, is grown on all substrates.

To further characterize the YMO films, RSM measurements obtained around the (200) symmetric and (031) asymmetric reflections of the substrate and the (040) symmetric and (161) asymmetric reflections of the film were performed on all films with Y/Mn=0.325 and number of injections from 500 to 4000 (see Appendix E). The out-of-plane and the in-plane lattice parameters derived from the RSM scans are plotted in Figure VI.26 for YMO films on STO, LSAT and LAO substrates. Note that on LAO substrate only the YMO films with 500 and 4000 injections have (010) domains. The d_{020} out-of-plane distances deduced from the $(040)_{YMO}$ RSM reflections (STO and LSAT) are equal (within the error bars) with those derived from the θ-2θ XRD patterns of the

films with different Y/Mn ratio in the injected solution (0.25 < Y/Mn < 1) marked by the horizontal dashed lines.

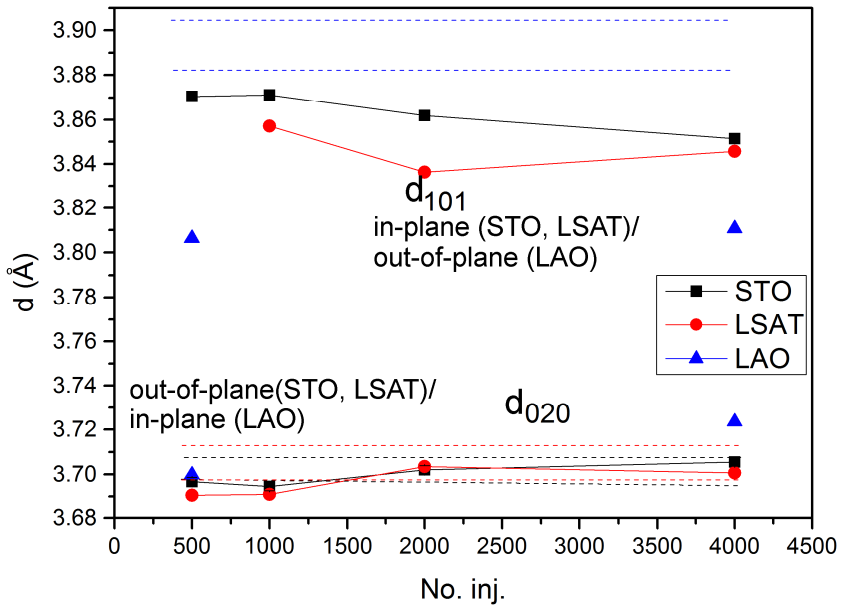

Figure VI.26. Out-of-plane (d_{020} for films on STO and LSAT substrate and d_{101} for those on LAO substrate) and in-plane (d_{101} for films on STO and LSAT substrate and d_{020} for those on LAO substrate) d-spacings extracted from RSM as function of the number of injections (Y/Mn=0.325). Horizontal dashed lines show the variation of the out-of-plane cell parameters derived from the θ-2θ XRD patterns of the films with different Y/Mn ratio in the injected solution (0.25 < Y/Mn < 1) on STO (in black), LSAT (in red) and LAO (in blue) substrates.

It can be observed from Figure VI.26 that the in-plane d_{101} distance is similar (although some minor differences exist) for the films grown on STO and LSAT substrates. The d_{101} values decrease from ~ 3.870 Å (for 20 nm YMO films) to ~ 3.836 (for 370 nm YMO films) moving away from the theoretical bulk value d_{101}=3.906 Å with the increase of the film thickness. This behavior is not expected from a relaxation mechanism as it has been observed in Figure VI.8 for 12 nm and 23 nm films on STO substrates and it is a further confirmation that the film thickness does not play any role in the strain mechanism; all the films are relaxed. The same behavior is observed for in-plane d_{020} distance of the YMO films on LAO substrate. Furthermore, the variation of the out-of-plane parameter due to the film thickness and that of the film composition has the same order of magnitude, indicating that the lattice parameters differences are due to a non-stoichiometry of the o-YMO phase.

Finally, the intensity of the RSM reflection spots (040 and 161) corresponding to the YMO films (see Appendix E) and the intensity measured in the θ-2θ XRD patterns increase with the film thickness.

Figure VI.27 shows the Raman shift evolution of the most intense Raman mode (B_{2g}) with the average Y/Mn_{film} for the YMO films deposited on LAO and LSAT substrates (see Appendix F for raw data). The values for the YMO films on STO substrates are in the same range (for simplicity and because of the uncertainties due to the intense substrate signal, they are not shown). It is observed that for all YMO films on either LAO or LSAT substrates, the B_{2g} mode is shifted toward high wavenumbers in comparison with the bulk. All the values are in the range 620-623 cm^{-1}, suggesting that the o-YMO phases present in the films have similar compositions, different from the stoichiometric $YMnO_3$, in agreement with the previous XRD and RSM results.

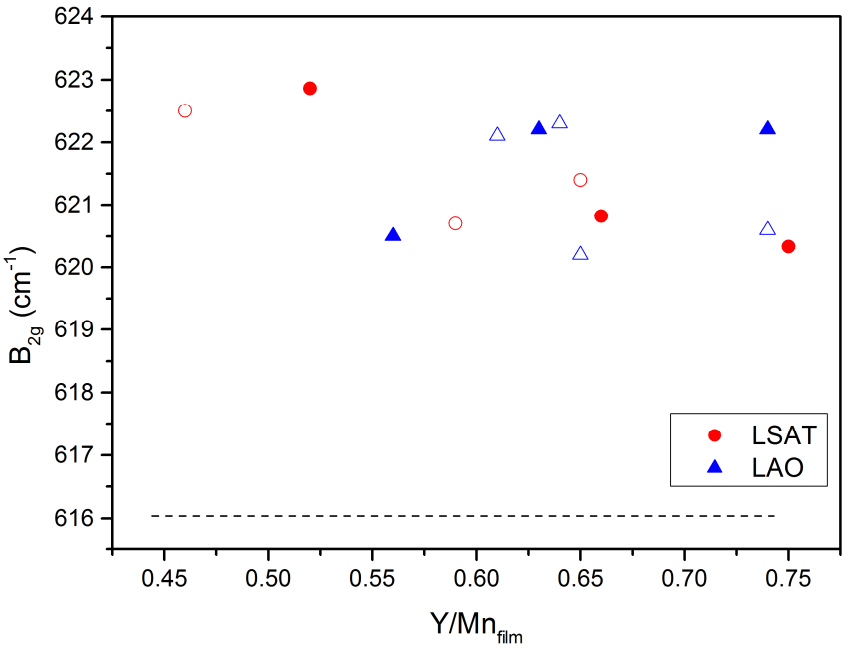

Figure VI.27. Composition dependence of the B_{2g} Raman shift in YMO films on LAO and LSAT substrates. Close symbols (resp. open symbols) are for films presenting mainly a composition dependence (resp. both a thickness and composition dependence). The dashed line represents the reference bulk value.

6.4. Magnetic characterization of non-stoichiometric YMO films

The magnetism of the non-stoichiometric films deposited on STO, LAO and LSAT substrates is more complex as the secondary phases (e.g. YMn_2O_5) are also magnetic and a discrimination of these contributions is impossible to establish. The antiferromagnetic YMn_2O_5 presents a transition from paramagnetic to antiferromagnetic at T_N=45 K modulated by an incommensurate magnetic ordering. A lock-in transition toward a commensurate magnetic phase takes place at T=39 K. The magnetic structure experiences a transition into a different incommensurate phase at T=19 K [7].

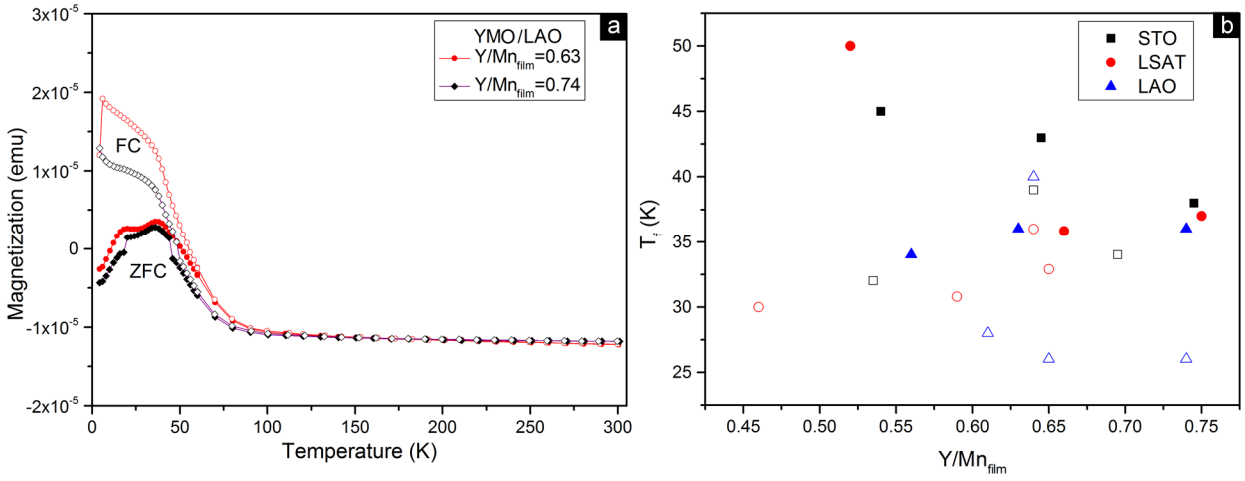

Figure VI.28. a); Temperature dependence of the magnetization (M(T) for the YMO/LAO films deposited with no. inj.=4000 and at two different $Y/Mn_{solution}$ (0.35 and 0.30) corresponding to Y/Mn_{film}=0.74 (in black) and Y/Mn_{film}=0.63 (in red); b)The freezing temperature (T_f) as derived from the ZFC curves for the YMO films on STO, LAO and LSAT substrates (the open symbols represent the films deposited at constant $Y/Mn_{solution}$ ratio and variable number of injections and the close symbols those with constant number of injections and variable $Y/Mn_{solution}$ ratio).

The M(T) magnetizations for all YMO films display a splitting of the ZFC-FC curves, indicating a spin-glass ordering, with a maximum in the ZFC curve at different temperatures. Figure VI.28b shows these maxima (T_f) as function of the Y/Mn_{film} ratio. A large spreading of the data is observed between 25 and 50 K. In some cases two kinks are observed in the ZFC curve, which are associated to both o-YMO and secondary phases. An example is shown in Figure VI.28b for the YMO films on LAO substrate (see Appendix G for more examples).

6.5 Summary and conclusions

o-YMO films, grown by both **MOCVD** and **PLD** techniques present a dense microstructure and homogenous surfaces, without aggregates of particles, independently of the substrate. The **MOCVD** produces a columnar growth with columns diameter between 10 and 20 nm and a smooth interface film-substrate. The morphology of the films grown by **PLD** depends on the O_2 pressure: very dense polygonal shaped grains, around 30 nm in size, are obtained at low P_{O2} ($1.4 \cdot 10^{-4}$ bar) while at higher P_{O2} ($3 \cdot 10^{-1}$ bar) round shaped grains, between 20 and 30 nm and compatible with a columnar growth are produced.

Epitaxial o-YMO films are mainly (010)-oriented on STO and LSAT substrates and (101)-oriented on LAO substrate. Detailed studies on 12 nm and 23 nm thick YMO/STO films have shown, in fact, that four types of domains are present. This is equivalent to having two types of domains, 90° in-plane rotated, with the following epitaxial relationships:

- $[010]_{YMO}//[100]_{STO}$ and $[100]_{YMO}//[011]_{STO}$
- $[010]_{YMO}//[100]_{STO}$ and $[100]_{YMO}//[0\text{-}11]_{STO}$
- $[10\text{-}1]_{YMO}//[100]_{STO}$ and $[010]_{YMO}//[010]_{STO}$
- $[10\text{-}1]_{YMO}//[100]_{STO}$ and $[010]_{YMO}//[001]_{STO}$

The *b* and *c* parameters are decreasing with the increase of the film thickness, while the *a* parameter is increasing with the increase of thickness from 12 to 23 nm. All values are tending toward the bulk values. The XRD and RSM analyses indicate strained films with a thickness-dependent relaxation mechanism. The lattice parameters of the o-YMO films are strongly affected by the oxygen pressure in the case of PLD growth.

TEM observations confirm the domain scenario for the 12 nm thick film. Additionally, high resolution TEM images reveal that the film is fully strained within a boundary layer of ~3 nm. Above this layer the film relaxes progressively.

Non-stoichiometric o-YMO films grown by MOCVD on top of (100)-oriented STO, LSAT and LAO substrates by varying the Y/Mn ratio in the initial solution of precursors have been obtained and their structural properties have been analyzed. Additionally, films with variable thicknesses and/or chemical compositions were also investigated.

Because the deviation from the stoichiometric composition was too large, the YMO films are not pure; they exhibit secondary phases such as YMn_2O_5 for the Mn-rich region ($0.25 < Y/Mn_{solution} <$

0.35) and Y_2O_3 for the Y-rich region ($Y/Mn_{solution}=1$). Small variations in the lattice parameters observed by XRD and RSM on one side and the Raman positions on the other side, indicate that the o-YMO phase present in most of the films is similar, but it is non-stoichiometric. Furthermore, due to the secondary phases, the variation of thickness (from 20 nm to 370 nm) has no strain influence and all the films are relaxed.

The variations in the lattice parameters or Raman modes of the non-stoichiometric films were close to those in films presented in section 6.1, which suggests a similar composition of the o-YMO phase (only the PLD films were different due to the O_2 variation during the deposition).

References:

1. Uusi-Esko, K., et al., *Characterization of RMnO3 (R=Sc, Y, Dy-Lu): High-pressure synthesized metastable perovskites and their hexagonal precursor phases.* Materials Chemistry and Physics, 2008. **112**(3): p. 1029-1034.
2. Chen, J., et al., *Tuning of transport and magnetic properties in epitaxial LaMnO3+x thin films.* Advances in Condensed Matter Physics, 2014. **2014**: p. 5.
3. Lei, D.Y., et al., *Spectroscopic ellipsometry as an optical probe of strain evolution in ferroelectric thin films.* Optics Express, 2012. **20**(4): p. 4419-4427.
4. Marti, X., et al., *Ferromagnetism in epitaxial orthorhombic YMnO3 thin films.* Journal of Magnetism and Magnetic Materials, 2009. **321**(11): p. 1719-1722.
5. Iliev, M.N., et al., *Raman spectroscopy of orthorhombic perovskitelike YMnO3 and LaMnO3* Physical Review B, 1998. **57**(5): p. 2872-2877.
6. Wenbin, W., K.H. Wong, and C.L. Choy, *The role of energetic plasma in pulsed laser deposition of epitaxial manganite films.* Journal of Physics D: Applied Physics, 1999. **32**(15): p. L57.
7. Chaudhury, R., et al., *Pressure-induced polarization reversal in multiferroic YMn2O5.* Physical Review B, 2008. **77**(22): p. 220104.

General conclusions

The main results presented in this thesis are summarized in the following. At the end, the future prospects are proposed as a continuation of this work.

Optimization of the growing conditions. Selective growth mechanism

YMO films have been grown by MOCVD technique on (100)-oriented Si, STO, LAO and LSAT substrates. An additional brief study concerns several YMO films grown by PLD on the same substrates. We show that the growth conditions have to be carefully optimized in order to obtain almost stoichiometric films of high-quality showing no significant spatial gradients in either thickness or composition.

The two main deposition parameters to be optimized for **MOCVD** are the Y/Mn ratio of the precursors in the injected solution and the deposition temperature.

A temperature dependent **MOCVD** selective growth of YMO/Si film is observed: samples near the optimized Y/Mn ratio deposited at 600°C are amorphous, those deposited at 750°C are orthorhombic and finally those deposited in the range 800-850°C are hexagonal.

A similar selective growth is found as a function of the O_2 pressure (with a fixed temperature) for the **PLD**: at low pressure the h-YMO is formed, in the intermediate O_2 pressure range an amorphous phase dominates, at high pressure the o-YMO phase is stabilized.

On perovskite type substrates the deposition parameters (temperature, Y/Mn ratio, oxygen pressure) have almost no influence and the orthorhombic YMO phase is stabilized by a strain mechanism.

Physico-chemical and structural characterizations of YMO films on Si(100) substrate

Optimized conditions lead to almost stoichiometric films of high-quality showing no significant spatial gradients in either thickness or composition. The obtained YMO films are amorphous or mainly polycrystalline/textured on Si substrates (eventually a 10-50 nm thin amorphous layer forms between the crystalline films and the Si). All the as-deposited **MOCVD** films follow a 3D columnar growth mode (columns of 15-40 nm in diameter depending on the samples), typical for the **MOCVD** process, with a cauliflower-like morphology.

The amorphous YMO phase in the films is easily formed and stable for the **MOCVD** growing conditions in a large range of compositions. Variation in the stoichiometric composition is observed for the crystalline YMO phases (indicated by the large variations in the cell parameters values). This is mainly related to the change in the Y/Mn ratio in the injected solution.

The h-YMO films are mainly *c*-axis textured for the MOCVD growth and mainly (11-20) and (11-21) oriented for the PLD growth. These orientations are strongly influenced by the deposition temperature and to a minor extent by the Y/Mn ratio in the solution (**MOCVD**) and are independent of the oxygen pressure (**PLD**). The **PLD** growth produces dense grains, mainly polygonal-shaped, between 90 and 150 nm.

The o-YMO phase is present in the films grown by both **MOCVD** and **PLD** techniques without any strain stabilization mechanism and free of the h-YMO phase. The o-YMO films are mainly polycrystalline. Beside the columnar growth characteristic of **MOCVD,** the o-YMO films present aggregates lying on the surface of the film (200-400 nm in size). **PLD** growth produces grains of 20-30 nm in size and aggregates of grains between 65 and 75 nm.

Phase transformations and stability

The investigations performed through *ex-situ* and *in-situ* thermal annealings in order to study the stability of the o-YMO phase have shown that an irreversible phase transformation from amorphous to crystalline o-YMO phase takes place in Y-Mn-O films deposited by **MOCVD** on Si(100) substrate at an almost constant temperature (~ 700 °C) and in a short period of time (~ min). The o-YMO phase thus obtained is stable at least up to 900°C. At higher temperature, a Si diffusion from the substrate into the film leading to the formation of a silicate phase was observed.

Physico-chemical and structural characterizations of YMO films on (100)-oriented STO, LAO and LSAT substrates

o-YMO films, grown by both **MOCVD** and **PLD** techniques present a dense microstructure and homogenous surface, without aggregates of particles, independently of the substrate. The **MOCVD** produces a columnar growth with columns diameter between 10 and 20 nm and a smooth film-substrate interface. The morphology of the films grown by **PLD** depends on the O_2 pressure: very dense polygonal shaped grains, around 30 nm in size, are obtained at low P_{O2}

($1.4 \cdot 10^{-4}$ bar) while at higher P_{O2} ($3 \cdot 10^{-1}$ bar) round shaped grains, between 20 and 30 nm and compatible with a columnar growth are produced.

Epitaxial o-YMO films are mainly (010)-oriented on STO and LSAT substrates and (101)-oriented on LAO substrate. Detailed studies on 12 nm and 23 nm thick YMO/STO films have shown that actually four types of domains are present. This is equivalent to having two types of domains, 90° in-plane rotated, with the following epitaxial relationships:

- $[010]_{YMO}//[100]_{STO}$ and $[100]_{YMO}//[011]_{STO}$
- $[010]_{YMO}//[100]_{STO}$ and $[100]_{YMO}//[0\text{-}11]_{STO}$
- $[10\text{-}1]_{YMO}//[100]_{STO}$ and $[010]_{YMO}//[010]_{STO}$
- $[10\text{-}1]_{YMO}//[100]_{STO}$ and $[010]_{YMO}//[001]_{STO}$

The *b* and *c* parameters are decreasing with the increase of the films thickness, while the *a* parameter is increasing with the increase of the thickness from 12 to 23 nm. All values are tending toward the bulk values. The XRD and RSM analyses indicate strained films with a thickness-dependent relaxation mechanism. The lattice parameters of the o-YMO films are strongly affected by the oxygen pressure in the case of PLD growth.

TEM observations confirm the domain scenario for the 12 nm thick film. Additionally, high resolution TEM images reveal that the film is fully strained within a boundary layer of ~3 nm. Above this layer the film relaxes progressively.

Magnetic properties

The magnetic properties of the YMO films (amorphous, orthorhombic or hexagonal) indicate a general spin-glass behavior. A weak ferromagnetic contribution is present at 5 K.

For the amorphous as-deposited films the magnetization presents a maximum in the ZFC curve between 11 and 19 K.

The magnetism for h-YMO films is characterized by a splitting of the ZFC-FC curve and a maximum in the ZFC curve at T_f=20 K. A splitting of the ZFC-FC curves was observed for polycrystalline powders at ~ 65 ($Y_1Mn_1O_3$) and 70 K ($Y_{0.95}Mn_1O_3$), without maximum in the ZFC. On the contrary, the h-YMO single crystal shows a pure antiferromagnetic ordering at T_N=70 K.

The magnetic measurements on o-YMO films on Si substrates indicate a spin-glass behavior, characterized by a splitting of the ZFC-FC curves, with a maximum in the ZFC curve at T_f= 20 K for the as-deposited o-YMO films and at T_f= 32 K for o-YMO films crystallized after annealings. Similarly, o-YMO films on STO, LAO and LSAT substrates, present the same splitting behavior of the ZFC-FC curves with maxima in the ZFC curve between 26 and 50 K.

Future prospects

Several directions can be envisaged for the continuation of our study.

The stability of the o-YMO phase was investigated under the thermal treatments throughout Raman experiments. A second step in the stability behavior of this phase would be to check the effect of applying high pressure (transforming h-YMO powder into the o-YMO phase and study the effect of pressure on the o-YMO phase) and to see if any transition occurs. Such a study was not reported in the literature.

Another line of research can be the study of ferroelectricity in strained single domain o-YMO films in order to have a complete picture of the multiferroic properties. This involves refining the optimal deposition parameters and the appropriate substrate to produce single oriented and stoichiometric o-YMO films. Then, non-stoichiometric $Y_{1-x}Mn_{1-x}O_{3\pm\delta}$ thin films would be interesting to study (strain, Raman, magnetism, ferroelectricity).

Among other properties existing in the YMO films it appears very interesting to investigate the resistive switching properties. In a recently published paper [1] it is shown that $YMnO_3$ thin films present unipolar, nonvolatile resistive switching which might be a promising route for the design and fabrication of novel resistive switching devices.

Finally, we propose the doping of the $YMnO_3$ phase, in particular with Fe and the synthesis of double perovskites (Y_2MnXO_6, X=Fe, Co, Ni) in the thin film or bulk form as the theoretical calculations predict a multiferroic behavior [2] and experimental results reported a Néel temperature of 328 K [3].

References:

1. Bogusz, A., et al., *Resistive switching in polycrystalline YMnO3 thin films.* AIP Advances, 2014. **4**(10): p. -.
2. Kumar, S., et al., *Theoretical prediction of multiferroicity in double perovskite Y2NiMnO6.* Physical Review B, 2010. **82**(13): p. 134429.
3. Liu F, L.J., Li Q, Wang Y, Zhao X, Hua Y, Wang C, Liu X., *High pressure synthesis, structure, and multiferroic properties of two perovskite compounds Y2FeMnO6 and Y2CrMnO6.* Dalton Trans., 2014. **43(4)**: p. 1691-8.

Appendix A: YMO growth on MgO(100) and YSZ(111) substrates

YMO/MgO(100)

The XRD θ-2θ pattern of the YMO film on MgO(100) substrate deposited with the vertical PI-MOCVD setup (T_s=800°C, Y/Mn=1) is shown in Figures A.1a. In this figure, the h-YMO phase is identified by the (11-20) intense peak and (11-22) and (20-26) weak peaks. The remaining peak is assigned to the 002 reflection of the MgO substrate. Thus, the h-YMO film grows mainly along the [11-20] direction ($11\text{-}20_{\text{h-YMO}}//100_{\text{MgO}}$).

Figure A.1b shows the Raman spectrum of YMO film on MgO(100) substrate. It is observed that the positon of the Raman lines is much higher than the values reported in [1] marked between parentheses, which may indicate a large non-stoichiometry of the h-YMO film.

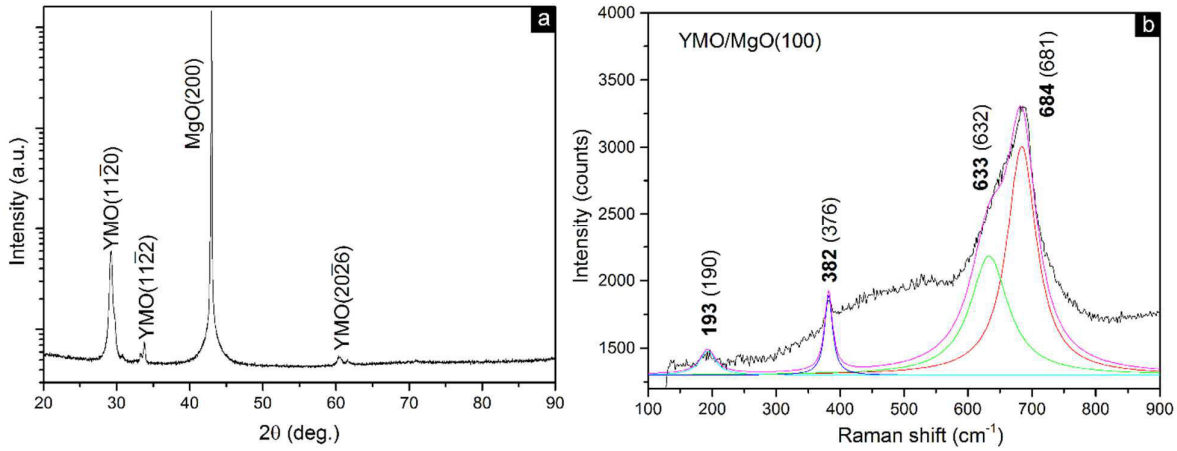

Figure A1. YMO film on MgO(100) substrate deposited with the vertical PI-MOCVD setup: a) XRD pattern; b) Raman spectrum in which the experimental position of each mode are marked by bold numbers (in parentheses are given the values from Iliev et al.[1]). The MgO does not have any active Raman mode.

Figure A.2a shows the XRD θ-2θ pattern of YMO film deposited on MgO(100) substrate in the horizontal PI-MOCVD setup (T_s=800°C, Y/Mn=1). The results clearly indicate that the h-YMO film is c-axis oriented ($0001_{\text{h-YMO}}//100_{\text{MgO}}$) as far as the XRD is concerned. This orientation corresponds very likely to an epitaxial growth represented in Figure A.3.

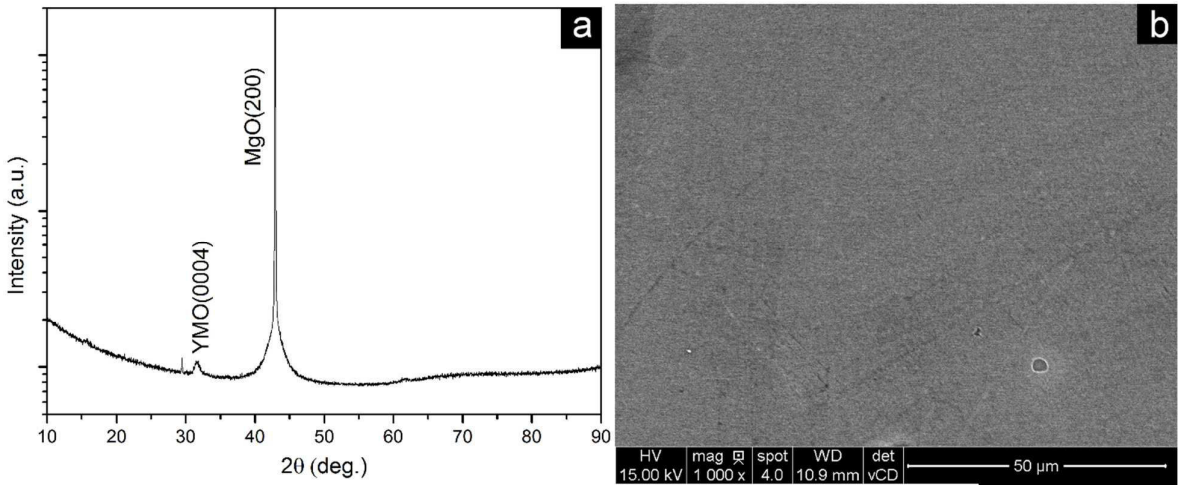

Figure A1. YMO film deposited on MgO(100) substrate with the horizontal PI-MOCVD setup: a) XRD pattern; b) SEM top-view image in BSE mode.

The top-view image (BSE mode) from Figure A.2b shows a smooth surface, with no indication of variable composition or agglomerates in agreement with the XRD results.

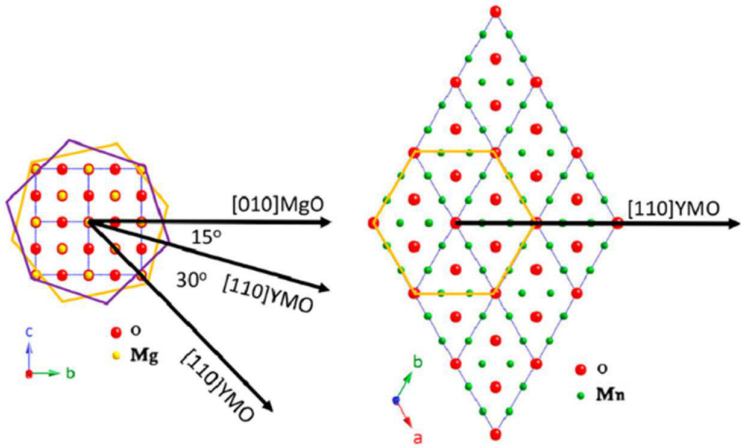

Figure A.3. Schematic representation of a possible epitaxial growth between the h-YMO(001) film and MgO(100) substrate (from [2]).

YMO/YSZ(111)

XRD pattern of the YMO film on YSZ(111) substrate deposited with the horizontal PI-MOCVD setup is show in Figure A.4. The pattern presents only the 000l peaks of the h-YMO phase together with the 111 reflections of the YSZ substrate. The film is textured with the c-axis perpendicular to the substrate. No other phase is observed in the film.

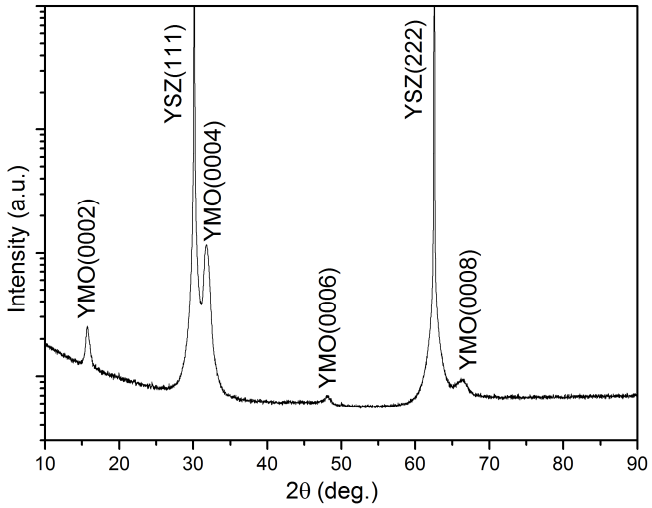

Figure A.4. XRD pattern of the YMO film deposited on YSZ(111) substrate with the horizontal PI-MOCVD setup.

These results show that h-YMO films can be epitaxially grown on MgO(100) and YSZ(111) substrates.

References

1. Iliev, M.N., et al., *Raman- and infrared-active phonons in hexagonal YMnO3: Experiment and lattice-dynamical calculations.* Physical Review B, 1997. **56**(5): p. 2488-2494.
2. Wu, K.H., et al., *Epitaxial-Strain Effects on Electronic Structure and Magnetic Properties of Hexagonal YMnO3 Thin Films Studied by Femtosecond Spectroscopy.* Journal of Superconductivity and Novel Magnetism, 2013. **26**(4): p. 801-807.

Appendix B: SEM images of non-stoichiometric YMO films grown on Si(100)

Mn-rich YMO films

Secondary phases, such as YMn_2O_5, are formed when using a Mn-rich solution of precursors (Y/Mn <1). The formation of the YMn_2O_5 phase, as observed from the SEM images in Figure B.1 is promoted by agglomeration of Mn-rich particles (highlighted by white contrast). Then, a dendritic 2D growth, starting from these particle occurs (see so called "flower" morphology). The formation of the YMn_2O_5 phase was observed between 800-850°C, although it appears less well crystallized at 800°C (see Figure B.1d).

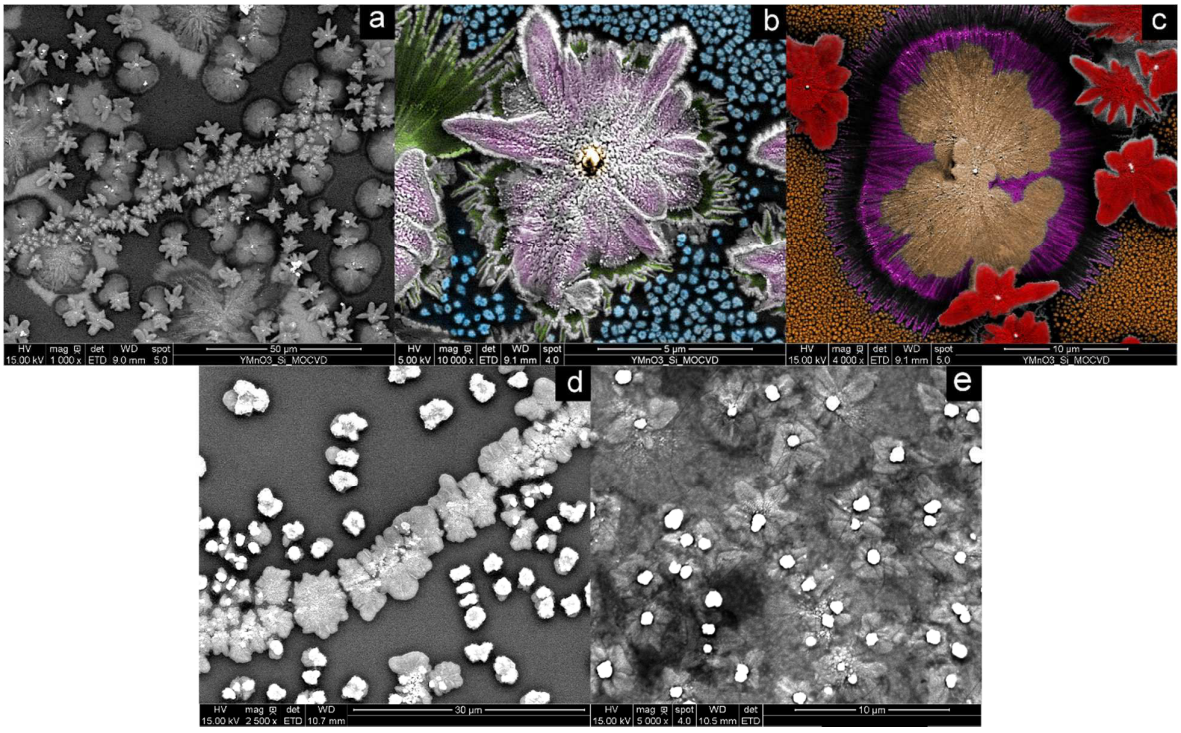

Figure B.1. Morphology of the YMO films deposited on Si substrate in the Mn-rich region by PI-MOCVD (horizontal) in the following conditions: a)-c) T_s=850°C and Y/Mn=0.5. The YMn_2O_5 phase is forming as precipitates represented by the "flowers" with white contrast (©images b and c are colorized as for NanoArt and FEI Image Contest); d) T_s=800°C and Y/Mn=0.5; e) Ts=850°C and Y/Mn=0.5 (a different sample from the one shown at a)-c)).

Y-rich YMO films

When working with Y-rich solutions of precursors (Y/Mn>1.4), a Y_2O_3 phase is forming in order to compensate the Y excess of the film. Figure B.2 shows two examples of morphological features found among these films.

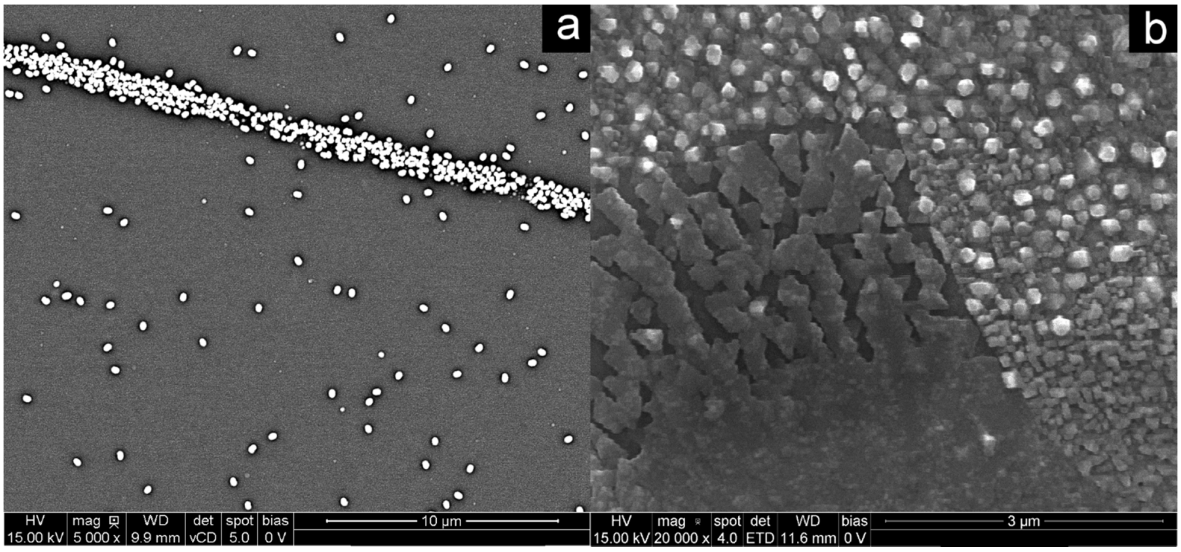

Figure B.2. Morphology of the YMO films deposited in the Y-rich region on Si substrate by PI-MOCVD in the following conditions: a) T_s=800°C and Y/Mn=1 (vertical MOCVD geometry), showing the presence of the Y_2O_3 phase highlighted by spherical particles with white contrast b) T_s=800°C and Y/Mn=4 (horizontal MOCVD geometry); the Y_2O_3 phase can be found on the entire surface.

Appendix C: Hexagonal $YMnO_3$ phase obtained as ceramic by solid state reaction

Hexagonal $YMnO_3$, $Y_{0.95}MnO_3$ and $YMn_{0.95}O_3$ have been obtained as powders by solid state reaction in order to be used as complementary references for the h-YMO films.

XRD characterization

The XRD patterns of the hexagonal $YMnO_3$, $Y_{0.95}MnO_3$ and $YMn_{0.95}O_3$ powders are shown in Figure C.1.

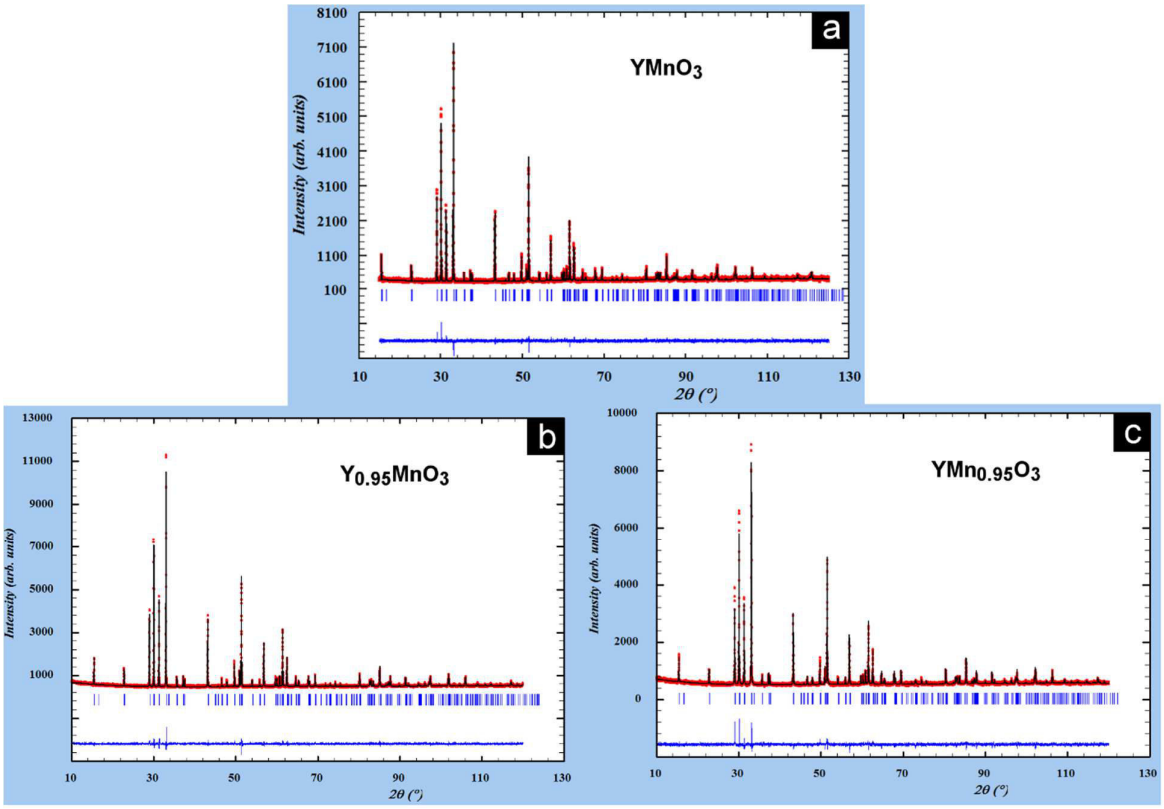

Figure C.1. Experimental θ-2θ XRD data (red symbols) for $YMnO_3$ (a), $Y_{0.95}MnO_3$ (b) and $YMn_{0.95}O_3$ (b). The solid black lines represents the calculated pattern with hexagonal ($P6_3cm$) symmetry. The blue lines in the figures indicate the difference between the observed and calculated diffraction patterns. The blue bars indicate the positions of the Bragg peaks. R factors for fitting are: $1.43 < \chi^2 < 1.86$, $3.85 < R_p < 4.18$, $4.90 < R_{wp} < 5.33$, $4.06 < R_{exp} < 4.50$ (credit A. Schulman).

The data were analyzed using Rietveld method and the refinement of the crystalline structure was carried out using the FullProf software. As far as this technique is concerned, the samples

are pure, without any impurities. The lattice parameters are in good agreement with the literature data.

The experimental cell parameters of the h-YMO phase are listed in Table C.1.

Sample	a (Å)	c (Å)
$YMnO_3$	6.1354	11.3944
$Y_{0.95}MnO_3$	6.1479	11.4056
$YMn_{0.95}O_3$	6.1339	11.3926

Table C.1. Structural parameters (a and c lattice constants) after the Rietveld refinement of patterns from Figure C.1.

The electron diffraction pattern (ED) and TEM images confirm the XRD results: the YMO phase of hexagonal symmetry with the lattice parameters in agreement with those obtained from the Rietveld refinement. One example is shown in Figure C.2 for the $YMnO_3$ sample.

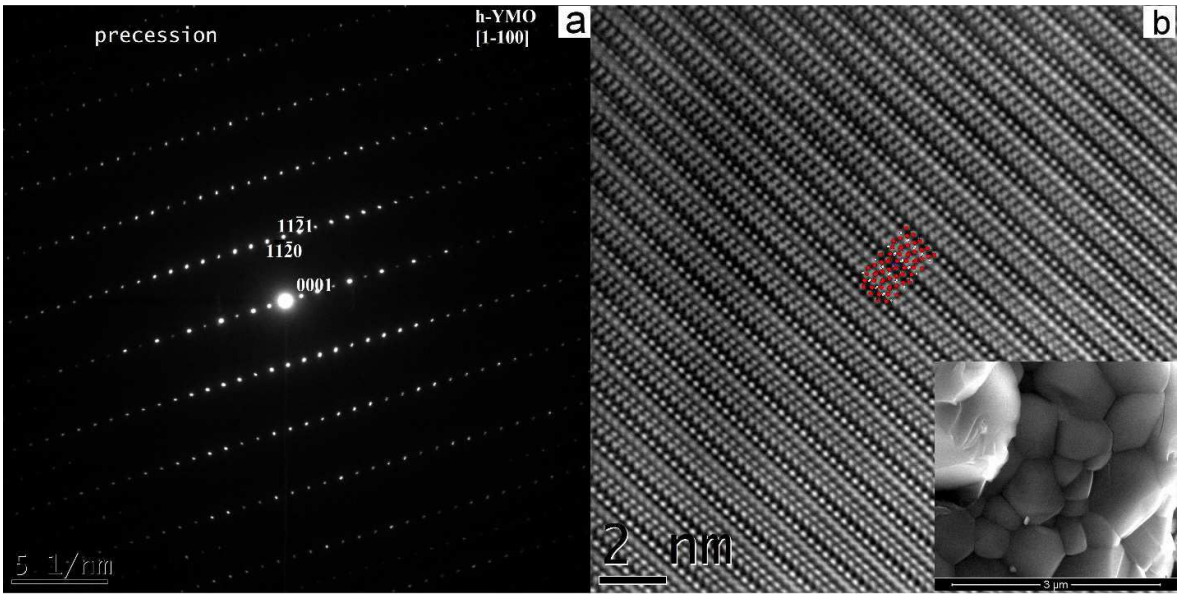

Figure C.1. ED pattern (a) in [1-100]-zone axis and corresponding TEM image (b) overlapped with the simulated structure (CarIne) of a crystalline particle (see SEM image in inset of b) from the $YMnO_3$ sample.

Additionally, the Raman spectra of the three samples, indexed with the h-YMO phase are shown in Figure C.3.

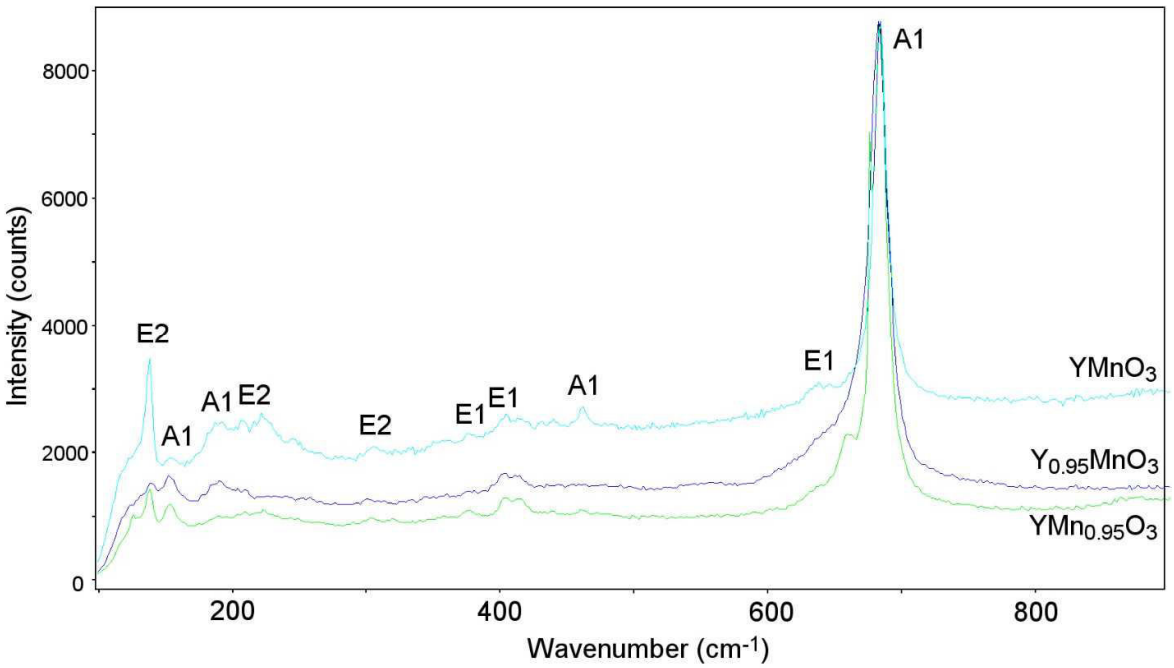

Figure C.3. Raman spectra of $YMnO_3$, $Y_{0.95}MnO_3$ and $YMn_{0.95}O_3$ samples. The modes of the h-YMO phase are marked on each peak.

Appendix D: Raman spectra and magnetization of bare STO, LAO and LSAT substrates

Raman

The determination of the position of the YMO modes has been performed by fitting the Raman spectra using Lorentzian profiles, after wavenumber calibration with a Si reference spectrum and subtraction of the baseline. The Raman spectra of bare STO, LAO and LSAT substrates are shown in Figure D.1; the position of the lines is marked on each spectrum.

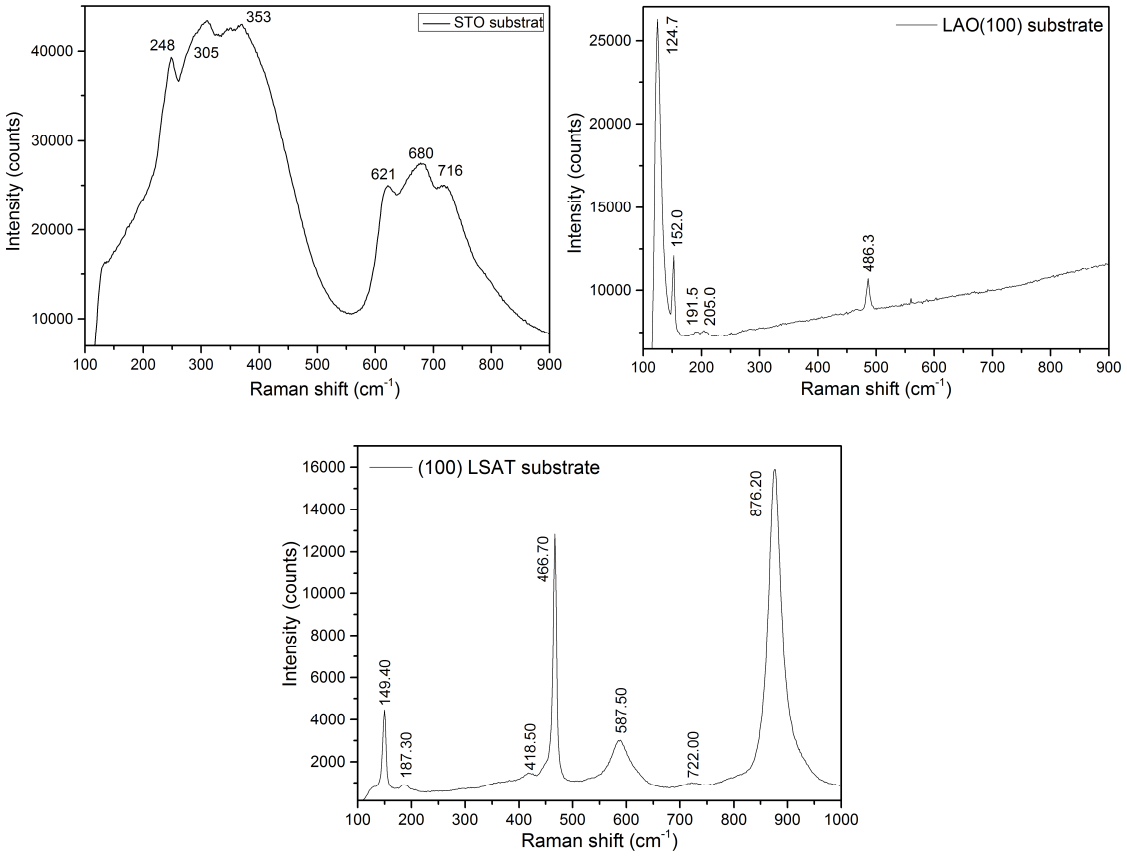

Figure D.1. Raman spectra of a bare (100)-oriented STO, LAO and LSAT substrate.

As it can be seen, the Raman spectrum of the STO substrate presents very large modes and, in general, the determination of the exact positions of the modes for the o-YMO phase was not always possible as the weak Raman signal from the film is masked by the substrate signal.

Magnetization

The temperature M(T) and field M(H) dependence of the magnetization of the bare LSAT substrate (5mm×5mm) is shown in Figure D.2. A negative signal, ranging from -8.5 to -3·10^{-6} emu, characteristic of diamagnetic material is observed (the magnetization of the sample holder (straw + plastic wrap) is also shown in Figure D.2). The M(H) data were recorded at 5 K and room temperature with applied fields between -50 and 50 kOe. A linear behavior, with negative slopes is observed at both temperatures confirming the diamagnetic nature of the LSAT substrate. The STO substrate displays the same features.

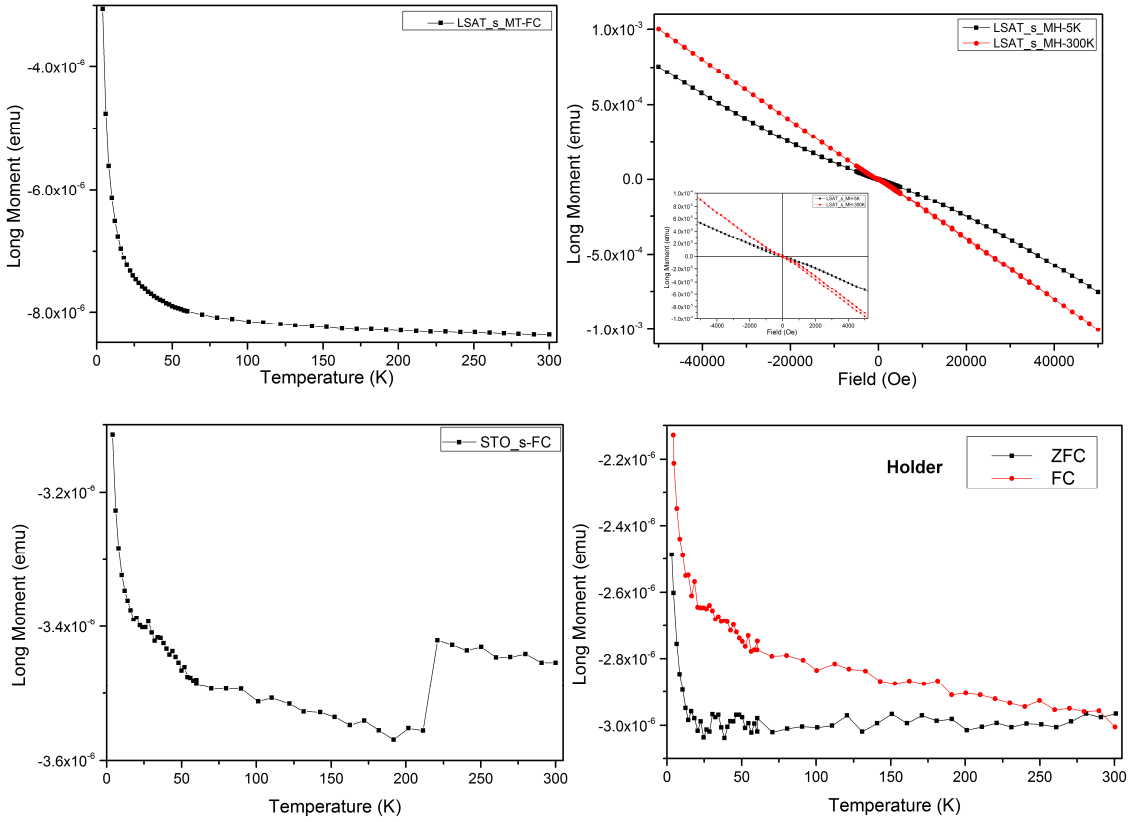

Figure D.2. Temperature dependence of the magnetization (M(T)) of bare LSAT and STO substrates and of sample holder (straw + plastic wrap) and field dependence of the magnetization (M(H)) for LSAT substrate.

Appendix E: RSM of YMO films on STO, LAST and LAO substrates

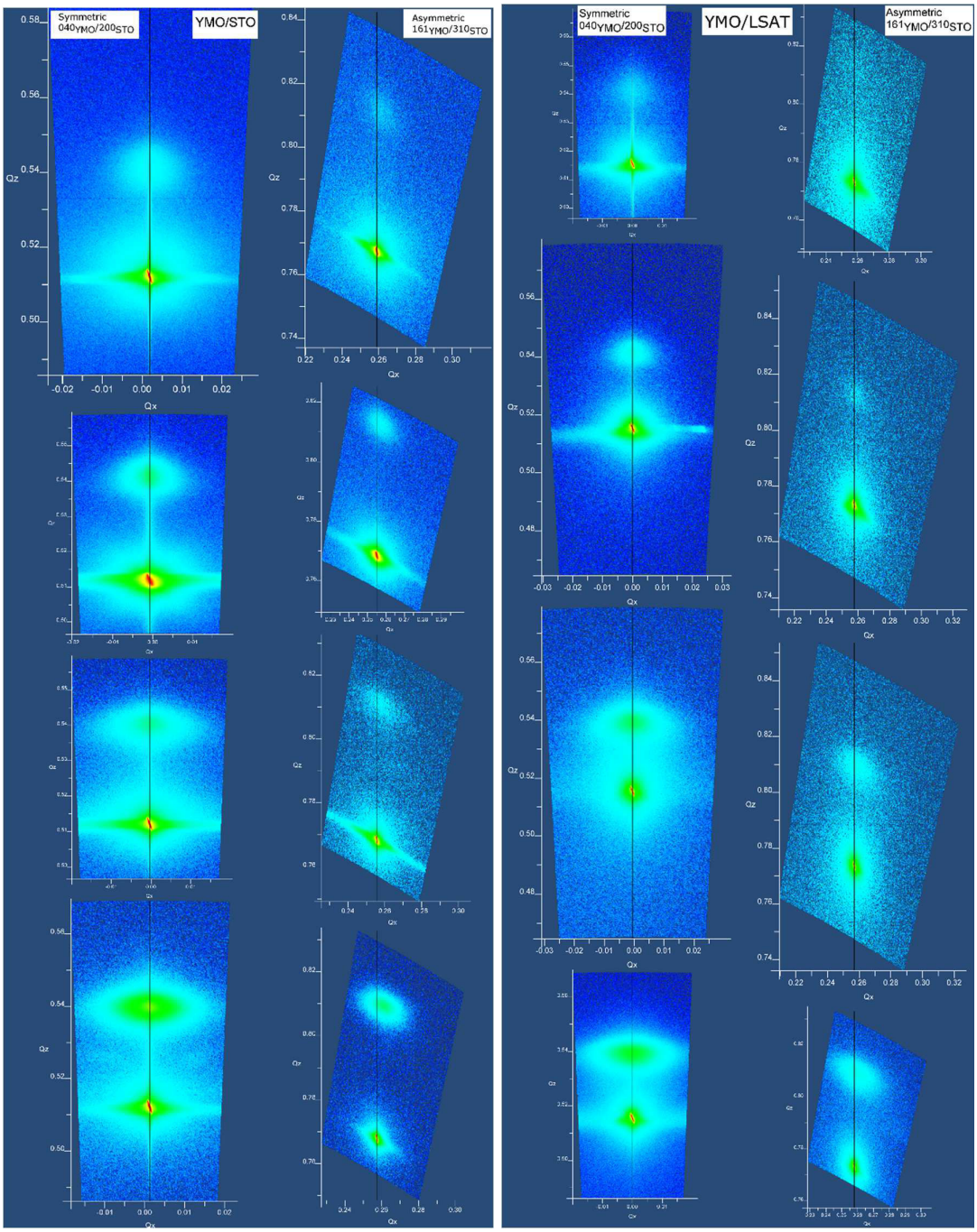

Figure E.1. RSM for YMO films on STO (left) and LSAT (right) substrates with different thicknessess (from top to bottom: 500, 1000, 2000 and 4000 inj.) at Y/Mn ct. ($Y/Mn_{solution}$=0.325) around the symmetric reflection 040_{YMO} and asymmetric reflection 161_{YMO}.

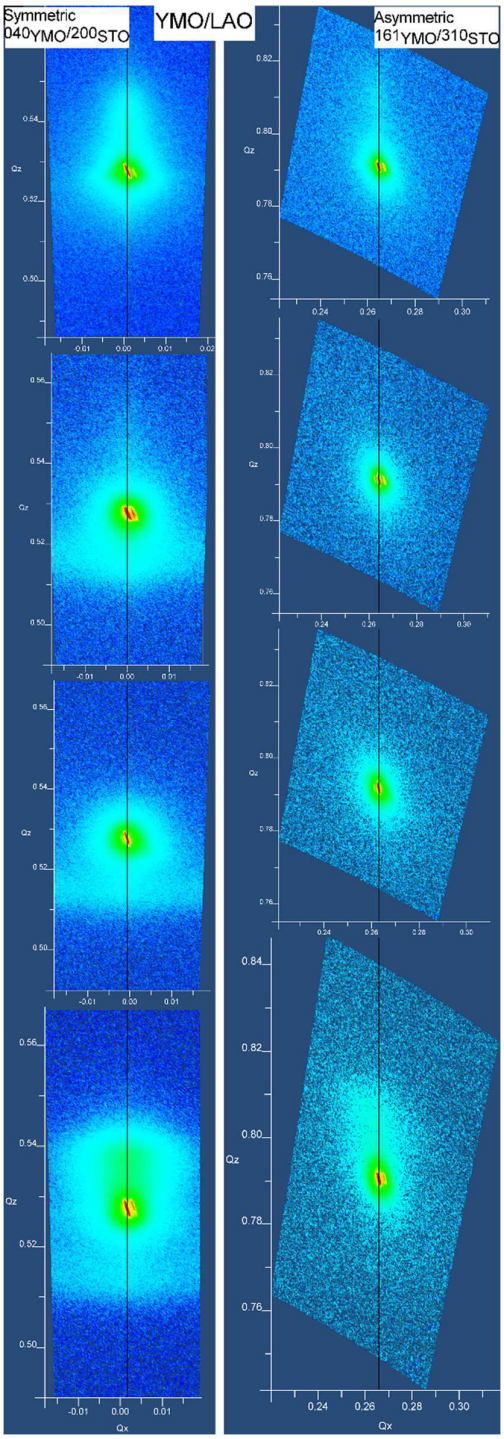

Figure E.1. RSM for YMO films on LAO substrate with different thicknessess (from top to bottom: 500, 1000, 2000 and 4000 inj.) at Y/Mn ct. ($Y/Mn_{solution}$=0.325) around the symmetric reflection 040_{YMO} and asymmetric reflection 161_{YMO}.

Appendix F: Raman spectra of YMO films on STO, LAO and LSAT substrates

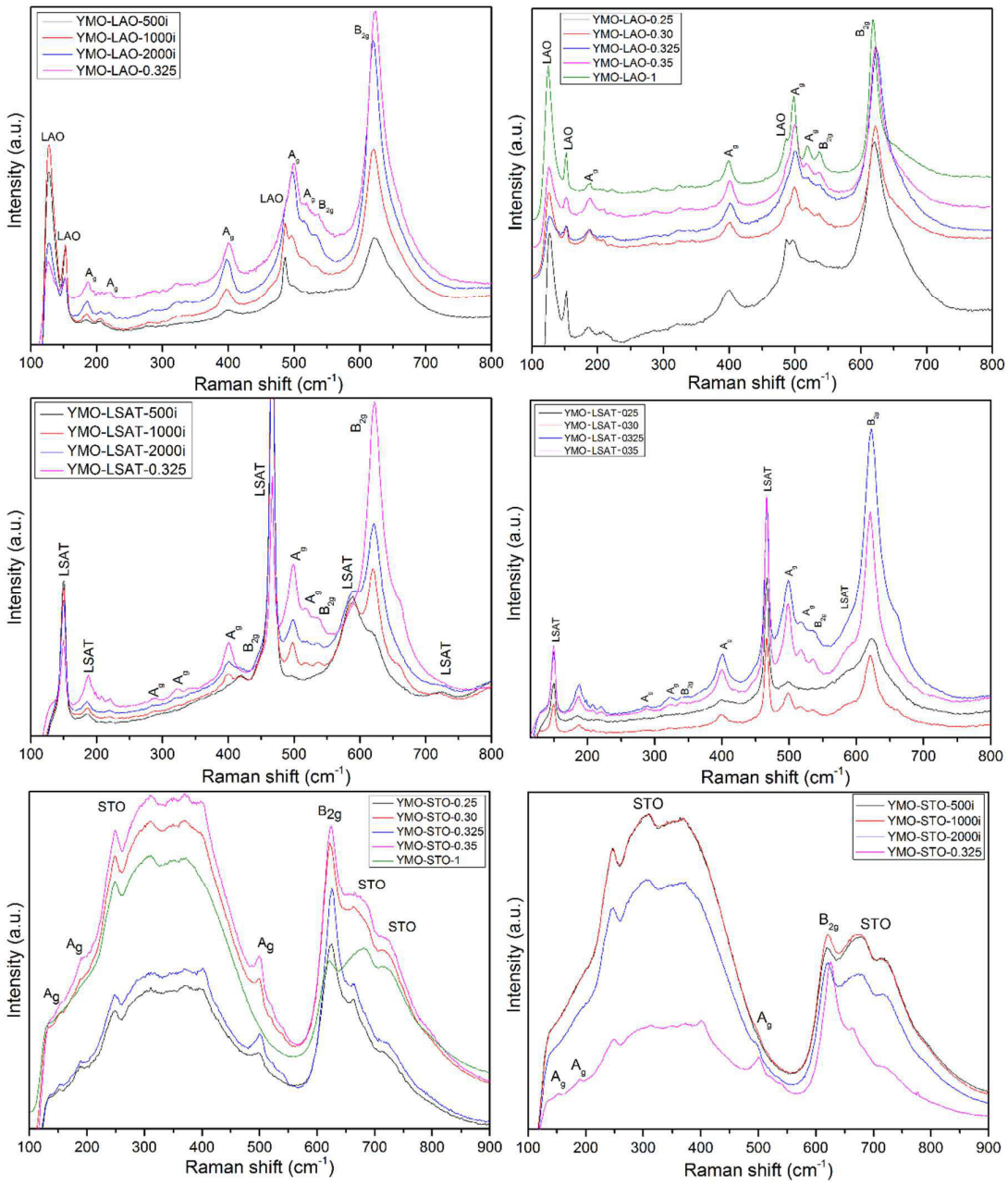

Figure F.1. Raman spectra of YMO films on STO, LAO and LSAT substrates deposited with different number of injections (from 500 to 4000) and constant $Y/Mn_{solution}$ ratio (0.325) (left) and deposited with different $Y/Mn_{solution}$ ratio (from 0.25 to 0.35) and constant number of injections (4000) (right).

Appendix G: Magnetization of YMO films on STO, LAO and LSAT substrates

The magnetization measurements M(T) and M(H) of YMO films on STO, LAO and LSAT substrates deposited with different number of injections (from 500 to 4000) and constant $Y/Mn_{solution}$ ratio (0.325) and deposited with different $Y/Mn_{solution}$ ratio (from 0.25 to 0.35) and constant number of injections (4000) are show below.

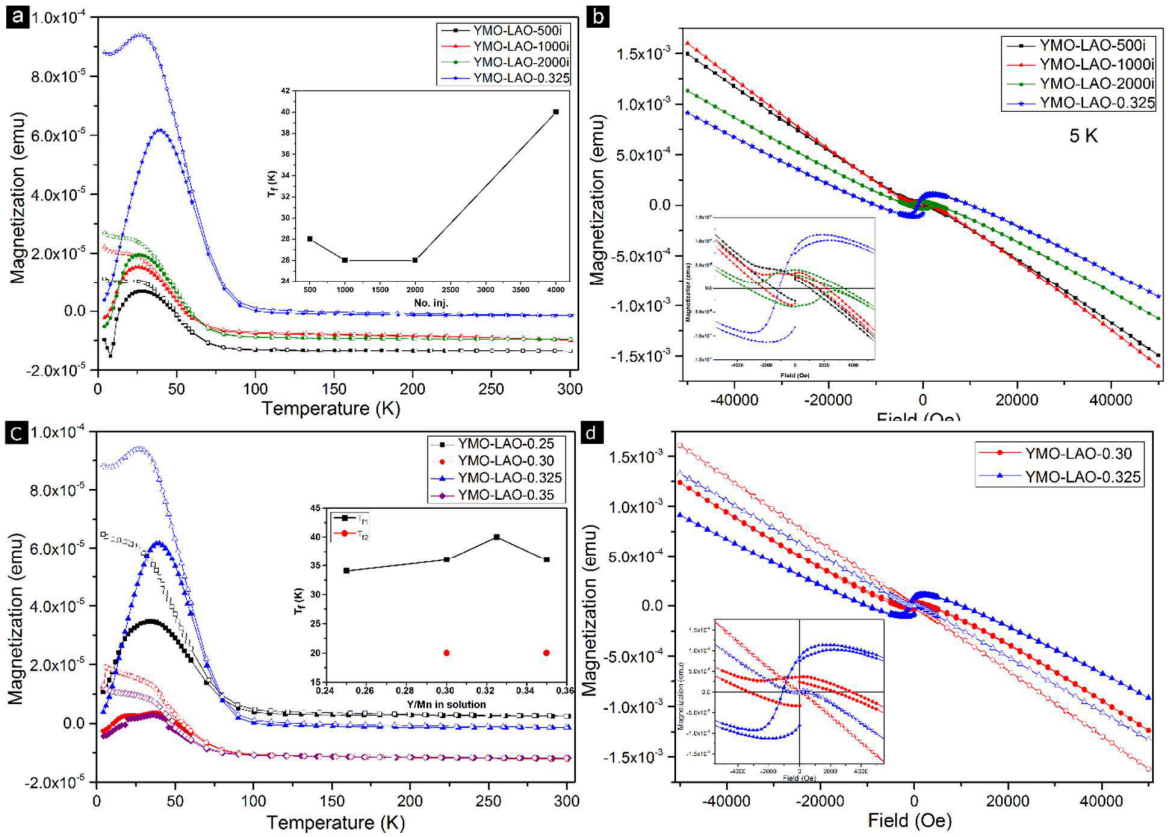

Figure G.1. Films on LAO substrate. Temperature dependence of the magnetization M(T): a) number of injections varying between 500 and 4000, $Y/Mn_{solution}$=0.325; b) Number of injections=4000, $Y/Mn_{solution}$ varying from 0.25 to 0.35. Field dependence of the magnetization M(H): c) idem as for a); d) idem as for b).

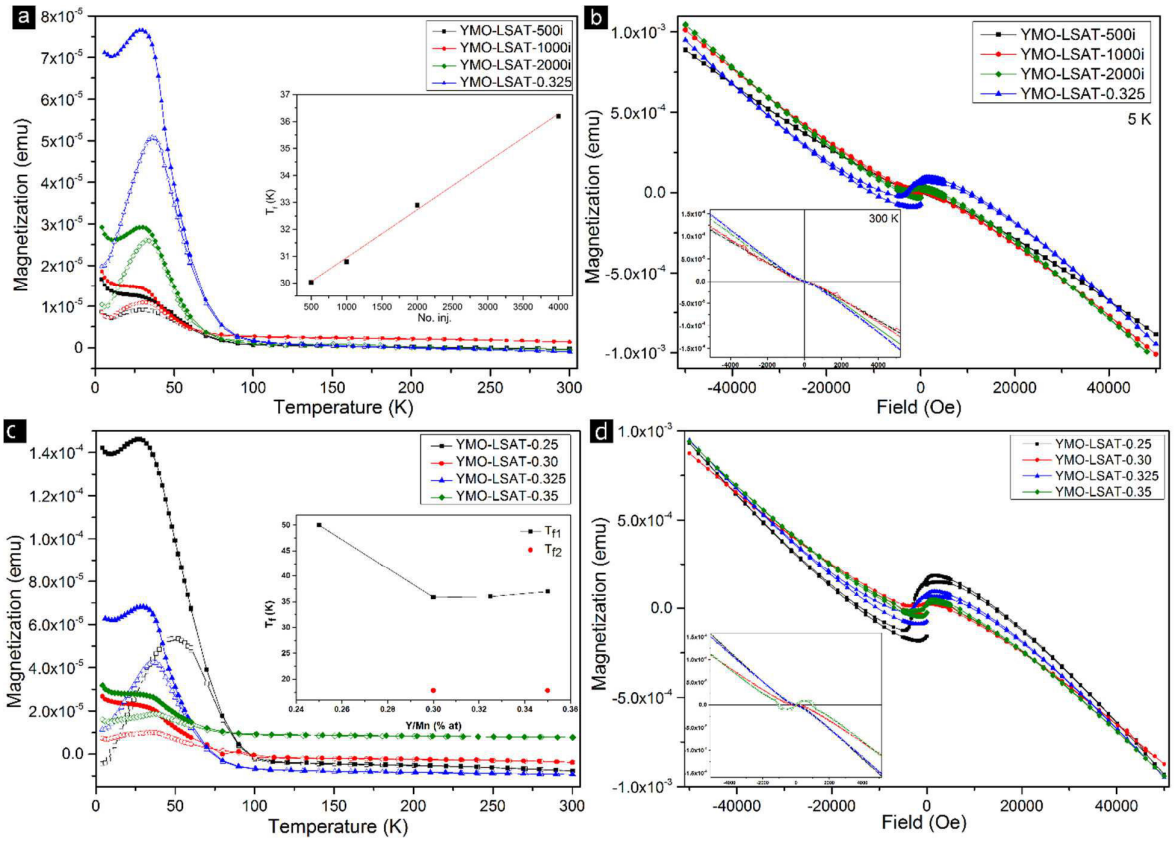

Figure G.2. Temperature and field dependences of the magnetization M(T) and M(H) for YMO films on LSAT substrate (a, b, c, d are the same as in Figure G.1).

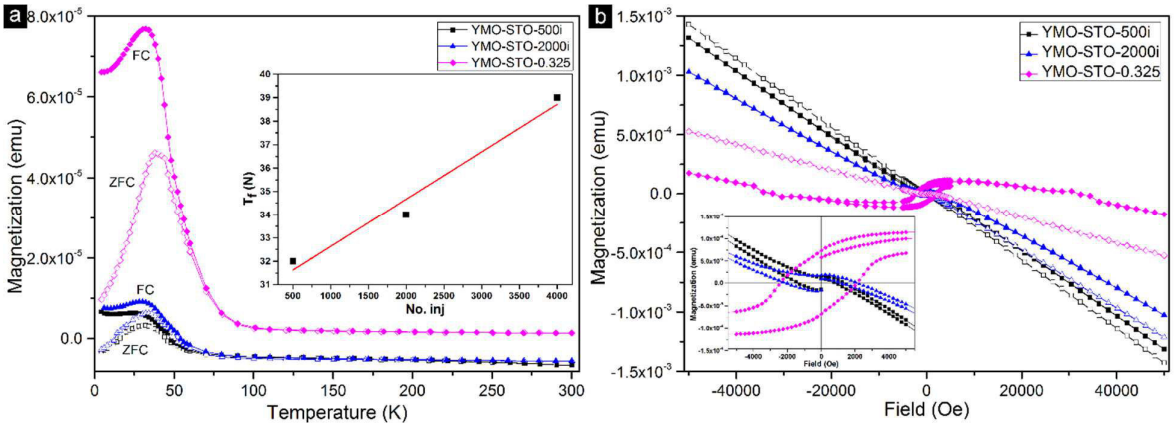

Figure G.3. Temperature and field dependences of the magnetization M(T) and M(H) for YMO films on STO substrate (a, b, c, d are the same as in Figure G.1).

Publication list

1. *Phase transformations and selective growth in YMnO3 films*, I Iliescu, M Boudard, O Chaix-Pluchery, L Rapenne and H Roussel, Journal of Solid State Chemistry, 2014 Vol. 220, 245-253 (Chapter 5 of the thesis treats this article)

2. *MOCVD selective growth of orthorhombic or hexagonal YMnO3phase on Si(1 0 0) substrate,* I. Iliescu, M. Boudard, L. Rapenne, O. Chaix-Pluchery, and H. Roussel, Appl. Surf. Sci. (2014), Vol. 306, 27-32 (this is discussed in detailed in Chapter 4)

3. *Growth and structural characterization of YMnO3 thin films grown by pulsed liquid injection MOCVD on Si and SrTiO3 substrates,* I. Iliescu, M. Boudard, S. Pignard, L. Rapenne, P. Chaudouet and H. Roussel, Phase Transitions, 2013 Vol. 86, No. 11, 1094–1103 (the work presented here is discussed in Chapter 3 and 4)

4. *Synthesis of LaAlO3 by metal organic decomposition on SrTiO3 substrates,* J.L. Ampuero, I. Iliescu, M. Boudard, A. Jamaoui, L. Rapenne, C. Jimenez and H. Roussel, Phase Transitions, 2013, Vol. 86, No. 11, 1060–1068

   This work was carried out at the beginning of my thesis. For reasons of homogeneity, this topic is not present in this manuscript. My contribution to the article was at the writing of the manuscript and participation on the MOD and TEM experiments.

Résumé français

Croissance, caractérisation et transformation de phase dans des couches minces d'$YMnO_3$

Introduction générale

La demande croissante de nouveaux matériaux fonctionnels, notamment dans le domaine du stockage de données et de la spintronique, a conduit à une intensification de la recherche dans les deux dernières décennies. Parmi les candidats les plus attrayants pour ce type d'applications on trouve les oxydes, dont les oxydes de manganèse ternaires de type $AMnO_3$ qui jouent un rôle clé. Certains de ces matériaux possèdent deux ou plusieurs ordres ferroïques spontanés dans la même phase et en l'absence de champs extérieurs, appelé multiferroïcité. Ces formes d'ordre ferroïque sont le (anti-) ferromagnétisme, la (anti-) ferroélectricité et la (anti-) ferroelasticité qui ont été récemment complété par la (anti-) ferrotoroïdicite (vortex magnétique spontanée).

Des effets magnéto-électriques géants et magnetocapacitance à température ambiante ont été trouvés dans le composé pérovskite $TbMnO_3$ par Kimura et al. [1]. Depuis, une étude approfondie sur les matériaux de type pérovskite a été réalisée. Dans le même temps, le nombre d'applications et de dispositifs potentiels a augmenté. Un des plus populaires est le dispositif de mémoire à 4-états, qui est basé sur le contrôle de la polarisation ferroélectrique (P) par un champ magnétique et, inversement, la commutation de l'aimantation (M) par un champ électrique. Par conséquent, quatre états de mémoire distincts sont possibles (+ P, -P, + M, -M).

En plus des applications technologiques intéressantes, les matériaux multiferroïques sont très intéressants et riches d'un point de vue fondamental en raison de fortes corrélations électroniques présentes dans ces systèmes.

Motivé par ces propriétés intéressantes, nous avons été intéressés par un membre représentant de la famille des manganites de terre rare ($RMnO_3$) qui est $YMnO_3$. Ce composé est multiferroïque dans les deux structures hexagonale et orthorhombique (pérovskite) en-dessous de ~ 70 ~ K et 40 K, respectivement. Bien que ces températures soient trop faibles pour les applications technologiques, nous pouvons nous attendre à être en mesure de modifier ces températures d'ordre. En fait, à travers la structure cristalline et les caractéristiques de microstructure, les propriétés des films sont souvent modifiées par l'effet du substrat.

Au cours de cette thèse, la structure $YMnO_3$ à la fois hexagonale (considérée comme stable) et orthorhombique (généralement considérée comme métastable) ont été étudiées principalement sous la forme de films minces. Dans un premier temps, nous avons étudié comment la croissance non épitaxiale sur des substrats de silicium agit sur la microstructure des films $YMnO_3$

orthorhombiques et hexagonales. Contrairement à la croyance générale de la littérature, nous avons constaté que la phase orthorhombique $YMnO_3$ métastable a été facilement obtenue sur des substrats de silicium par deux méthodes différentes de dépôt (MOCVD et PLD). Nous avons également testé la stabilité de la phase orthorhombique $YMnO_3$ par recuit thermique et nous avons constaté que cette phase est stable dans une plage de température définie. Dans un deuxième temps, nous avons étudié la croissance épitaxiale de la phase orthorhombique $YMnO_3$ sur différents substrats de type pérovskite (STO, LAO et LSAT).

Les multiferroïques

Les matériaux ferroïques sont caractérisés par un ordre spontané, dont la direction peut être basculée par un champ externe: un ferromagnétique est décrit par une aimantation spontanée (M) et présente un cycle d'hystérésis sous un champ magnétique appliqué (H), un ferroélectrique a une polarisation spontanée (P) et comporte une hystérésis sous un champ appliqué électrique (E) et un ferroélastique possède une déformation spontanée (ε) et présente une hystérésis sous une contrainte appliquée (σ). L'aimantation, la polarisation et la déformation sont contrôlées par le champ magnétique, le champ électrique et la contrainte, respectivement. Dans un multiferroïque, la coexistence d'au moins deux ordres conduit à des couplages croisés supplémentaires. Dans ce travail, la multiferroïcité sera généralement considérée comme la coexistence de (anti) ferromagnétisme et (anti-) ferroélectricité. A noter que les matériaux multiferroïques ne sont pas équivalents avec les matériaux magnéto-électriques. La Figure R.1 résume la relation entre les propriétés des matériaux multiferroïques et magnétoélectriques.

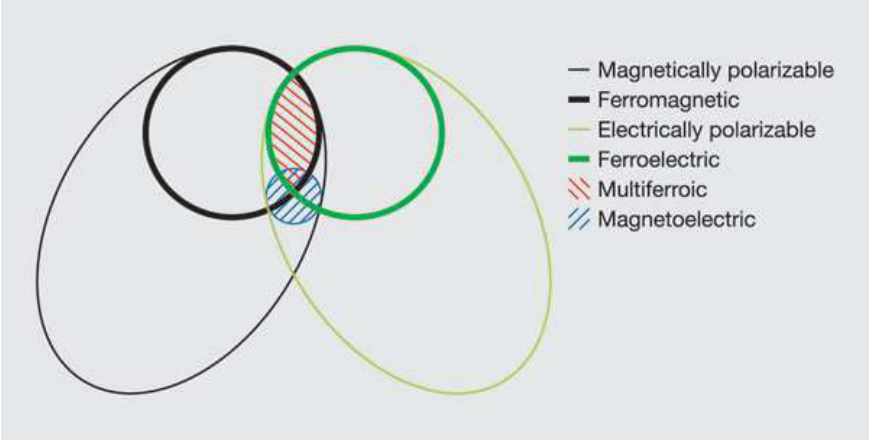

Figure R.1. Relation entre les propriétés des matériaux multiferroïques et magnétoélectriques (d'après [2]).

Les multiferroïques sont classés en deux catégories: type I (connu sous le nom multiferroïques propre) et de type II (multiferroïques impropre) [3] [4]. L'origine microscopique de magnétisme est bien connu et est relie aux électrons localisés dans les orbitales partiellement remplis *d* ou *f* des métaux de transition ou de terres rares. Dans le cas des propriétés ferroélectriques plusieurs sources ont été identifiées. Ainsi, dans les multiferroïques de type I, la ferroélectricité et le magnétisme ont différentes sources et sont indépendants (température de transition différente et généralement couplage faible, comme par exemple $BiFeO_3$, $YMnO_3$ hexagonal etc.). Il existe plusieurs sous-types, en fonction du mécanisme de la ferroélectricité [3]:

- déplacements hors centre du site B ($BaTiO_3$, $Pb(ZrTi)O_3$)
- doublet non liant ($BiFeO_3$, $BiMnO_3$, $PbVO_3$)
- ordre de charge ($LuFe_2O_4$, $(PrCa)MnO_3$, Fe_3O_4, $RNiO_3$)
- matériaux ferroélectriques géométriques ($YMnO_3$)

Dans les multiferroïques de type II, la ferroélectricité et le magnétisme sont fortement couplés du fait que l'ordre magnétique engendre la ferroélectricité. Du point de vue de mécanisme de génération, les multiferroïques impropre de type II sont divisés en:

- matériaux de type spiral
- matériaux de type colinéaire.

Manganites de terres rares $RMnO_3$. Stabilité de phase

En général, la famille $RMnO_3$ (R = terre rare, y compris Y ou Sc) cristallise dans deux types de structures cristallines dans les conditions ambiantes: orthorhombique ou hexagonal. La structure orthorhombique (Figure R.4a) de type $GdFeO_3$ (groupe d'espace *Pnma* ou *Pbnm*, selon le choix des axes de symétrie) se retrouve pour les grands rayons ioniques de R (R = La-Dy). Cette structure est dérivée de la structure cubique idéale des pérovskites de formule générale ABO_3, où A et B sont grands et petits cations, respectivement, représentée sur la Figure R.2.

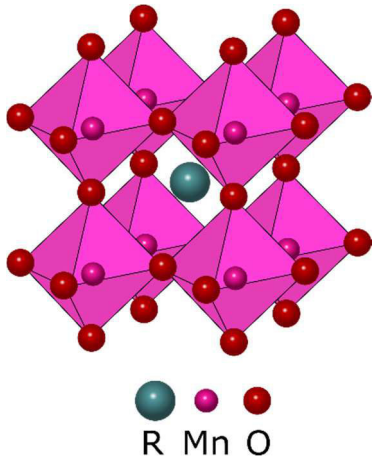

Figure R.2. La structure pérovskite cubique idéale (d'après [5]).

Les pérovskites cubiques sont basées sur un empilement cubique compact d'AO_3 avec les cations B dans des positions octaédriques. Chaque cation A est coordonné de façon équidistante par douze anions O et chaque cation B est coordonné par six anions O, disposés aux sommets d'un octaèdre régulier. Ainsi, les anions O sont entourés par deux cations B et quatre cations A. Ce réseau génère un espace libre autour de l'ion A, qui est entouré par huit octaèdres BO_6. Si la structure idéale des pérovskites est caractéristique pour des matériaux tels que $SrTiO_3$, dans le cas des manganites de terres rares, elle est déformé. Cette déformation est liée à la frustration structurale causée par les différentes tailles ioniques de R et Mn. Un indicateur pour la stabilité de la structure pérovskite est donné par le facteur de tolérance de Goldschmidt.

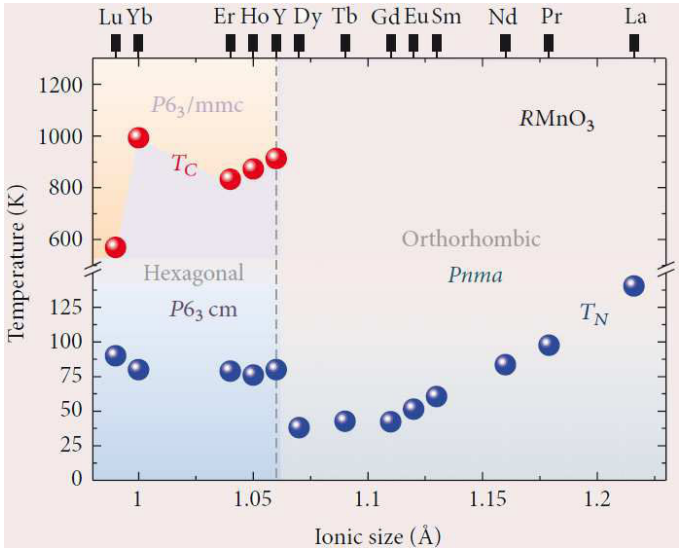

Figure R.3. Structure cristalline, température de Néel (T_N) et de Curie (T_C) de $RMnO_3$ en fonction de la taille ionique de la terre rare [6].

La compatibilité avec la structure est obtenue si la taille ionique de A correspond avec celle des anions O^{2-} pour former des couches d'empilement compact et les cations B s'accommodent dans les sites interstitiels formés par les anions O^{2-} afin d'avoir des octaèdres de BO_6 liés par leurs sommets. Sous cette condition, le rayon ionique de A, B et O doit satisfaire la relation:

$r_A + r_O = \sqrt{2}(r_B + r_O)$. Le facteur de tolérance Goldschmidt est défini comme $t = \frac{r_A + r_O}{\sqrt{2}(r_B + r_O)}$ [7].

Le facteur de tolérance Goldschmidt, utilisé comme un indicateur de la stabilité et de la distorsion des structures cristallines, est généralement considéré comme le facteur déterminant la limite entre les structures hexagonales et orthorhombiques.

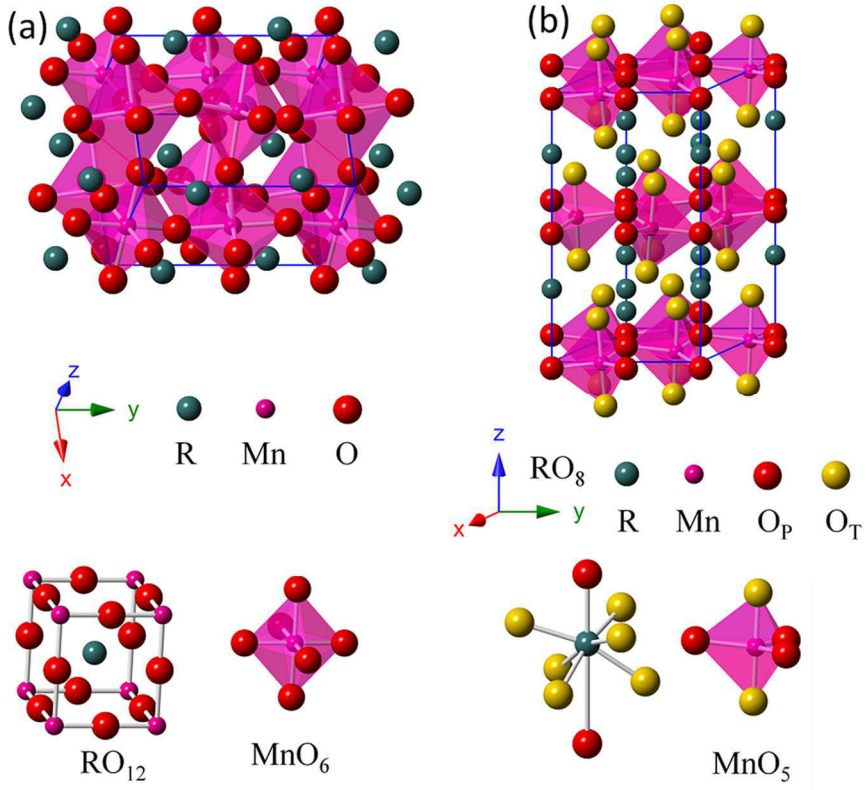

Figure R.4.a) La structure cristalline orthorhombique $RMnO_3$ avec MnO_6 et RO_{12} comme éléments de base; b) la structure cristalline hexagonale $RMnO_3$ avec MnO5 et RO8 comme éléments de base ([8]).

Dans cette perspective, la phase pérovskite orthorhombique est stable pour t > 0.855, correspondant à $r_R > r_{Dy}$ alors que pour t <0.855 ($r_R < r_{Ho}$), la phase hexagonale prévaut [9] (pour une pérovskite idéal t = 1).

Les deux structures et leurs éléments de base sont représentés dans la Figure R.4.

Pour la structure hexagonale (groupe d'espace *P6₃cm*) (R = Y, Ho-Lu), l'octaèdre BO_6 se transforme en bipyramides trigonales de BO_5. Chaque ion B est entouré d'anions O dont trois sont dans le plan et deux sont apicaux, formant les bipyramides trigonales BO_5 qui sont séparés par des couches de cations A (coordination 8).

La Figure R.3 résume la structure (symétrie) et les propriétés physiques (température de Néel - T_N, température de Curie - T_C) de la famille $RMnO_3$ en fonction de la taille de l'ion R.

Du point de vue thermodynamique, la stabilité des deux phases a été étudiée compte tenu de l'énergie libre de formation de Gibbs de $RMnO_3$ à partir de R_2O_3 et Mn_2O_3 à 900 °C et à la pression ambiante [10]. Les résultats sont présentés dans la figure R.5 et on observe que la transition entre les polytypes orthorhombique et hexagonal se déroule autour de R = Ho, qui est en accord avec les résultats basés sur le facteur de tolérance Goldschmidt.

En extrapolant les données thermodynamiques, la phase métastable peut être stabilisé sous forme de films épitaxiés si la différence entre les énergies de formation de Gibbs de deux polymorphes ne dépasse pas 10 à 15 kJ mol^{-1}.

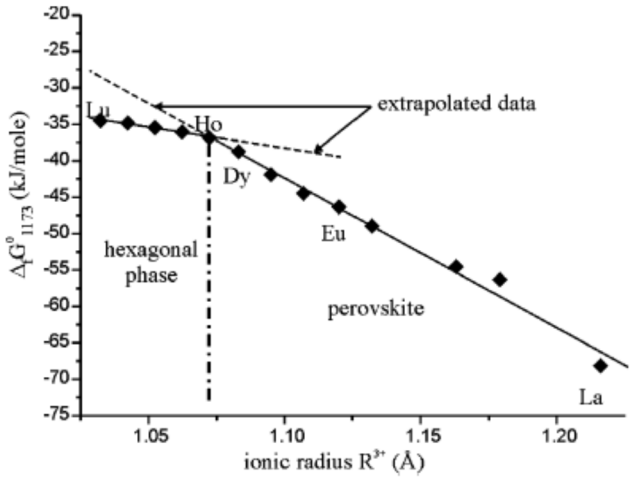

Figure R.5. L'énergie libre de formation de Gibbs de $RMnO_3$ à partir de R_2O_3 et Mn_2O_3 à 900 °C et à la pression ambiante ([10]).

Par exemple, les films minces de $RMnO_3$ (R = Gd, Eu, Sm) de structure stable orthorhombique en massif ont été stabilisés dans la forme hexagonale par épitaxie lors de la croissance sur des substrats cubiques ($ZrO_2(Y_2O_3)$ orientés (111)) par MOCVD [11].

La phase $YMnO_3$ hexagonale

La phase de $YMnO_3$ hexagonale est généralement considérée comme stable et cristallise dans le groupe spatial $P6_3cm$ avec les paramètres de maille a = b = 6.1453 Å et c = 11.3714 Å [12].

Magnétisme dans la phase $YMnO_3$ hexagonale

La température de transition de Néel de la phase $YMnO_3$ hexagonal est T_N = 72 K. La structure magnétique consiste en un arrangement triangulaire de spins Mn^{3+} dans le plan basal *ab* à 120 °. L'interaction magnétique principale est basée sur le superéchange antiferromagnétique entre les Mn-O-Mn coplanaires, tandis que le superéchange Mn-O-O-Mn entre des plans adjacents est de deux ordres de grandeur plus faible [13].

Ferroélectricité dans la phase $YMnO_3$ hexagonale

La transition paraélectrique-ferroélectrique (température de Curie ~ 914 K [14]) est associée à la transition de la structure centrosymétrique de groupe d'espace $P6_3/mmc$ à la structure non-centrosymétrique $P6_3cm$ dans lequel les plans de symétrie perpendiculaires à l'axe c hexagonale sont perdus. En outre, le flambage des bipyramides MnO_5 génère un décalage dans le plan des ions apicaux O^{2-} et un décalage vertical des ions Y^{3+}. En raison de ces déplacements, un environnement asymétrique des ions Y est produit et, par conséquent, une polarisation électrique nette.

La phase $YMnO_3$ orthorhombique

La phase o-YMO est considérée comme métastable et cristallise dans le groupe d'espace *Pnma* avec les paramètres de maille a = 5.8361 Å, b = 7.3571 Å et c = 5.2580 Å [15].

Magnétisme dans la phase $YMnO_3$ orthorhombique

Le magnétisme dans la phase o-YMO est complexe. La transition antiferromagnétique a lieu à T_N = 45 K. Entre 40 et 45 K, un état sinusoïdal avec une inclinaison de spin le long de l'axe *b* est présent. En dessous de 40 K, la phase magnétique sinusoïdale se transforme en une structure magnétique cycloïdale avec l'aimantation le long de l'axe *b*. A des températures inférieures à 35 K, la coexistence des états cycloïdaux et de l'état de type E a été observée.

Ferroélectricité dans la phase $YMnO_3$ orthorhombique

La polarisation ferroélectrique se produit à basse température (T_C ~ 30 K [8]), intimement liée à l'ordre magnétique, ainsi la phase o-YMO est un multiferroïque de type II. D'après [16], la ferroélectricité dans l'état colinéaire de type E est entraînée par la magnétostriction asymétrique le

long des axes *a* et *c* qui brise le centre de symétrie du réseau cristallin, produisant une polarisation le long de l'axe *c*. Les déplacements atomiques (~ 10^{-3} Å), associés à la formation d'une structure alternée de liaisons Mn-O-Mn dans le plan *ac*, donnent lieu à des dipôles électriques et donc à de la ferroélectricité.

Le dépôt des films $YMnO_3$ et l'optimisation du processus

La croissance des films YMO a été principalement réalisée par MOCVD (sauf quelques échantillons déposés par PLD) sur des substrats de Si, $SrTiO_3$ (STO), $LaAlO_3$ (LAO) et $(LaAlO_3)_{0.3}(Sr_2AlTaO_6)_{0.7}$ (LSAT). Le choix des substrats appropriés est important pour permettre une croissance sélective des phases hexagonales ou orthorhombique d'$YMnO_3$ et une épitaxie des films.

Dans le cas de films $YMnO_3$ déposés par MOCVD, plusieurs autres facteurs sont également importants: le choix de la température de dépôt, la composition de la solution injectée, la pression et l'atmosphère du système, les précurseurs, la température d'évaporation, etc. Parmi ces paramètres, on a choisi d'étudier plus en détail l'influence de la température de dépôt, la composition de la solution, l'épaisseur du film et de la pression d'oxygène (dans le cas du PLD).

Dans la littérature, les précurseurs organométalliques principaux utilisés étaient $Y(tmhd)_3$ et $Mn(tmhd)_3$, où tmhd = 2,2,6,6-tétraméthyl-3,5-heptane-dionate, et avec la formule $YC_{33}H_{57}O_6$ et $MnC_{33}H_{57}O_6$, respectivement, qui ont été dissous dans le solvant monoglyme (1,2-diméthoxyéthane de formule $C_4H_{10}O_2$). Les deux précurseurs sont mélangés dans le réservoir étanche de l'injecteur. Les précurseurs organométalliques solides de type tmhd sont souvent préférés en raison de leur stabilité à la température ambiante et de leur non-toxicité par rapport à d'autres précurseurs liquides ou solide de type *acac* (acétylacétonate d'hydrate). En outre, ils sont chimiquement compatibles entre eux et avec le solvant.

Les conditions typiques de dépôt utilisées dans ce travail pour l'élaboration de films sont résumées dans le tableau R.1. Deux installation MOCVD ont été utilisées, nommées horizontale et verticale, avec les mêmes principes de fonctionnement. Chaque croissance de couche dans le réacteur MOCVD horizontal a été suivie d'un recuit in-situ à la même température que le dépôt, pendant 30 minutes dans l'air avec un flux supplémentaire d'O_2 pour oxygéner complètement le film. Dans le cas du dispositif PI-MOCVD vertical, aucun recuit n'a été effectué.

On a trouvé que la température du substrat et le rapport atomique Y/Mn dans la solution injectée jouent un rôle clé dans la cristallinité des films. Différents nombre d'injections et temps de dépôt ont été utilisés afin de réaliser différentes épaisseurs de film.

Parameter	Horizontal PI-MOCVD	Vertical PI-MOCVD
Substrates (100-oriented)	Si, STO, LAO, MgO, YSZ*	Si, STO, LAO, LSAT, MgO
Substrate temperature (°C)	600 − 850	600 − 800
Evaporation temperature (°C)	230	250
Deposition time (min)	10 − 40	10 − 80
Metalorganic precursors	$Y(tmhd)_3$ and $Mn(tmhd)_3$	$Y(tmhd)_3$ and $Mn(tmhd)_3$
Y/Mn in the injected solution	0.5 − 2	0.25 − 1.33
Solution concentration (mol/l)	0.02	0.02
Transport gas	$Ar + O_2$	$Ar + O_2$
Ar flow rate (cm^3/min)	300	300 − 1700
O_2 flow rate (cm^3/min)	300	220 − 400
Deposition total pressure (Torr)	5	5
Number of injections	450 − 2030	500 − 4000
Injection frequency (Hz)	1	1
Injection time (ms)	2	2
Annealing temperature (°C)	600 − 850	−
Annealing time (min)	30	−

*Table R.1. Les conditions typiques de dépôt utilisées pour la croissance des films minces YMO par PI-MOCVD. *orientation (111).*

Sur la base des plusieurs tentatives pour faire varier le débit de l'argon et d'oxygène ainsi que leur proportion, nous avons conclu que à des débits élevés les films sont très inhomogènes.

Les substrats

D'une part, des films non-contraints ont été déposés sur Si (a = 5.43 Å) en vue de l'intégration dans des dispositifs. Des substrats de Si ont été utilisés dans une première étape d'élaboration pour optimiser le processus de dépôt ayant l'avantage d'être peu coûteux.

D'autre part, les films épitaxiés avec différentes valeurs de contrainte ont été déposés sur des substrats de STO, LAO et LSAT orientés (100).

Les paramètres de maille des substrats sont 3.792 Å pour LAO [17] (pseudocubique), 3.872 Å pour LSAT [18] et 3.905 Å pour STO [17]. Les paramètres de maille de la phase o-YMO en massif sont les suivants: a = 5.8361 Å, b = 7.3571 Å et c = 5.2580 Å [4].

Selon ces valeurs, les valeurs de « mismatch » le long d'une direction donnée calculées comme $f=100\cdot(d_{substrate}-d_{o\text{-}YMO})/d_{o\text{-}YMO}$ sont présentées dans le tableau R.2. Il semble que la croissance le

long de l'axe *b* (*b* out-of-plane) est bien accommodée pour le substrat STO, tandis que pour le substrat de LAO, l'axe *b* dans le plan (*b* in-plane) est plus favorable. Les orientations possibles sont illustrées dans la figure R.21.

Substrate	**Lattice parameter (Å)**	**Substrate diagonal (011) (Å)**	**Mismatch (%)**			
			***b* in-plane**		***b* out-of-plane**	
			f_{010}	f_{101}	f_{100}	f_{001}
LAO	3.792* [17]	5.362	3.08	-2.93	-8.12	+1.98
LSAT	3.872 [18]	5.475	5.26	-0.88	-6.19	+4.13
STO	3.905 [17]	5.522	6.15	-0.03	-5.38	+5.02

Table R.2. Le désaccord paramétrique entre les substrats STO, LAO (pseudocubique) et LSAT et la phase orthorhombique YMO (voir définitions dans le texte).*

La température de dépôt

L'évolution de la composition des films, la microstructure et la morphologie ont été étudiées pour différentes températures et compositions. Il a été observé que sur les substrats de Si les échantillons près du rapport Y/Mn optimal et déposé à 600 °C sont amorphes, ceux qui sont déposés à 750 °C sont orthorhombiques et enfin ceux qui sont déposés dans la gamme 800-850 °C sont hexagonaux.

Le rapport Y/Mn

Le contrôle de la composition du film est l'un des principaux défis de la croissance MOCVD d'oxydes et donc une attention particulière a été accordée à l'optimisation de ce paramètre.

Dans les conditions expérimentales utilisées, le précurseur $Y(tmhd)_3$ ne réagit pas de la même manière que le $Mn(tmhd)_3$. En conséquence, il existe une différence dans le rapport Y/Mn dans la solution injectée et dans le film. Nos résultats ont montré que le contrôle de la composition des films est fortement influencé par la géométrie de l'appareil de MOCVD expérimental et dans une moindre mesure cette composition est influencée par la température de dépôt.

Le rapport optimal Y/Mn dans la solution nécessaire pour obtenir un rapport Y/Mn proche de 1 dans le film sont compris entre 1 et 1.4 dans la configuration du MOCVD horizontale et autour de 0.5 dans la configuration du MOCVD verticale.

En dehors de ces compositions, des phases secondaire ont été formées afin de compenser l'excès de Y (Y_2O_3 pour Y/Mn>1.4 ou Y/Mn>0.5 dans le MOCVD horizontal ou vertical, respectivement)

ou de l'excès de Mn (Mn_3O_4 ou YMn_2O_5 pour Y/Mn <1 ou Y/Mn<0.5 dans le MOCVD horizontal ou vertical, respectivement).

La variation des deux principaux paramètres (température et rapport Y/Mn) conduit à une croissance sélective des films d'YMO/Si comme illustré sur la Figure R.6.

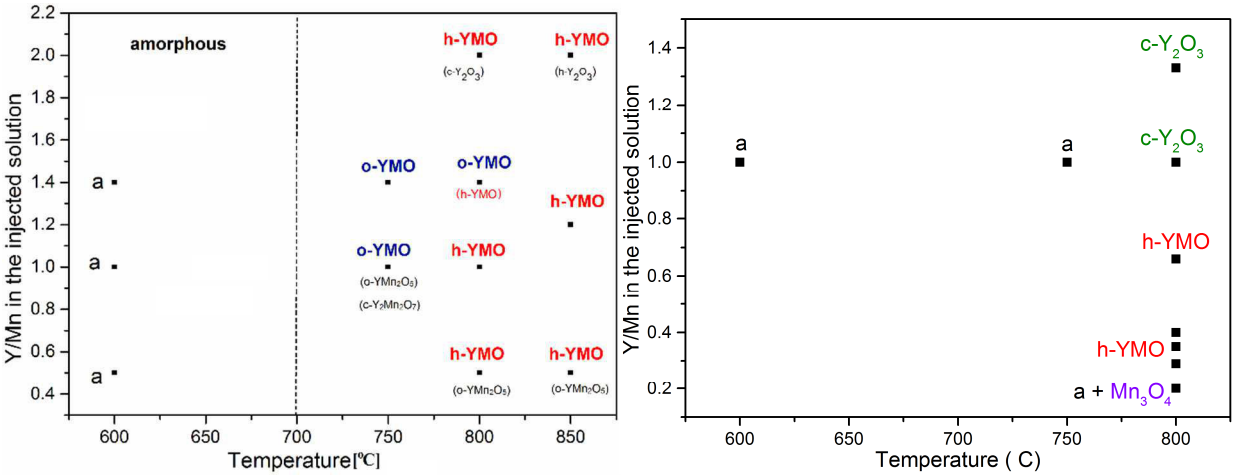

Figure R.6. Dépendance de la structure cristalline en fonction de la température et le rapport Y/Mn dans la solution injectée pour le réacteur PI-MOCVD vertical (a) et horizontal (b).

Une croissance sélective similaire est trouvée en fonction de la pression d'O_2 (avec une température fixe T = 800 °C) pour le PLD. À basse pression, la phase h-YMO est formée, dans la plage de pression d'O_2 intermédiaire une phase amorphe domine et à haute pression la phase o-YMO est stabilisée.

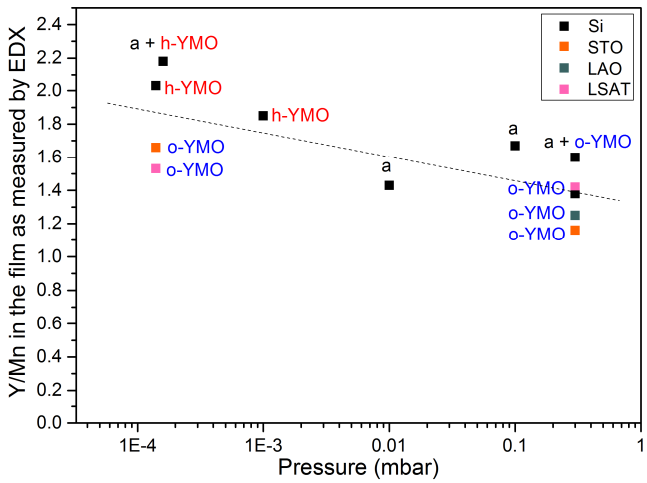

Figure R.7. La formation des phases en fonction de la pression d'O_2 et le rapport atomique Y/Mn dans les films déposés par PLD sur différents substrats à 800 °C.

Sur les substrats de type pérovskite les paramètres de dépôt (température, rapport Y/Mn, pression d'oxygène) ont presque aucune influence et la phase orthorhombique YMO est stabilisée par un mécanisme de contrainte.

Caractérisation structurale de films $YMnO_3$ sur des substrats Si(100)

Caractérisation des films amorphes

Les films YMO déposés à 600 ° C sont amorphes dans une large gamme de compositions ($0.5 < Y/Mn_{solution} < 2$), ce qui indique que la phase amorphe est facilement formée et stable pour les conditions de croissance MOCVD. Cette phase se forme avant la cristallisation de phases soit o-YMO ou h-YMO, même si des substrats appropriés (STO, LAO, GaN) favoriseraient les phases cristallines o-YMO ou h-YMO [19], [20].

La formation de la phase amorphe YMO est indépendante de la méthode de synthèse, la composition initiale des précurseurs ou la pression d'oxygène. Les films déposés par MOCVD suivent un mode de croissance colonnaire 3D avec des colonnes de diamètre compris entre 15 et 20 nm et une morphologie de “chou-fleur”. Un exemple typique d'une section transversale observée au TEM pour un film amorphe déposé par MOCVD (T = 600 °C, Y/Mn = 1.4) est représenté sur la Figure R.8.

Les images TEM en faible grossissement (Figure R.8a) illustrent la croissance colonnaire du film YMO déposé sur le substrat Si couvert d'une couche d'oxyde naturel de SiO_x de quelques nanomètres (voir encadré de la Figure R.8a). Les colonnes individuelles de l'ordre de 20 nm de diamètre sont mises en évidence dans l'image HRTEM sur la Figure R.8b. Le SAED correspondant d'un amorphe est caractérisée par la présence d'un anneau de diffraction, clairement visible dans la Figure R.8d.

Les mesures d'aimantation (M(T)) ont été réalisées sur les films amorphes dans les modes ZFC (refroidissement sans champ) et FC (refroidissement avec champ). Elles suggèrent un comportement de verre de spin avec un maximum dans la courbe ZFC entre 11 et 19 K.

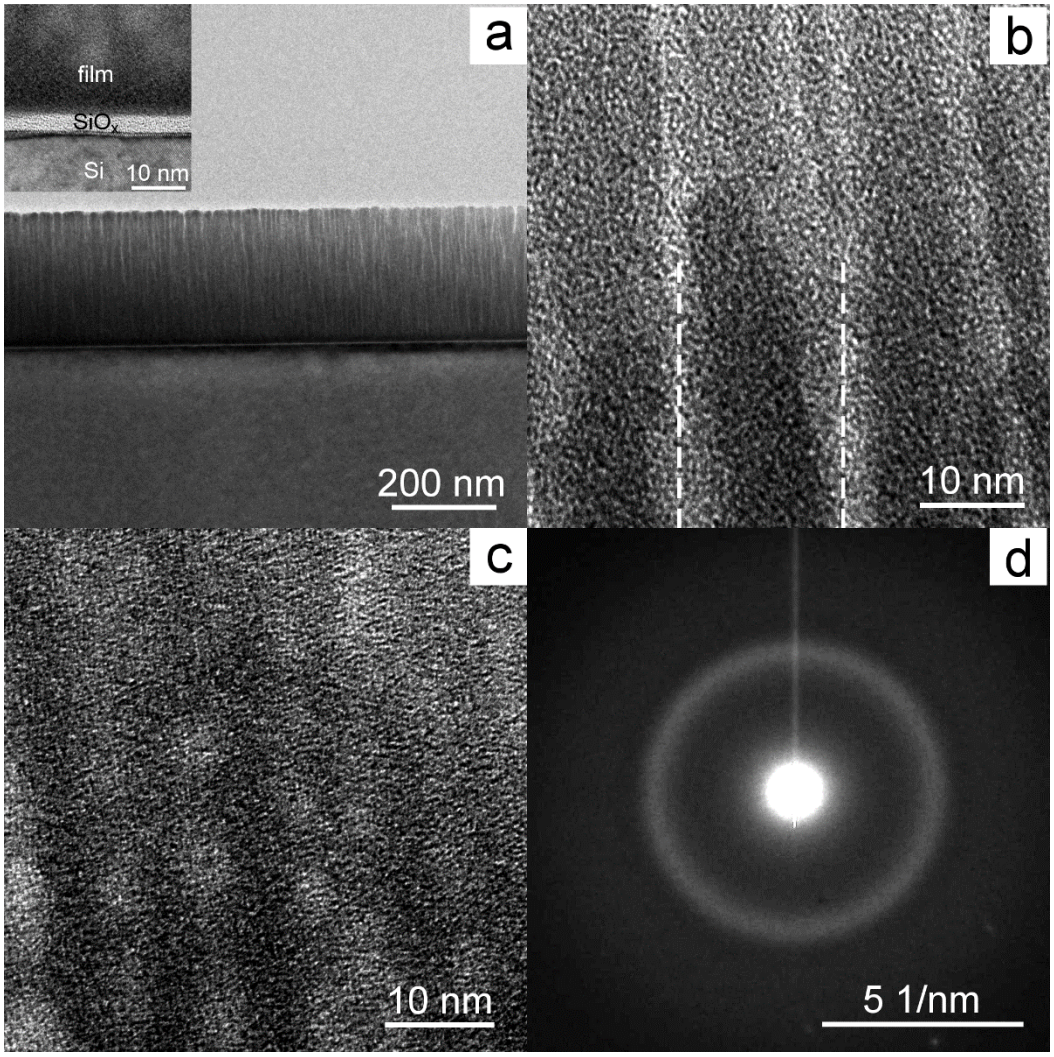

Figure R.8. Observations TEM, en section transversale du film YMO-600-1.4: a) faible grossissement TEM montrant la structure colonnaire (en encadré l'interface substrat-film avec la couche SiO_x entre les deux); b) l'image HRTEM des colonnes individuelles; c) HRTEM typique de la structure amorphe YMO d) le SAED correspondant de c).

Caractérisation des films hexagonaux YMO

Les films h-YMO, déposés par MOCVD ou PLD ont été caractérisés par plusieurs techniques et les caractéristiques suivantes en résulte:

- Orientation

En ce qui concerne l'orientation, les films MOCVD sont principalement textures selon l'axe *c*, fortement influencée par la température de dépôt et, dans une moindre mesure le rapport Y/Mn dans la solution (voir Figure R.9a). Ainsi, les diagrammes de diffraction XRD sont caractérisés

par des pics intenses (0002) et (0004) de la phase h-YMO pour les films déposés à 800 ° C (bien que des petits pics (11-20) et (11-21) soient également observés). Les diagrammes de XRD des films déposés à 850 °C sont représentés par le pic intense (11-21) et par de pics moins intenses de la famille {000l} et (11-20).

D'autre part, les films par PLD sont principalement orientés (11-20) et (11-21), indépendamment de la pression d'oxygène utilisée ($1.4 \cdot 10^{-4} < P_{O2} < 3 \cdot 10^{-1}$). Par rapport aux films MOCVD texturés, dans les films par PLD l'orientation selon l'axe *c* est complètement supprimée (voir Figure R.9b).

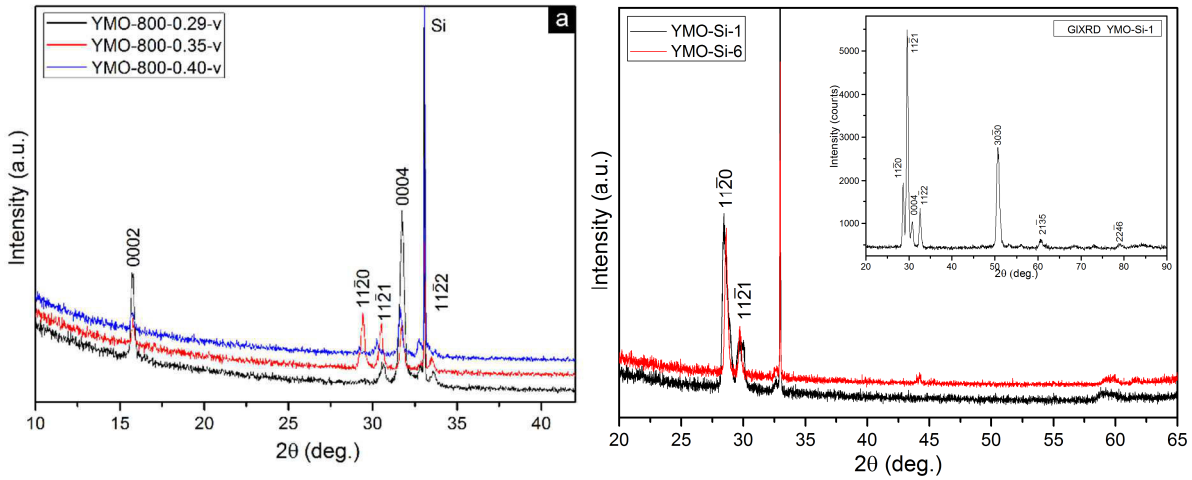

Figure R.9. a) Diagrammes XRD de films YMO indexés avec la phase h-YMO (JCPDS card No. 11-9577); b) les diffractogrammes XRD θ-2θ de films h-YMO déposés par PLD à différentes pressions d'O_2. En encadré: Le GIXRD de l'échantillon YMO-Si-1.

- Les paramètres de maille

Des grandes variations dans les valeurs de paramètres de maille sont produites par le rapport Y/Mn dans le film (DRX et Raman à la fois sont sensibles à ces variations). En conséquence la phase h-YMO peut être formée dans une gamme large de non-stoechiométrie. La Figure R.10 résume les valeurs de paramètres *a* et *c* obtenus pour les films h-YMO déposées par MOCVD et PLD en fonction du rapport Y/ Mn dans le film mesuré par EDX.

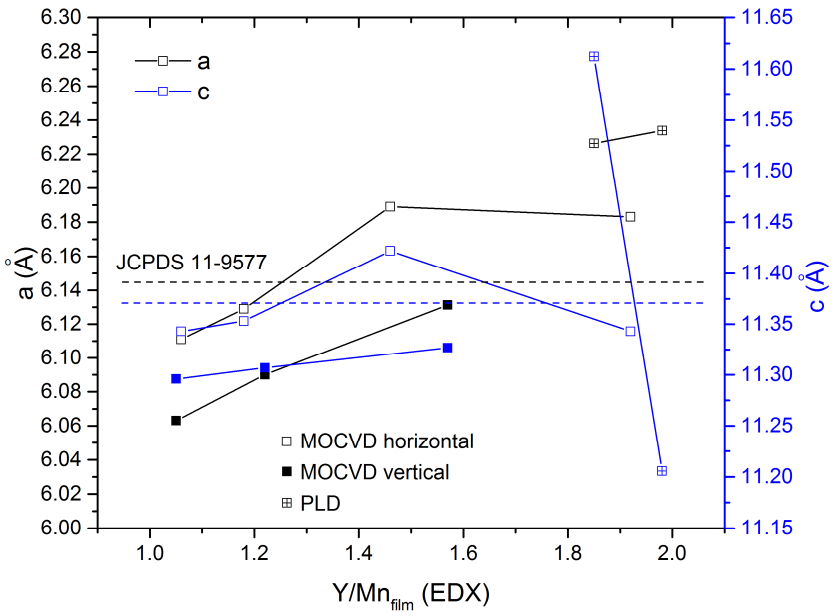

Figure R.10. Les valeurs des paramètres a et c obtenues pour les films h-YMO déposés par MOCVD et PLD en fonction du rapport Y/Mn dans le film.

La microstructure

Les films h-YMO par MOCVD présentent une croissance colonnaire (voir Figure R.11a), qui est typique du procédé MOCVD avec un diamètre de grain entre 20-40 nm. Une couche amorphe (10 à 50 nm) se forme entre les films h-YMO et le substrat de Si, indépendamment de la température ou le rapport Y/Mn (voir Figure R.11a).

La croissance PLD produit des grains denses de forme polygonale, notamment, entre 90 à 150 nm.

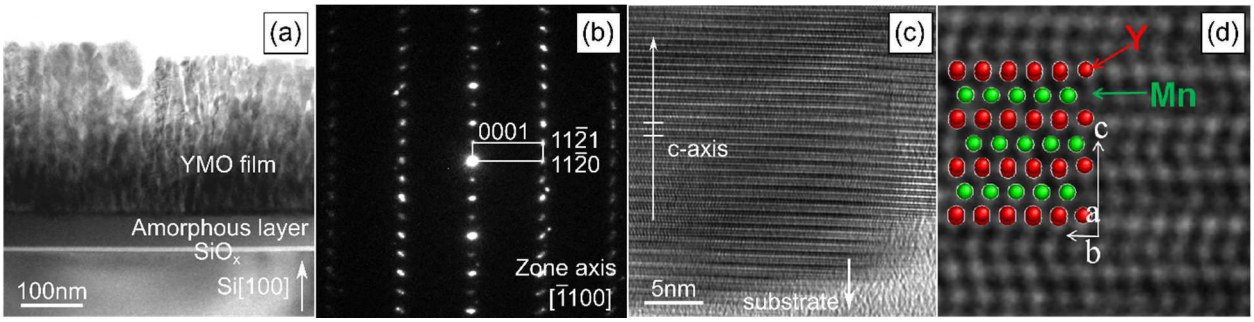

Figure R.11. Les images TEM du film YMO-800-1-s1 déposé par MOCVD: (a) image TEM à faible grossissement en coupe transversale montrant trois couches différentes sur le Si; (b) SAED d'une petite région de (a) contenant plusieurs grains colonnaires; (c) image HRTEM d'un grain en forme de colonne orienté selon l'axe c; (d) élargissement de (c) superposé avec la simulation de la structure.

- Magnétisme

Un comportement de verre de spin, caractérisé par une séparation des courbes ZFC-FC et d'un maximum dans la courbe ZFC à T_f = 20 K a été observé pour les films h-YMO. Une faible contribution ferromagnétique est présente à 5 K dans la courbe M(H).

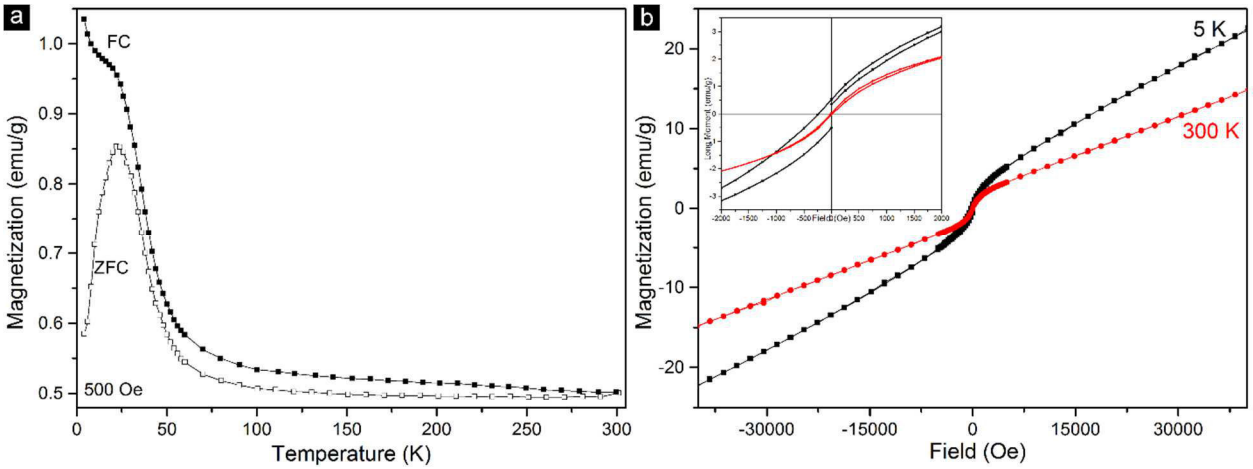

Figure R.12. a) L'aimantation en fonction de la température (M(T)) pour le film YMO-800-1-s1. Les symboles ouverts (pleines) représentent M(T) dans le mode ZFC (FC); b) la dépendance de l'aimantation en fonction du champ (M(H)) à 5 et 300 K. En encadré: l'élargissement de la courbe M(H) pour les faibles valeurs d'aimantation.

Une séparation des courbes ZFC-FC a été observée pour les poudres polycristallines de référence à ~ 65 K ($Y_1Mn_1O_3$) et 70 K ($Y_{0.95}Mn_1O_3$), sans maximum dans la ZFC. Contrairement, le monocristal de référence h-YMO présente (à la fois M(T) et M(H)) un ordre antiferromagnétique pur à T_N = 70 K.

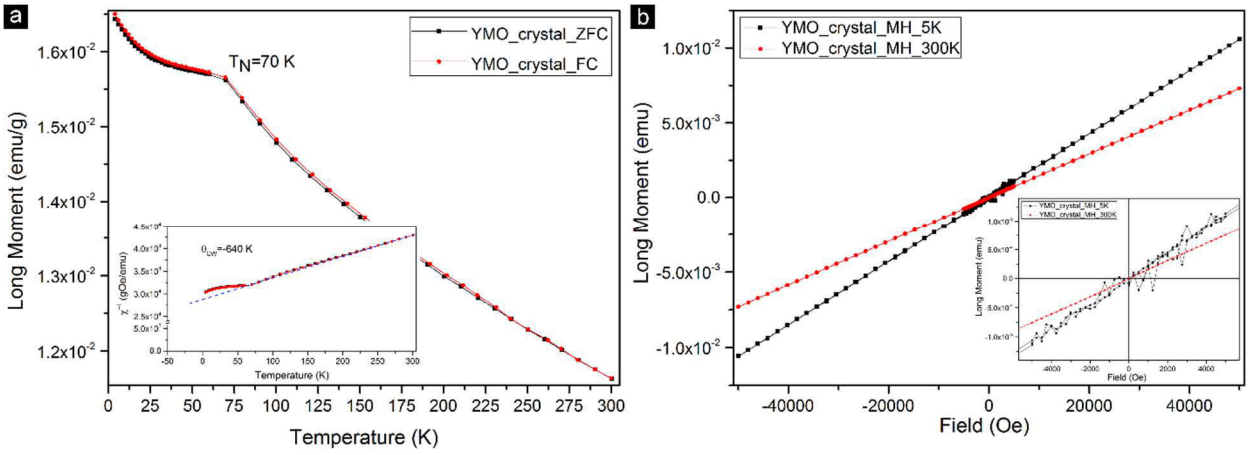

Figure R.13. Les mesures de l'aimantation de monocristal $YMnO_3$: a) L'aimantation M(T) en mode ZFC-FC. Dans l'encadré la courbe de Curie-Weiss (χ^{-1} vs. T); b) M(H) à 5 et 300 K.

Caractérisation des films YMO orthorhombiques

Les films o-YMO ont été déposés sur des substrats Si(100) à la fois par MOCVD et PLD sans aucun mécanisme de stabilisation epitaxiale et sans la phase h-YMO (la phase secondaire $Y_2Mn_2O_7$ identifiée dans la Figure R.14b a été obtenue dans certains cas, à cause de la stœchiométrie de la solution de précurseur).

Les principaux résultats de la caractérisation des films o-YMO, déposés par MOCVD ou PLD sont les suivantes:

- Orientation
  - Les films sont principalement polycristallins. Les diagrammes de XRD (θ-2θ et GIXRD) sont caractérisés par la présence de tous les pics de la phase o-YMO avec l'intensité des pics proche de celles du massif (Figure R.14).
  - Des régions de grains texturés sont observées à l'échelle nanométrique par SEM et TEM en vue de dessus (Figure R.15).

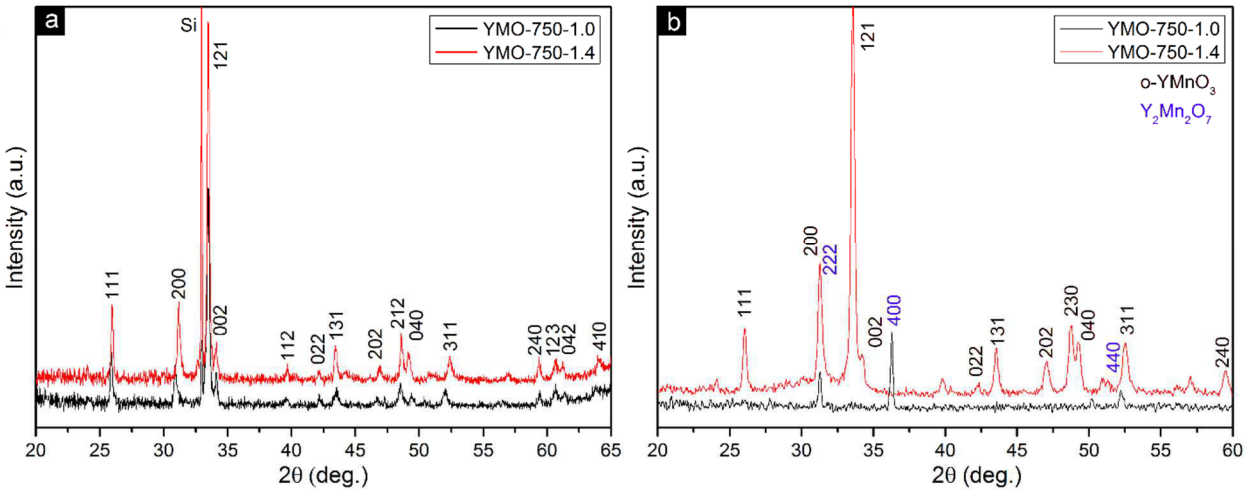

Figure R.14. Diagrammes XRD de films o-YMO: YMO-750-1 (ligne noire) et YMO-750-1.4 (ligne rouge): a) les diffractogrammes θ-2θ indexés avec la phase o-YMO; b) les diffractogrammes GIXRD indexées avec la phase $Y_2Mn_2O_7$ pour le film YMO-750-1 et avec la phase o-YMO pour le film YMO-750-1.4.

- Les paramètres de maille
  - Certaines variations dans les valeurs des paramètres de maille sont produites par le rapport Y/Mn dans le film (MOCVD) et P_{O2} (PLD): de 5.732 à 5.791 Å pour *a*, de

7.338 à 7.402 Å pour *b* et de 5.237 à 5.253 Å pour *c*. En conséquence, la phase o-YMO peut être formée dans une gamme relativement large de non-stoechiométrie.

- La microstructure
  - Une croissance colonnaire est observée pour les films o-YMO par MOCVD avec des colonnes entre 15 à 30 nm et des agrégats de grains allant de 200 à 400 nm. De même, la croissance par PLD produit des grains de 20 à 30 nm et des agrégats de grains entre 65 et 75 nm.
  - Une couche amorphe d'environ 10 nm est formée à l'interface film o-YMO - substrat Si, indépendamment de la composition initiale Y/Mn.

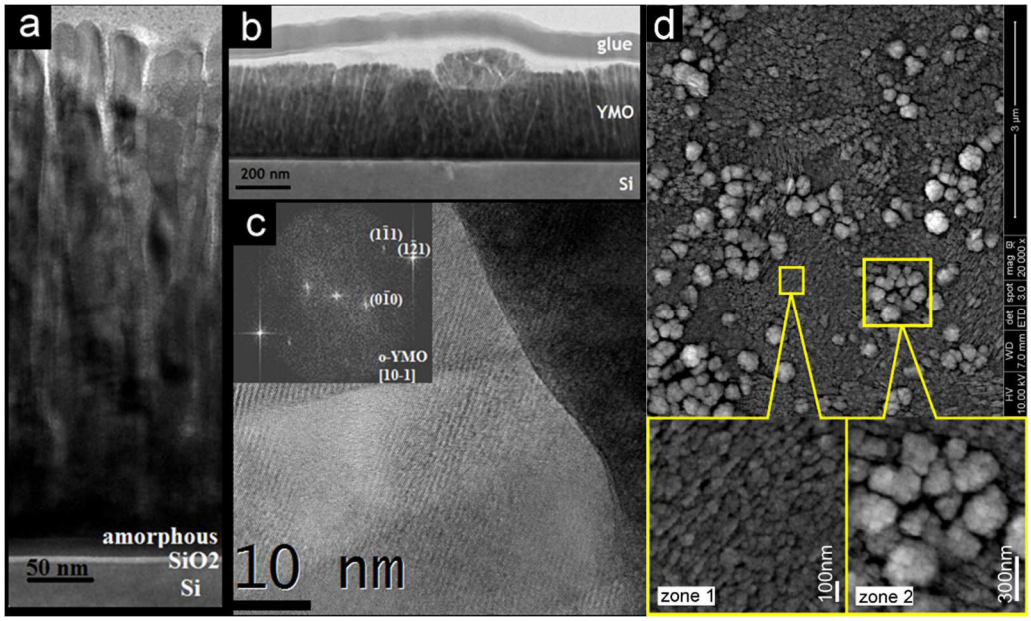

Figure R.15. Observations TEM en section transversale pour le film YMO-750-1: a) image montrant les différentes couches sur le dessus du substrat de Si et la morphologie de croissance colonnaire b) image à faible résolution montrant l'aspect général du film avec deux types de morphologies; c) image à haute résolution d'une région agrandie de a) et la FFT associée (en encadré) indiquant la même orientation pour deux colonnes voisines correspondant à l' axe de zone [10-1] de o-YMO; d) images MEB en vue de dessus du film YMO-750-1.4: deux types de morphologies peuvent être identifiés: colonnaire (zone 1) et dendritique (zone 2).

- Magnetisme
  - Les mesures magnétiques indiquent un comportement de verre de spin, caractérisé par une separation des courbes ZFC-FC, avec un maximum dans la courbe ZFC à T_f = 20 K. Une faible contribution ferromagnétique est observée à 5 K.

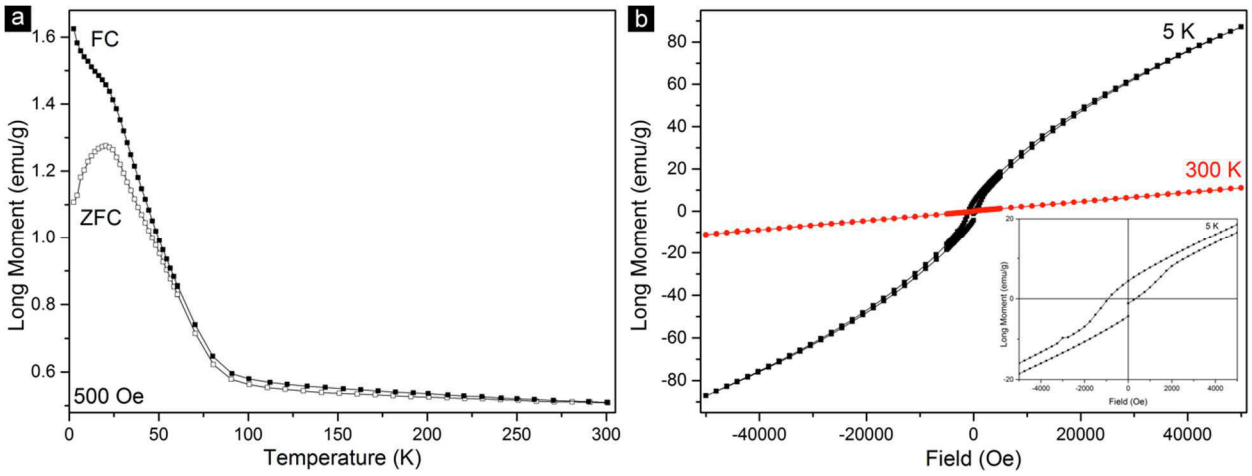

Figure R.16. L'aimantation en fonction de la température (M(T)) pour le film YMO-750-1.4. Les symboles ouverts (pleines) représentent le M(T) acquis dans le mode ZFC (FC); b) La dépendance de l'aimantation en fonction du champ (M(H)) à 5 et 300 K. En encadré: l'élargissement de la courbe M(H) pour les faibles valeurs d'aimantation.

Transformations de phase et études de stabilité thermique dans les films $YMnO_3$ sur de substrats Si(100)

Cette partie couvre les transformations de phase et la stabilité de la phase o-YMO dans les films amorphes et dans les films o-YMO, respectivement. Des expériences in-situ et ex-situ ont été effectuées afin d'étudier la transformation de films amorphes YMO en phase o-YMO et le comportement du film o-YMO lors de recuits thermiques. La transformation de l'état amorphe à la phase o-YMO et sa stabilité ont été étudiées en détail en utilisant DRX, MEB, MET et la spectroscopie Raman.

La Figure R.17 montre le diagramme de diffraction des rayons X des films YMO-600-1 (T_s=600 °C, Y/Mn=1, Figure R.17a) et YMO-600-1.4 (T_s=600 °C, Y/Mn=1.4, Figure R.17b) recuits entre 750 et 900 °C sous une atmosphère d'air pendant 1h à chaque étape. En comparaison avec les diagrammes de XRD du dépôt initial, dans laquelle aucun pic n'a été observé (sauf le substrat en Si), la Figure R.17 montre la présence de pics cristallins indexés avec la phase o-YMO.

Plus précisément, les films initialement amorphes se transforment de manière irréversible dans la phase o-YMO dans la plage de température de 675 à 700 ° C comme le montre l'expérience Raman in-situ sur la Figure R.18. Les spectres Raman ont été enregistrés lors du recuit à partir de la température ambiante jusqu'à 1100 ° C, sous atmosphère d'Ar.

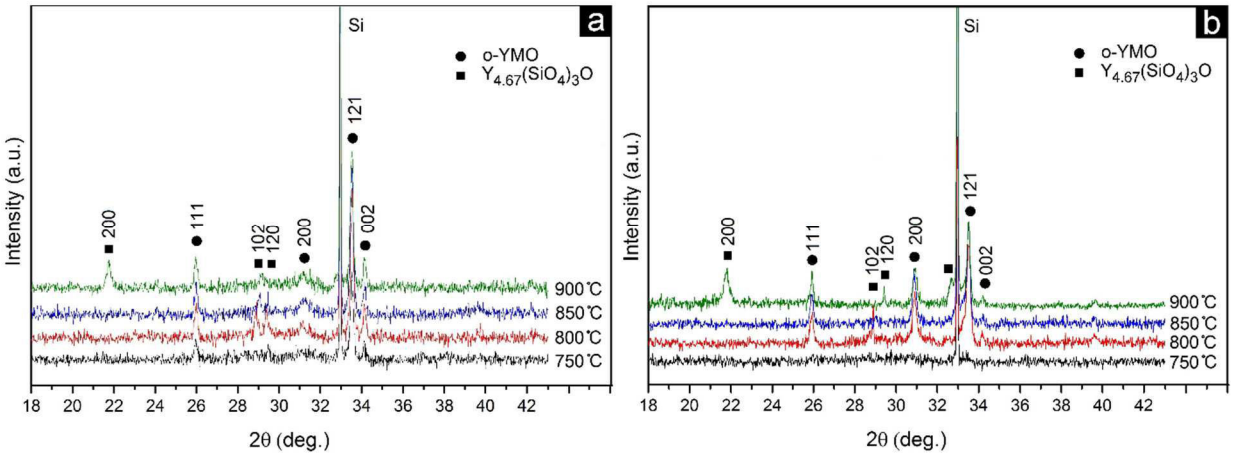

Figure R.17. Diagrammes de XRD des films recuits YMO-600-1 (a) et YMO-600-1.4 (b) sous air pour 1h à chaque étape. La température de recuit est indiquée sur chaque diffractograme.

Lors du chauffage de la RT à 675 °C sous atmosphère d'argon, la bande large caractéristique de l'échantillon amorphe se décale progressivement de ~ 650 cm^{-1} à RT à ~ 637 cm^{-1} à 675 °C avec, simultanément, une diminution de l'intensité et un élargissement des raies, comme attendu pour la dilatation thermique. Un changement brusque par rapport à la transformation de phase est observé dans le spectre avec augmentation supplémentaire de la température à 700 °C (voir spectre rouge dans la Figure R.18).

A 700 °C, trois raies Raman apparaissent ~ à 306, 381 et 609 cm^{-1} et sont indexées avec les modes Raman $A_g(4)$, $A_g(5)$ et $B_{2g}(4)$ de la phase o-YMO, en tenant compte du déplacement du à la dilatation thermique. Une fois que la phase o-YMO a été formée, elle reste stable pendant le chauffage jusqu'à 900 °C.

Un changement irréversible dans l'échantillon a lieu à 1000 °C (voir l'encadré de la Figure R.18), qui est liée à la formation d'une nouvelle phase en raison de la diffusion de Si dans le film.

La stabilité de la phase o-YMO dans la gamme RT-900 °C (pendant le chauffage et le refroidissement) a également été confirmée par la réalisation d'une expérience Raman in-situ (voir

la Figure R.19) en utilisant l'échantillon pour lequel la phase o-YMO a été initialement déposée (YMO-750-1.4, T_s=750 °C, Y/Mn=1.4).

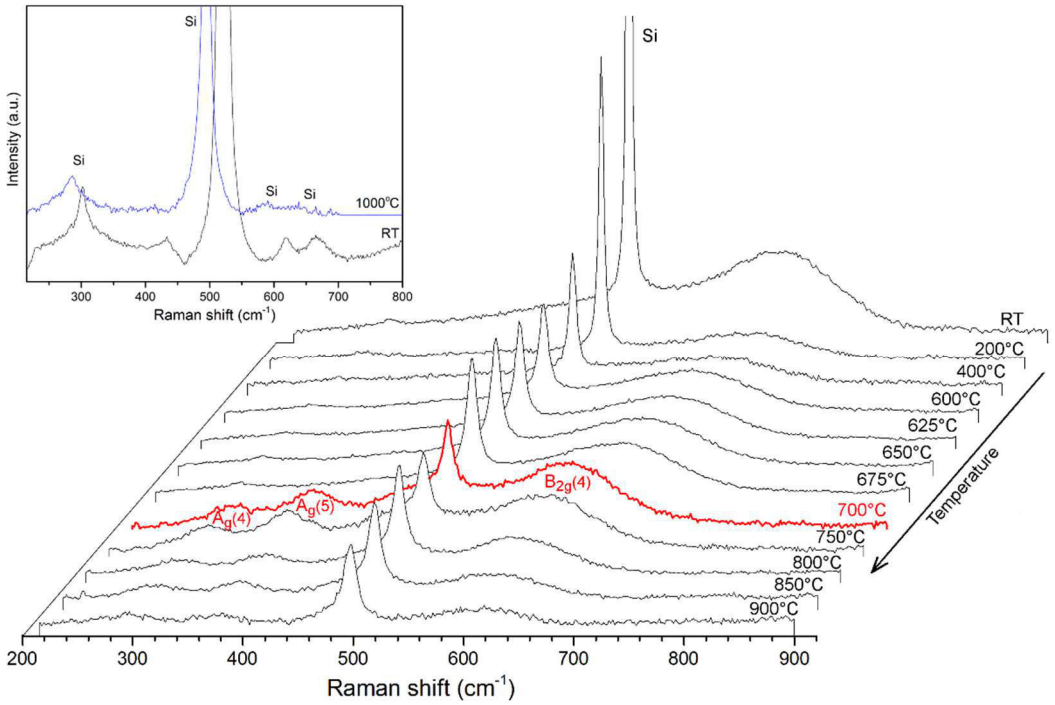

Figure R.18. Les spectres Raman en fonction de la température du film YMO-600-1 dans la plage de température RT-900 °C. Le spectre rouge marque la cristallisation de la phase o-YMO depuis l'amorphe. En encadré: les spectres à 1000 °C et après refroidissement à la température ambiante.

Tous les modes Raman à l'exception de la ligne Si peuvent être indexés avec la phase o-YMO sur toute la plage de température. Un déplacement des lignes vers les faibles nombres d'onde, une diminution de l'intensité et des élargissements de ligne sont observés lorsque la température augmente pour toutes les lignes, comme prévu par la dilatation thermique. Aucun autre changement ne se produit, indiquant que le film o-YMO est stable et ne subit aucune transition de phase dans la gamme de température utilisée. En outre, les spectres mesurés pendant le refroidissement sont identiques à ceux mesurés à la même température pendant le chauffage.

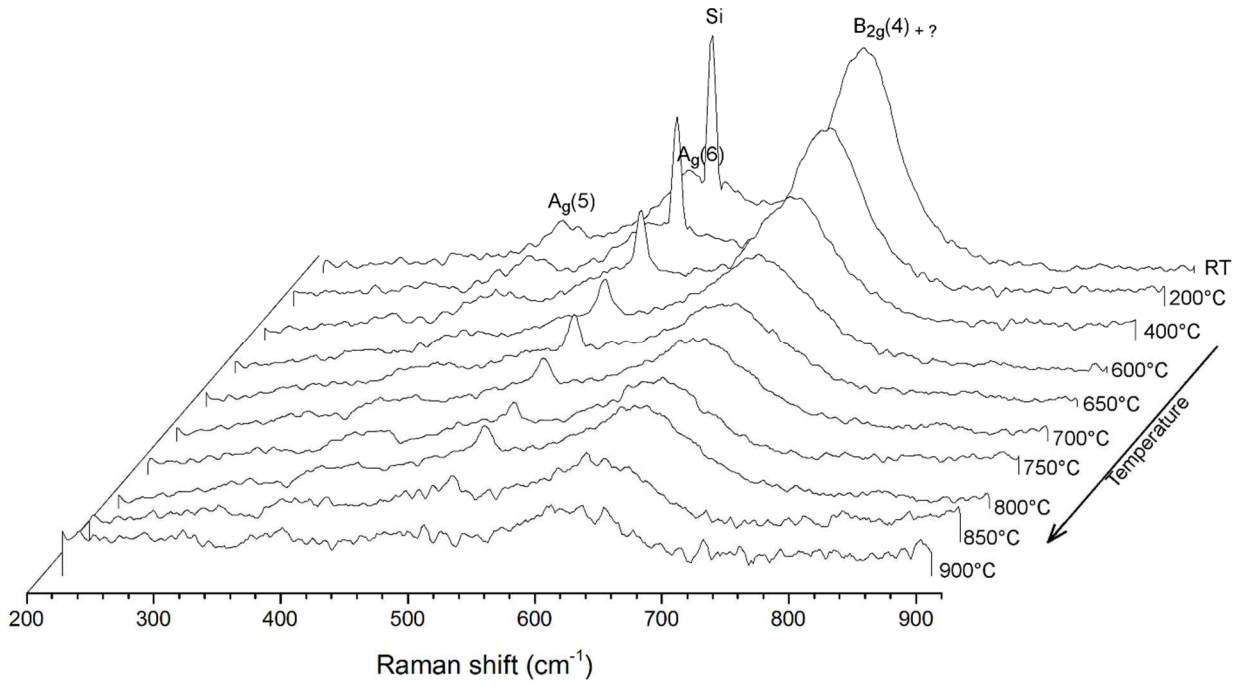

Figure R.19. L'expérience Raman in-situ sur le film YMO-750-1.4 initialement déposée: les spectres Raman en fonction de la température dans la gamme de température RT-900 °C sous atmosphère d'Ar.

Ces résultats expliquent les mécanismes de croissance sélective MOCVD déjà signalés: les films déposés sur le substrat de Si en dessous de 700 °C sont amorphes; ils cristallisent dans la phase orthorhombique pure quand ils sont déposés dans la gamme 750-800 °C, et dans la structure hexagonale pour des températures de dépôt supérieures à 800 °C. La phase YMO amorphe est la phase stable en dessous de 700 °C en accord avec les résultats sur des échantillons en massif préparés par une procédure fondée sur des solutions via complexation par citrates rapportés dans [21]. De cette manière, un carbonate d'oxyde inorganique amorphe a été obtenue (cuisson finale à 350–450 ° C). Cette phase amorphe cristallise principalement dans la phase o-YMO dans la gamme de température de 700-900 °C dans l'air ou en atmosphère d'O_2.

Sous atmosphère de N_2 ou de CO_2, la phase h-YMO prédomine ce qui suggère que la pression partielle d'oxygène a une grande influence sur la proportion en o-YMO. Ces résultats semblent très proches de nos résultats MOCVD et attestent que les mécanismes de croissance et les conditions de procédé pour obtenir la phase o-YMO sont assez similaires: la formation d'une phase amorphe intermédiaire, le recuit à basse température et l'atmosphère oxydante. Les petites différences de température peuvent être dues à différents états amorphe avant la cristallisation [21].

Les paramètres utilisés dans notre travail semblent particulièrement intéressants car aucune phase h-YMO n'est présente dans toute la plage de température étudiée, ce qui améliore la sélectivité du processus de croissance.

On doit noter que la transition prévue de la phase o-YMO dans la phase stable à haute température h-YMO a été signalée près de 1100 °C [8, 21]. Cela explique pourquoi aucune indication de cette transition n'a été obtenue dans notre étude, qui a été limitée à 900 °C, en raison de la diffusion de Si.

Les films épitaxiaux d'$YMnO_3$ déposées sur de substrats orientés (100) de type pérovskites ($SrTiO_3$, $LaAlO_3$ et $(LaAlO_3)_{0.3}(Sr_2AlTaO_6)_{0.7}$)

Les films o-YMO, déposés par les deux techniques MOCVD et PLD présentent une microstructure dense et des surfaces homogènes, sans agrégats de particules, indépendamment du substrat (Figure R.20).

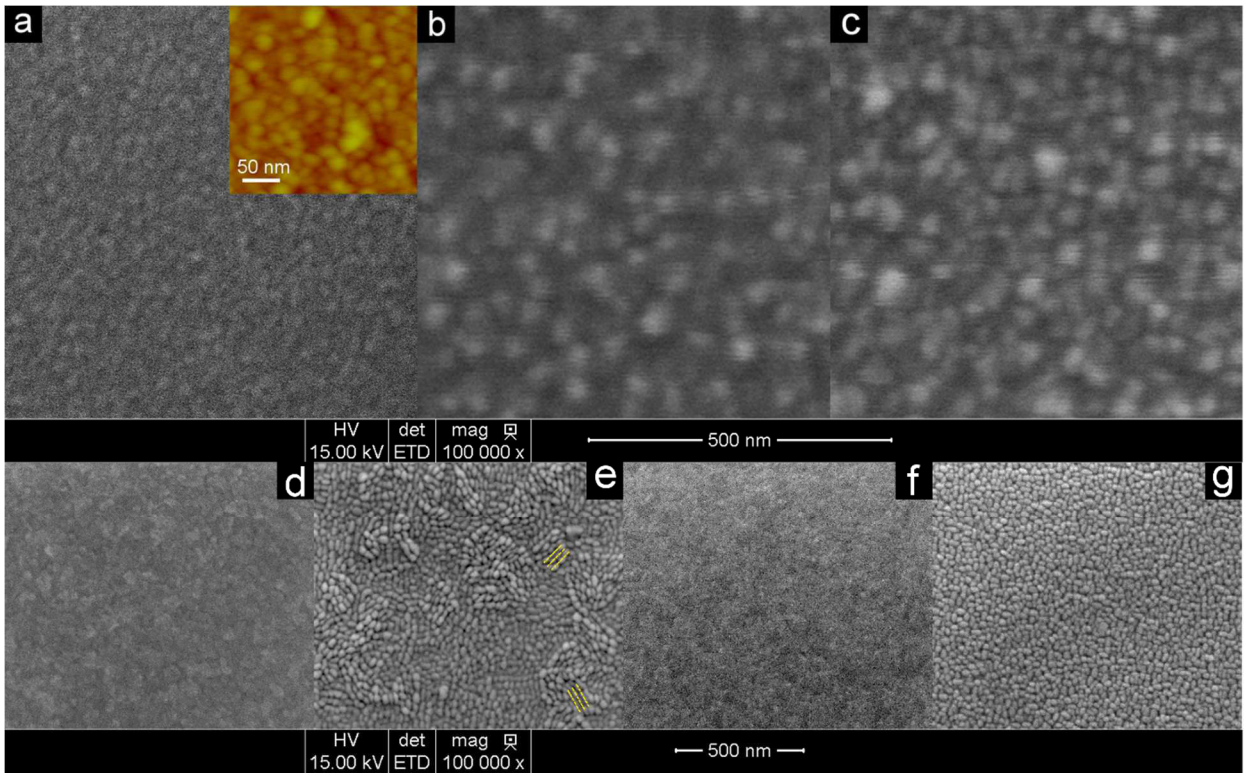

Figure R.20. Images MEB en vue dessus de films o-YMO sur: substrat de STO avec une épaisseur de a) 12 nm (en encadré l'image AFM correspondante) et b) 23 nm; c) film YMO de 20 nm épaisseur sur substrat de LAO ; films de YMO déposés par PLD sur STO à d) $1.4 \cdot 10^{-4}$ bar et à e) $3 \cdot 10^{-1}$ bar ; f) sur LSAT à $1.4 \cdot 10^{-4}$ bar ; g) sur LAO à $3 \cdot 10^{-1}$ bar.

Le MOCVD produit une croissance colonnaire avec des colonnes de diamètre entre 10 et 20 nm et une interface substrat-couche lisse. La morphologie des films déposées par PLD dépend de la pression d'O_2: des grains de forme polygonales très denses, environ 30 nm de diamètre, sont obtenus à faible P_{O2} ($1.4 \cdot 10^{-4}$ bar) tandis que a P_{O2} plus élevées ($3 \cdot 10^{-1}$ bar) des grains de forme ronde, entre 20 et 30 nm et compatible avec une croissance colonnaire sont produits (Figure R.20). Les films épitaxiés o-YMO sont principalement orientés (010) sur les substrats de STO et LSAT et (101) sur le substrat de LAO. Des études détaillées sur des films d'YMO/STO de 12 nm et 23 nm d'épaisseur ont montré qu'en fait quatre types de domaines sont présents. Ceci est équivalent à avoir deux types de domaines tourné de 90° dans le plan donnés par la relation épitaxiale suivante:

- $[010]_{YMO}//[100]_{STO}$ et $[100]_{YMO}//[011]_{STO}$
- $[010]_{YMO}//[100]_{STO}$ et $[100]_{YMO}//[0\text{-}11]_{STO}$
- $[10\text{-}1]_{YMO}//[100]_{STO}$ et $[010]_{YMO}//[010]_{STO}$
- $[10\text{-}1]_{YMO}//[100]_{STO}$ et $[010]_{YMO}//[001]_{STO}$

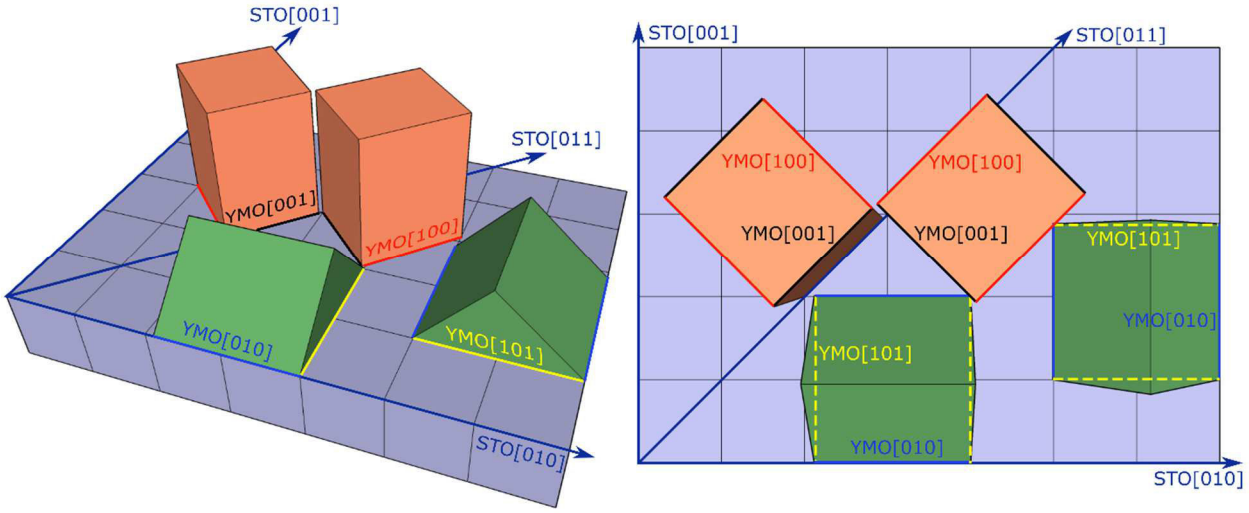

Figure R.21. Représentation schématique 3D de la structure de domaine YMO sur le substrat de STO (la partie gauche de la figure: vue de côté, partie de droite: vue de dessus). En bleu, le substrat de la STO (plusieurs cellules) est représenté par des carrés; en orange et vert, YMO (cellules individuelles) est représenté par des rectangles.

Les paramètres *b* et *c* diminuent avec l'augmentation des épaisseurs de films tandis que le paramètre *a* augmente avec l'augmentation de l'épaisseur du 12 à 23 nm. Toutes les valeurs tendent

vers les valeurs en massif. Les analyses de diffraction des rayons X et RSM indiquent des films contraints avec un mécanisme de relaxation qui dépend de l'épaisseur. Les paramètres de maille des films o-YMO sont fortement affectés par la pression d'oxygène dans le cas des films déposés par PLD.

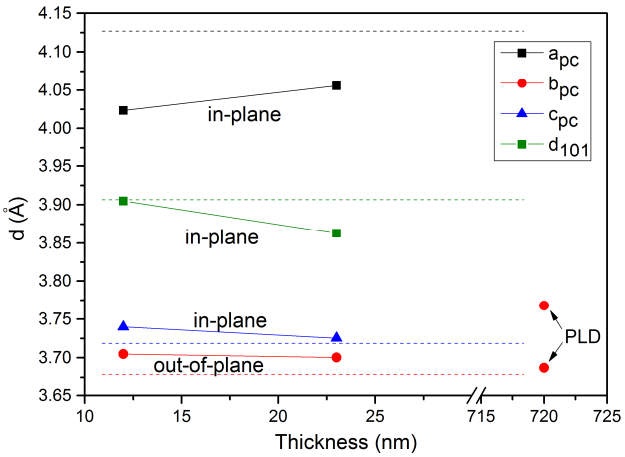

Figure R.22. Les paramètres de maille dans le plan et hors du plan ($a_{pc}=a/\sqrt{2}$, $b_{pc}=b/2$, $c_{pc}=c/\sqrt{2}$) en fonction de l'épaisseur du film (12 et 23 nm) pour les échantillons déposés par MOCVD sur le substrat de STO. Les films YMO épais (720 nm) déposés par PLD sur des substrats de STO à deux pressions différentes d'oxygène sont inclus. Les pointillés horizontaux marquent les valeurs du massif pour les paramètres de maille a, b et c de l'o-YMO [15].

Les observations TEM confirment le scénario de domaines pour le film d'épaisseur 12 nm. En outre, les images TEM haute résolution ont révélé que le film est complètement contraint avec une couche limite de ~ 3 nm. Au-dessus de cette couche le film commence à se relaxer progressivement.

Des films d'YMO non-stoechiométriques ont été déposés par MOCVD sur des substrats de STO, LSAT et LAO orientés (100) en faisant varier le rapport Y/Mn dans la solution initiale de précurseurs et leurs propriétés structurales ont été analysés. En outre, les films ayant des épaisseurs et/ou des compositions chimiques variables ont également été étudiés.

Parce que l'écart par rapport à la composition stoechiométrique était trop grande, les films YMO ne sont pas purs; ils présentent des phases secondaires tels que YMn_2O_5 pour la région riche en Mn ($0.25 < Y/Mn_{solution} < 0.35$) et Y_2O_3 pour la région riche en Y ($Y/Mn_{solution}=1$). De petites variations dans les paramètres de maille observées par diffraction des rayons X et RSM d'un côté et les positions Raman de l'autre côté, indiquent que la phase o-YMO présente dans la majorité des

films est similaire, mais est non-stoechiométrique. En outre, du fait des phases secondaires, la variation de l'épaisseur (de 20 nm à 370 nm) s'est révélée être sans conséquence et les films sont tous relaxées.

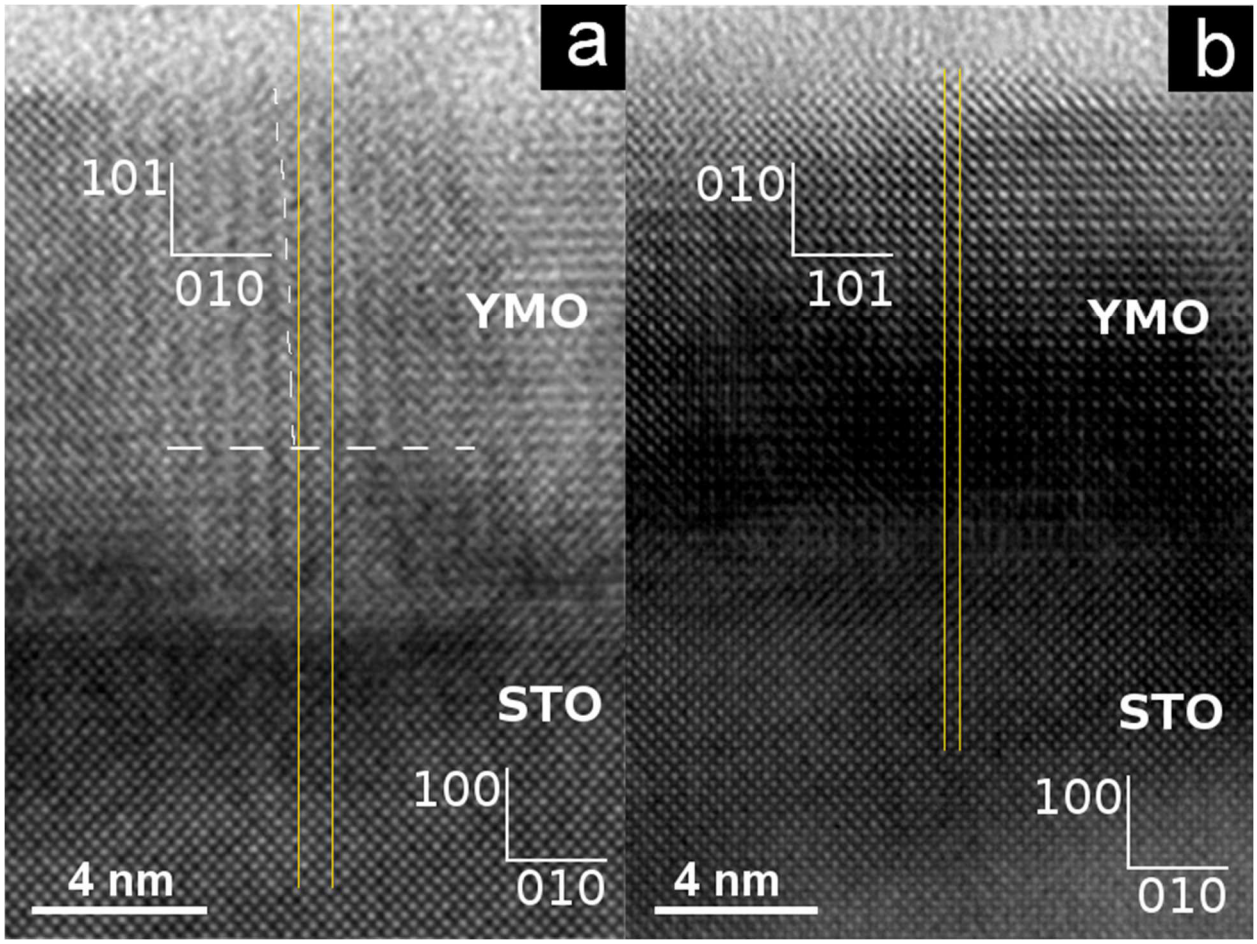

Figure R.23. Image TEM haute résolution en section transversale à l'interface pour différents domaines avec différents état de déformation: (a) la figure montre un relâchement rapide de l'axe b lors du déplacement loin de l'interface avec le substrat de STO pour les domaines similaires à ceux de la région 3 (des lignes horizontales en pointillé indiquent l'épaisseur critique d'environ 3,5 nm); (b) la figure montre que les domaines semblables à la région 1 ne présentent pas de relaxation et sont entièrement contraints (épaisseur critique égale à l'épaisseur du film). Les lignes jaunes sont des guides pour les yeux.

Les variations dans les paramètres de maille ou dans les modes Raman sont proches de films MOCVD présentés à la section 6.1, ce qui suggère une composition similaire de la phase o-YMO (seulement les films PLD étaient différents en raison de la variation O_2 pendant le dépôt).

Conclusions générales

L'optimisation des conditions de croissance. Mécanisme de croissance sélective

Les films YMO ont été déposés par la technique MOCVD sur des substrats de Si, STO, LAO et LSAT orientés (100). Une brève étude supplémentaire concerne plusieurs films YMO déposés par PLD sur les mêmes substrats. Nous montrons que les conditions de croissance doivent être soigneusement optimisées afin d'obtenir des films presque stoechiométriques de haute qualité présentant pas de gradients spatiaux significatifs soit dans l'épaisseur ou la composition.

Les deux principaux paramètres de dépôt optimisés pour le MOCVD sont le rapport Y/Mn des précurseurs dans la solution injectée et la température de dépôt. On observe une croissance MOCVD sélective de films YMO/Si dépendante de la température: les échantillons proches du rapport Y/Mn optimisé déposé à 600 °C sont amorphes, ceux qui sont déposés à 750 °C sont orthorhombiques et enfin ceux qui sont déposés dans l'intervalle de 800 à 850 °C sont hexagonaux.

Une croissance sélective similaire est trouvée en fonction de la pression en O_2 (avec une température fixe) pour le PLD: à basse pression la phase h-YMO est formée, dans la gamme de pression O_2 intermédiaire la phase amorphe domine, tandis que à une pression élevée la phase o-YMO est stabilisée.

Sur des substrats de type pérovskite les paramètres de dépôt (température, rapport Y/Mn, pression d'oxygène) ont presque aucune influence et la phase o-YMO est stabilisé par un mécanisme de contrainte.

Caractérisation physico-chimiques et structurelles de films YMO sur substrat de Si(100)

Des conditions optimisées conduisent à des films presque stœchiométriques de haute qualité montrant aucun gradient spatial significatif dans soit l'épaisseur ou la composition. Les films YMO obtenus sont amorphes ou principalement polycristallins/texturés sur des substrats de Si (éventuellement une couche mince amorphe de 10 à 50 nm se forme entre les films cristallins et le Si). Tous les films déposés par MOCVD suivent un mode 3D de croissance colonnaire (colonnes de 15 à 40 nm de diamètre, en fonction des échantillons), typique pour le procédé MOCVD, avec une morphologie de chou-fleur.

La phase amorphe dans les films YMO est facilement formée et stable pour les conditions de croissance MOCVD dans une large gamme de compositions. La variation de la composition

stœchiométrique est observée pour les phases cristallines YMO (indiqué par les grandes variations dans les valeurs des paramètres de maille). Ceci est principalement lié à la modification du rapport Y Mn dans la solution injectée.

Les films h-YMO sont principalement texturés selon l'axe *c* pour la croissance MOCVD et orienté principalement (11-20) et (11-21) pour la croissance PLD. Ces orientations sont fortement influencées par la température de dépôt et, dans une moindre mesure par le rapport Y/Mn dans la solution (MOCVD) et sont indépendants de la pression d'oxygène (PLD).

La phase o-YMO est présente dans les films déposés par les deux techniques MOCVD et PLD sans aucun mécanisme de stabilisation épitaxiale et libre de la phase h-YMO. Les films o-YMO sont principalement polycristallins. En plus de la croissance colonnaire caractéristique pour le MOCVD, les films o-YMO présentent des agrégats se trouvant sur la surface du film (200 à 400 nm en taille). La croissance PLD produit des grains de 20-30 nm en taille et des agrégats de grains entre 65 et 75 nm.

Transformations et stabilité de phase

Les expériences menées par des recuits thermiques ex-situ et in-situ afin d'étudier la stabilité de la phase o-YMO ont montré qu'une transformation de phase irréversible de l'état amorphe à la phase cristalline o-YMO se déroule dans les films Y-Mn-O déposés par MOCVD sur le substrat Si(100) à une température à peu près constante (~ 700 °C) et dans une courte période de temps (~ min). La phase o-YMO ainsi obtenue est stable au moins jusqu'à 900 °C. A température plus élevée, une diffusion du substrat de Si dans la couche, conduit à la formation d'une phase silicate.

Caractérisation physico-chimique et structurelle de films YMO sur de substrats STO, LAO et LSAT à orientation (100)

Les films o-YMO, déposés par les deux techniques MOCVD et PLD présentent une microstructure dense et des surfaces homogènes, sans agrégats de particules, indépendamment du substrat. Le MOCVD produit une croissance colonnaire avec des colonnes de diamètre entre 10 et 20 nm et une interface substrat-couche lisse. La morphologie des films déposées par PLD dépend de la pression d'O_2: des grains de forme polygonales très denses, environ 30 nm de diamètre, sont obtenus à faible P_{O2} ($1.4 \cdot 10^{-4}$ bar) tandis qu'à P_{O2} plus élevées ($3 \cdot 10^{-1}$ bar) des grains de forme ronde, entre 20 et 30 nm et compatible avec une croissance colonnaire sont produites.

Les films épitaxiés o-YMO sont principalement orientés (010) sur les substrats de STO et LSAT et (101) sur le substrat de LAO. Des études détaillées sur des films d'YMO/STO de 12 nm et 23 nm d'épaisseur ont montré qu'en fait quatre types de domaines sont présents. Ceci est équivalent à avoir deux types de domaines tourné de 90° dans le plan donnes par la relation épitaxiale suivante:

- $[010]_{YMO}//[100]_{STO}$ et $[100]_{YMO}//[011]_{STO}$
- $[010]_{YMO}//[100]_{STO}$ et$[100]_{YMO}//[0\text{-}11]_{STO}$
- $[10\text{-}1]_{YMO}//[100]_{STO}$ et $[010]_{YMO}//[010]_{STO}$
- $[10\text{-}1]_{YMO}//[100]_{STO}$ et $[010]_{YMO}//[001]_{STO}$

Les paramètres *b* et *c* diminuent avec l'augmentation des épaisseurs de films tandis que le paramètre *a* augmente avec l'augmentation de l'épaisseur du 12 à 23 nm. Toutes les valeurs tendent vers les valeurs du massif. Les analyses de diffraction des rayons X et RSM indiquent des films contraints avec un mécanisme de relaxation qui dépend de l'épaisseur. Les paramètres de maille des films o-YMO sont fortement affectés par la pression d'oxygène dans le cas des films déposés par PLD.

Les observations TEM confirment le scénario de domaines pour le film d'épaisseur 12 nm. En outre, les images TEM haute résolution ont révélé que le film est complètement contraint avec une couche limite de ~ 3 nm. Au-dessus de cette couche le film commence à se relaxer progressivement.

Les propriétés magnétiques

Les propriétés magnétiques des films YMO (amorphes, orthorhombiques ou hexagonales) indiquent un comportement général de verre de spin. Une faible contribution ferromagnétique est présente à 5 K.

Pour les films initialement amorphes l'aimantation présente un maximum dans la courbe ZFC entre 11 et 19 K.

Le magnétisme pour les films h-YMO est caractérisé par une division de la courbe ZFC-FC et d'un maximum dans la courbe ZFC à T_f = 20 K. Une séparation des courbes ZFC-FC a été observée pour les poudres polycristallines à ~ 65 ($Y_1Mn_1O_3$) et 70 K ($Y_{0.95}Mn_1O_3$), sans maximum dans le ZFC. Au contraire, le monocristal h-YMO montre un ordre antiferromagnétique pur à T_N = 70 K.

Les mesures magnétiques sur les films initialement o-YMO sur des substrats de Si indiquent un comportement de verre de spin, caractérisé par une séparation des courbes ZFC-FC, avec un maximum dans la courbe ZFC à T_f = 20 K et au T_f = 32 K pour les films o-YMO cristallisés après recuits. De même, les films o-YMO sur STO, LAO et LSAT, présentent le même comportement de séparation des courbes ZFC-FC avec des maxima de la courbe ZFC entre 26 et 50 K.

Les perspectives futures

Plusieurs directions peuvent être envisagées pour la poursuite de notre étude. La stabilité de la phase o-YMO a été étudiée dans le cadre des traitements thermiques à travers des expériences Raman. Une deuxième étape dans l'étude de la stabilité de cette phase serait de vérifier l'effet de l'application de la haute pression (transformer la poudre h-YMO dans la phase o-YMO et étudier l'effet de la pression sur la phase o-YMO) et voir si une transition se produit. Cette étude n'a pas été rapportée dans la littérature.

Un autre axe de recherche peut être l'étude de la ferroélectricité dans les films monodomaines o-YMO contraints afin d'avoir une image complète des propriétés multiferroïques. Cela implique d'affiner les paramètres de dépôt optimaux et trouver le substrat approprié pour produire des films o-YMO monodomaines et stœchiométriques. Ensuite, il serait intéressant d'étudier les films minces non-stœchiométriques $Y_{1-x}Mn_{1-x}O_{3\pm\delta}$ (contraintes, Raman, magnétisme, ferroélectricité).

Parmi d'autres propriétés existantes dans les films YMO il semble très intéressant d'étudier les propriétés de commutation résistive. Dans un article publié récemment [22] il est démontré que les films minces $YMnO_3$ présentèrent une commutation résistive unipolaire et non volatile qui pourrait être une voie prometteuse pour la conception et la fabrication de dispositifs nouveaux.

Enfin, nous proposons l'étude du dopage de la phase $YMnO_3$, en particulier avec du Fe et la synthèse des pérovskites doubles (Y_2MnXO_6, X=Fe, Co, Ni) sous forme de film mince ou en massif au vu de calculs théoriques qui prédisent une comportement multiferroïque [23] et des résultats expérimentaux qui ont signalé une température de Néel de 328 K [24].

Références

1. Kimura, T., et al., *Magnetic control of ferroelectric polarization.* Nature, 2003. **426**(6962): p. 55-58.
2. Eerenstein, W., N.D. Mathur, and J.F. Scott, *Multiferroic and magnetoelectric materials.* Nature, 2006. **442**(7104): p. 759-765.
3. Khomskii, D., *Classifying multiferroics: Mechanisms and effects.* Physics, 2009. **2**: p. 20.
4. Jeroen van den, B. and I.K. Daniel, *Multiferroicity due to charge ordering.* Journal of Physics: Condensed Matter, 2008. **20**(43): p. 434217.
5. Green, M.A., A. Ho-Baillie, and H.J. and Snaith, *The emergence of perovskite solar cells.* Nat Photon, 2014. **8**(7): p. 506-514.
6. Wang, Y.T., C.W. Luo, and T. Kobayashi, *Understanding Multiferroic Hexagonal Manganites by Static and Ultrafast Optical Spectroscopy.* Advances in Condensed Matter Physics, 2013. **2013**: p. 13.
7. Rabe, K.M., C.H. Ahn, and J.M. Triscone, *Physics of Ferroelectrics: A Modern Perspective*. 2007: Springer.
8. Liu, S.-H., et al., *Structural transformation and charge transfer induced ferroelectricity and magnetism in annealed YMnO3.* AIP Advances, 2011. **1**(3): p. -.
9. Bos, J.-W.G., B.B. van Aken, and T.T.M. Palstra, *Site Disorder Induced Hexagonal−Orthorhombic Transition in Y3+1-xGd3+xMnO3.* Chemistry of Materials, 2001. **13**(12): p. 4804-4807.
10. Graboy, I.E., et al., *HREM Study of Epitaxially Stabilized Hexagonal Rare Earth Manganites.* Chemistry of Materials, 2003. **15**(13): p. 2632-2637.
11. I. E. Graboy, A.A.B., O. Yu. Gorbenko, A. R. Kaul, C. Dubourdieu, J.-P. Sénateur, V. L. Svetchnikov, and H. W. Zandbergen *HREM Study of Epitaxially Stabilized Hexagonal Rare Earth Manganites.* Chem. Mater. , 2003. **15**: p. 2632-2637.
12. Malo, S., et al., *Structural and magnetic properties of the solid solution (0<x<1) YMn1−x(Cu3/4Mo1/4)xO3.* Solid State Sciences, 2005. **7**(12): p. 1492-1499.
13. Toulouse, C., et al., *Lattice and spin excitations in multiferroic h-YMnO3.* Physical Review B, 2014. **89**(9): p. 094415.
14. Huang, Z.J., et al., *Coupling between the ferroelectric and antiferromagnetic orders in YMnO3.* Physical Review B, 1997. **56**(5): p. 2623-2626.
15. Uusi-Esko, K., et al., *Characterization of RMnO3 (R=Sc, Y, Dy-Lu): High-pressure synthesized metastable perovskites and their hexagonal precursor phases.* Materials Chemistry and Physics, 2008. **112**(3): p. 1029-1034.
16. J. Fontcuberta, I.F., L. Fabrega, F. Sanchez, X. Marti, V. Skumryev, *Ferroelectricity and strain effects in orthorhombic YMnO3 thin films.* Phase Transitions, 2011. **84**(5–6): p. 555–568.
17. Chen, J., et al., *Tuning of transport and magnetic properties in epitaxial LaMnO3+x thin films.* Advances in Condensed Matter Physics, 2014. **2014**: p. 5.
18. Lei, D.Y., et al., *Spectroscopic ellipsometry as an optical probe of strain evolution in ferroelectric thin films.* Optics Express, 2012. **20**(4): p. 4419-4427.
19. Balasubramanian, K.R., et al., *Growth and structural investigations of epitaxial hexagonal YMnO3 thin films deposited on wurtzite GaN(001) substrates.* Thin Solid Films, 2006. **515**(4): p. 1807-1813.
20. Uusi-Esko, K., J. Malm, and M. Karppinen, *Atomic Layer Deposition of Hexagonal and Orthorhombic YMnO3 Thin Films.* Chemistry of Materials, 2009. **21**(23): p. 5691-5694.

21. H. W. Brinks, H.F., A. Kjekshus, *Synthesis of Metastable Perovskite-type YMnO3 and HoMnO3.* JOURNAL OF SOLID STATE CHEMISTRY 1997. **129**: p. 334-340
22. Bogusz, A., et al., *Resistive switching in polycrystalline YMnO3 thin films.* AIP Advances, 2014. **4**(10): p. -.
23. Kumar, S., et al., *Theoretical prediction of multiferroicity in double perovskite Y2NiMnO6.* Physical Review B, 2010. **82**(13): p. 134429.
24. Liu F, L.J., Li Q, Wang Y, Zhao X, Hua Y, Wang C, Liu X., *High pressure synthesis, structure, and multiferroic properties of two perovskite compounds Y2FeMnO6 and Y2CrMnO6.* Dalton Trans., 2014. **43(4)**: p. 1691-8.

Abstract

Multiferroic $YMnO_3$ (YMO) films have been grown by MOCVD on (100)-oriented Si, STO, LAO and LSAT substrates. The effect of the film thickness and the chemical composition on structural and magnetic properties has been investigated. YMO can crystallize in two structure: hexagonal (h-YMO) and orthorhombic (o-YMO), generally considered as stable and metastable phases, respectively. Both phases, together with their amorphous precursor phase, are studied in this thesis. On one side, a selective growth of the amorphous, o-YMO or h-YMO phase is achieved on Si substrates through the deposition conditions. An extensive study of the optimal conditions has been carried out. An irreversible phase transformation from amorphous to crystalline o-YMO phase takes place at an almost constant temperature (~ 700 °C) and in a short period of time (~ min). The o-YMO phase thus obtained is stable at least up to 900 °C.

On the other side, the o-YMO phase is epitaxially stabilized on perovskite type substrates (STO, LAO, LSAT). The films on STO and LSAT substrates present mainly the (010) orientation while those on LAO substrate are (101)-oriented. Secondary domain orientation are observe in particular on STO substrates: (010) in plane with 90° rotation. Strained films are observed for small thicknesses. The magnetic measurements show a spin glass behavior for either o- or h-YMO phase, independently of the substrate.

Keywords: MOCVD; YMnO3; thin films; Si, STO, LAO and LSAT substrates; phase transformation, epitaxial stabilization

Résumé

Couches minces multiferroiques d'$YMnO_3$ (YMO) films ont été synthétisée par MOCVD sur de substrats de Si, STO, LAO et LSAT orientées (100). L'effet de l'épaisseur des couches et de la composition chimique sur les propriétés structurales et magnétiques a été étudié. YMO peut cristalliser dans deux structure : hexagonale (h-YMO) et orthorhombique (o-YMO), généralement considérée comme les phases stables et métastables, respectivement. Les deux phases, ainsi que leur phase précurseur amorphe sont étudiées dans cette thèse. D'un côté, une croissance sélective de la phase amorphe, h-YMO ou o-YMO est réalisé sur des substrats de Si en ajustant les conditions de dépôt. Une étude approfondie des conditions optimales a été réalisée. Une transformation de phase irréversible de l'état amorphe à la phase cristalline o-YMO a lieu à une température à peu près constante (~ 700 ° C) et dans un court période de temps (min ~). La phase o-YMO ainsi obtenue est stable au moins jusqu'à 900 ° C.

De l'autre côté, la phase o-YMO est stabilisé par épitaxie sur des substrats de type perovskite (STO, LAO, LSAT). Les films sur STO et LSAT présentent principalement l'orientation (010) tandis que ceux sur les substrats de LAO sont orientées (101). Une orientation secondaire de domaines est observée en particulier sur des substrats de STO: rotation de 90 ° dans le plan du domaine (010). A des faibles épaisseurs les couches sont contraintes. Les mesures magnétiques montrent un comportement de verre de spin pour chacune de phase o- ou h-YMO, indépendamment du substrat.

Mots-clés: MOCVD; $YMnO_3$; couches minces; substrats de Si, STO, LAO et LSAT; transformation de phase, stabilisation épitaxiale